Quantitative analysis of ion transport in human airway epithelial cells

Donal Liam O'Donoghue

A thesis submitted to

University College London

for the degree of

Doctor of Philosophy

Centre for Mathematics and Physics in the Life Sciences and Experimental Biology

University College London

August 1, 2014

I, Donal Liam O'Donoghue, confirm that the work presented in this thesis is my own. Where information has been derived from other sources, I confirm that this has been indicated in the thesis.

Abstract

In the human airways, transepithelial ion transport is facilitated by a complex arrangement of ion channel, pump, cotransporter and tight junction proteins. The transepithelial potential difference (V_t), which shows characteristic changes in cystic fibrosis (CF) disease, is commonly measured in the study of epithelial ion transport. In this thesis I develop a mathematical model of ion transport in human nasal epithelia (HNE), in order to quantitatively investigate the relationship between individual transport protein activities and the transepithelial potential generated.

In the first part of this work, I investigate the biophysical basis of hyperpolarised basal V_t and increased amiloride sensitive V_t in CF HNE cells. Using published electrophysiological measurements from *in vitro* experiments, I estimate the value of apical Na^+ and apical Cl^- permeability in both CF and non-CF HNE cells. I find apical Na^+ permeability is increased in CF relative to non-CF cells, and apical Cl^- permeability is decreased in CF, suggesting increased epithelial sodium channel (ENaC) activity, as well as decreased activity of anion specific CFTR channels, is responsible for the abnormal bioelectric properties of CF HNE cells.

In the second part of this work, I focus on the nasal potential difference (NPD) test commonly made in patients with CF, investigating the biophysical basis of interpatient variability in NPD measurements. I find that the variation in amiloride insensitive V_t observed in a group of CF patients, cannot be accounted for by variation in apical Na^+ and Cl^- permeability alone. It is necessary to assume incomplete block of ENaC channels by amiloride, and patient to patient variability in other physiological parameters, in order to fully explain the observed variability in this cohort of NPD traces.

Acknowledgements

I would like to thank my supervisors, Paola, Vivek and Guy, for their guidance, help and support throughout the course of my PhD, and Dr Nicholas Simmonds for kindly allowing me to use his clinical data in my work. Thanks to members of the Vergani and Moss labs past and present that I've shared an office with over the past four years, Sam, Matt, David, Emily and Rosie, for helpful discussions and conversations over many a cup of tea or coffee.

I would also like to mention fellow CoMPLEX students that shared the MRes/PhD experience with me, and who were always available to talk about work and life in general, thank you to David, Niclas, Abby, Nicolas and Mirna. Finally, thanks to my parents Margaret and Peter, for supporting me throughout my education and helping me get to this point, and of course, to Mary Clare, for support and encouragement throughout my time at UCL.

Contents

List of Figures

List of Tables

Chapter 1

Introduction

My research investigates the pathogenesis of cystic fibrosis (CF), a genetic disorder, by considering theoretically the biophysical basis of transepithelial ion transport in human airway epithelia. This approach is inherently interdisciplinary in nature, and lies at the interface between physiology and applied mathematics. Hence in the following sections I will first introduce some important concepts in epithelial physiology and ion transport, then discuss CF disease and how it affects airway epithelial electrophysiology. I will go on to review the previous mathematical analyses of epithelial ion transport processes, and finally outline some of the specific research goals of my thesis, in the context of this previous work.

1.1 Physiology of epithelial ion transport in the human airways

1.1.1 Form and function of epithelial tissue

Epithelial tissue consists of planar arrangements of closely packed cells which can line internal structures and compartments, or form thick secretory glands. In the human lungs, there is a continuous epithelium from the nasal pharynx, through the trachea and bronchus, all the way to the distal airways (see Figure 1.1). To a first approximation, the structure of the human airway epithelium (HAE) is that of a single monolayer of cells, which separates the airway lumen from the interstitial fluid (Figure 1.2). This form underlies two of the primary functions of this epithelium; (a) to create a physical boundary layer between the airway lumen and the internal body compartments, and (b) to regulate transport of small molecules and fluids between these two compartments (Wills et al., 1996).

A schematic diagram of an idealised epithelial monolayer is shown in Figure 1.2. A thin layer of liquid (the airway surface liquid or ASL) sits on top of the monolayer of epithelial cells, protecting them from inhaled bacterial pathogens (this is discussed further in Section

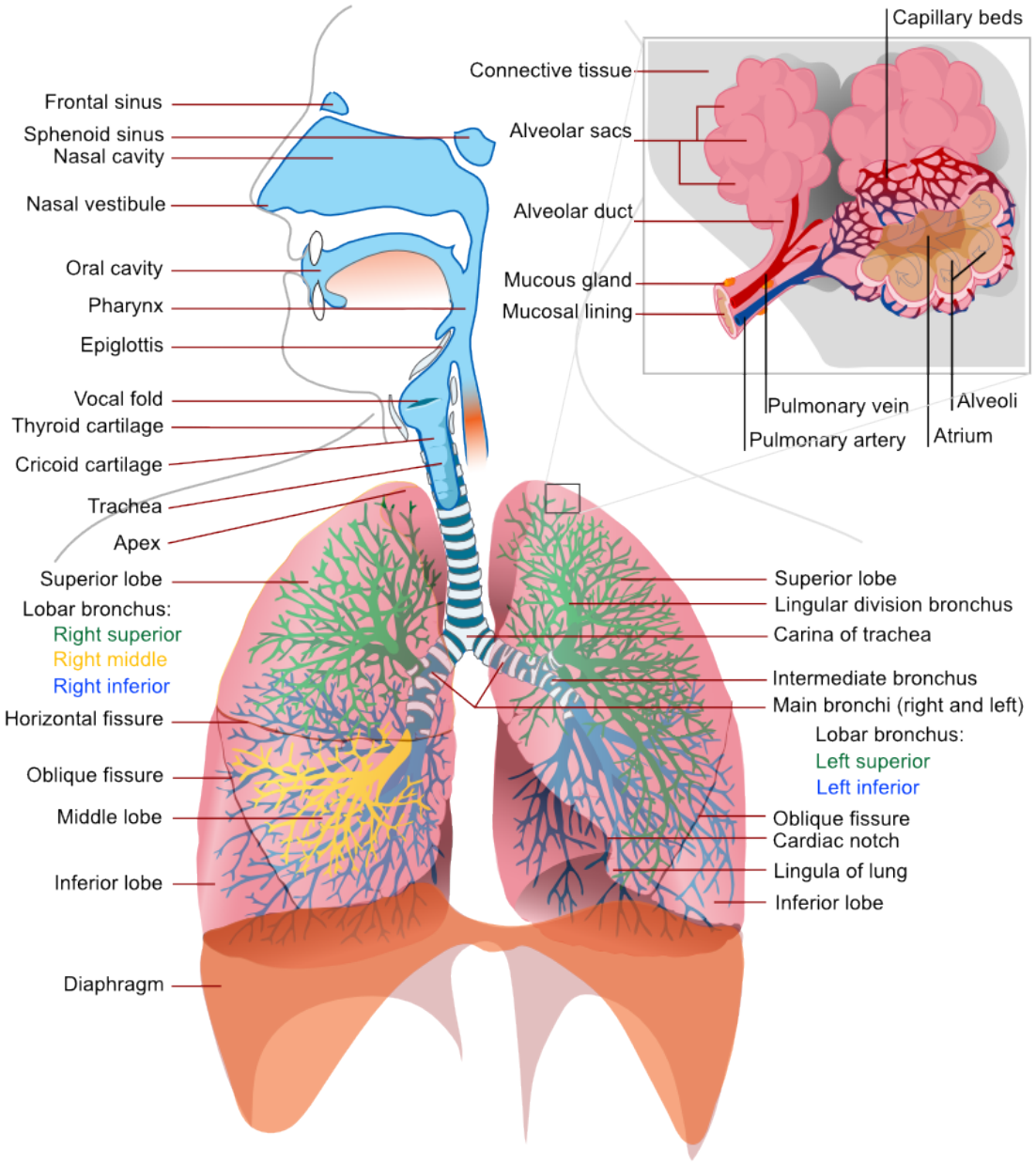

Figure 1.1: Diagram showing a cross-sectional view of the human respiratory system (Villareal, 2007a). The surface of the airways is covered by an epithelial layer that extends continuously from the nasal cavity, through the trachea and bronchus, towards the alveoli.

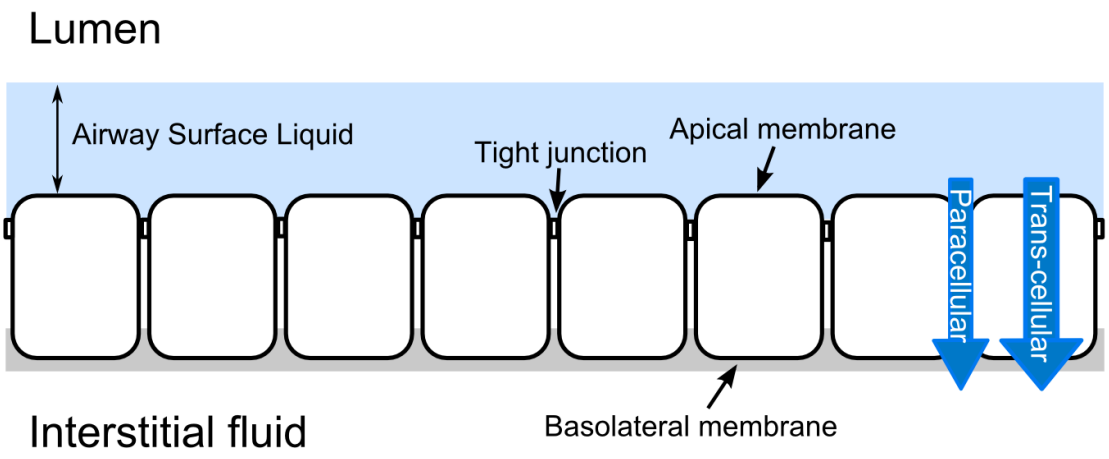

Figure 1.2: Schematic diagram of idealised human airway epithelia. The airway surface liquid (ASL) covers a monolayer of polarised epithelial cells, which separates the lumen from the interstitial fluid. Tight junction proteins bind epithelial cells together laterally, and divide the cell membrane into apical and basolateral areas. Transepithelial transport can occur via the transcellular route across apical and basolateral membrane, or via the paracellular route through the tight junctions and lateral intracellular space.

1.2.2). Individual epithelial cells are polarised and have two distinct membrane regions, the lumen-facing *apical* membrane, and the internal facing *basolateral* membrane. Tight junction proteins, which bind the lateral membranes of epithelial cells together, demarcate the boundary between these two regions and give the epithelial monolayer structural integrity. Transepithelial transport of small molecules is possible via two routes, along the *transcellular* pathway via the apical and basolateral membranes, and along the paracellular pathway through the tight junctions.

As well as being in contact with different compartments, the apical and basolateral membranes also differ intrinsically since they contain different sets of membrane proteins. Having an asymmetric distribution of membrane proteins allows the epithelium to direct transport vectorially across the monolayer. Net transport of small molecules across an epithelial barrier can thus be carried out.

1.1.2 Mechanisms of membrane transport in airway epithelia

The co-ordinated regulation of ion transport along the paracellular route, by tight junction proteins, and the trans-cellular route via membrane proteins, allows an epithelium to perform its role as a controller of ion transport. There are several modes of ion transport that are important to consider; passive, active and secondary active.

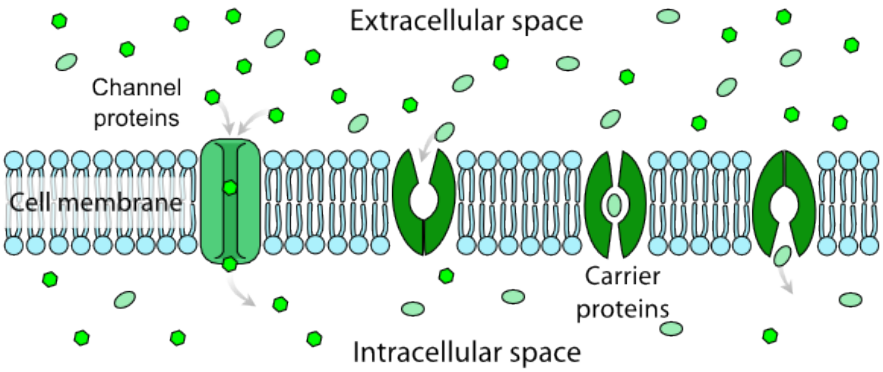

Figure 1.3: Small hydrophilic molecules cannot easily diffuse across lipid bilayer membranes with hydrophobic interiors. Mammalian cells facilitate movement of small molecules via channel or carrier proteins inserted in the lipid bilayer. Channel proteins form a small hydrophilic pore through which charged ions can diffuse, while carrier proteins bind molecules on one side of the membrane and release them on the other side, facilitating net transmembrane movement. Image from Villareal (2007b).

1.1.2.1 Passive transport in epithelia

Passive transport is so called, as it does not require any explicit energy input from the cell to take place. If there is an existing chemical or electric potential gradient, free ions in solution will diffuse down the gradient to the area of lower potential energy, providing there is no barrier to movement. However, small hydrophilic ions like Na^+ or Cl^- cannot diffuse across the hydrophobic centre of the cell's lipid bilayer membrane. Passive ion transport across the cell membrane must therefore be facilitated by proteins such as ion channels or transporters inserted in the cell membrane, as highlighted schematically in Figure 1.3.

In the case of passive transport, ion channel proteins provide a hydrophilic pore through which ions can diffuse, unimpeded by the hydrophobic interactions of the lipid bilayer. In the presence of an electrochemical gradient, ions will diffuse passively across the cell membrane, if there are ion channels whose pores are open - the cell is not using energy explicitly in the movement of these ions, but rather utilizing the free energy inherent in the potential energy gradient.

In airway epithelia, various ion channels localised in the apical and basolateral membranes facilitate passive transport. Tight junction proteins also allow passive transport of certain ions along the paracellular pathway of HAE.

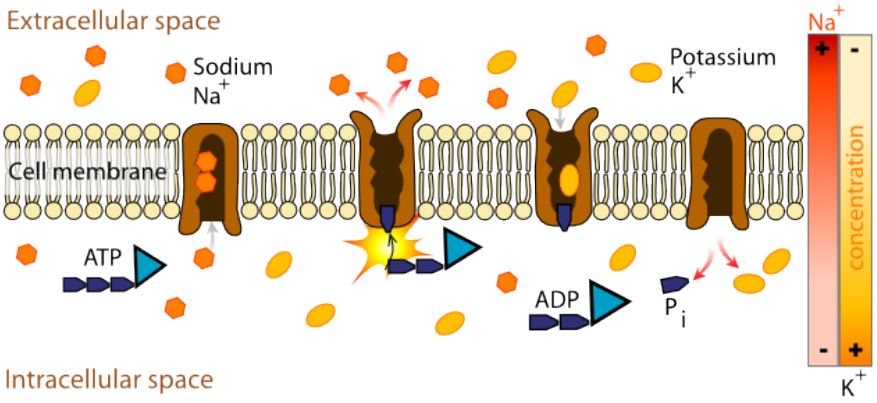

Figure 1.4: The $Na^+ - K^+ - ATPase$ actively transports Na^+ against an electrochemical gradient, by coupling the reaction cycle to the hydrolysis of ATP molecules. Image from Villareal (2007c).

1.1.2.2 Active transport in epithelia

Without the active energy input from a cell, all electro-chemical gradients would eventually dissipate, and no further passive transport would be possible. However if there is energy input from the cell to keep the internal ionic concentrations away from equilibrium, electro-chemical gradients can be maintained.

Active transport of ions against an electrochemical gradient is mediated by pumps. Rather than simply provide a pathway for movement, as in the case of channel proteins, carrier proteins must physically translocate the molecules from one side of the cell membrane to the other. This involves binding the transported molecule on one side of the membrane, and undergoing a conformational change which leaves the binding site exposed on opposite side of the membrane, from where the molecule can finally unbind from the carrier having been transported across the membrane.

Perhaps the most important protein to carry out active transport is the $Na^+ - K^+ - ATPase$, which is ubiquitous in animal cells. The $Na^+ - K^+ - ATPase$ is expressed in the basolateral membrane of HAE cells, and moves K^+ ions into the cell, while pumping Na^+ out, against an electrochemical gradient (a schematic diagram of this process is shown in Figure 1.4). The pump uses energy from the hydrolysis of an ATP molecule to drive the reaction cycle in the direction necessary to move Na^+ ions out of the cell.

1.1.2.3 Co-transport in epithelia

Co-transport proteins can also move molecules across a membrane without direct energy input. In a similar manner to active transport, the carrier protein physically binds the molecules to be

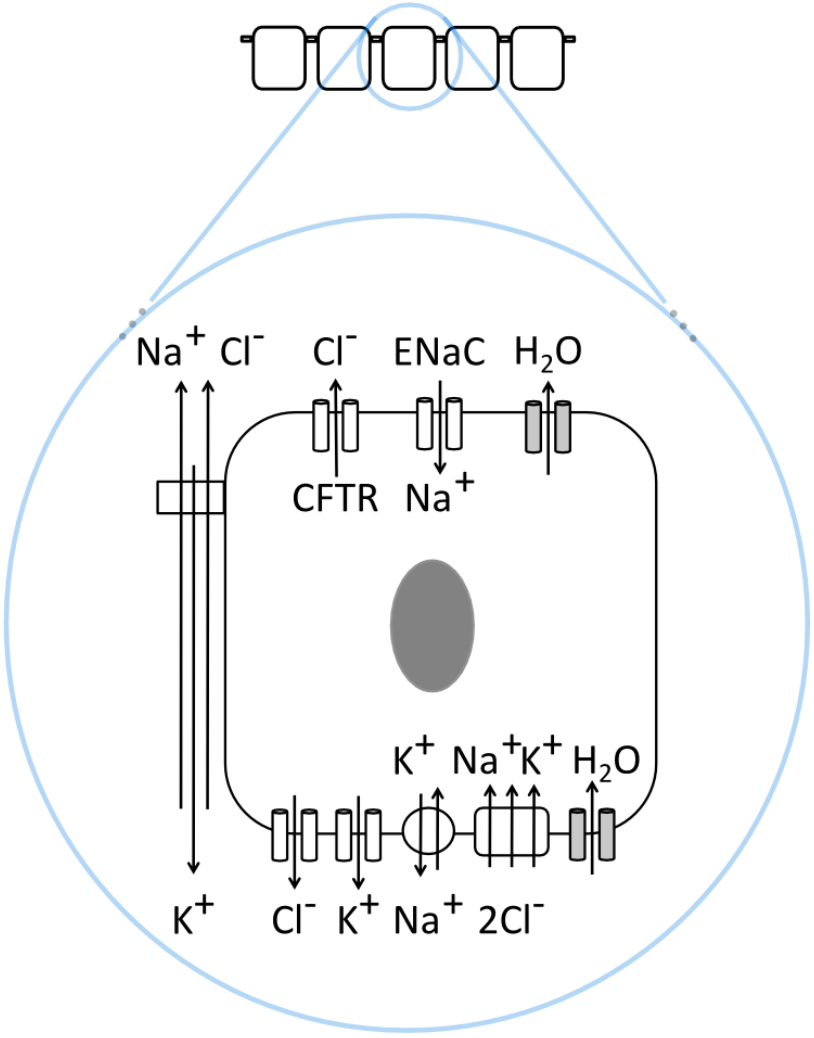

Figure 1.5: Diagram showing the major ion transport proteins in human nasal epithelial cells. In the apical membrane there are channel proteins, and in the basolateral membrane there are channel and carrier proteins (pumps and cotransporters).

transported. In contrast to active transport however, the movement of the bound molecules is not always against an electrochemical gradient. Typically one of the bound species will be moving in an energetically favourable direction, and the energy gained from this movement helps the conformational change required to move a second species against a potential energy gradient. This type of transport is referred to as *secondary active*, as it does not require explicit energy input from the cell, but does require the cell to keep ion gradients away from equilibrium. It is also referred to as *cotransport* or *symport* as typically two or more ions or molecules are transported simultaneously.

1.1.3 Ion transport pathways in human airway epithelia

Ion transport in the human airways is mediated by a collection of ion channels, pumps and co-transporters. Figure 1.5 shows a schematic diagram highlighting several of the major transport pathways in a typical human nasal epithelial (HNE) cell. The apical membrane contains Na^+ and Cl^- ion channels, the epithelial sodium channel (ENaC) and the cystic fibrosis transmembrane conductance regulator (CFTR). The basolateral membrane of these epithelial cells contain Cl^- and K^+ ion channels, as well as $\mathrm{Na}^+ - \mathrm{K}^+ - \mathrm{ATPase}$ pumps, and $\mathrm{Na}^+ - \mathrm{K}^+ - 2\mathrm{Cl}^-$ cotransporters. The tight junctions of the epithelia also allow transport of ions such as Na^+, Cl^- and K^+, directly between the ASL and interstitial fluid.

1.1.3.1 Ion channel proteins

The *epithelial* Na^+ *channel*, ENaC, is known for its high affinity for amiloride, a potassium sparing diuretic. In concert with the $\mathrm{Na}^+ - \mathrm{K}^+ - \mathrm{ATPase}$, ENaC is involved in active reabsorption of Na^+ in several epithelia - in humans it is expressed in the kidney, colon, lung and sweat glands (Garty and Palmer, 1997). As a result ENaC activity is important in maintaining homeostasis of Na^+ and K^+ in the body, and has been implicated in the pathogenesis of several diseases. These include hypertension resulting from improper function of ENaC in the kidneys (Bubien, 2010), and cystic fibrosis, which I will discuss further in Section 1.2.

In the human airways, ENaC channels are constitutively active, therefore play an important role in regulating ASL composition. ENaC activity in the airways can be regulated by myriad factors, although regulation by proteases, intracellular, extracellular and membrane bound, predominates (for a review see Gaillard et al. (2010)). There is also evidence that ENaC activity can be regulated by CFTR channel activity, directly through physical interaction (Berdiev et al., 2009), or indirectly via intracellular messengers such as cAMP (Stutts et al., 1995), although this regulatory interaction remains a matter of debate.

Cystic fibrosis trans-membrane conductance regulator (CFTR) is an ATP gated, anion specific channel, which is activated by phosphorylation, primarily by protein kinase A, following a rise in intracellular cAMP. CFTR is localised to the apical membrane of secretory epithelia, and in humans is expressed in the respiratory and digestive systems, the pancreas and in sweat glands (Gadsby et al., 2006). The primary role of CFTR in the airways is to facilitate secretion of Cl^- and HCO_3^- by epithelial cells, regulating the ionic composition of the ASL. Mutations in the *CFTR* gene are responsible for cystic fibrosis disease, but there are multiple hypotheses

as to how the disease progresses from malfunctioning channel to persistent lung infections. The presence of a putative regulatory interaction between CFTR and ENaC, that is lost in CF, has been particularly controversial. In Section 1.2.2 and 1.2.5 I discuss these issues in more detail.

Other ion channels expressed in the apical membrane of airway epithelia include *Calcium-activated* Cl^- *channels* (CaCC), and K^+ channels. CaCC channels are not thought to be basally active, but are interesting in the context of CF disease, as they provide an alternate route for Cl^- transport, that could form part of a therapeutic strategy (Cuthbert, 2011). There is limited evidence for voltage gated KCNQ type K^+ channels expressed in the apical membrane of certain cell types (Moser et al., 2008; Bardou et al., 2009), but they have not yet been implicated in the pathogenesis of CF lung disease.

The basolateral membrane of airway epithelial cells expresses a number of different types of K^+ channels. Evidence of functional voltage gated (KvLQT1) and calcium activated (KCa3.1) K^+ channels has been found in human nasal epithelial cells (Bardou et al., 2009), and they have been shown to influence Cl^- secretion in studies of ion transport in epithelial cells (Cowley and Linsdell, 2002). These channels provide a route for K^+ that enters the cell via the $Na^+ - K^+ - ATPase$ to be recycled, and hence are important for cellular homeostasis. As K^+ channels can influence the basolateral membrane potential, and hence the electric potential across the apical membrane, they can be stimulated to induce Cl^- secretion from epithelial cells (Cotton, 2000).

Basolateral Cl^- channels have been reported, distinct from the CFTR and CaCC channels that are found apically (Itani et al., 2007). Their exact physiological role in regulating transport is not yet clear, but may involve regulating the driving force for Cl^- secretion by appropriately altering the basolateral membrane potential (He et al., 2011), and again similarly to the basolateral K^+ channels, provide a route for recycling the Cl^- ions that enter the cell via the $Na^+ - K^+ - 2Cl^-$ co-transporter.

1.1.3.2 Carrier proteins

The $Na^+ - K^+ - ATPase$ pump is expressed in the basolateral membrane of all epithelial cells in the human airways. As outlined previously (Section 1.1.2.2) the pump uses energy from the hydrolysis of one ATP molecule to transport three Na^+ ions out of the cell and two K^+ ions into the cell per cycle. The action of the ion pump ensures that sodium concentrations within the cell are kept low, and potassium concentrations high. Maintaining these concentra-

tion gradients is essential for other transport mechanisms, such as co-transport and diffusion through ion channels. As well as maintaining ion concentrations away from equilibrium, the $\mathrm{Na}^+ - \mathrm{K}^+ - \mathrm{ATPase}$ strongly couples the transport of Na^+ and K^+ ions, and is implicated in cell volume regulation. The pump can be blocked by the cardiac glycoside ouabain, which is used in experimental studies of epithelial transport.

The $\mathrm{Na}^+ - \mathrm{K}^+ - 2\mathrm{Cl}^-$ cotransport protein (NKCC) is expressed in the basolateral membrane of several secretory epithelia, including the intestines, airways and salivary glands. In the airways the NKCC1 isoform of the protein is expressed, and under normal physiological conditions it couples the movement of two Cl^- ions into the cell (along with one Na^+ and one K^+ ion), which can then be secreted onto the airway lumen via apical Cl^- channels. As the NKCC co-transporter couples the transport of three osmotically important ions, its activity has been linked to cell volume regulation. NKCC co-transport can be inhibited by loop diuretics such as furosemide and bumetanide. Readers interested in a further details of NKCC co-transport in secretory epithelia can consult the review of Haas and Forbush (2000).

1.1.3.3 Tight junction proteins

Ion transport directly between the luminal and serosal compartments occurs via tight junctions and the lateral intracellular space, together referred to as the paracellular pathway. The tight junctions are formed by *claudins*, a family of complex proteins that adhere to the lateral membrane of epithelial cells. Claudins maintain the structural integrity of the epithelial barrier and also determine the electrical resistance of the paracellular pathway. Depending on the claudin proteins expressed, the conductance of the pathway and its ion selectivity can vary dramatically (Coyne et al., 2003), and in the human airways there is limited evidence for cation selectivity (Coakley et al., 2003).

An important characteristic of an epithelial monolayer's electrophysiology, is how permeable the paracellular junctions are. Highly permeable paracellular pathways are termed *leaky*, as current is *shunted* through the less resistant paracellular path. Epithelia which can support a large transepithelial electric potential difference (PD) are referred to as *tight*, and have significantly less paracellular permeability. As a rule of thumb, epithelia are considered tight if their junctional resistance is greater than $500\ \Omega\ \mathrm{cm}^2$ and they can generate a transepithelial PD on the order of $10 - 100\ \mathrm{mV}$ (Wills et al., 1996). For comparison, the mean shunt resistance of human nasal epithelium has been previously estimated to be $412\ \Omega\ \mathrm{cm}^2$ and $623\ \Omega\ \mathrm{cm}^2$ in

non-CF and CF cultures respectively (Willumsen and Boucher, 1989).

1.1.3.4 HCO_3^- and H^+ transport in airway epithelia

The focus of this thesis is understanding ion transport in human nasal epithelial cells, with particular emphasis on understanding the transepithelial potential difference (PD) that is generated by this epithelium. As ion transport in nasal epithelial cells is expected to be dominated by Na^+, Cl^- and K^+ movements, I have thus far focused on outlining the major proteins involved in the transport of these three ions. In general however, there will also be movement of other ions into and out of nasal epithelial cells.

Bicarbonate (HCO_3^-) and proton (H^+) transport are of particular note. Although it is not known if HCO_3^- and H^+ currents significantly influence the transepithelial PD in nasal epithelial cells, they are important in regulating cell pH and have been implicated in a number of hypotheses regarding the pathogenesis of CF disease in the airways (discussed in detail in Section 1.2.2). Hence I will now introduce several transport mechanisms that are involved in the movement of these ions.

It is known that HCO_3^- can permeate through CFTR ion channels, although it is less permeable than Cl^-, with the permeability ratio of $Cl^- : HCO_3^-$ being estimated as $\approx 4 : 1$ (Poulsen, 1994). There is also evidence that these ions are transported by several carrier proteins located in the basolateral membrane of airway epithelial cells. Calu-3 cells, cells derived from human bronchial submucosal glands, express sodium bicarbonate cotransporters (NBC), which move both Na^+ and HCO_3^- ions into the cell. The stoichiometry of $Na^+ : HCO_3^-$ cotransport by NBC can be either 1:2 or 1:3 depending on which protein variant is expressed, but in Calu-3 cells the stoichiometry has yet to be determined definitively (Kreindler et al., 2006). Other carrier proteins known to be expressed in several regions of bronchial epithelia, include cation exchangers (NHE), which move one H^+ out and one Na^+ into the cell per cycle, and anion exchangers (AE), which can exchange one Cl^- for one HCO_3^- ion in either direction (Dudeja et al., 1999).

1.1.4 Investigating epithelial electrophysiology experimentally

A common experimental apparatus used in the study of epithelial electrophysiology, is the Ussing chamber, named after the Danish physiologist Hans Ussing who pioneered studies of electrogenic transport in frog skin epithelia. An Ussing chamber typically consists of two half chambers separated by a semi-permeable membrane. An epithelial monolayer can be cultured

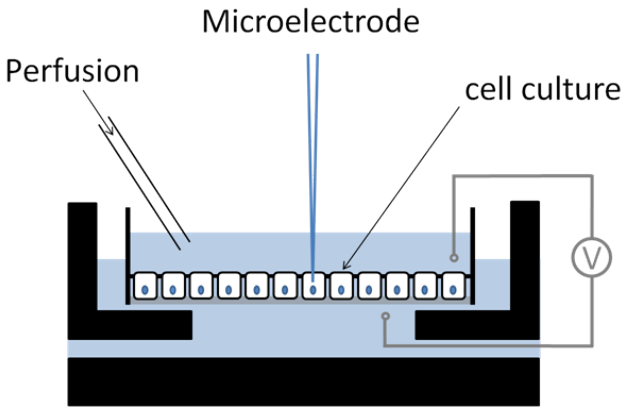

Figure 1.6: An Ussing chamber type experimental set up, modified to allow intracellular microelectrode recordings. An epithelial monolayer is cultured on a permeable support, and is bathed on either side by physiological saline solutions. The electric PD across the epithelium can be recorded while the composition of either the lumenal or serosal compartments is altered during an experiment.

on the permeable support and placed in the chamber, and the epithelium will be bathed on both sides by physiological solution. Electrodes inserted into both half-chambers, on either side of the monolayer, allow transepithelial electrical recordings to be performed. By adding pharmacological compounds into either of the chambers, an experimentalist can selectively inhibit or activate transport proteins expressed in the apical or basolateral membrane of the epithelium, and record the resulting change in the electrical properties that result. Similarly, the ionic composition of the bathing solutions can be manipulated to probe mechanisms of ion transport.

Two common modes of recording are the *open circuit* and *short circuit* configurations. In an open circuit recording, the spontaneous transepithelial PD is recorded, and no external current is driven across the monolayer. This scenario reproduces the conditions that epithelia would operate in, *in vivo*, under normal physiological circumstances. In the short circuit configuration, an external current is injected across the epithelium to clamp the transepithelial PD (V_t) to 0 mV. If the solutions on both sides of the monolayer are identical, then with $V_t = 0$ mV, there will be no passive transport, and hence the epithelium is said to be short circuited. In this manner an experimentalist can focus exclusively on changes in the short circuit current I_{sc} that arise from active transport mechanisms.

Figure 1.6 has a schematic diagram of a modified Ussing chamber, showing a cross-section of the apparatus. This works on the same principle as a standard Ussing chamber - transepithelial electrical recordings are made while the solutions bathing the monolayer are altered. However here the luminal chamber is open, so that a microelectrode can gain direct access

to the monolayer and make electrical recordings from inside epithelial cells. In this set up, intracellular concentrations and individual membrane potentials can be measured, as well as transepithelial potential and current recordings.

This is the experimental scenario I aim to model mathematically, primarily because of the extensive data sets available in the literature for these types of experiment, which I can use for parameter estimation purposes. In particular, there are data sets covering the electrophysiological response of CF HNE cells and non-CF HNE cells to amiloride addition in the luminal bath, and also removal of Cl^- from the lumen perfusate (Willumsen et al., 1989b; Willumsen and Boucher, 1989, 1991b,a). If I can simulate these experimental perturbations computationally, then I can make predictions required to estimate parameter values from these data sets.

1.2 Cystic fibrosis disease and abnormal epithelial transport

1.2.1 Overview of CF disease

Cystic fibrosis (CF) is an autosomal, recessive genetic disorder that impairs quality of life and reduces life expectancy (Davies et al., 2007). CF is prevalent amongst Caucasians, being the most common lethal single gene disorder found in people of European descent, and on average 1 in 2500 children born in the UK will suffer from the disease (Dodge et al., 2007).

The disease is caused by loss of function mutations in the *CFTR* gene. *CFTR* was first identified in 1989 (Rommens et al., 1989), and since then over 1900 different disease causing mutations have been recorded in CF patients (see www.genet.sickkids.on.ca/cftr). Mutations are classified according to how they manifest at the level of protein function. The most common, the $\Delta\mathrm{F508}$ mutation, is present in 90% of patients (in one or two copies). $\Delta\mathrm{F508}$ mutations result in incorrect protein folding and subsequent premature degradation, prior to trafficking and membrane insertion (class II) (Rowe et al., 2005; Lukacs and Verkman, 2012). Other classes of mutations produce proteins with reduced or absent ion channel activity (class III and IV), or decrease the amount of transcripts of CFTR being produced (class V).

Since CFTR is expressed in several tissues in the body, CF has several different symptoms including chronic lung infections, fibrosis of the pancreas, gastrointestinal difficulties, abnormal function of the sweat glands and infertility in male patients (Ratjen and Döring, 2003). The most common cause of death amongst CF sufferers is lung failure resulting from persistent bacterial infections (Kerem et al., 1992) and the median survival age is 40 years in the UK (Simmonds et al., 2011).

1.2.2 Pathogenesis of CF disease in the human airways

While the genetic origins of CF are known and have been extensively characterised at the molecular level, how exactly the absence of functioning CFTR anion channels leads to the chronic lung infections observed in CF, is not understood to the same degree. There is a consensus that CFTR channels, either directly or indirectly, are involved in the failure of the lungs' mucociliary clearance mechanism, responsible for defence against inhaled bacterial pathogens (Boucher, 2003). In order to begin to understand the link between the two, I first must look at how the airway surface microenvironment differs between healthy and CF patients.

1.2.2.1 Airway surface microenvironment in health and disease

Figure 1.7 shows a schematic diagram of the microenvironment present on the surface of the human airways under normal physiological conditions. Covering a monolayer of ciliated epithelial cells lies a thin liquid layer, the airway surface liquid (ASL) layer. The ASL itself consists of two separate phases, an upper gel like layer of mucins (mucus layer) sitting atop a thin liquid layer bathing the cilia that protrude from the epithelial cells, known as the periciliary liquid (PCL) layer. The mucus layer can be transported by co-ordinated beating of the cilia. Any pathogens that enter the airways and get stuck in the mucus can be removed from the lungs via this mucociliary clearance mechanism. Maintaining a suitable ASL volume is critical to the proper functioning of this defence mechanism. As the airway epithelial cells are highly water permeable, the ionic content of the ASL will largely determine its depth. It has hence been hypothesised that disrupted ion transport can lead to abnormal ASL depth, contributing to lung disease in CF airways.

Figure 1.8 shows a schematic diagram of the airway epithelium surface microenvironment in tissue with a CF mutation. The mucus layer is thicker and more viscous than in healthy tissue, and there is some evidence that the depth of the PCL is reduced. Cilia cannot beat effectively in this environment, and this reduces efficacy of the mucociliary clearance mechanism. As a thick mucus layer builds up, and as inhaled bacterial pathogens are not removed rapidly, bacterial colonies can grow and take hold in the ASL. The major cause of morbidity and mortality in CF patients arises from chronic lung infections (and resulting inflammatory responses) that begin in this manner.

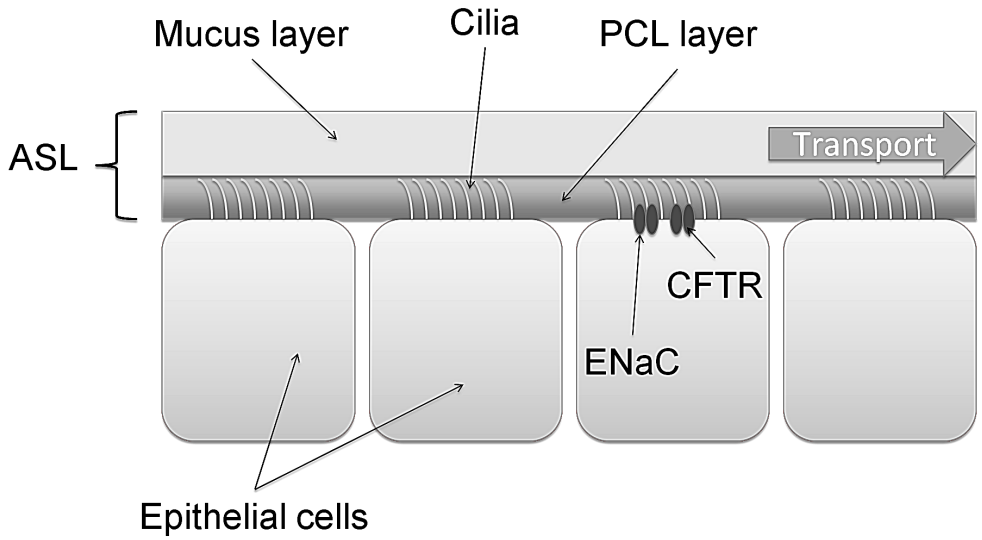

Figure 1.7: Schematic diagram of airway surface liquid (ASL) microenvironment on the surface of an epithelial monolayer. The volume of the periciliary liquid layer (PCL) is tightly regulated by movement of ions and water controlled by epithelial cells. Maintaining PCL depth at the same height as cilia, allows for efficient transport of mucus by a ciliary beating mechanism.

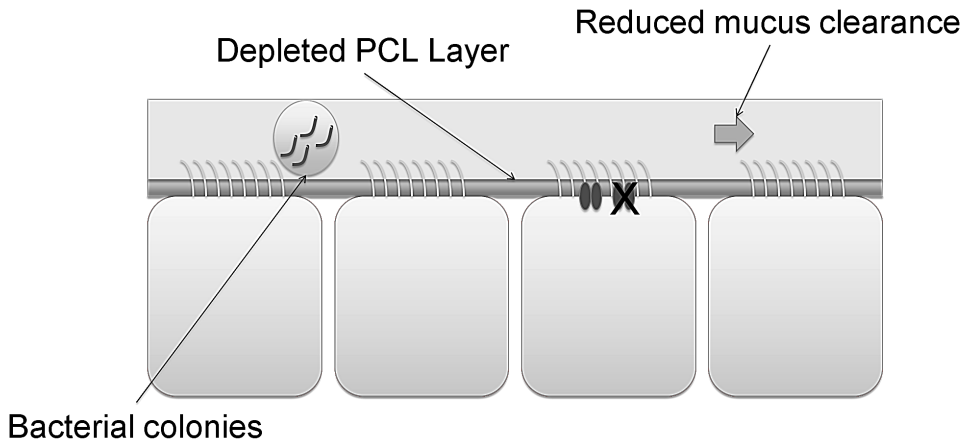

Figure 1.8: Schematic diagram of airway epithelial surface in the presence of a CFTR gene defect. Lack of functioning chloride channels in the apical membrane of epithelial cells disrupts normal electrolyte transport. As a result the mucus layer becomes dehydrated and viscous, mucociliary clearance is reduced, and bacterial infections can take hold in thick mucus layer.

1.2.2.2 ASL dehydration hypothesis

There are various theories as to why loss of function of CFTR channels in the airways results in this pathogenesis, and one of these is the dehydration hypothesis. This theory claims co-ordinated regulation of ion and water transport is crucial to maintaining adequate ASL depth and sufficiently hydrated mucus. Under normal circumstances, Cl^- transport via CFTR and CaCC channels, along with Na^+ transport through ENaC channels, is necessary to maintain the fluid balance between ASL and cell (Tarran et al., 2006). In CF this co-ordination is lost, and there is hyper-absorption of Na^+ and an inability to adequately secrete Cl^-. This leads to excess fluid absorption and loss of volume from the ASL. Implied in these theories is mis-regulation of ENaC as a major contributing factor to CF pathogenesis. For interesting reviews see Boucher (2007a,b) and Gaillard et al. (2010).

1.2.2.3 Abnormal mucin hypothesis

A second hypothesis claims that CF lung disease is the result of a direct involvement of CFTR in the production and secretion of mucins in the airways. One common line of reasoning here is that bicarbonate rich secretions allow mucins to acquire certain physicochemical properties that favour low viscosity and prevent adhesion of mucus plaques to the airway surface. With the loss of HCO_3^- transport through CFTR channels in CF, bicarbonate concentrations during mucin secretion are lower, and it is theorised that mucins become quite dense as a result (Quinton, 2008, 2010). While there is limited evidence of this happening *in vivo* in the human airways, there have been studies giving evidence that inhibiting Cl^-/HCO_3^- exchange in the submucosal glands of porcine distal bronchi leads to mucus obstruction of these airways (Inglis et al., 1998). Whether or not this phenomenon is critical to CF pathogenesis in the human airways is however still an open question.

1.2.2.4 Innate immune hypothesis

There is another line of thought that considers deficiencies in the lungs' innate immune system to be the primary cause of bacterial infections in the airways of CF patients. Under normal circumstances, the mucus layer of the ASL contains antimicrobial molecules which prevent inflammation and infection when bacterial pathogens are inhaled (Parker and Prince, 2011). In CF the activity or expression of these antimicrobial agents in the mucus layer may be reduced - and hence the inability to prevent persistent bacterial infections arises (Smith et al., 1996). The reduced effectiveness of these agents could be the result of the abnormal ASL microenvironment

in CF - there is evidence that in the CF pig lung, airway surface pH can negatively impact on the ability of antimicrobial molecules to kill bacterial pathogens (Pezzulo et al., 2012). There is also evidence that reduced fluid secretion by submucosal glands in the airways results in lower numbers of these innate immune proteins being present in the mucus layers, which would give rise to a similar inability to defend against bacterial infection (Wine and Joo, 2004).

1.2.3 Abnormal electrophysiological properties of CF epithelia

Before the *CFTR* gene was isolated, it was known that cystic fibrosis disease was causing problems in the human airways related to ion permeation and transport. In a series of studies in the early 1980's, transepithelial potential difference (PD) was measured in the airways of CF and non-CF patients (Knowles et al., 1981, 1983). These studies found that CF patients had increased baseline transepithelial PD, increased amiloride sensitive transepithelial PD, and reduced or absent response in PD when Cl^- in the lumen perfusate was removed. Initially it was not known if excessive Na^+ absorption was responsible for these abnormalities, or if it was possible they were due to problems with a Cl^- secretion pathway.

Indeed in subsequent studies, these transepithelial PD properties were measured *in vitro* in studies on primary cultures of airway epithelial cells from CF patients (Stutts et al., 1985; Boucher et al., 1986, 1988). It was shown with the use of ion replacement experiments that CF epithelial cells did not have a Cl^- conductance in their apical membrane, in contrast to non-CF cells. CF cells also appeared to have increased apical Na^+ permeability, inferred from an increased amiloride sensitive short circuit current.

Further studies on primary cultures of CF and non CF human nasal epithelial (HNE) characterised the electrophysiological differences quantitatively (Willumsen et al., 1989a,b; Willumsen and Boucher, 1991a,b). Willumsen and Boucher estimated the apical Na^+ permeability of CF HNE cells to be approximately 2-3 fold increased relative to non-CF HNE cells, and apical Cl^- permeability was estimated to be an order of magnitude smaller in CF, however these findings remain controversial.

1.2.4 Nasal potential difference measurements in the clinic

The transepithelial potential generated by the nasal epithelium is widely measured in patients with CF, as it is currently the only means of measuring ion transport function *in vivo* in the human airways. Information about the rate of Na^+ and Cl^- transport in a patient can be inferred from the transepithelial potential recording, and thus it can be used to assess the underlying

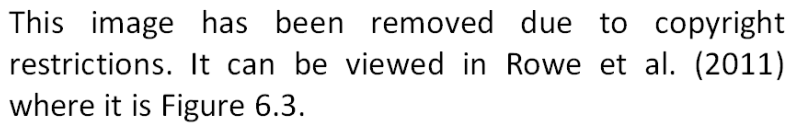

Figure 1.9: Standard nasal potential difference measurement protocol for studies of ion transport in CF. Basal V_t is measured initially, before amiloride is added to block ENaC channels. The change in V_t caused by amiloride addition is referred to as $\Delta V_t{+}\mathrm{amiloride}$, in this figure it is taken as the value of V_t in the second rectangle minus the value of V_t in the first. This is followed by manoeuvres to elicit Cl^- secretion, the first removing Cl^- from the lumen perfusate, and recording the change in V_t. This is referred to as $\Delta V_t{+}0[\mathrm{Cl}^-]_\mathrm{l}$ and is found by taking the value of V_t in the second rectangle from the value of V_t in the third rectangle. The second manoeuvre is adding isoproterenol to stimulate CFTR channel activity, and finally, adding ATP in order to stimulate and calcium activated Cl^- channels present. The metrics $\Delta V_t{+}\mathrm{iso.}$ and $\Delta V_t{+}\mathrm{ATP}$ can be measured from the values of V_t before and after the respective solution exchanges. Image from Rowe et al. (2011).

CFTR and ENaC channel activity (Middleton et al., 1994; Knowles et al., 1995). Nasal potential difference measurements are often taken as outcome measures in clinical trials of therapies aimed at rescuing CFTR activity in CF patients (Wilschanski and Yahav, 2003; Konstan et al., 2004), and they can also be used for diagnosis of CF in cases where the sweat test does not give a definitive result (Goubau et al., 2009).

A typical nasal potential difference (NPD) test consists of several stages (Rowe et al., 2011). Initially the basal level of ion transport is assessed by making a recording of the stable potential difference generated under normal physiological circumstances (see Figure 1.9). This recording is made with one probe placed in the airway lumen as saline solution is passaged over the surface of the nasal epithelium, while a second electrode is placed subcutaneously in order to measure the potential of the interstitium. The second stage involves passing a saline solution with amiloride across the mucosal surface, and recording the depolarisation that occurs

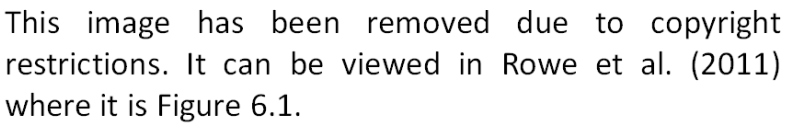

Figure 1.10: Comparison of a typical CF (red) and non-CF (black) NPD trace. In CF there is a hyperpolarised basal V_t, increased amiloride sensitive V_t, and little or no Cl^- secretion responses through CFTR channels. Image from Rowe et al. (2011).

due to blocking any amiloride sensitive Na^+ channels that are active under basal conditions. Following this, a solution with a low Cl^- concentration is perfused in place of the standard saline solution, usually a Na^+-$\mathrm{gluconate}^-$ solution replaces the NaCl. If there are any basally active Cl^- channels present at this stage, a large hyperpolarisation of the transepithelial PD will be observed, as there is now a favourable electrochemical gradient for Cl^- ions to leave the cell (which is not present under normal conditions). The magnitude of the change in V_t evoked at this stage is usually inferred as an indicator of the level of CFTR channel activity present. The next stage is to add a beta agonist, such as isoproterenol, or add forskolin, to the Na^+-$\mathrm{gluconate}^-$ solution (which still contains amiloride). This acts to raise the cAMP level in the cell, leading to further activation of CFTR channel activity, if any are present, and a consequent further hyperpolarisation of the V_t level. Finally, in some NPD protocols, ATP is added to the solution that has been perfusing in the lumen, in order to raise internal Ca^{2+} levels in the cell, and determine if there are a significant number of calcium activated Cl^- channels present, by looking at the following change in V_t if any.

Typical NPD traces taken from a CF and non-CF patient are shown in Figure 1.10. The characteristic features are a hyperpolarised basal V_t and increased amiloride sensitive V_t in CF, and reduced or no response in CF to manoeuvres aimed at stimulating Cl^- secretion. While the

value of V_t or ΔV_t at any of the stages is on average different between groups of CF and non-CF patients, the actual range of individual values recorded can overlap between the two groups. In order to overcome this variation when diagnosing a patient, a combination of the different V_t metrics can be used, as this gives more discriminatory power. For example, the Wilschanskii ratio, defined as $\exp\{((\Delta V_t + \text{isoproterenol}) + (\Delta V_t{+}0\text{Cl}^-))/(\Delta V_t{+}\text{amiloride})\}$, is one such measure that is used for diagnosis. It remains an open question however, as to where the variation in the individual V_t metrics arises. Is the variation in the response to low Cl^- due to variations in CFTR activity? If so, do some CF patients have residual CFTR activity while others do not? Could this be related to disease severity or to a particular genotype? These are some of the questions of interest that arise from the clinical nasal potential test that I will begin to address in Chapters 5 and 6.

1.2.5 Activity of CFTR and ENaC channels in CF epithelia

While the bioelectric properties of CF epithelia as just outlined arise as result of mutations in the *CFTR* gene, which encodes an anion channel, it is not clear they can all be explained simply due to a loss of apical Cl^- transport. Indeed many of the early studies into abnormal ion transport in CF suggested issues with Na^+ absorption and permeability, and the loss of Cl^- channel function does not have an explicit effect on Na^+ transport.

In microelectrode studies on both non-CF and CF HNE cells, it was shown that Cl^- was at or near electrochemical equilibrium across the apical membrane. Therefore in these HNE cells, Cl^- secretion was not significant, and it was the large level of Na^+ absorption that was generating the transepithelial PD. The question then arises, can the loss of an apical Cl^- channel cause this increase in Na^+ transport indirectly? Are Na^+ and Cl^- currents coupled electrically by the apical membrane potential to such an extent to allow the observed phenomena to arise? Or are there other mechanisms causing Na^+ transport to be increased.

It has been suggested that CFTR also regulates the activity of other transport processes in epithelial cells, in particular ENaC activity, although the mechanism is unclear and is the cause of much debate (Donaldson and Boucher, 2007; Berdiev et al., 2009; Collawn et al., 2012). Studies focusing on CFTR-ENaC interactions found that co-expressing CFTR with ENaC can decrease the basal Na^+ current (Stutts et al., 1995), and that CFTR can decrease the apical Na^+ permeability, by reducing mean open time and open probability of ENaC (Stutts, 1997). If this regulation is also lost in CF, then airway epithelial cells will have a higher basal level

of apical Na^+ conductance, and this could explain some of the abnormal electrophysiological measurements in CF epithelia.

More recent studies investigating these phenomena, have shed some doubt on the increased ENaC activity hypothesis. Electrophysiological studies on *in vitro* differentiated primary cultures of cells from CF patients failed to find evidence of increased Na^+ conductance and increased Na^+ absorption (Itani et al., 2011). This followed on from a previous study on bronchial and tracheal epithelial studies from a pig CF model, which also found no electrophysiological evidence for increased ENaC activity (Chen et al., 2010). Both studies suggest that the loss of anion conductance alone can account for hyperpolarised baseline transepithelial PD, as well as the increased amiloride-sensitive transepithelial PD observed. The authors suggest that it is simply the electrical coupling of the CFTR and ENaC currents which gives rise to the abnormal electrophysiological properties.

1.3 Review of mathematical models of epithelial ion transport

1.3.1 Early models of Na^+ transporting epithelia

In the late 1950's the first model to explain active sodium transport was proposed by Koefoed-Johnsen and Ussing, while they were working on ion transport in frog skin epithelia (Koefoed-Johnson and Ussing, 1958). They put forward a *two-membrane* model which became known as the Koefeod-Johnsen-Ussing (KJU) model, shown schematically in Figure 1.11. This model assumed that Na^+ was actively pumped out of the cell across a first, inward facing membrane, and in order to maintain steady Na^+ levels in the cell, it entered from the lumen via Na^+-specific ion channels in a second, outward facing membrane. K^+ is pumped into the cell by the same mechanism that moves Na^+ out, and in order to maintain homeostasis of K^+ in the cell, there are channels in the inward facing membrane that allow K^+ to move back out to the interstitial fluid. This was called the *pump-leak* mechanism (Reuss, 2001). Although this was a vastly simplified model, it captured the essential features of active Na^+ transport, which we know today to be co-ordinated by the activity of $Na^+ - K^+ - \mathrm{ATPase}$ pumps and ENaC channels.

The first mathematical analyses of epithelial transport appeared in the late 1970's. Schultz et al. (1977) described a phenomenological model of a Na^+ transporting epithelium, which elaborated on the concepts introduced in the simple double-membrane hypothesis of the KJU model. Their model proposed paracellular Na^+ transport, in parallel to the transcellular active

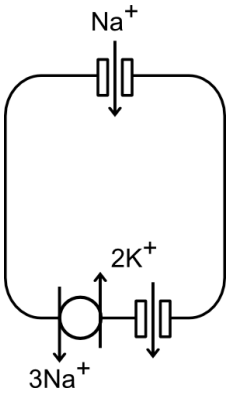

Figure 1.11: Original Koefoed-Johnson and Ussing model of the frog skin epithelium. Na^+ is actively transported across the epithelium with a combination of pumps in the basolateral membrane and channels in the apical membrane. A pump-leak mechanism recycles the K^+ that is entering the cell across the basolateral membrane, as a result of the active Na^+ transport.

Na^+ transport route, as well as passive diffusional movement of a second general ion. They use an equivalent electrical circuit description to relate the different transcellular and paracellular currents to one another. The authors focused on deriving the analytical expressions relating individual circuit elements (Na^+ membrane conductances, electromotive driving force and intracellular potential) which arise from their proposed model, and outline how these properties could be measured quantitatively from electrophysiological experiments on amiloride sensitive epithelia.

Lew et al. (1979) published one of the earliest numerical simulation studies of an epithelial ion transport model. Their model cell also has two membranes, an apical membrane permeable to Na^+, Cl^- and K^+, and a serosal facing membrane which also contains electrogenic Na^+-K^+ pumps. Rather than use an equivalent electrical circuit description as Schultz et al. had, they take a compartment based approach. The lumen, cell and serosa are considered as independent entities, with their state changing due to mass transfer of ions between compartments. The variables in Lew et al.'s model are the ionic concentrations of the intracellular compartment, and the electrical potential difference between the cellular and extracellular compartments.

Their study was also the first to simulate time courses of cellular properties after the epithelial cell is perturbed. For example they simulate amiloride addition by reducing the apical membrane permeability to Na^+, and they perform ion substitution experiments by changing external Na^+ and Cl^- concentrations. Their model reproduces several features of a tight, Na^+-transporting epithelium, such as abolition of the short circuit current in response to amiloride addition and dissipation of ionic gradients after ouabain application. Interestingly, the authors

also point out the utility of mathematical models in highlighting shortfalls in our understanding when predictions diverge from experimental observations. Their original model predicted steady state intracellular Cl^- concentration which was much lower than the level observed. However on inclusion of a basolateral $Na^+ - Cl^-$ co-transport mechanism, a more realistic concentration was achievable. This is an important observation to make in general about models of physical systems; it is often when a model makes an incorrect prediction that it is most informative, as it points out a misunderstanding on the part of the modeller. In this case Lew et al. discovered they could not reproduce physiological conditions with only passive and active transport elements – co-transport of ions was necessary to create a realistic model system.

Latta et al. (1984) put forward a general framework for the formulation and solution of epithelial transport kinetic simulations. Their method is based on the principles of conservation of mass and electro-neutrality in the cellular compartment, much like the model of Lew et al., but generalised so that any combination of ionic species or transport mechanisms can be taken into consideration. They also put forward numerical schemes for simulating open-circuit, short-circuit and current clamped experimental protocols, allowing comparison between model predictions and experimental data for those scenarios. Following on from this work, many different mathematical models of epithelial transport have been studied which utilise the framework of Latta et al., only differing in the tissue specific components and parameter values used. These include models of proximal tubule (Weinstein, 1992, 2004), pancreatic duct (Whitcomb and Ermentrout, 2004), corneal epithelial (Levin et al., 2006), cochlear marginal (Quraishi and Raphael, 2007) and bronchial epithelial cells (Novotny and Jakobsson, 1996a,b). From here on I will discuss the specific details of several of the airway epithelial models which are interesting because of their relevance to my own modelling work.

1.3.2 Models of airway epithelial transport

The first study focusing on the relevant epithelial electro-kinetics was from Hartmann and Verkman (1990), focusing on the kinetics and regulation of transepithelial chloride secretion across canine tracheal epithelial cells. The cellular transport components incorporated in their model included apical Na^+, Cl^- and K^+ conductance, a non-specific paracellular conductance, basolateral K^+ conductance, and basolateral Na^+, Cl^- and K^+ symport. Hartmann and Verkman also included intracellular second messengers in their model, which allowed for regulatory mechanisms of ion channel conductance to be simulated. By choosing appropriate parame-

ters estimated using experimental data found on canine tracheal cells, their model was able to recreate short and open-circuit currents from these cells in response to stimulation from cAMP and Ca^{2+} dependent signaling pathways. A particular feature of note, was the attempt of the authors to determine quantitatively the effect of each individual transport protein on properties of the whole epithelium, such as short circuit current, by altering their value independently and observing how the model system responded to the perturbation.

The first model of human airway epithelial cells was from Duszyk and French (1991). While they only studied steady state and not kinetic model behaviour, their analysis was interesting for similar reasons to the Hartmann and Verkman model. Rather than changing transport properties and looking at how the system evolved in time, in response to the change, Dusyk and French determined how transport parameters changed the *steady state* properties of the system. This was particularly relevant to our research, as they asked questions such as how do short circuit current and Na^{+} flux vary as a function of apical Na^{+} or Cl^{-} permeability? Their model predicted that Na^{+} flux would be much greater than Cl^{-} flux into the cell, even when Na^{+} permeability was much less than Cl^{-} permeability.

Horisberger (2003) developed a simple model of renal epithelial transport in A6 cells. Although Horisberger used estimates from a non-airway epithelial cell line to parameterize his model, as many of the transport mechanisms in his model are common to airway epithelia also, his analysis is relevant to our research. This study is also of interest because it addresses the question of how the relative values of apical Na^{+} and Cl^{-} permeabilities influence the magnitude of amiloride-sensitive V_t. This question is particularly relevant to the debate over CFTR and ENaC interactions in CF disease, and it has been suggested that the apical Cl^{-} conductance could be driving the increased amiloride sensitive V_t observed in CF airway epithelia. The paper does indeed show how the change in short circuit current due to amiloride block could be decreased by increasing apical Cl^{-} conductance, highlighting how simple electrical coupling could account for this phenomenon without the proteins needing to interact directly. The study only looked at one particular set of parameter values, specific to A6 cells, however, and did not speculate as to the quantitative relationship between CFTR permeability and amiloride sensitive I_{sc}, simply showing that qualitatively there was an inverse relationship between the two.

Another mathematical model relevant to consider here, is the recent model of Garcia et al. (2013). The authors develop a generic model of human airway epithelia, that is similar to that

of Hartmann and Verkman in terms of transport proteins and not in itself very novel. The novelty is in their description of a methodology for making quantitative estimates of the constituent ionic permeabilities, given electrophysiological data on cell behaviour during a number of Ussing chamber experimental scenarios. While this study focused primarily on the methodological parameter estimation aspect, rather than interpreting the physiological meaning of the estimates they arrive at, it is relevant to my work as it validates the principle of inferring permeability information on individual transport pathways, from measurements of whole epithelium properties, an approach I will take in analysing my model in later chapters.

1.4 Specific research aims of this thesis

Before outlining my research aims I will first summarise what I have presented so far. I have shown that ion transport in human airway epithelia is relatively well understood, and there is a consensus as to the main ion transport processes involved in electrolyte transport in a typical HAE cell. A lot is also known about cystic fibrosis, and how it affects airway ion transport; loss-of-function mutations in CFTR anion channels (expressed throughout the airways) lead to abnormalities in epithelial Na^+ and Cl^- transport. However there is a controversy over the precise link between mutations in the *CFTR* gene and the disrupted transport properties. Is it simply the CFTR ion channel function that is lost? Or is there a CFTR-ENaC regulatory interaction that is also lost in CF, meaning ENaC channels are hyperactive in the disease?

I have also seen that it is possible to develop physiologically realistic mathematical models of airway epithelial transport processes. Given that major ion transport pathways are known, knowledge of how channel and carrier proteins work individually can be integrated into whole-epithelium models. Models can then be used to investigate the effect of experimental scenarios such as ion substitution experiments and inhibition or activation of different transport proteins, on membrane potentials and intracellular concentrations. Experimental electrophysiological data can hence be used for model validation and parameter estimation purposes.

The goal of this thesis is to develop a biophysical model of this type, and to use it to investigate the pathogenesis of CF in the human airways, focusing on what is underlying the characteristic changes in CF HNE cell electrophysiology. Particularly I want to understand quantitatively how the hyperpolarised basal transepithelial PD and increased amiloride sensitive PD arise in CF, in terms of changes to cell membrane ion permeabilities. With this in mind, the specific aims of my research project are:

- *Develop a physiologically realistic model of ion transport processes in human nasal epithelial (HNE) cells.* The model will describe the biophysical details of passive, active and secondary active transport via channels, pumps and co-transporters. It will describe the electrophysiology of HNE cells (ion concentrations, membrane potentials) as a function of the activity of its constituent ion transport proteins.

- *Simulate common Ussing chamber experiments using mathematical model.* Perform model simulations that can be compared with experimental electrophysiological recordings, particularly interventions where the lumen perfusate is altered, either by adding pharmacological compounds or changing its ionic composition.

- *Estimate transport parameters from electrophysiological data.* Given a biophysical model capable of simulating Ussing chamber experiments, along with appropriate electrophysiological data, perform parameter estimation in order to determine membrane permeabilities of HNE cells.

- *Determine activity of transport proteins in both CF and non-CF HNE cells*. Investigate the quantitative evidence for differences in apical Cl^- and Na^+ permeability between non-CF and CF HNE cells.

- *Investigate quantitatively the relative influence of model parameters on electrophysiological properties.* Determine quantitatively which transport proteins are important in determining properties such as transepithelial PD and amiloride sensitive PD.

- *Simulate clinical nasal PD recordings.* In a similar manner to the Ussing chamber experiments, attempt to reproduce clinical nasal PD measurements by altering the composition of lumenal perfusate. Relate model predictions to clinical data.

- *Investigate viability of parameter estimation from clinical nasal PD traces.* Determine if it is possible to uniquely estimate transport parameter values from clinical nasal PD traces. Discuss the consequences of interpreting this data incorrectly in clinical trials.

Chapter 2

Ion transport model development and analysis methods

2.1 Physical models of ion transport across cell membranes and epithelia

One of the aims of this thesis is to develop a mathematical model of ion transport by the airway epithelial system. As we have seen in Section 1.1.3, this transport system co-ordinates a complex set of different channel and carrier mediated processes. In order to develop an integrated mathematical description of this system, it is first necessary to have models of how the individual transport processes work. Consequently, in this section I will outline the quantitative models of active, passive and secondary active ion transport processes, that I will use in my mathematical description of epithelial transport. In particular I will describe how the rate of ion transport by the different transport processes is functionally related to the cell's physiological state, in terms of its intracellular ion concentrations and transmembrane electrical potentials.

2.1.1 Passive transport - Goldman-Hodgkin-Katz flux equation

In the previous chapter (Section 1.1.2) I described how, in the case of channel mediated transport, ion flux is simply the result of diffusion down an electrochemical gradient. Here I will give a brief overview of the mathematical description of this physical process, and how it can be applied to the specific case of ion transport across a cell membrane. Readers interested in a full theoretical treatment of this topic can refer to excellent discussions in Hille (2001) and Weiss (1996).

The Nernst-Planck equation describes the general theory of electrodiffusion, it is given here for the one dimensional case, where concentration c and electric potential Ψ are both

functions of distance x

$$I_n = -z_n F D_n \left(\frac{dc}{dx} + \frac{z_n F c}{RT} \frac{d\Psi}{dx} \right) \tag{2.1}$$

For a given ion n with a valence of z_n, the current density I_n due to electrodiffusion is linearly related to both the concentration gradient (dc/dx) and the electric potential gradient $(d\Psi/dx)$, and is also directly proportional to its diffusion coefficient in the relevant medium D_n. Note here F is the Faraday constant, R is universal gas constant, and T is temperature.

A commonly used form of equation 2.1, the Goldman-Hodgkin-Katz (GHK) flux equation, is applicable to channel mediated electrodiffusion across a cell membrane.

$$I_n = P_n z_n^2 \frac{V_m F^2}{RT} \frac{a_i - a_o \exp\left(-z_n F V_m / RT\right)}{1 - \exp\left(-z_n F V_m / RT\right)} \tag{2.2}$$

In this special case of equation 2.1, the electric field across the membrane is assumed to be constant, hence the electrical potential changes linearly within the membrane. This is known as the *constant field* approximation and a full derivation of equation 2.2 in given in Appendix A.2. The membrane potential, V_m, is defined as the difference between the electric potential inside the cell and outside the cell, $\psi_i - \psi_o$. In 2.1 the current is expressed in terms of D_n whereas in the new expression it is in terms of P_n, the permeability of the membrane to ion n. Membrane permeability is related to the diffusion coefficient of the ion within the membrane, via the expression $P_n = D_n k_n / L$, where L is the width of the membrane and k_n is the partition coefficient. The partition coefficient is defined as the ratio of ionic concentrations on either side of the membrane interface at equilibrium, and is discussed in more detail in Appendix A.2.

Note also that the GHK flux equation 2.2 is expressed in terms of the thermodynamic activity of the transported ion (a_i and a_o). This is necessary as the intracellular and extracellular solutions will not necessarily behave as ideal electrolyte solutions governed solely by their chemical concentration (c_i and c_o). Activity and concentration are related via $a = \gamma c$ where γ is the activity coefficient of the ion in question. The activity coefficient of an electrolyte solution is dependent on various factors such as its concentration, its composition and the temperature. Hille gives the activity coefficient of a $100\ \mathrm{mM\ NaCl}$ solution to be $\gamma = 0.77$ (Hille, 2001). This is sufficiently close to the composition of the physiological solutions I will consider in my work, and so I use this activity coefficient throughout for converting concentrations of $\mathrm{Na^+}$, $\mathrm{K^+}$ and $\mathrm{Cl^-}$ to their respective activities.

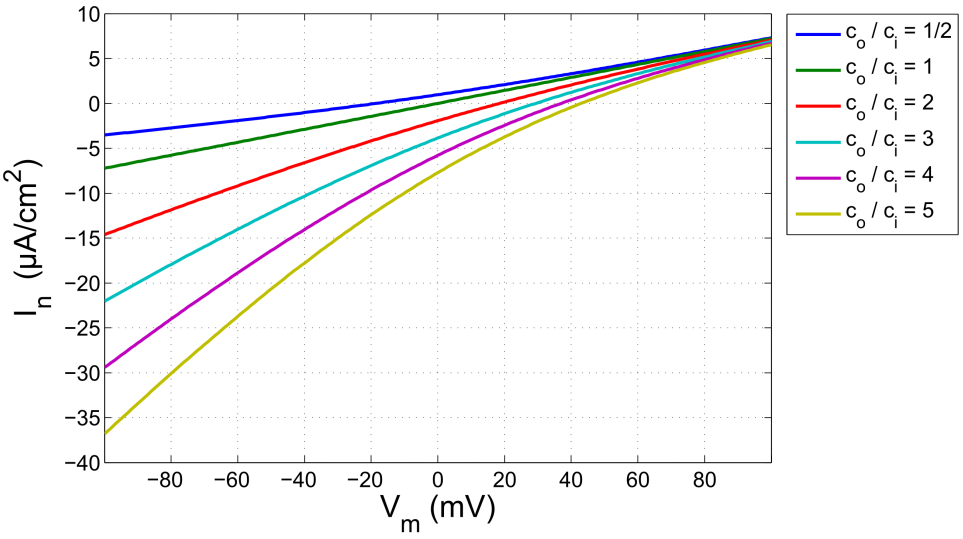

Figure 2.1: Current I_n of a univalent positive ion $(z_n = +1)$ across a membrane with permeability $P_n = 0.01\ \mu\mathrm{m/s}$ predicted by the GHK flux equation. The internal ion concentration c_i is fixed at 20 mM, while I-V curves are plotted for different external activities; $c_o = \{10, 20, 40, 60, 80, 100\}$ mM. (Note this is for an ideal electrolyte, such that the activity coefficient $\gamma = 1$.)

In the constant field GHK model, the ionic current I_n is simply proportional to the membrane permeability, P_n, modulated by a non-linear function of the membrane potential and ionic concentration gradient, $I_n = P_n f\,(V_m, c_i, c_o)$. We can gain intuition for the functional relationship between these physiological variables and the predicted current by looking at a number of features of the GHK flux equation:

- When there is no difference in the electric potential on either side of the membrane, the current is directly proportional to the transmembrane concentration gradient, $\Delta c_m = c_i - c_o$. This is intuitively what one would expect from Fick's law of diffusion.

$$\lim_{V_m \to 0} I_n = \frac{P_n z_n F}{\gamma}\,(c_i - c_o) \tag{2.3}$$

- The membrane potential at which no current will flow, called the reversal potential (V_{rev}), can be found by setting $I_n = 0$ and solving for V_m. The expression for V_{rev} reduces to that of the well known Nernst potential

$$V_{rev} = \frac{RT}{z_n F} \ln \frac{c_o}{c_i} \tag{2.4}$$

- The GHK flux equation predicts that the membrane is *rectifying*. That is, the effective conductance of the membrane changes with voltage, and rectification is characterised by non-linear $I - V$ relationships. Figure 2.1 shows the predicted current I_n for a given V_m, at different concentration gradients. At negative membrane potentials (favourable for positive ions to enter the cell), the greater the external - internal concentration gradient, the greater the magnitude of the inward current. However at positive membrane potentials, the concentration gradient has little effect on current.

At this point it is important to note that in using the GHK flux equation and the constant field approximation, we are not utilising any information about the physical structure of the channels through which the ions are moving, their gating properties or how they are regulated. The GHK flux model simply characterises the ease through which ions can traverse the cell membrane for a given electrochemical driving force.

For example, consider the case of modelling transmembrane transport by CFTR channels. If I assume that the apical membrane has a certain permeability to Cl^- ions, $P^{ap}_{Cl^-}$, I can determine the transmembrane Cl^- current $I^{ap}_{Cl^-}$, provided I know the apical membrane potential V^{ap}_m, and lumen and cell Cl^- concentrations. I do not use information on how many channels are present in the membrane, how many are open, or information about the single channel conductance of CFTR. Similarly, if I want to model Na^+ transport in epithelial cells via ENaC channels, then given the membrane potential and sodium concentration gradient, I can compute the current $I^{ap}_{Na^+}$ if I know $P^{ap}_{Na^+}$.

Finally, the GHK flux equation can also be used to model paracellular current flows. As in the case of ion channels, I can use permeability as the transport parameter that characterises the ease with which current flows through tight junctions. I can then compute the paracellular current for a given ion, say K^+, if I assume a certain permeability $P^{pa}_{K^+}$, and if I know transepithelial PD and lumen / serosal K^+ concentration. When simulating the paracellular flux of several ions, I can assume they will all flow with the same ease characterised by one common paracellular permeability (i.e. $P^{pa}_{Na^+} \equiv P^{pa}_{Cl^-} \equiv P^{pa}_{K^+}$), or I can investigate selectivity in this pathway by allocating different permeabilities to anions and cations.

2.1.2 Active ion transport models - $\mathrm{Na}^+ - \mathrm{K}^+ - \mathrm{ATPase}$ pump

Carrier mediated transport is a more complex process to model in general than channel mediated transport. This is because carrier mediated transport necessarily involves several distinct

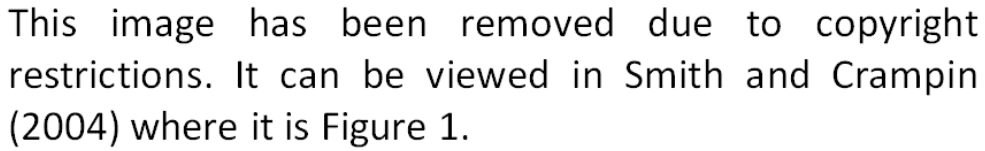

Figure 2.2: Post-Albers model of the $\mathrm{Na}^+ - \mathrm{K}^+ - \mathrm{ATPase}$ reaction cycle, highlighting the sequence of binding and unbinding of Na^+ and K^+ ions, conformational changes and the hydrolysis of MgATP. P_1-P_{15} represent the 15 intermediate states in the reaction cycle. Image from Smith and Crampin (2004)

processes, such as the binding and unbinding of ions to the carrier protein, or conformational changes in the protein in order to translocate bound ions across the membrane. In general there may be several ions that bind the carrier protein during each translocation cycle, and there may also be a strict sequence in which they must associate with the carrier protein. In order to quantitatively model this process I need to know several pieces of information; the order in which ions bind, the rate of binding and unbinding of each ion to the carrier, the rate at which the conformational change occurs, and whether or not any of these stages are voltage or concentration dependent. In comparison, for electrodiffusion I only needed one parameter to characterize the transport process - the permeability of the membrane to the ion of interest. However, as in the case of channel mediated transport, there are theoretical models in the literature than I can use to compute the rate of active transport, given knowledge of the physiological state of the cell.

I focus my attention on models of active transport by $\mathrm{Na}^+ - \mathrm{K}^+ - \mathrm{ATPase}$ pumps, as these are expressed in human airway epithelial cells. As outlined in the previous chapter (Sec-

tion 1.1.3.2) one of the primary functions of $\mathrm{Na}^+ - \mathrm{K}^+ - \mathrm{ATPase}$ pumps is to keep cell Na^+ concentration low, and cell K^+ concentration high. This movement requires work to be done by the pump, as it is moving both Na^+ and K^+ against their respective electro-chemical gradients. In order to perform this work the pump couples the translocation of these ions to the hydrolysis of ATP, and the net outcome of a single reaction cycle can be summarised as follows:

$$3Na_i^+ + 2K_s^+ + ATP \rightleftharpoons 3Na_s^+ + 2K_i^+ + ADP + P_{io} \tag{2.5}$$

For every cycle of a pump, 3 Na^+ ions are moved from the intracellular compartment (subscript i) to the serosal compartment (subscript s). In the same process, 2 K^+ are moved from the serosal compartment into the cell, and one molecule of ATP is hydrolysed to give a molecule of ADP and an inorganic phosphate $\mathrm{P_{io}}$. There is a net movement of one positive ion per cycle moved out of the cell by the activity of $\mathrm{Na}^+ - \mathrm{K}^+ - \mathrm{ATPase}$ pumps, therefore it contributes an electric current across the basolateral membrane of epithelial cells.

The binding of Na^+ and K^+ ions, as well as MgATP molecules, occurs in a strict sequence. The model of Albers and Post outlines the various binding and unbinding stages, as well as the translocation stages of the $\mathrm{Na}^+ - \mathrm{K}^+ - \mathrm{ATPase}$ reaction cycle (Post et al., 1972; Albers, 1967). Their model contains 15 distinct stages, and is shown schematically in Figure 2.2. A reduced, 4 stage cycle was derived from the Post-Albers scheme by Smith and Crampin (2004), for use in whole cell modelling. To achieve this reduction in complexity the authors make the assumption that association and dissociation reactions are in a rapid equilibrium with each other, as they happen on a much faster time scale than the rates that the enzyme undergoes translocation (see Figure 2.3).

In the Smith and Crampin model, it is assumed that the pump reaction cycle itself is in a quasi-steady state. The turnover rate of a single pump ν_{NaK} can be determined based on the difference between the rate of movement around the cycle in the clockwise direction ($\alpha^+_{1\to4}$) relative to the anti-clockwise ($\alpha^-_{1\to4}$) directions.

$$\nu_{NaK}(t) = \frac{\alpha_1^+\alpha_2^+\alpha_3^+\alpha_4^+ - \alpha_1^-\alpha_2^-\alpha_3^-\alpha_4^-}{\Sigma} \tag{2.6}$$

Here Σ is a combinatorial function of these rates, which can be found using the Hill diagrammatic method . $\alpha^{+/-}_{1\to4}$ contain information regarding the separate association and dissociation

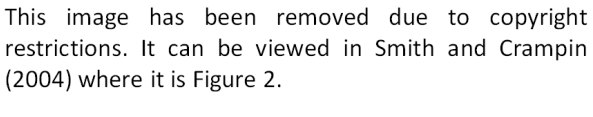

Figure 2.3: Reduced 4 stage kinetic model of active transport by $\mathrm{Na}^+ - \mathrm{K}^+ - \mathrm{ATPase}$ pumps. Ion binding and dissociation events are lumped together, as they are assumed to be in rapid equilibrium, relative to the rate of translocation of the substrate. Image from Smith and Crampin (2004).

reactions that are assumed to be in rapid equilibrium in the Smith and Crampin model. These rates are functionally dependent on internal and external Na^+ and K^+ concentrations amongst other factors (a full derivation of the Smith and Crampin model is outlined in Appendix A.3). For my purposes here, it suffices to comment that if I know the concentrations of Na^+ and K^+ inside and outside of the cell, as well as basolateral membrane potential V_m^{ba}, I can compute the individual rates $\alpha_{1\to4}^{+/-}$, and hence the net turnover rate of a pump, ν_{NaK}.

Knowing the turnover rate of an individual pump allows us to compute the total transmembrane pump current as

$$I_{NaK}(t) = \rho_{NaK}\nu_{NaK}(t)z_{Na^+}F \tag{2.7}$$

Here the parameter ρ_{NaK} is the number of moles of $\mathrm{Na}^+ - \mathrm{K}^+ - \mathrm{ATPase}$ per unit area of the cell membrane. Now I have reduced my model to a form similar to the GHK equation in 2.1. The current is directly proportional to a *transport parameter* modulated by a non-linear function of concentrations and membrane potentials. Here the transport parameter is the number of pump proteins, ρ_{NaK}, previously it was the membrane permeability, P_n, and both of these parameters will be proportional to the expression level of the relevant protein in the cell membrane. The expression level of the transport protein is an intrinsic property of the cell in this model, whereas the information about the local electrochemical environment is the variable quantity which may change over time.

Figures 2.4 and 2.5 show how the ion translocation rate changes as a function of intracel-

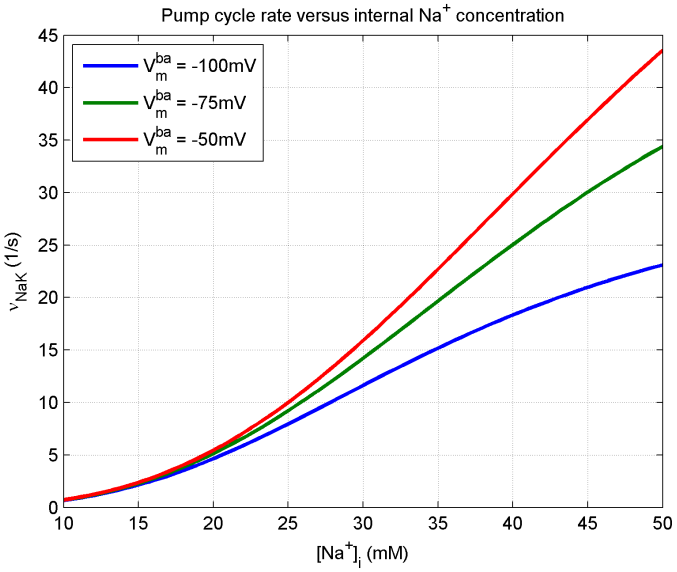

Figure 2.4: Plot of ν_{NaK} as a function of intracellular Na^+ concentration at three different membrane potentials, $V_m = (-100, -75, -50)$ mV, as predicted by the Smith and Crampin model. Intracellular $[\mathrm{K}^+]$ is fixed at 120 mM, and extracellular concentrations are assumed to be that of physiological saline, $[\mathrm{Na}^+]_s = 140$ mM and $[\mathrm{K}^+]_s = 5$ mM. The translocation rate increases approximately linearly in the range 10 mM $\leq [\mathrm{Na}^+]_i \leq$ 50 mM, concentrations likely to be found *in vivo* in human airway epithelial cells. ν_{NaK} is relatively insensitive to membrane potential in the range of $[\mathrm{Na}^+]_\mathrm{i}$ values that are physiologically realistic (20 mM $\leq [\mathrm{Na}^+]_\mathrm{i} \leq$ 35 mM).

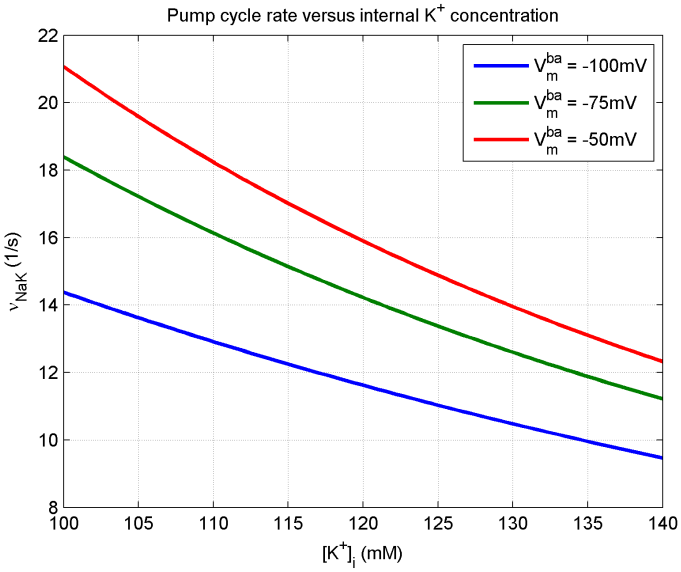

Figure 2.5: Translocation rate of $\mathrm{Na}^+ - \mathrm{K}^+ - \mathrm{ATPase}$, ν_{NaK}, as a function of intracellular K^+ concentration, at various membrane potential values. Intracellular Na^+ is fixed at 30 mM, and extracellular concentrations are assumed to be that of physiological saline, $[\mathrm{Na}^+]_s = 140$ mM and $[\mathrm{K}^+]_s = 5$ mM. Here the translocation rate decreases in an approximately linear manner, as K^+ increases, although the rate of change is not as large as that in Figure 2.4.

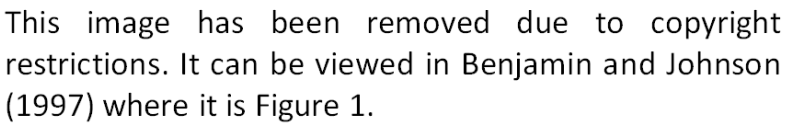

Figure 2.6: 10 stage model of the $\mathrm{Na}^+ - \mathrm{K}^+ - 2\mathrm{Cl}^-$ co-transporter ion translocation activity, proposed by Lyttle and McManus. Image taken from Benjamin and Johnson (1997).

lular Na^+ and K^+ concentrations, and the basolateral membrane potential. Over the ranges of these variables which are physiologically realistic in airway epithelial cells, we see that pump activity increases with intracellular Na^+ and decreases with intracellular K^+, and is relatively insensitive to basolateral membrane potential by comparison. This is how we would expect the pump to work intuitively, given its function is to keep cell Na^+ low and cell K^+ high. If Na^+ builds up in the cell, it will begin to work harder to pump it out, and similarly, if K^+ begins to lower, it will increase activity to bring more K^+ into the cell raising its concentration level.

2.1.3 Secondary active transport - $\mathrm{Na}^+ - \mathrm{K}^+ - 2\mathrm{Cl}^-$ model

In contrast to the $\mathrm{Na}^+ - \mathrm{K}^+ - \mathrm{ATPase}$ which requires active energy input to function, the $\mathrm{Na}^+ - \mathrm{K}^+ - 2\mathrm{Cl}^-$ transports Na^+, Cl^- and K^+ in to the cell passively. It couples the transport of K^+ and Cl^- ions, to that of Na^+, as Na^+ is moving in an energetically favourable direction down an electrochemical gradient.

The NKCC co-transporter binds Na^+, K^+ and 2 Cl^- ions on one side of the membrane, in the sequence Na^+, Cl^-, K^+, Cl^-, before translocating the ions to the opposing side and unbinding in the same sequence, in a first on - first off manner.

Benjamin and Johnson (1997) wrote down relevant differential equations which quantify

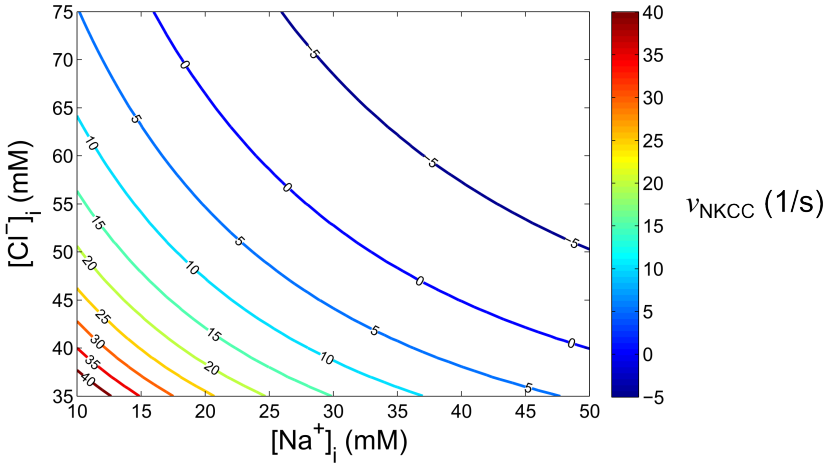

Figure 2.7: The rate at which ions are translocated into the cytoplasm by the NKCC co-transporter, is plotted here as a function of intracellular Na^+ and Cl^- concentrations. Intracellular K^+ concentration is fixed at $120\ \mathrm{mM}$, and extracellular concentrations of $[\mathrm{Na}^+]_s = 140\ \mathrm{mM}$, $[\mathrm{Cl}^-]_s = 120\ \mathrm{mM}$ and $[\mathrm{K}^+]_s = 5\ \mathrm{mM}$. Under physiological conditions in HNE cells, intracellular Na^+ will typically be less than $40\ \mathrm{mM}$ and Cl^- less than $75\ \mathrm{mM}$. With both concentrations below these bounds, ν_{NKCC} is positive, and ions will be moved *into* the cell by this cotransport mechanism.

these rates, giving quasi-steady state turnover rate of an individual NKCC co-transporter of

$$\nu_{NKCC}(t) = \frac{k_f^{full}\, k_f^{empty} [Na^+]_s\, [K^+]_s\, [Cl^-]_s^2 - k_b^{full} k_b^{empty} [Na^+]_i\, [K^+]_i\, [Cl^-]_i^2}{\sum_{n=1}^{16} Z_{nkcc}^n} \tag{2.8}$$

Here Z_{nkcc}^n are associated with rates of moving between states of the 10 stage reaction cycle (see Figure 2.6), similar to the rates $\alpha_{1\to 4}^{+/-}$ in the case of the $\mathrm{Na}^+ - \mathrm{K}^+$ pump, and Benjamin and Johnson provide estimates of these rate constants. Therefore given the relevant intracellular and extracellular Na^+, Cl^- and K^+ concentrations, I can compute ν_{NKCC}.

In contrast to the $\mathrm{Na}^+ - \mathrm{K}^+ - \mathrm{ATPase}$ which is electrogenic, a turnover of the NKCC protein does not produce net movement of charge, as 2 cations ($\mathrm{Na}^+ + \mathrm{K}^+$) move in the same direction as 2 anions ($2\ \mathrm{Cl}^-$). Transport due to NKCC activity is then said to be electrically silent, or electroneutral. While this means there is no net current, $I_{NKCC} = 0$, it is still necessary to model net ion flux due to cotransport. If I assume, as in the case of the pumps, that I know the surface density of NKCC protein, ρ_{NKCC}, then I can compute the relevant ion flux into the cell, as $\rho_{NKCC}\nu_{NKCC}$ for Na^+ and K^+, and $2\rho_{NKCC}\nu_{NKCC}$ in the case of Cl^- (due to the $1:1:2$ stoichiometry of the reaction cycle). Figure 2.7 shows the relationship between intracellular Na^+ and Cl^- concentrations, and the cycling rate of the NKCC co-transporter.

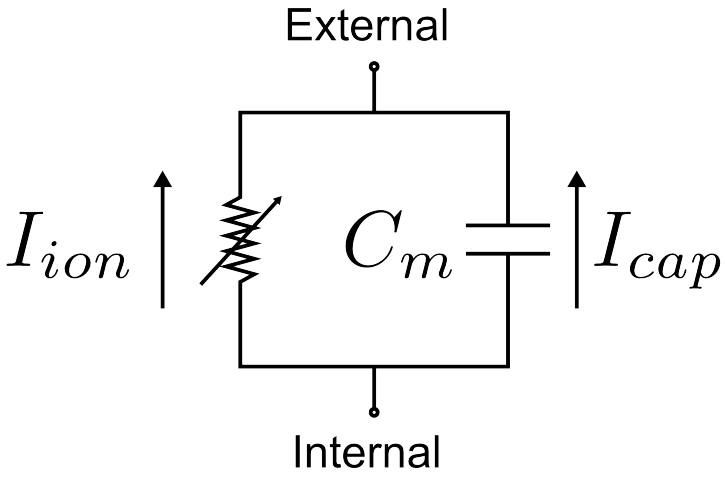

Figure 2.8: Equivalent electrical circuit description of a cell membrane. The plasma membrane acts as a capacitor separating the internal and external ionic solutions, in parallel with a resistor, which represents the fact that the membrane can conduct current to a certain extent. If there are no external current sources flowing into the system, then the the sum of the ionic and capacitive currents must equal zero ($I_{ion} + I_{cap} = 0$).

The NKCC co-transporter tends to move Na^+ and Cl^- towards an equilibrium concentration level. For the example of Cl^-, below a certain concentration threshold (dependent on $[\mathrm{Na}^+]_i$) Cl^- will be moved into the cell, i.e. $\nu_{NKCC} > 0$. This will tend to increase $[\mathrm{Cl}^-]_i$, and the value of ν_{NKCC} will decrease and move towards 0. Similarly above a certain $[\mathrm{Cl}-]_\mathrm{i}$ level, ν_{NKCC} will become negative, the co-transport process will work in reverse, moving Cl^-ions *out* of the cell, and their concentrations may decrease, moving ν_{NKCC} in a positive direction back towards its own equilibrium value of 0.

2.1.4 Equivalent electrical circuit description of epithelial ion transport

Figure 2.8 shows the equivalent electrical circuit commonly used to describe a single cell membrane. The circuit assumes that a cell membrane acts like a parallel plate capacitor in parallel with a resistor. The capacitor element takes into account the fact that the plasma membrane creates a separation of electric charge between the cell cytoplasm and the external physiological fluid. The membrane can also conduct electric current via ion channels (or via other routes) and this is represented by a resistive element in parallel with the capacitor.

The relationship between transmembrane ion current I_{ion} and electric potential difference V_m across the membrane can be determined by comparing the capacitive current I_{cap} to I_{ion}.

The charge q on a parallel plate capacitor is given by the formula

$$q = C_m V_m \tag{2.9}$$

where C_m is the capacitance of the parallel plates (assumed not to vary in time), and V_m is the electric potential difference, or voltage, across the plates. The rate of change of that charge q, or the capacitive current, is then given by

$$I_{cap} = \frac{dq}{dt} = C_m \frac{dV_m}{dt} \tag{2.10}$$

Assuming there are no additional current sources into this circuit, then it follows from Kirchoff's Laws that the net currents in the circuit must add to zero.

$$I_{cap} + I_{ion} = 0 \tag{2.11}$$

Replacing the expression for I_{cap} derived in 2.10 into 2.11 and re-arranging, one can write

$$\frac{dV_m}{dt} = -\frac{1}{C_m} I_{ion} \tag{2.12}$$

The rate of change of membrane potential V_m is directly proportional to the transmembrane current I_{ion}.

The electrical state of an epithelium can also be described by an equivalent electrical circuit. The equivalent circuit is more complex than the single membrane system, as an epithelium effectively consists of two separate membranes (apical and basolateral) in series, in parallel with the current flowing through the paracellular pathway. This is shown schematically in Figure 2.9. In order to understand how the transepithelial potential difference, V_t, changes as a function of the currents across the apical membrane I_{ap}, basolateral membrane I_{ba} and paracellular current I_{pa}, one must first understand how the individual currents change the apical and basolateral membrane potentials.

Using the same logic as with the simpler circuit, one can determine expressions for the capacitive current across the apical membrane, $C_m dV_m^{ap}/dt$, and across the basolateral membrane, $C_m dV_m^{ba}/dt$. However in this situation the paracellular current I_{pa} must be accounted for, and the sum of the capacitive and transmembrane currents in each of the individual paral-

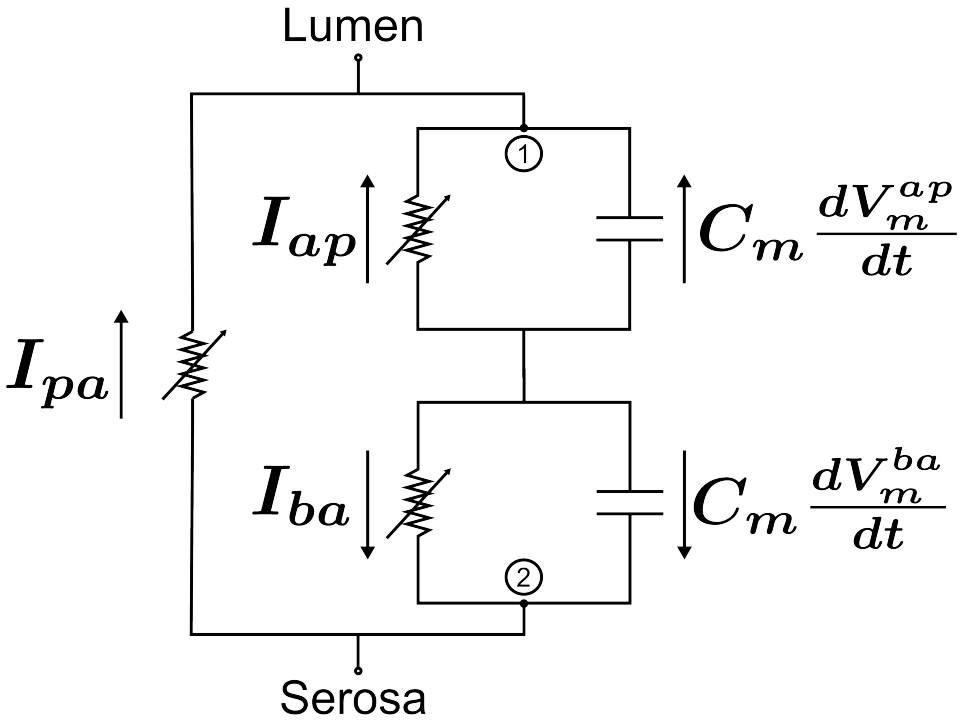

Figure 2.9: Equivalent electrical circuit description of an epithelium. The apical and basolateral membranes are represented as two resistor-capacitor circuits in series, and the paracellular transport route is represented by a resistive circuit element in parallel with the trans-cellular route. Assuming no external current flows into the system, and using Kirchoff's current law, we can relate the paracellular current I_{pa} to the ionic and capacitive current at each membrane, where I_{pa} is by convention positive for the flow of positive ions in the serosal to luminal direction. At point 1, the current leaving the RC circuit must equal the current entering it, therefore $I_{ap} + C_m dV_m^{ap}/dt = -I_{pa}$, and similarly at point 2, $I_{ba} + C_m dV_m^{ba}/dt = I_{pa}$.

lel resistor-capacitor circuits (RC) is no longer simply equal to zero. In the case of the apical current, if we apply Kirchoff's junction rule at point 1 (in Figure 2.9), one finds

$$I_{ap} + C_m \frac{dV_m^{ap}}{dt} = -I_{pa} \tag{2.13}$$

Similarly, looking at the basolateral RC circuit and applying Kirchoff's junction rule at point 2, one finds

$$I_{ba} + C_m \frac{dV_m^{ba}}{dt} = +I_{pa} \tag{2.14}$$

These equations can then be re-arranged to give expressions for the rate of change of each membrane potential with respect to time

$$\frac{dV_m^{ap}}{dt} = -\frac{1}{C_m}\left(I_{ap} + I_{pa}\right) \tag{2.15}$$

$$\frac{dV_m^{ba}}{dt} = -\frac{1}{C_m}\left(I_{ba} - I_{pa}\right) \tag{2.16}$$

It is clear from this equivalent electrical circuit description how the coupling of the apical and basolateral membrane potentials arises - as the paracellular or shunt current I_{pa} influences the rate of change of both V_m^{ap} and V_m^{ba}.

Note in both the apical and basolateral membrane cases, the same convention regarding current has been used as in the single membrane case, namely the movement of positive charge out of the cell constitutes a positive current. For the paracellular current, I use the convention that the movement of positive charge in the serosal to luminal direction constitutes a positive current. Membrane potentials are commonly expressed as the electric potential inside of the cell minus the electric potential outside the cell. For an epithelium there are three different electric potentials to consider, the potential of the lumen V_l, the potential inside the cell V_i, and the serosal potential V_s. The apical and basolateral membrane potential differences can then be written as $V_m^{ap} = V_i - V_l$ and $V_m^{ba} = V_i - V_s$ respectively. In the study of epithelial electrophysiology, the transepithelial potential difference is commonly recorded with respect to the potential of the serosal or interstitial compartment, that is V_t = V_l - V_s. This can be expressed in terms of the membrane potential differences in place of the electric potential of the compartments themselves

$$V_t = V_l - V_s = (V_i - V_m^{ap}) - (V_i - V_m^{ba}) = V_m^{ba} - V_m^{ap} \tag{2.17}$$

2.1.5 Transmembrane water transport

Transmembrane water flux ensures the intracellular compartment is always iso-osmolar with the extracellular fluid. The osmolarity of a solution is defined as

$$\sum_h \phi_h n_h [C]_h \tag{2.18}$$

where the $[C]_h$ is the molar concentration of the h-th solute in the solution, n_h is number of particles that this solute dissociates into, and ϕ_h is its osmotic coefficient. The osmotic coefficient accounts for certain factors, such as interactions between charged particles, which may cause an ionic solution to deviate from ideal behaviour. Solutions of NaCl and KCl at physiological concentrations do not deviate from ideality by more than 10% (Weiss, 1996), hence I assume in all my calculations that $\phi = 1$.

With this assumption, in my model the osmolarity $[\mathrm{S}]$ of any of the compartments is the sum of the concentrations of all ions present in that compartment. If I consider a compartment which consists primarily of Na^+, K^+, and Cl^- ions in solution, then the osmolarity of the compartment would be as follows

$$[S] = [\mathrm{Na}^+] + [\mathrm{Cl}^-] + [\mathrm{K}^+] + [\psi] \tag{2.19}$$

Here $[\psi]$ accounts for the presence of all other impermeable anions. In the model the values of $[\psi]$ used for each compartment are chosen so that the compartment is initially electroneutral, and iso-osmolar with all other compartments to begin with. For example, in the extracellular compartments if I assume concentrations in mM of $[\mathrm{Na}^+] = 140$, $[\mathrm{K}^+] = 5$, and $[\mathrm{Cl}^-] = 120$, (and these are the only ions modelled) then I would set $[\psi] = 25\ \mathrm{mM}$ in both the lumen and serosa. This means the total osmolarity is $290\ \mathrm{mOsm}$ and there are equal amounts of cations and anions present.

The water flux across the apical (J_w^{ap}) or basolateral (J_w^{ba}) membrane is assumed to be linearly related to the difference in osmolarity across that membrane, and assumed to be positive in the serosal to luminal direction,

$$J_w^{ap} = L_w \nu_w \left([S]_l - [S]_i\right) \tag{2.20}$$

$$J_w^{ba} = L_w \nu_w \left([S]_i - [S]_s\right) \tag{2.21}$$

Here L_w is the hydraulic conductivity of the cell membrane, and ν_w is the partial molar volume of water. Available literature values were used for these parameters (see Appendix A.1, Table A.1).

2.2 Whole cell model of ion transport in human nasal epithelial cells

Figure 1.2 shows the basis for the model epithelial system which I analyse. The mathematical model represents a mono-layer of HNE cells placed between two well perfused compartments containing physiological saline solution. This scenario approximates the environment experienced by HNE cells *in vitro* during an Ussing chamber experiment, where the two compartments represent the half chambers on the mucosal and serosal sides of the epithelium. Equally it approximates the situation *in vivo* during measurement of the nasal transepithelial potential when the airway surface is flooded, where the compartments are representative of the airway lumen on the apical side, and interstitial fluid on the basolateral side. The transport processes I include are those which are most significant in contributing to the generation of the transepithelial potential difference in the airways. In particular in this model I consider the movement of Na^+, Cl^-, K^+ and $\mathrm{H_2O}$ directly between interstitial fluid and airway lumen (paracellular route) and between the cell and external solutions via transport processes in the apical and basolateral plasma membranes (transcellular route). Focusing on this system allows us to use experimental Ussing chamber data for model validation and parameter estimation purposes, and also allows us to simulate ion transport kinetics during a clinical nasal potential difference measurement - both of which are amongst the aims outlined at the start of this thesis.

2.2.1 Modelling framework: state variables, parameters and fluxes

The framework I use for modelling ion transport in HNE cells is motivated by the general methodology proposed by Latta et al. (1984) for developing and simulating models of epithelial transport. In this approach, the behaviour of a single representative epithelial cell is assumed to be a good description of the entire epithelial layer. The epithelial cell is modelled as a single compartment described by several *state variables*. These variables are related to the physiological quantities I am interested in modelling, such as the intracellular ionic concentrations and transmembrane potentials. In this approach, the flux due to each type of transport protein expressed in the cell is modelled individually, and by summing the contribution from all

transport proteins present, the net movement of each ion type into or out of the cell can be determined. By enforcing conservation of mass in the intracellular compartment, I can write down state equations, which describe the time evolution of the physiological state variables. Hence in this framework, given the initial state of the cell and its surroundings, one can compute the flux along each transport pathway, update the state of the cell, and continue in this fashion to numerically simulate the epithelial ion transport kinetics.

In the case of a HNE cell model which I develop, its state at any time is described by six variables, cell volume, $W_i(t)$, moles of Na^+, Cl^-, and K^+, ($Na_i^+(t)$, $Cl_i^-(t)$, $K_i^+(t)$), and apical and basolateral membrane potentials, ($V_m^{ap}(t)$ and $V_m^{ba}(t)$ respectively) (subscript i denotes intracellular quantities). Therefore cell volume and ionic composition vary in time, as well as its electrical state. The transport pathways considered include CFTR and ENaC channels in the apical membrane, characterized by apical Cl^- permeability ($P_{Cl^-}^{ap}$) and apical Na^+ permeability ($P_{Na^+}^{ap}$) respectively; K^+ and Cl^- channels in the basolateral membrane are characterized by the basolateral K^+ ($P_{K^+}^{ba}$) and Cl^- ($P_{Cl^-}^{ba}$) permeabilities. Transport via $\mathrm{Na}^+ - \mathrm{K}^+ - \mathrm{ATPase}$ pump proteins and NKCC cotransport proteins in the basolateral membrane, are also considered, and they are characterized by their densities per unit area of the membrane, ρ_{NaK} and ρ_{NKCC} respectively. Paracellular transport modelled includes movement of Na^+, K^+ and Cl^- through the tight junctions, as well as $\mathrm{gluconate}^-$ transport along the paracellular pathway in some simulations. Finally, water transport across the apical and basolateral membranes is incorporated into the model HNE cell.

Note that all ion channel currents are modelled using the GHK flux equation, as described in 2.1.1, and all paracellular currents are also modelled in this manner. The $\mathrm{Na}^+ - \mathrm{K}^+$ pump flux is determined using the Smith and Crampin model, as outlined in Section 2.1.2, and the NKCC co-transport flux is determined using the Benjamin and Johnson model as described in Section 2.1.3.

With this framework how the relative expression levels of different transport proteins influence the physiological state of the cells can be determined by varying the appropriate transport parameters. Similarly, one can simulate inhibition or activation of different proteins, by appropriate manipulation of the transport parameter characterising their expression level, and how this would be expected to perturb the model cell can be observed.

2.2.2 Kinetics of cellular variables

Each cellular variable x_h has a state equation associated with it. The state equations are derived from the principle of conservation of mass in the case of ions and water, and the conservation of current (Kirchoff's laws) in the case of membrane potentials. Since creation or destruction of ions or small molecules in the epithelial cell is not considered (i.e. no chemical reactions are modelled), the number of ions of a particular species (or the number of water molecules) can only change if there is a net influx or efflux of that particular particle into the cell. Specifically, this can be formulated in terms of the rate of change of species number, dx_h/dt, and the rate at which that species enters or leaves the cell, via different transport pathways

$$\frac{dx_h}{dt} = \sum \left(J_h^{in} - J_h^{out} \right) \tag{2.22}$$

The fluxes from all relevant pathways are included. This can be explicitly written in the case of each cellular variable that is to be included in the proposed HNE cell model. Starting with cell volume, W_i (note subscript i refers to an intracellular quantity), which will change if there is a net flow of water into or out of the cell

$$\frac{dW_i}{dt} = J_w^{ba} - J_w^{ap} \tag{2.23}$$

Here J_w^{ap} is the H_2O flux across the apical membrane, and J_w^{ba} is the corresponding flux across the basolateral membrane, computed as described in Section 2.1.5. I use the convention that water flux in the serosal to luminal direction is positive. Next, considering the number of Na^+ ions in the cell, I write down the appropriate state equation.

$$\frac{dNa_i^+}{dt} = \rho_{NKCC}\nu_{NKCC} - 3\,\rho_{NaK}\nu_{NaK} - \frac{I_{Na^+}^{ap}}{Fz_{Na^+}} \tag{2.24}$$

In the model system there are three routes by which Na^+ can enter the cell. ENaC channels expressed in the apical membrane facilitate an apical current, $I_{Na^+}^{ap}$. In the basolateral membrane, pump and co-transporter proteins create two separate pathways for Na^+ movement, characterised by the flux terms $\rho_{NaK}\nu_{NaK}$ and $\rho_{NKCC}\nu_{NKCC}$. Note the stoichiometry of the pump means that 3 Na^+ ions are extruded on every cycle, and $I_{Na^+}^{ap}$ has been normalised by the Faraday constant F in order to convert a current, expressed in terms of electric charge movement, as a flux in terms of movements of moles of Na^+.

Using an analogous approach, I can write down the state equation for the number of moles of Cl^- in the cell. This will change due to the apical CFTR current, $I^{ap}_{Cl^-}$, the basolateral Cl^- channel current, $I^{ba}_{Cl^-}$, and the activity of the NKCC cotransporter, $\rho_{NKCC}\nu_{NKCC}$, (note 2 Cl^- ions transported per cycle)

$$\frac{dCl^-_i}{dt} = 2\,\rho_{NKCC}\nu_{NKCC} - \frac{I^{ap}_{Cl^-}}{Fz_{Cl^-}} - \frac{I^{ba}_{Cl^-}}{Fz_{Cl^-}} \tag{2.25}$$

Cell potassium levels will change due to the basolateral K^+ channels, $I^{ba}_{K^+}$, and as in the case of Na^+, due the presence of $\mathrm{Na}^+ - \mathrm{K}^+ - \mathrm{ATPase}$ and NKCC proteins in the basolateral membrane (note two K^+ ions enter the cell per pump cycle)

$$\frac{dK^+_i}{dt} = \rho_{NKCC}\nu_{NKCC} + 2\,\rho_{NaK}\nu_{NaK} - \frac{I^{ba}_{K^+}}{Fz_{K^+}} \tag{2.26}$$

In the case of the apical and basolateral membrane potentials, I use the conservation of current along with the equivalent electrical circuit description of the plasma membrane / epithelium (described in Section 2.1.4) to write down the following state equations

$$\frac{dV^{ap}_m}{dt} = -\frac{1}{C_m}(+I^{ap}_{Na^+} + I^{ap}_{Cl^-} + I^{pa}_{Na^+} + I^{pa}_{Cl^-} + I^{pa}_{K^+} + I^{pa}_{gluc^-}) \tag{2.27}$$

$$\frac{dV^{ba}_m}{dt} = -\frac{1}{C_m}(I^{ba}_{Cl^-} + I^{ba}_{K^+} + I_{NaK} - I^{pa}_{Na^+} - I^{pa}_{Cl^-} - I^{pa}_{K^+} - I^{pa}_{gluc^-}) \tag{2.28}$$

The net apical current is the sum of the CFTR and ENaC currents, $I^{ap}_{net} = I^{ap}_{Na^+} + I^{ap}_{Cl^-}$, using the convention that apical current is positive in the cell to lumen direction. The net basolateral current is $I^{ba}_{net} = I^{ba}_{Cl^-} + I^{ba}_{K^+} + I_{NaK}$, noting that $I_{NKCC} = 0$ since an equal number of cations and anions are transported at the same time by the $\mathrm{Na}^+ - \mathrm{K}^+ - 2\mathrm{Cl}^-$ cotransporter. For paracellular currents I use the convention that the flow of cations in the serosal to mucosal direction defines a positive paracellular current ($I_{pa} > 0$). The net paracellular current is the sum of sodium, chloride and potassium currents along this pathway, $I^{pa}_{net} = I^{pa}_{Na^+} + I^{pa}_{Cl^-} + I^{pa}_{K^+}$. In some cases, if additional ions are being simulated in the lumen these may also be transported along the paracellular pathway. For example, when NaCl is replaced in the lumen with $\mathrm{Na}^+\mathrm{gluconate}^-$, gluconate ions will permeate through the tight junction proteins and contribute a term $I^{pa}_{gluc^-}$ to net paracellular current I^{pa}_{net}.

2.2.3 Mathematical form of model system

I can formalise the description of my model HNE cell as follows. The state of a dynamical system at time t is defined by a state vector

$$\mathbf{x}(t) = (x_1(t), x_2(t), \ldots, x_{n_x}(t)) \tag{2.29}$$

where x_h are the n_x state variables. The system is characterised by a parameter vector

$$\theta = (\theta_1, \theta_2, \ldots, \theta_{n_\theta}) \tag{2.30}$$

where θ_j are the n_θ model parameters. The time evolution of state variables is a function of both the current state of the system, $\mathbf{x}(t)$, and the parameter vector θ

$$\frac{d\mathbf{x}(t)}{dt} = f(\mathbf{x}(t), \theta) \tag{2.31}$$

This defines a system of first order, ordinary differential equations (ODEs). Given the initial state of the system $\mathbf{x}(0) = \mathbf{x}_0$ one can attempt to determine the system dynamics, $\mathbf{x}(t)$, by numerically integrating (2.31) over a time period of interest.

In the case of my model HNE cell, the state vector is given by

$$\mathbf{x}(t) = \left(W_i(t), Na_i^+(t), Cl_i^-(t), K_i^+(t), V_m^{ap}(t), V_m^{ba}(t)\right) \tag{2.32}$$

and the parameter vector for my model system contains amongst others:

- Transport pathway information, such as membrane permeabilities and protein densities $P^{ap}_{Na^+}$, $P^{ap}_{Cl^-}$, $P^{ba}_{K^+}$, $P^{ba}_{Cl^-}$, ρ_{NaK}, ρ_{NKCC}, $P^{pa}_{Na^+}$, $P^{pa}_{K^+}$, $P^{pa}_{Cl^-}$.
- Ionic composition of bathing solutions $[\mathrm{Na}^+]_l$, $[\mathrm{Cl}^-]_l$, $[\mathrm{K}^+]_l$, $[\psi]_l$, $[\mathrm{Na}^+]_s$, $[\mathrm{Cl}^-]_s$, $[\mathrm{K}^+]_s$, and $[\psi]_s$.
- Physical constants, such as the Faraday constant F, universal gas constant R and temperature T

The right hand side of equations 2.23-2.28 are dependent on both the current state of the cell $\mathbf{x}(t)$ and the model parameters θ, and hence are of the form $f(\mathbf{x}(t), \theta)$. The particular form of the functions used in my HNE cell model will in general be non-linear. For example

Model element	Notation	Index	Quantity
Variables	x	h	n_x
Parameters	θ	j	n_θ
Observation times	t	k	n_t
Observables	y	l	n_y
Outputs	Y	m	n_Y

Table 2.1: Overview of nomenclature and notation used for different quantities in analysis of mathematical model.

we saw in Section 2.1.1 that the transmembrane current I_m predicted by the GHK equation has a non-linear dependence on the transmembrane potential V_m. We also saw how the cycle rate of NKCC cotransporters ν_{NKCC} is non-linearly dependent on the internal Cl^- concentration (Section 2.1.3).

Another feature of the model ODE system is that the rates of change of the state variables are strongly coupled. That is, elements of $f_h\left(\mathbf{x}(t), \theta\right))$ involved in determining the rate of change of a particular variable x_h, are dependent on other state variables in $\mathbf{x}$. One such example is the particle flux due to the $\mathrm{Na}^+ - \mathrm{K}^+ - \mathrm{ATPase}$ pump $\rho_{NaK}\nu_{NaK}$, which is functionally related to Na_i^+ and V_m^{ba} and also appears in the rate equation for intracellular K_i^+.

2.2.4 Assumptions implicit in model

While the approach described above can give us powerful insights into the kinetics of epithelial transport in the human airways, it is only an approximate description of the true physiology of complex, living HNE cells. There are several simplifications and assumptions implicit in the model formalism which we need to remain conscious of:

- It is assumed that the behaviour of the whole epithelial monolayer can be understood by investigating ion transport in a single idealised, ciliated epithelial cell. Using parameter values (such as membrane permeabilities) that are normalised to the surface area of the epithelium, allows one to scale up appropriately. Also, airway epithelia will consist of a mixture of ciliated, secretory, undifferentiated and basal cells (Crystal et al., 2008), but for my model I assume as a first approximation a monolayer consisting only of ciliated epithelial cells.

- Only transport between lumen and cell, cell and serosa, and lumen and serosa are considered in the model. Lateral transport or communication between cells is not modelled

and it is assumed that these processes are not necessary to describe the transepithelial electrical properties of the airway epithelium.

- It is assumed that the electrical properties of an airway epithelium are accurately described by the equivalent electrical circuit shown in 2.9.

- There is no description of the cell's pH, metabolic state, Ca^{2+} concentration or cAMP levels. These properties of the HNE cell are assumed to be constant throughout any simulations that are implemented, and are assumed not to be responsible for any observed changes in state variables.

- There are no channel gating variables in the model. Transmembrane ion currents are assumed to be adequately described by the GHK flux equation 2.2. The underlying channel activity facilitating these currents is characterised solely by the ionic permeability per unit surface area.

- Solutions in all compartments are assumed to be well stirred. There is no description of cell geometry or spatial variation in variables, so it is implicitly assumed that concentrations in the cell are homogeneous throughout.

- The ionic composition of the extracellular compartments do not change due to transmembrane or transepithelial fluxes. This assumes that they are effectively infinite in extent when compared with the cell volume, and act as reservoirs for ions and water.

- Cell volume changes due to transmembrane water fluxes only. It is assumed that the volume of transmembrane ion fluxes are negligible in comparison and do not contribute to changes in volume.

2.3 Methods of analysis of mathematical model

In this section I will outline the various mathematical analysis methods I use to study the biophysical ion transport model defined by equations 2.23-2.28. This includes methods to determine model steady states, as well as the methods used to simulate ion transport kinetics. Methods of estimating model parameter values from experimental observations are also discussed.

2.3.1 Determining steady states and numerically integrating model ODEs

2.3.1.1 Determining steady states of model system

The system of ODEs 2.23-2.28 define the kinetics of ion transport processes of interest in a typical HNE cell. However as these cells are not excitable, under normal physiological conditions we would not expect the physiological variables that I consider, concentrations and membrane potentials, to be varying in time. We would expect that HNE cells are capable of maintaining a stable, constant volume, and capable of balancing the movement of ions into and out of the cell, in such a way that no concentration grows indefinitely or collapses to zero. Therefore, when I am studying these cells I am quite often interested in the conditions necessary for constant volume and ionic concentrations to be maintained. To posit this question in the framework of the mathematical model, I am interested in determining the set of conditions which allow $f(\mathbf{x}^*, \theta) = 0$. Here I use $\mathbf{x}^*$ to refer to a specific set of variable values which give a steady state of the model system. In full, for a steady state of the model system, the following conditions must be true

$$0 = J_w^{ba} - J_w^{ap} \tag{2.33}$$

$$0 = J_{NKCC} - 3J_{NaK} - \frac{I_{Na^+}^{ap}}{Fz_{Na^+}} \tag{2.34}$$

$$0 = 2J_{NKCC} - \frac{I_{Cl^-}^{ap}}{Fz_{Cl^-}} - \frac{I_{Cl^-}^{ba}}{Fz_{Cl^-}} \tag{2.35}$$

$$0 = J_{NKCC} + 2J_{NaK} - \frac{I_{K^+}^{ba}}{Fz_{K^+}} \tag{2.36}$$

$$0 = I_{Na^+}^{ap} + I_{Cl^-}^{ap} + I_{Na^+}^{pa} + I_{Cl^-}^{pa} + I_{K^+}^{pa} \tag{2.37}$$

$$0 = I_{Cl^-}^{ba} + I_{K^+}^{ba} + I_{NaK} - I_{Na^+}^{pa} - I_{Cl^-}^{pa} - I_{K^+}^{pa} \tag{2.38}$$

Equations 2.33 to 2.38 comprise a set of non-linear equations of the form $f(\mathbf{x}, \theta) = 0$. Assuming I know the parameter values θ, I can find the steady state variable values $\mathbf{x}^*$ which solve $f(\mathbf{x}, \theta) = 0$ using the *fsolve* function in MATLAB Optimisation Toolbox (MATLAB, 2010).

2.3.1.2 Numerically integrating model ODEs

The system of ordinary differential equations that describe the model are first order ODEs as only the first derivative of the dependent variable $\mathbf{x}$, with respect to the independent variable time t, is present. The specific problem I need to solve is an *initial value problem*, as I want to

know how the system evolves in time from an initial starting point $\mathbf{x}_0$. This is summarised as

$$\begin{aligned} \frac{d\mathbf{x}}{dt} &= f(\mathbf{x}, \theta) \\ \mathbf{x}(t=0) &= \mathbf{x}_0 \end{aligned} \tag{2.39}$$

Initial value problems can be solved in MATLAB using a number of different numerical integration algorithms. In my work I used the function *ode15s*, as this is specifically designed for solving systems of stiff ODEs. A set of ODEs is said to be stiff if the variables in the system are changing on very different timescales. In the case of the model HNE system, membrane potentials tend to equilibrate on the time scale of milliseconds, where as cell volume and concentrations tend to equilibrate on the timescale of seconds to minutes. Hence I have a stiff ODE system and must use appropriate algorithms, such as *ode15s*, when numerically integrating them.

2.3.2 Estimating model parameters via error minimisation

In the previous section I described how, given a set of parameter values θ, one could determine model variables at steady state, $\mathbf{x}^*$, or given parameter values and initial variables values, $\mathbf{x}_0$, solve for the state variable values as a function of time, $\mathbf{x}(t)$. Now I describe the inverse problem, that is, how to find the values of parameters, $\hat{\theta}$, given a set of experimental data $\hat{\mathbf{y}}(t)$ which is functionally related to the time evolution of model variables $\mathbf{x}(t)$. In this case I *estimate* model parameter values by minimising the error between what my model predicts for certain observables, and the experimental values that have been measured for them.

I construct the parameter estimation problem by first considering a model ODE system which describes the dynamics of state variables $\mathbf{x}(t, \theta)$, given parameters θ, as before in 2.39. I then expand this framework, to consider a set of observables $\mathbf{y}(t)$ which are functionally related to the dynamics of my variables by some function $g\left(\mathbf{x}(t, \theta), \theta\right)$. My model system and experimental measurements are defined by

$$\begin{aligned} \frac{d\mathbf{x}}{dt} &= f(\mathbf{x}, \theta) \\ \mathbf{x}(t=0, \theta) &= \mathbf{x}_0\left(\theta\right) \\ \mathbf{y}(t, \theta) &= g\left(\mathbf{x}(t, \theta), \theta\right) + \epsilon(t) \end{aligned} \tag{2.40}$$

The observables $\mathbf{y}$ will typically only be measured at discrete time points $t_k, k = 1, \ldots, n_t$, and

there will also generally be measurement noise $\epsilon(t_k)$ associated with each of these data points.

If I perform a forward simulation of the model ODE system, by solving 2.39 for a given θ, I can then determine the values of $\mathbf{y}$ that my system would predict. If I compare my predictions at the time points t_k, $\mathbf{y}(t_k, \theta)$, with the observations at the n_t different measurement times, $\hat{\mathbf{y}}(t_k)$, I can compute the weighted sum of squared errors, or sum of squared residuals, using

$$\chi^2(\theta) = \sum_{l=1}^{n_y} \sum_{k=1}^{n_t} \left(\frac{\hat{y}_l(t_k) - y_l(t_k, \theta)}{\hat{\sigma}_{lk}^2} \right)^2 \tag{2.41}$$

Here the summation is over the n_y different observables in the vector $\mathbf{y}$, and over each of the n_t measurement time points, weighted by the measurement errors $\hat{\sigma}_{lk}$ at each $\hat{y}_l(t_k)$.

As before, I can use an algorithm to minimize the objective function $\chi^2(\theta)$. I define the *best fit* or *optimal* parameter set $\hat{\theta}$, as that which minimizes the objective function.

$$\hat{\theta} = \arg\min_{\theta} \quad \left\{ \chi^2(\theta) \right\} \tag{2.42}$$

If I assume the measurement noise is normally distributed, such that $\epsilon \sim N\left(0, \sigma^2\right)$, then $\chi^2(\theta)$ is related to the statistical likelihood $L(\theta)$ as follows (Raue et al., 2009)

$$\chi^2(\theta) = constant - 2 \log L(\theta) \tag{2.43}$$

Since the sum of the weighted square residuals and the likelihood only differ by a constant, minimising $\chi^2(\theta)$ will maximise $L(\theta)$. Hence I can find the maximum likelihood estimate (MLE) of $\hat{\theta}$ via 2.42.

In order to determine how tightly constrained my estimates of a particular parameter $\hat{\theta}_j$ are, I can compute confidence intervals of the form $[\theta_j^-, \theta_j^+]$ for the estimate. A *Monte Carlo* approach is possible here. I can randomly generate a large number (N_{sim}) of synthetic noisy data sets of the form

$$\tilde{y} = \hat{y}\left(1 + N(0, \hat{\sigma}^2)\right) \tag{2.44}$$

Minimising 2.41 for each synthetic data set $\tilde{y}$ independently, will leave us with a distribution of N_{sim} estimates for each particular parameter, $\left\{(\theta_j)^1, (\theta_j)^2, \ldots, (\theta_j)^{N_{sim}}\right\}$. Looking at the median of one of these distributions allows one to make an estimate of the true value of the parameter in question, and by computing the interquartile (IQR) range one determine the relative

uncertainty in that estimate.

2.3.3 Monte Carlo parameter sampling and filtering

In my analysis of ion transport in HNE cells, I am interested in understanding what is causing the differences in physiological properties observed between cells with a CF mutation, and those without a mutated *CFTR* gene. The differences observed in physiology manifest in the cell's steady state properties, such as baseline transepithelial PD, and also manifest in the cell's response to experimental interventions, such as increased sensitivity of transepithelial PD to amiloride addition, or lack of response to removal of Cl^- from the lumen perfusate.

In terms of analysing my mathematical model, the physiological properties just described can be thought of as a set of n_Y model outputs $\mathbf{Y} = (Y_1, Y_2, \ldots, Y_{n_Y})$ which are a functionally related to model inputs, the transport parameters $\theta = (\theta_1, \theta_2, \ldots, \theta_{n_\theta})$. If I can determine the mapping from transport parameter values to each of the model outputs, $Y_m = f(\theta_1, \theta_2, \ldots, \theta_{n_\theta})$, then I can hope to understand how the differences in $\mathbf{Y}$ correspond to differences in θ.

To investigate the differences in transport physiology between non-CF and CF cells, I can first quantify these differences by defining the different ranges each Y_m takes in CF and non-CF states. For example, in the case of transepithelial PD, in non-CF HNE cells *in vitro* one might expect to observe $-15\ \mathrm{mV} \leq V_t \leq -5\ \mathrm{mV}$, but in a CF HNE cell one might expect it to be in the range $-45\ \mathrm{mV} \leq V_t \leq -20\ \mathrm{mV}$. Repeating this for a group of several different model outputs $\mathbf{Y}$, I can describe bounds on allowed outputs in non-CF cell, $\mathbf{B}_{non-CF}$, and a separate set of bounds $\mathbf{B}_{CF}$ for CF cells. If these bounds on allowed outputs can be mapped to constraints on allowed inputs, I can gain insight into what parameters are critical to the observed physiological changes and which are not.

In general the mappings $Y_m = f(\theta_1, \theta_2, \ldots, \theta_{n_\theta})$ will have to be found numerically. This is because the outputs will require solving both (a) the set of non-linear equations, 2.33 - 2.38, for steady state properties like basal transepithelial PD, and (b) the set of non-linear ODEs 2.23 - 2.28, for metrics like the change in V_t due to amiloride addition. One approach to determine the mapping numerically, is to perform a Monte Carlo sampling on the input parameter space, generating many sample parameter vectors θ, and compute the corresponding outputs $\mathbf{Y}(\theta)$ at each point of parameter space sampled. The set of individual $\mathbf{Y} = f(\theta)$ that are computed, are then used to filter the sampled parameter vectors into separate distributions, depending on

whether $\mathbf{Y}$ falls within the constraints $\mathbf{B}_{non-CF}$ or $\mathbf{B}_{CF}$.

This is an approach referred to as Monte Carlo Filtering (MCF) (Saltelli, 2004), and an algorithm for performing it is as follows:

- Define a set of model outputs $\mathbf{Y}$ to use as a basis of the MCF analysis. These could be steady state properties, based on x^*, or functions of the model's kinetic behaviour, $\mathrm{x}(t)$.
- Define two distinct sets of bounds for the values of $\mathbf{Y}$ being considered (here I define $\mathbf{B}_{non-CF}$ and $\mathbf{B}_{CF}$).
- Randomly generate a large number of parameter sets, covering the input parameter space of interest. Compute $\mathbf{Y}$ for each sample θ.
- Filter model inputs θ based on whether the computed $\mathbf{Y} = f(\theta)$ falls within $\mathbf{B}_{non-CF}$ or $\mathbf{B}_{CF}$. This will leave you with two sets of parameter values that come from unknown distributions, $f_1\left(\theta|\mathbf{B}_{non-CF}\right)$ and $f_2\left(\theta|\mathbf{B}_{CF}\right)$.
- Differences between the distribution of each parameter value $(\theta_1, \theta_2, \ldots, \theta_{n_\theta})$ can be observed to find what is responsible for differences in Y.

2.3.4 Variance based parameter sensitivity analysis

As well as determining how individual transport parameters θ_j will differ between CF and non-CF epithelia, which I can address with an MCF analysis, I would also like to know the relative influence of each individual transport parameter θ_j on each output Y_m. This can help us gain a quantitative insight into which changes in transport physiology are most likely responsible for the changes in electrophysiology observed in CF. This requires us to perform a sensitivity analysis on my model system, in order to be able to rank the parameters θ_j in order of influence on a given output Y_m.

As discussed in the previous section, the relationship between model inputs and outputs $\mathbf{Y} = f\left(\theta_1, \theta_2, \ldots, \theta_{n_\theta}\right)$ will not be known in the general case. I can investigate it numerically by generating Monte Carlo realisations of θ and $\mathbf{Y}$. If I assume I know the form of the mapping $f(.)$ relating the inputs and outputs, I can then quantitatively relate the variance in inputs to the variance in outputs.

One approach to performing a variance based sensitivity analysis, is to assume the relationship between model inputs and outputs can be captured satisfactorily with a multiple linear

regression model. A linear regression model relates some response or output y to a linear combination of predictor terms $f(x)$ which are functions of model inputs x. If there are several input variables x this is referred to as a multiple linear regression. An example, linking input parameters $\mathbf{x} = (x_1, x_2)$, to an output y, is as follows:

$$y = b_0 + b_1 x_1 + b_2 x_2 + b_{11} x_1^2 + b_{22} x_2^2 + b_{12} x_1 x_2 \tag{2.45}$$

$$y = \mathbf{Bx} \tag{2.46}$$

Here the model has predictor terms that are both linear and quadratic in the input variables, for example terms $b_1 x_1$ and $b_{11}(x_1)^2$ respectively, as well as predictor terms based on interactions between model inputs, here $b_{12} x_1 x_2$. It is important to note however that the regression itself is linear combination of predictor functions $f(x)$.

Taking this approach, I can use the following regression model to map model parameters θ_j to a given model output Y_m:

$$Y_m = b_0 + \sum_{j=1}^{n_\theta} \left(b_j \theta_j + b_{jj} \theta_j^2 \right) + \sum_{j=1}^{n_\theta} \sum_{j'=j+1}^{n_\theta} b_{jj'} \theta_j \theta_{j'} \tag{2.47}$$

In this model, regression co-efficients b_j determine the strength of linear correlation between a single parameter θ_j and the output Y_m. By comparing the magnitude of the linear regression co-efficients I have a means of determining the relative influence a given transport parameter has on a model output (physiological observable) of interest.

2.3.5 Practical identifiability of model parameters via profile likelihood

The mathematical model I use to describe ion transport kinetics in HNE cells, has more parameters θ than variables x (i.e. $n_\theta \geq n_x$). In practice, it may be technically difficult to measure all of these variables simultaneously, so the amount of measured observable data available for parameter estimation (n_y observables $\times n_t$ measurement time points) may also be similar in quantity to or less than n_θ. It is important therefore that I understand the relationship between the goodness of fit function $\chi^2(\theta)$, and the amount of data I am using for parameter estimation. Given a model system and experimental data set, I would like to be able to answer questions such as, is it possible to make unique estimates of parameter values of interest, or is there insufficient information in the observed data to identify constraints on estimated parameter values? Here I will outline how one can systematically investigate these issues of parameter identifia-

bility using the *profile likelihood*.

2.3.5.1 Likelihood based confidence intervals

Before introducing the profile likelihood I will outline how one can compute likelihood based confidence intervals. Assuming I know the maximum likelihood estimate $\hat{\theta}$, I can compute a confidence interval for finding the true value $\theta^{\dagger}$, based on thresholds in the value of the likelihood. Since $\chi^2(\theta)$ and $L(\theta)$ differ only by a constant (as defined by 2.43), I can equally define the threshold in terms of $\chi^2(\theta)$.

$$\left\{\theta | \left(\chi^2(\theta) - \chi^2(\hat{\theta})\right) < \Delta_\alpha\right\} \text{ with } \Delta_\alpha = \chi^2(\alpha, df) \tag{2.48}$$

The true value $\theta^{\dagger}$ will be in the region where $\chi^2(\theta)$ is less than the minimum value $\chi^2(\hat{\theta})$ plus some threshold value Δ_α. The threshold will depend on the significance level I want to assign to the confidence interval. For a confidence level α, the threshold is found from the α-th quantile of the relevant χ^2 distribution, $\chi^2(\alpha, df)$, where df is the degrees of freedom. Using $df = 1$ gives a pointwise interval for the estimate of θ.

2.3.5.2 Structural and practical identifiability

In a model system of the form described in 2.40, it may not be possible to uniquely estimate model parameters, depending on the mapping between model variables $\mathbf{x}$ and observable data $\mathbf{y} = g(\mathbf{x}(t, \theta), \theta)$. If there is a subset of model parameter values θ_{sub} which can always be combined in such a way that $\chi^2(\theta)$ remains constant, then the system is said to be *structurally unidentifiable*. This can be stated formally as

$$\chi^2(\theta) = \chi^2(\hat{\theta}) \Leftrightarrow h(\theta_{sub}) = 0 \tag{2.49}$$

There is some function $h(.)$ that defines a relationship between parameters in θ_{sub}, such that $\chi^2(\theta)$ will always remain constant regardless of individual parameter values, so long as the condition $h(\theta_{sub}) = 0$ is met. The corresponding confidence intervals for θ_j may then be infinite. Hence I cannot assign confidence intervals and the system is said to be structurally unidentifiable. An illustration of this can be seen in Figure 2.10(a), where $\chi^2(\theta_1, \theta_2)$ does not change along the manifold $h(\theta_1, \theta_2) = \theta_1\theta_2 - 10$.

If a parameter is structurally identifiable, it still may be impossible to determine finite confidence intervals for that value to an arbitrary confidence α. In this case the parameter in

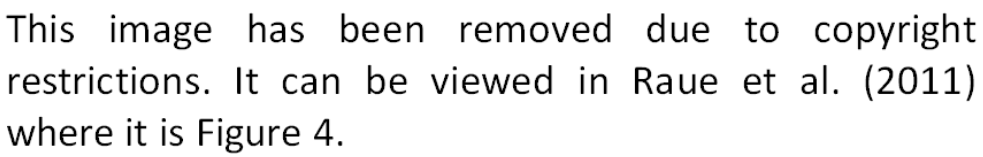

Figure 2.10: Diagram showing profile likelihood (dashed line) of a given parameter θ_1 overlaid on a contour plot of the sum of squared residuals, $\chi^2(\theta_1, \theta_2)$. In panel (a) there is a functional relationship between θ_1 and θ_2, along which the value of χ^2 remains the same. This means the profile likelihood for θ_1 is flat (b) and signifies a structural identifiability issue. The case in (c) highlights a practical identifiability issue. There is a minimum in $\chi^2(\theta)$, but the landscape is not convex. In (d) I see that $\chi^2_{PL}(\theta_1)$ does not breach the Δ_α threshold as $\theta_1 \to \infty$, hence I cannot define an upper bound for θ_1 to a confidence level α. Finally, in (e), there is a global minimum in the optimisation landscape, and confidence limits can be found for θ_1 since its profile likelihood is convex (f). Image from Raue et al. (2011).

question is said to be *practically unidentifiable*. This usually arises due to insufficiencies with observed data, due to measurement noise or a small number of data points. An illustration of this phenomenon this can be seen in 2.10(c), here the MLE of θ_1 is about 4, but as $\theta_1 \to \infty$, it is always possible to find the same minimum value of $\chi^2(\theta)$, given the appropriate value of θ_2.

2.3.5.3 Profile likelihood

One approach to assessing issues of identifiability in ODE based models, involving analysing the profile likelihood function, was put forward by Raue and co-workers (Raue et al., 2009, 2011). The profile likelihood function is defined from the weighted sum of square residuals function 2.42 as follows

$$\chi^2_{PL}(\theta_j) = \underset{\theta_{p\neq j}}{\text{minimise}} \left[\chi^2(\theta)\right] \tag{2.50}$$

The objective function $\chi^2(\theta)$ is minimised by varying the parameters $\theta_{p\neq j}$, while one parameter θ_j is fixed at a particular value. By fixing θ_j at a range of different values, and re-optimising $\chi^2(\theta)$ as a function of $\theta_{p\neq j}$ each time, I can compute $\chi^2_{PL}(\theta_j)$ for a region of interest.

The identifiability of the parameter in question θ_j can then be assessed from its profile likelihood. If χ^2_{PL} never changes as θ_j is changed then it is structurally unidentifiable. If χ^2_{PL} has a minimum, but the profile does not rise above a certain threshold, then the parameter may be practically unidentifiable. Finally, if χ^2_{PL} is a convex function of θ_j it is possible to define appropriate confidence intervals and that parameter is identifiable. These concepts are illustrated schematically in Figure 2.10(b,d,f).

To compute the profile likelihood one requires an appropriate algorithm. It should (1) increment the parameter θ_j from its maximum likelihood value, (2) minimise the objective function 2.50 as a function of $\theta_{p\neq j}$, and (3) repeat steps (1) and (2) until the profile likelihood has passed a specified threshold value (Δ_α). To this end I used the *PLdriver* algorithm developed using MATLAB by Joep Vanlier and coworkers (http://bmi.bmt.tue.nl/sysbio/software/pua.html) which allows a profile likelihood to be computed for a user supplied objective function (Vanlier et al., 2012).

2.4 Model validation

Before carrying out analysis of the mathematical ion transport model, I first needed to validate its basic properties and behaviour. By validate here I mean a couple of things. One, I needed to ensure that the model would reproduce known properties of a HNE cell, given appropriate

Table 2.2: Initial baseline values used for transport parameter values.

Parameter	Value	Units	Reference
$P^{ap}_{Na^+}$	0.028	μm/s	(Willumsen and Boucher, 1991b)
$P^{ap}_{Cl^+}$	0.072	μm/s	(Willumsen and Boucher, 1991b)
$P^{ba}_{K^+}$	0.080	μm/s	(Falkenberg and Jakobsson, 2010)
$P^{ba}_{Cl^+}$	0.100	μm/s	(Falkenberg and Jakobsson, 2010)
ρ_{NaK}	0.400	10^{-10}mol/cm^2	author estimate
ρ_{NKCC}	0.400	10^{-10}mol/cm^2	author estimate
$P^{pa}_{Na^+}, P^{pa}_{Cl^-}, P^{pa}_{K^+}$	0.035	μm/s	(Willumsen and Boucher, 1989)

estimates for model parameter values found in the literature. For example, under physiological conditions these cells should be primarily Na^+ absorbing, and produce a lumen-negative transepithelial potential. Secondly, I needed to ensure that the model is capable of maintaining stable kinetics in response to small perturbations in physiological variables.

2.4.1 Baseline transport parameter values

The overarching theme of my PhD research is to understand how the activity of different transport proteins influences the electrophysiology of airway epithelial cells. To this end, the model parameters that I focus on are those that are proportional to the expression level of ion channels, pumps and co-transporters in human nasal epithelial cells. Specifically they are $\left(P^{ap}_{Na^+}, P^{ap}_{Cl^-}, P^{ba}_{K^+}, P^{ba}_{Cl^-}, \rho_{NaK}, \rho_{NKCC}, P^{pa}_{Na^+}, P^{pa}_{Cl^-}, P^{pa}_{K^+}\right)$, and I refer to these as *transport parameters*. Throughout the work that follows, all other parameter values will be assumed fixed at a certain value unless otherwise stated. The values I use for these fixed parameters are taken from the scientific literature and recorded in the Appendix A.1, see Table A.1.

I will now describe the source of the *baseline* estimates of the transport parameters of interest that I initially use, which are listed in Table 2.2. Willumsen and Boucher published estimates of apical Na^+ ($P^{ap}_{Na^+}$) and apical Cl^- ($P^{ap}_{Cl^-}$) permeabilities in HNE cells with non-CF CFTR (Willumsen et al., 1989b; Willumsen and Boucher, 1991a). They also estimated the resistance of the paracellular pathway in these cell types, and an estimate of the corresponding paracellular permeability can be made from this data (Willumsen and Boucher, 1989). Falkenberg and Jakobsson published estimates of the expected basolateral K^+ ($P^{ba}_{K^+}$) and Cl^- ($P^{ba}_{Cl^-}$) permeabilities in Calu-3 and human bronchial epithelial (HBE) cells, based on data in the studies of Cowley and Linsdell (2002), Fischer et al. (2007) and Itani et al. (2007). Estimates of Na^+-K^+ pump (ρ_{NaK}) and NKCC (ρ_{NKCC}) co-transporter membrane densities were not available in

Table 2.3: Selected steady state properties of model HNE cell, given literature estimates of transport parameters.

Property	Value	Units
$[\mathrm{Na}^+]_i$	16.7	mM
$[\mathrm{Cl}^-]_i$	69.3	mM
$[\mathrm{K}^+]_i$	114.0	mM
V_m^{ap}	-12.3	mV
V_m^{ba}	-23.7	mV
V_t	-11.4	mV
$DF_{Na^+}^{ap}$	-69.2	mV
$DF_{Cl^-}^{ap}$	+2.3	mV
$I_{Na^+}^{ap}$	-33.6	$\mu\mathrm{A/cm}^2$
$I_{Cl^-}^{ap}$	+4.2	$\mu\mathrm{A/cm}^2$

the literature, so I chose values which allowed a realistic steady state of the ODE system when the other baseline parameter values were used.

2.4.2 Baseline model properties

Using these initial literature parameter estimates, one can assess whether or not my model is giving realistic predictions for physiological variables associated with HNE cells. Table 2.3 lists the values of several physiological variables predicted by my model, found by solving the set of non-linear equations 2.33-2.38 given parameter values in tables 2.2 and A.1.

Even though my transport parameter estimates are taken from disparate sources, I predict a realistic picture of a HNE cell. Internal Na^+ is low, and internal K^+ is high, as one would expect, and I also find that the transepithelial potential difference is lumen-negative. Interestingly, there is a large driving force for Na^+ absorption across the apical membrane ($DF_{Na^+}^{ap}$ in Table 2.3), and the corresponding driving force for Cl^- ($DF_{Cl^-}^{ap}$) is very low in comparison. This is reproducing the fact that these HNE cells will actively absorb Na^+ under normal conditions, but Cl^- will be near to equilibrium across the apical membrane. Here I see that I predict a larger apical Na^+ current than apical Cl^-, despite $P_{Cl^-}^{ap}$ being greater than $P_{Na^+}^{ap}$, due to the aforementioned differences in driving forces.

2.4.3 Model stability analysis

I carried out model validation to assess the stability of the model dynamical system to small perturbations to model variables. The perturbations were introduced for numerical validation only, to determine if the system remained stable and behaved in a physiologically realistic

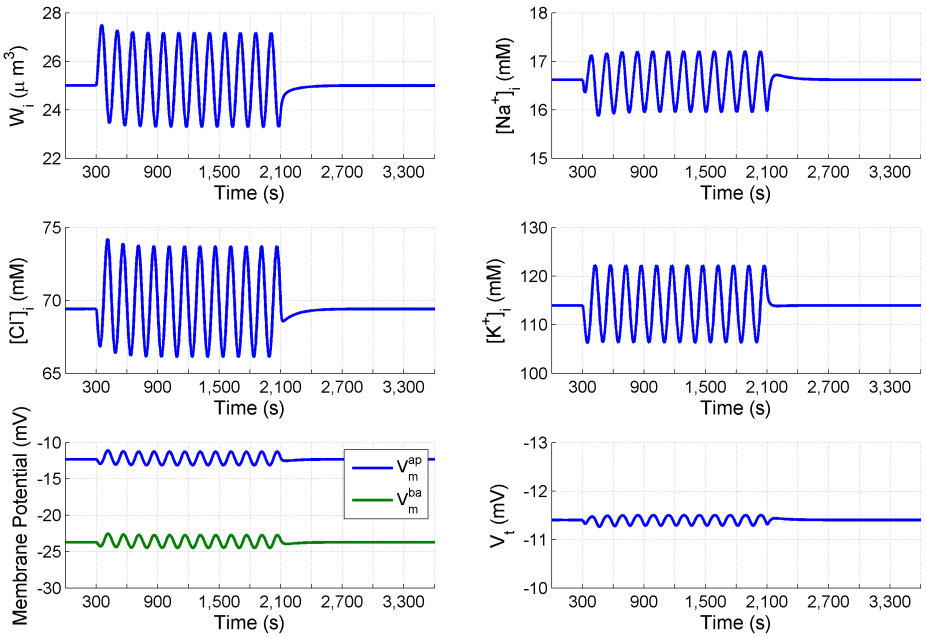

Figure 2.11: Between times $T_1 = 300$ s and $T_2 = 2100$ s the ODE for the rate of change of W_i is perturbed by a sinusoidally varying forcing term of the form $u(t) = u_0 sin(\omega t)$, where $\omega = \pi/75$ s^{-1} and $u_0 = 0.18$ μm^3/s. All other model variables are perturbed because of the coupled nature of the system, which nonetheless remains stable throughout.

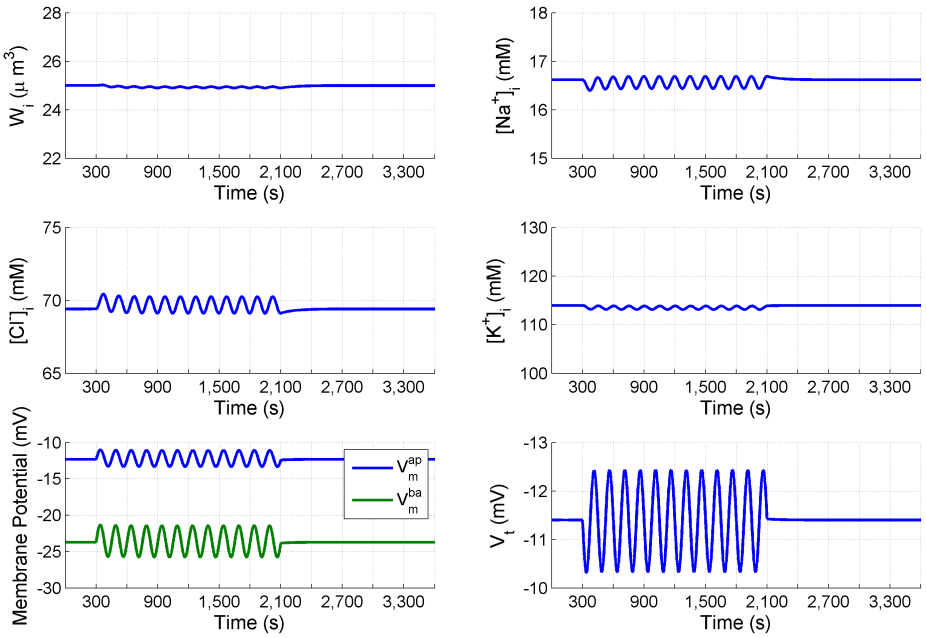

Figure 2.12: Between times $T_1 = 300$ s and $T_2 = 2100$ s the ODE for the rate of change of V_m^{ba} is perturbed by a sinusoidally varying forcing term of the form $u(t) = u_0 sin(\omega t)$, where $\omega = \pi/75$ s^{-1} and $u_0 = 1.00 \times 10^6$ mV/s. The system remains stable despite the perturbation.

manner given baseline parameter estimates. The perturbations introduced were not intended to simulate a particular physiological phenomenon.

Model validation was implemented by adding a sinusoidally varying forcing term $u(t)$ to the right hand side of the model ODEs 2.23-2.28, one ODE at a time. The term is of the form $u(t) = u_0 sin(\omega t)$ with frequency $\omega = \pi/75\ \mathrm{s}^{-1}$ and the forcing term was only switched on for a fixed time interval $T_1 \rightarrow T_2$, after which the system was allowed to return to its original state. For each cellular quantity of interest (volume, ionic concentrations, membrane potentials), I recorded the magnitude of the maximum displacement caused by the perturbation, as a percentage of the initial steady state value of that property. For each ODE, I chose a different value for the amplitude of the forcing term u_o. I chose the values manually such that the magnitude of the resulting maximum displacement in that particular cellular variable would be approximately 10% of its steady state value.

Examples of this type of simulation can be seen in Figures 2.11 and 2.12. Here the variables being perturbed are cell volume, W_i, and basolateral membrane potential, V_m^{ap}, respectively. I found that with the baseline estimates of transport parameter values, the system remains stable during and after these sinusoidal perturbations of model variables, regardless of the particular variable (ODE) being perturbed. The magnitude of the maximum displacement of variable values not being forced directly, was never greater than 20% of the original steady state level, and on average these displacements were smaller in magnitude than that the change observed in the quantity that was being perturbed directly. This suggests that this model is relatively robust to small changes in variable values. The results of this model validation exercise can be seen in Table 2.4.

Table 2.4: Amplitude of oscillations in cellular properties (as $\%$ of steady state value) caused by adding a forcing term to a single model ODE, of the form $u_0 \sin(\pi t/75s)$.

		Perturbed variable					
Cell property	u_0	W_i	$\mathrm{Na_i^+}$	$\mathrm{Cl_i^-}$	$\mathrm{K_i^+}$	V_m^{ap}	V_m^{ba}
Volume	$0.18\ \mu\mathrm{m}^3/\mathrm{s}$	10.0%	1.2%	3.0%	6.6%	0.2%	0.4%
$[\mathrm{Na}^+]_i$	$2.43\times10^{-17}\ \mathrm{mol/s}$	4.5%	10.0%	7.7%	5.9%	0.8%	1.3%
$[\mathrm{Cl}^-]_i$	$6.05\times10^{-17}\ \mathrm{mol/s}$	6.9%	3.4%	10.0%	6.3%	0.7%	1.5%
$[\mathrm{K}^+]_i$	$10.60\times10^{-17}\ \mathrm{mol/s}$	7.3%	1.7%	4.3%	10.0%	0.3%	0.8%
V_m^{ap}	$4.48\times10^{5}\ \mathrm{mV/s}$	9.7%	9.5%	19.1%	13.1%	10.0%	10.5%
V_m^{ba}	$1.00\times10^{6}\ \mathrm{mV/s}$	4.9%	6.9%	12.0%	8.3%	2.6%	10.0%
V_t		1.2%	4.2%	4.3%	3.2%	5.7%	9.5%

Chapter 3

Estimating transport parameters from *in vitro* electrophysiological recordings

3.1 Introduction

In the first chapter of this thesis I described the fundamental concepts behind epithelial transport mechanisms, and highlighted the major ion transport proteins that are expressed in the human airway epithelium. In the second chapter I described how one could model transport by each of these proteins, and integrate these descriptions into a whole cell model of epithelial ion transport. I also described several methods that could be used to investigate the properties of the whole cell model, and how one could use the model to infer quantitative information about the activity of different proteins from observed experimental data.

In this chapter I will now describe how I used the mathematical model to simulate Ussing chamber experiments, common in the study of epithelial electrophysiology, in order to estimate transport parameters from electrophysiological data. In particular, I make estimates of membrane permeabilities to Na^+ and Cl^- ions, in both CF and non-CF primary cultures of HNE cells, in order to understand how they differ in cystic fibrosis.

3.2 Methods

3.2.1 Simulating Ussing chamber experiments

In order to perform parameter estimation using the approach outlined in Section 2.3.2, it is necessary to have a set of experimental observations $\{\hat{\mathbf{y}}(t_k), \sigma(t_k) | k = 1, \ldots, n_t\}$, and a model that can make predictions as to what values the observables should take as a function of model parameters, $\mathbf{y}(t_k, \theta)$. I have previously described the mathematical model in detail (see Section 2.2), now I will describe the type of experiment and type of data I will use for parameter

estimation.

The two types of simulated or *in silico* experiment that I implement are (i) pharmacological block of ENaC channels with amiloride, and (ii) removing Cl^- from the solution in luminal compartment of the Ussing chamber. Addition of amiloride and reduction of $[\mathrm{Cl}^-]$ in the luminal perfusing solution are also used when obtaining patient nasal potential difference measurements, and therefore are of considerable clinical interest. The effect of (i) is to block all apical Na^+ channels, thus reducing the current $I^{ap}_{Na^+}$ to zero. The loss of this apical Na^+ current will cause the apical membrane potential to change, as per equation 2.27, and hence the transepithelial PD will change as well. The change in V_t due to this manoeuvre is usually referred to as *amiloride-sensitive* V_t, or $\Delta V_t + \mathrm{amiloride}$. This metric (and the corresponding amiloride-dependent change in nasal PD) is of interest as it tends to be increased on average in CF HNE cells, as discussed in Section 1.2.3. As the magnitude of $\Delta V_t + \mathrm{amiloride}$ will be influenced by the permeability of the apical membrane to Na^+, this is regularly used as a surrogate measure of ENaC channel activity in epithelial cells.

The effect of (ii) is to increase the driving force for Cl^- secretion across the apical membrane. Typically Cl^- will be at or close to thermodynamic equilibrium across the apical membrane when lumen $[\mathrm{Cl}^-]$ is approximately $120\ \mathrm{mM}$ (see Figure 4 in (Willumsen et al., 1989b)). If then the external concentration is lowered significantly, there will be a favourable driving force for Cl^- to exit the cell, $I^{ap}_{Cl^-}$ will change as a result, leading to a corresponding change in the transepithelial V_t. By recording the change in V_t, commonly referred to as $\Delta V_t + 0[\mathrm{Cl}^-]_l$, one can make inferences about the level of CFTR channel activity that is facilitating the Cl^- current.

These perturbations can be modelled with the ODE system described in Section 2.2, by choosing an appropriate initial condition $\mathbf{x_0}$ and making the necessary changes to the parameter vector θ, in order to represent the different bath solutions perfused on the luminal side of the nasal epithelial cells. Table 3.1 lists the relevant parameter values used to model the different lumen solutions. A physiological saline solution (NaCl) is used to determine the initial model steady state, then the system of ODEs is integrated with either a $\mathrm{NaCl} + \mathrm{amiloride}$ or $\mathrm{Na}^+ - \mathrm{gluconate}^-$ solution.

Table 3.1: Ionic composition of lumen bath solutions used during Ussing Chamber experiments.

	Lumen bath solutions (concentrations in mM)		
	NaCl	$\mathrm{NaCl} + \mathrm{Amiloride}$	$\mathrm{Na}^+ - \mathrm{gluconate}^-$
$[\mathrm{Na}^+]_\mathrm{l}$	140	140	140
$[\mathrm{Cl}^-]_\mathrm{l}$	120	120	3
$[\mathrm{K}^+]_\mathrm{l}$	5	5	5
$[\mathrm{gluconate}^-]_\mathrm{l}$	0	0	117
$[\psi]_\mathrm{l}$	25	25	25
$P^{ap}_{Na^+}$	$P^{ap}_{Na^+} > 0$	$P^{ap}_{Na^+} = 0$	$P^{ap}_{Na^+} > 0$

3.2.2 Amiloride block of ENaC channels

The effect of blocking ENaC channels in a HNE cell with amiloride, can be implemented in the following manner. Given a certain set of parameter values θ, which includes a non-zero apical Na^+ permeability ($P^{ap}_{Na^+}$), I determine the steady state variables values $\mathbf{x}^*$ by solving $f(\mathbf{x}, \theta) = 0$ by the method described in Section 2.3.1.1. This steady state $\mathbf{x}^*$ is then used as the initial condition $\mathbf{x}_0$ for an initial value problem (IVP) of the form 2.39. When solving this IVP, a different parameter vector θ' is used, which is the same as θ except the value of $P^{ap}_{Na^+}$ is equal to zero. The system then evolves in time in a state which has no apical Na^+ permeability.

This approach assumes that the system is initially in a steady state configuration, then at a certain point all ENaC channels are blocked simultaneously, at which point the system must relax to a new steady state. The assumption that amiloride only inhibits ENaC, and no other transport protein, is commonly made in experimental as well as modelling studies (Horisberger, 2003; Falkenberg and Jakobsson, 2010; Garcia et al., 2013) and is also the basis for interpretation of amiloride sensitive V_t measurements in the standard nasal PD test (Knowles et al., 1995).

A representative example of this type of *in silico* experiment, using baseline parameter values, can be seen in Figures 3.1 (traces of model variables) and 3.2 (traces of individual currents and fluxes). One can see a significant depolarisation in V_t on blocking ENaC channels (resulting from a large hyperpolarisation of the apical membrane and a smaller hyperpolarization of the basolateral one), which is a characteristic of airway epithelia. One can also observe how the internal Na^+ concentration decreases, as the flux across the basolateral membrane does eventually reach zero after the loss of the ENaC current, but is rate limited by the slow kinetics of the pump and cotransport pathways.

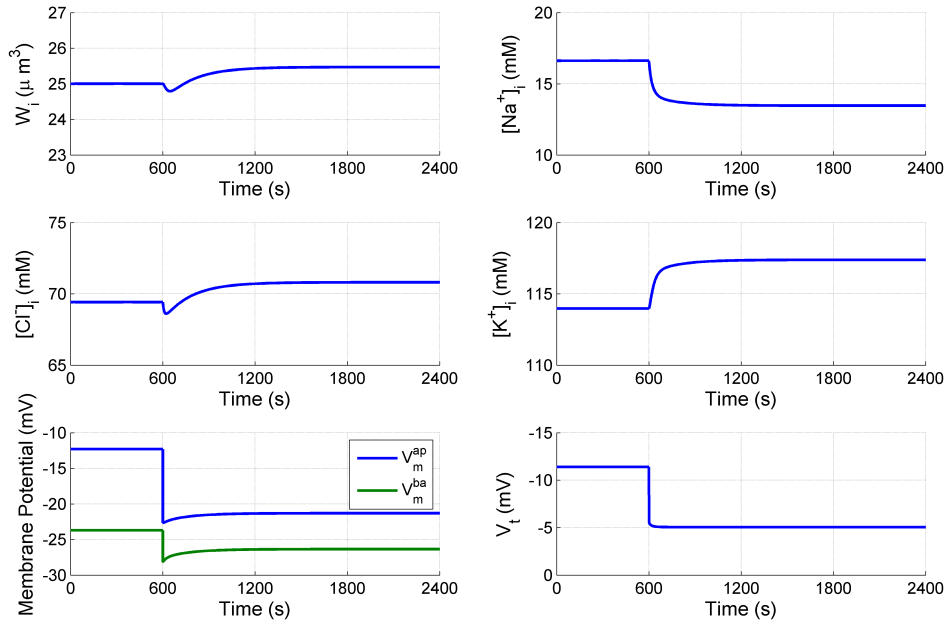

Figure 3.1: Simulation to investigate the effect of blocking apical ENaC channels in a HNE cell. At $t = 600s$ the apical Na^+ permeability is changed to 0, and the cellular variables such as membrane potentials and concentrations must relax to a new steady state after the loss of the apical Na^+ current.

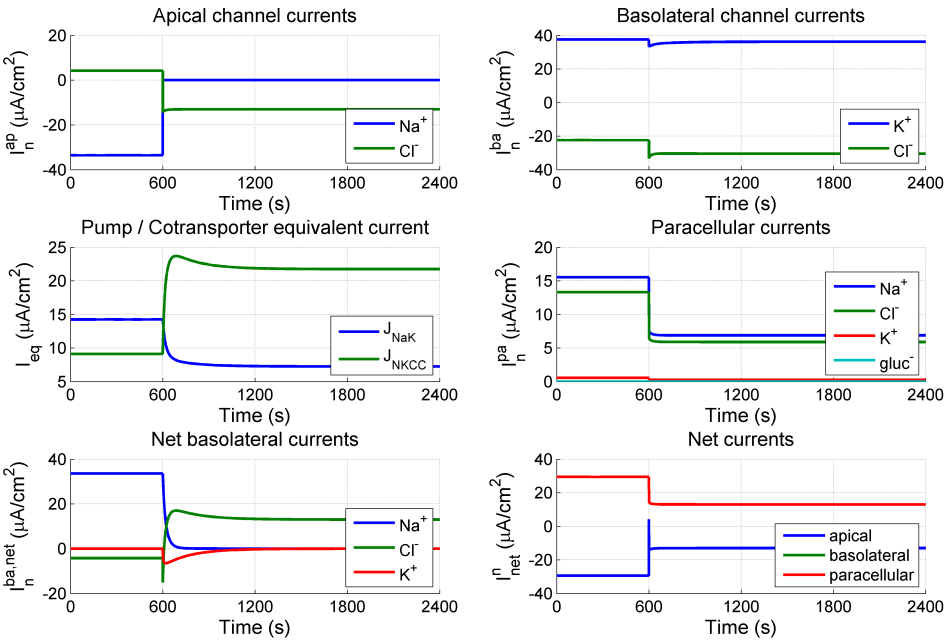

Figure 3.2: Various ionic currents and fluxes in the HNE cell model, during an *in silico* amiloride addition experiment. $I_{Na^+}^{ap} \rightarrow 0$ at $t = 600s$ and the resulting changes in driving force cause all other currents and fluxes to change correspondingly. Note all currents displayed are in units of $\mu\mathrm{A}/\mathrm{cm}^2$.

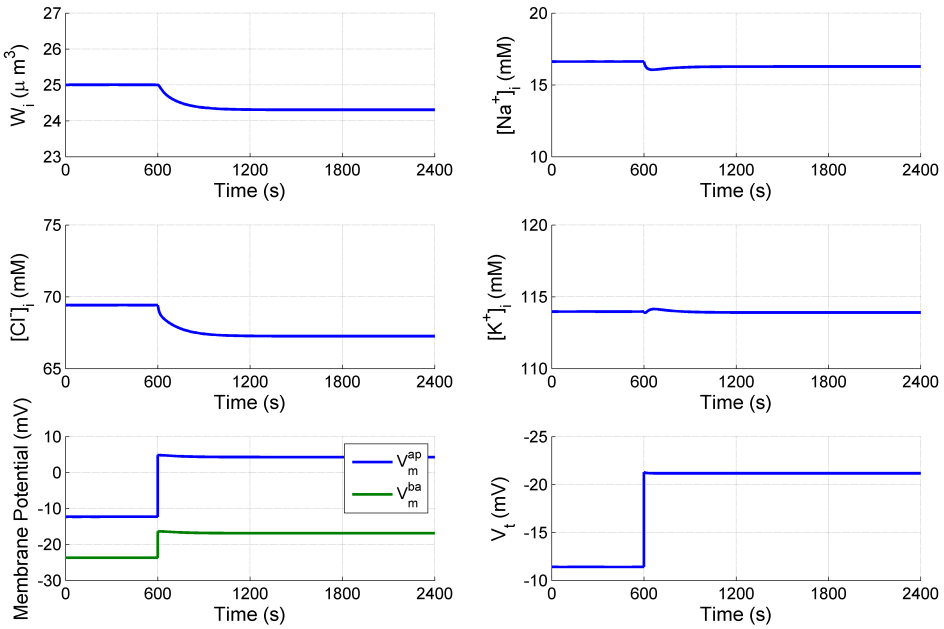

Figure 3.3: Simulation to investigate the effect of removing Cl^- from the lumen perfusate. At $t = 600s$, $[\mathrm{Cl}^-]_l$ goes from 120 mM $\rightarrow$ 3 mM. As there is a significant apical Cl^- permeability, this maneouveur causes an increase in Cl^- secretion, and hyperpolarisation of V_t.

3.2.3 Removing Cl^- from the luminal compartment

In analogy to how I implement the amiloride addition simulation, I simulate removal of Cl^- from the luminal compartment, by making an appropriate choice of steady state conditions $\mathbf{x}^*$ and also making necessary changes to the model parameter vector θ. Initial conditions are chosen which give a steady state when the lumen solution has $[\mathrm{Cl}^-]_l = 120$ mM. The ODE system is then numerically integrated from this initial condition, but with external Cl^- concentration changed to 3 mM. NaCl is typically replaced with $\mathrm{Na}^+ - \mathrm{gluconate}^-$ in these experiments, so this also needs to be modelled. I assume initially that there are no $\mathrm{gluconate}^-$ ions in the system, before the Cl^- solution exchange is made, therefore when solving for the initial steady state I set $[\mathrm{gluconate}^-]_l = 0$ mM. Before numerically integrating the ODEs however, I change this parameter such that $[\mathrm{gluconate}^-]_l = 117$ mM, as $\mathrm{gluconate}^-$ is used as an osmotic substitute for luminal Cl^-. I assume $\mathrm{gluconate}^-$ cannot permeate through the cell membrane, but will diffuse along the paracellular pathway, adding a term $I^{pa}_{gluc^-}$ to the total paracellular current.

Figures 3.3 and 3.4 show the impact of this perturbation on the variables and individual currents respectively, when I use the baseline transport parameter values. The model reproduces

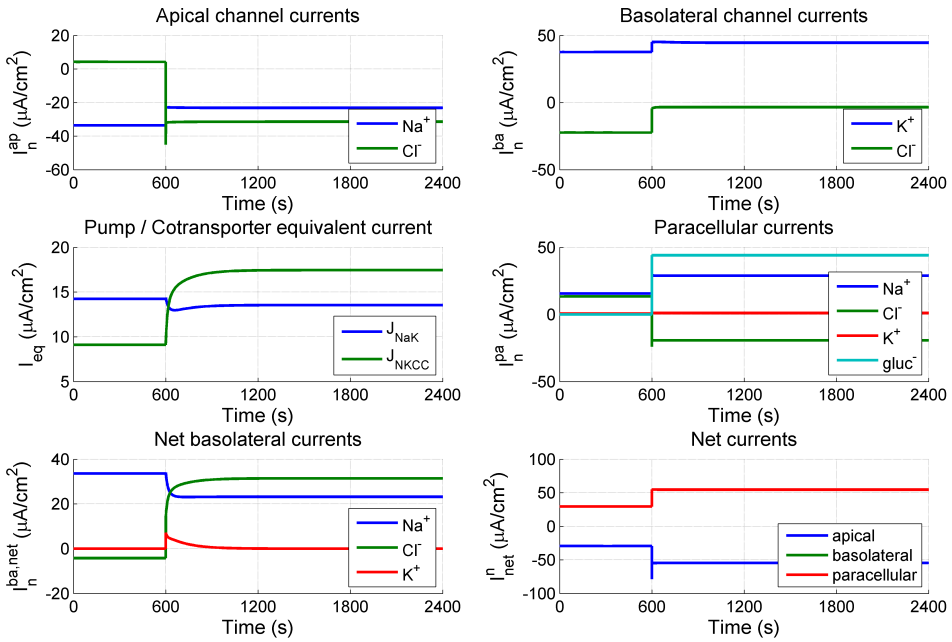

Figure 3.4: Various ionic currents and fluxes in the HNE cell model, during an *in silico* experiment to simulate removal of Cl^- from the solution in the luminal compartment. Note all currents displayed are in units of $\mu\mathrm{A}/\mathrm{cm}^2$.

the gross behaviour one would expect to see in airway epithelia with normal levels of CFTR activity. On removal of Cl^- from the lumen, a large driving force for Cl^- secretion is introduced, $I^{ap}_{Cl^-}$ is increased, V^{ap}_m depolarizes more than V^{ba}_m, and consequently V_t is hyperpolarised.

3.2.4 *In vitro* data used to constrain transport parameter values

One of the primary motivations for specifically modelling human nasal epithelial (HNE) cells over other airway epithelial cells, is that the biophysical properties of both normal and CF HNE cells have been characterised in detail by Willumsen and Boucher in a series of studies, providing a large body of useful electrophysiological data that I can use for model validation and parameter estimation purposes (Willumsen et al., 1989a,b; Willumsen and Boucher, 1989, 1991a,b).

I used a combination of data from Willumsen and Boucher's amiloride addition experiments, where intracellular $[\mathrm{Na}^+]$ and $[\mathrm{Cl}^-]$ as well as potentials V^{ap}_m and V_t were recorded, along with data from their Cl^- removal experiment, where they recorded the individual membrane potentials with simultaneous intracellular $[\mathrm{Cl}^-]$ measurements. The data used for parameter estimation can be inspected in Tables 3.2 and 3.3. Note for the amiloride addition experiments, two separate sets of data were available, as only one intracellular concentration

Table 3.2: Experimental data used for estimation of *non-CF* transport parameters. Concentrations are given in mM, membrane potentials in mV, and time in seconds (s). Data is presented as mean $\pm$ standard error.

Experiment	k	Time (t_k)	Observed data			
			$\hat{[\mathrm{Na}^+]}_i(t_k)$	$\hat{[\mathrm{Cl}^-]}_i(t_k)$	$\hat{V_m}^{ap}(t_k)$	$\hat{V}_t(t_k)$
+amiloride	1	0	27.2±3.3	—	-19.0±1.5	-12.6±3.1
	2	1050	24.2±4.4	—	-27.4±3.1	-5.0±1.1
	3	0	—	57.0±3.5	-25.9±2.5	-11.8±1.5
	4	1050	—	52.2±4.7	-36.6±2.2	-5.0±0.6
+zero Cl-	5	0	—	55.5±5.2	-22.5±1.4	-12.4±2.4
	6	1050	—	35.1±4.5	-10.4±2.5	-21.8±2.2

Table 3.3: Experimental data recorded in CF HNE cells *in vitro*. Concentrations are given in mM, membrane potentials in mV, and time in seconds (s). Data is presented as mean $\pm$ standard error.

Experiment	k	Time (t_k)	Observed data			
			$\hat{[\mathrm{Na}^+]}_i(t_k)$	$\hat{[\mathrm{Cl}^-]}_i(t_k)$	$\hat{V_m}^{ap}(t_k)$	$\hat{V}_t(t_k)$
+amiloride	1	0	25.9±3.5	—	-7.5±4.8	-42.3±6.1
	2	1050	—	—	-49.5±3.5	-2.0±1.5
	3	0	—	67.7±5.6	-8.2±5.0	-37.4±8.4
	4	1050	—	66.6±6.8	-43.6±4.0	-1.2±1.1
+zero Cl-	5	0	—	62.7±6.2	-20.0±6.1	-27.7±9.2
	6	1050	—	65.1±6.4	-17.1±5.5	-31.0±9.5

was measured at a time. Therefore when there are two data points for a membrane potential at a given time point, I weight the error by $1/2$ to compensate.

3.2.5 Implementing numerical parameter estimation

The task of estimating the subset of model parameter values θ_{sub} = ($P^{ap}_{Na^+}$, $P^{ap}_{Cl^-}$, $P^{ba}_{K^+}$, $P^{ba}_{Cl^-}$, ρ_{NaK}, ρ_{NKCC}) from experimental observations of the physiological quantities $\hat{\mathbf{y}} = (\hat{[\mathrm{Na}^+]}_i, \hat{[\mathrm{Cl}^-]}_i, \hat{V}^{ap}_m, \hat{V}_t)$ was carried out by minimising the sum of squared errors between values predicted for these quantities by the model and their observed values. This is formally stated as minimising the following objective function:

$$\underset{\theta_{sub}}{\text{minimize}} \sum_{k=1}^{q} \frac{\hat{[\mathrm{Na}^+]}(t_k) - Na^+_i(t_k)/W_i(t_k)}{\hat{\sigma}_{[\mathrm{Na}^+]_i k}} + \frac{\hat{[\mathrm{Cl}^-]}(t_k) - Cl^-_i(t_k)/W_i(t_k)}{\hat{\sigma}_{[\mathrm{Cl}^-]_i k}} \cdots + \frac{\hat{V^{ap}_m}(t_k) - V^{ap}_m(t_k)}{\hat{\sigma}_{V^{ap}_m k}} + \frac{\hat{V}_t(t_k) - V_t(t_k)}{\hat{\sigma}_{V_t k}} \tag{3.1}$$

The first parameter estimation problem I solved was to find θ_{non-CF} which minimised the residuals between observed data from non-CF HNE cells (Table 3.2) and model output, for a combined data set from two experiments, $+\mathrm{amiloride}$ and $+0[\mathrm{Cl}^-]_\mathrm{l}$. Model simulations are performed as outlined in Section 3.2.1. The second, separate parameter estimation problem was to find θ_{CF} which would minimise residuals between observed data from CF HNE cells (Table 3.3) and model predicted variable values, again for data from a combination of $+\mathrm{amiloride}$ and $+0[\mathrm{Cl}^-]_\mathrm{l}$ experiments.

The minimisation problem 3.1 was solved repeatedly for $N_{sim} = 200$ different noisy realisations (see Section 2.3.2) of the non-CF HNE cell data (Table 3.2), and separately, for 200 noisy realisations of the CF HNE cell data (Table 3.3). I implemented each individual minimisation using the *lsqnonlin* function in MATLAB Optimisation Toolbox. Repeating the minimisation for each of the N_{sim} noisy data sets, I built up a distribution of parameter values, in both the CF and non-CF cases, from which the median and interquartile ranges could be determined.

3.2.5.1 Note on implementation of parameter estimation

The experimental data set I used to estimate transport parameter values in CF HNE cells does not include the value of intracellular Na^+ concentration after amiloride addition (Table 3.3), whereas I have used this information for estimating transport parameter values in non-CF HNE cells (Table 3.2). Willumsen and Boucher (1991b) reported that on average Na^+ concentration increased in CF HNE cells after the addition of amiloride, from an initial value of $25.9 \pm 3.5\ \mathrm{mM}$ to a new steady state value of $40.1 \pm 5.7\ \mathrm{mM}$. This behaviour is qualitatively different from what is observed in non-CF cells, where the internal Na^+ concentration intuitively decreases after the inward apical Na^+ flux is completely blocked by application of amiloride. My ion transport model can qualitatively reproduce the reported $[\mathrm{Na}^+]_\mathrm{i}$ decrease in the non-CF case, but the model is incapable of reproducing an increase in $[\mathrm{Na}^+]_\mathrm{i}$ after $P^{ap}_{Na^+} \to 0$, for any values of the other transport parameters.

For this reason I decided to exclude the post-amiloride addition $[\mathrm{Na}^+]_\mathrm{i}$ value from the CF parameter estimation exercise. I did not want to cause parameters to take on unrealistic values by forcing the model to attempt to reproduce a behaviour it was not capable of. In the appendix (see Section A.6) I show the different parameter estimates and model kinetics predicted if one does indeed include this additional $[\mathrm{Na}^+]_\mathrm{i}$ observation in the fitting process. The estimated

values of $P^{ap}_{Na^+}$ and $P^{ap}_{Cl^-}$ are not changed significantly relative to their estimated values shown in Table 3.4 (given the uncertainty in each estimate).

It is worth noting that several similar models of epithelial ion transport display comparable Na^+ kinetics in this situation. The models of Garcia et al. (2013), Falkenberg and Jakobsson (2010) and Levin et al. (2006) all predict a decrease in internal sodium on amiloride addition, and to the best of my knowledge there is no biophysical model of this kind that reports an increase in internal sodium induced by amiloride addition. It may be that this behaviour can only be explained if one takes into account the activity of cation exchangers and sodium bicarbonate transporters present in these epithelial cells.

3.3 Results

3.3.1 Estimates of transport parameter values in CF and non-CF HNE cells

The results of this parameter estimation work are summarised in Table 3.4. There the median and interquartile range found from the distribution of $N_{sim} = 200$ estimates of each parameter are shown. It is clear that some parameters are tightly constrained by the data used for estimation, while others are not. For example the IQR in the non-CF case for $P^{ap}_{Na^+}$ is 16% of the median value, and 20% of the estimated value in the CF case. Compare this with $P^{ba}_{Cl^-}$ in the non-CF case, where the ratio of the IQR to the median is 120%, and for ρ_{NKCC} in the non-CF case, where it is over 800%.

Table 3.4: Estimated values of transport parameters in CF and non-CF HNE cells. Parameter estimates are displayed as (median $\pm$ IQR) of each θ_j's distribution.

Parameter	Units	non-CF	CF
$P^{ap}_{Na^+}$	μm/s	0.024±0.004	0.070±0.014
$P^{ap}_{Cl^-}$	μm/s	0.066±0.017	0.005±0.004
$P^{ba}_{K^+}$	μm/s	0.101±0.073	1.540±6.835
$P^{ba}_{Cl^-}$	μm/s	0.096±0.115	0.568±2.414
ρ_{NaK}	10^{-10}mol/cm^2	0.133±0.091	1.250±4.239
ρ_{NKCC}	10^{-10}mol/cm^2	0.199±0.408	1990 ±16267

3.4 Discussion

3.4.1 Significance of CF / non-CF transport parameter differences

By examining the scatter plots of estimated parameter values we can see where some of the large uncertainties arise from. Figures 3.5 and 3.6 show the distributions of $P^{ap}_{Na^+}$ and $P^{ap}_{Cl^-}$

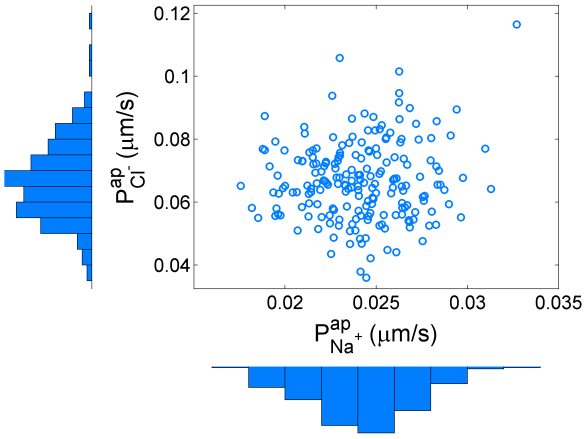

Figure 3.5: Estimates of $P^{ap}_{Na^+}$ and $P^{ap}_{Cl^+}$ made from noisy realisations of non-CF HNE cell data in Table 3.2. Note that both parameters are approximately normally distributed and there is no significant correlation between these two parameters.

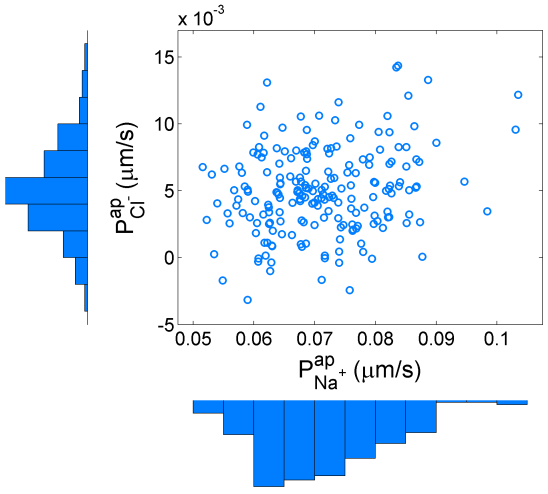

Figure 3.6: Estimates of $P^{ap}_{Na^+}$ and $P^{ap}_{Cl^+}$ made from noisy realisations of CF HNE cell data in Table 3.3. As in the non-CF case these estimates are approximately normally distributed, and there is no significant correlation between the estimates.

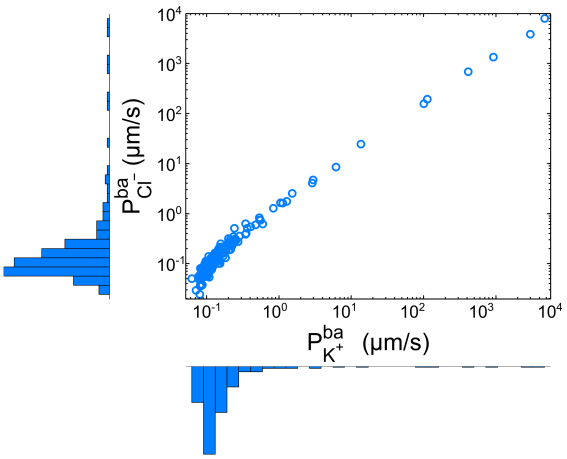

Figure 3.7: Estimates of P^{ba}_{K+} and P^{ba}_{Cl-} made from noisy realisations of non-CF HNE cell data in Table 3.2. Estimates are not constrained very well, and there is a significant correlation between the two distributions.

in non-CF and CF cases respectively. The distributions of each parameter are approximately Gaussian, and there is no significant correlations between the parameter values. Outside of these narrow ranges of parameter values there is essentially zero probability that you could accurately reproduce the HNE cell data in either CF or non-CF cases. Contrast this on the other hand, with the scatter plot of P^{ba}_{K+} and P^{ba}_{Cl-}, shown in Figure 3.7 for the non-CF case. Here the parameter estimates are plotted on a log log scale as they are not normally distributed, and in fact the estimated parameter values span several orders of magnitude. This suggests that the value of these parameters is not tightly constrained by the goodness of fit function $\chi^2(\theta)$. There is also a clear correlation between the two parameters which suggests an identifiability issue. One can get an equally good fit to data with any value of P^{ba}_{Cl-}, so long as an appropriate value of P^{ba}_{K+} is chosen.

These observations have consequences when we assess the statistical significance of differences between CF and non-CF parameter estimates. Our estimate of $P^{ap}_{Na^+}$ is increased in CF, and we can say with high confidence that it is a statistically significant increase, as in both cases it is tightly constrained by the data, and the interquartile ranges do not overlap. Similarly, we estimate a statistically significant decrease in P^{ap}_{Cl-} in CF HNE cells, as one might expect. On the other hand the differences between CF and non-CF estimates of P^{ba}_{K+}, P^{ba}_{Cl-}, ρ_{NaK} and ρ_{NKCC} are not significant given the uncertainty in the estimated CF values.

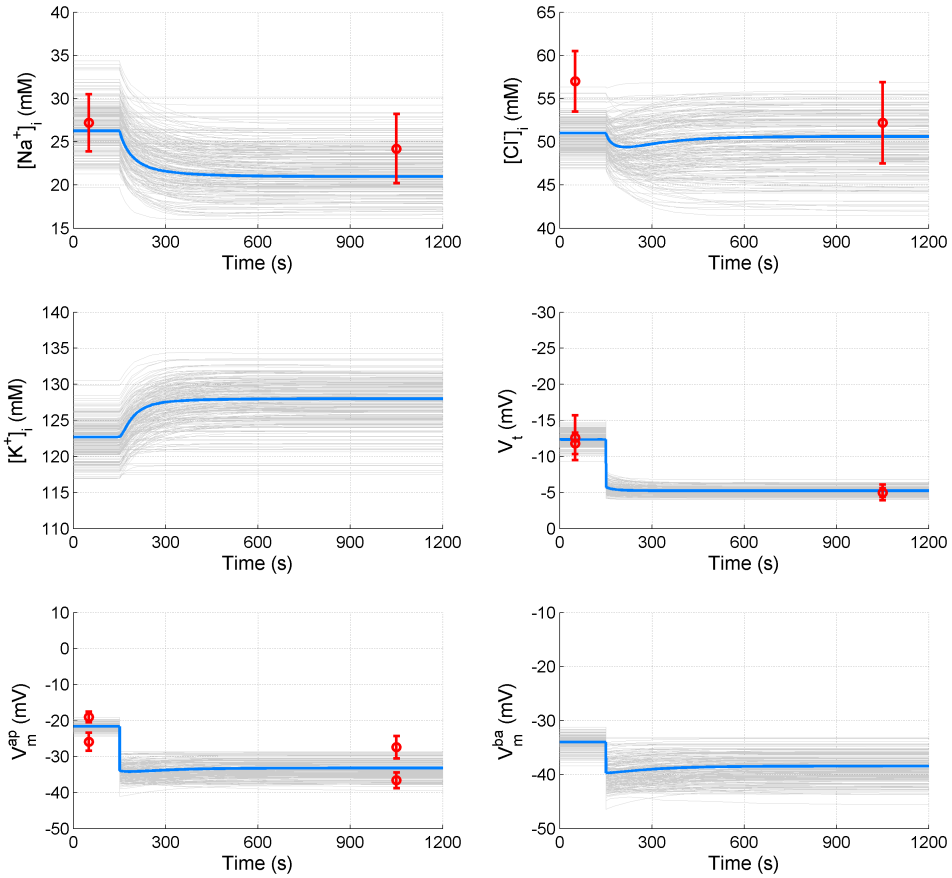

Figure 3.8: Model dynamics produced by $N_{sim} = 200$ different sets of non-CF parameter estimates for θ_{sub} (gray lines) along with the model dynamics predicted by the median estimated non-CF parameter values (blue line) shown in Table 3.4. Simulation shown is for an amiloride addition experiment on non-CF HNE cells, with observed data in red.

3.4.2 Physiologically realistic simulations

Figures 3.8 and 3.9 show the different solutions corresponding to the $N_{sim} = 200$ different estimated sets of parameter values θ_{sub} in the non-CF case. The solution predicted by the parameter values shown in Table 3.4 is also shown overlayed as a blue trace, and the data used for parameter estimation is shown in red. Qualitatively the agreement between model simulations and observed data is in general good, and quantitatively it is also quite good for most variables, especially the apical membrane potential and the transepithelial PD. One aspect that is not quite captured satisfactorily is the change in internal Cl^- concentration in the external Cl^- removal experiment, where all simulations predict changes lower than the 20 mM drop observed.

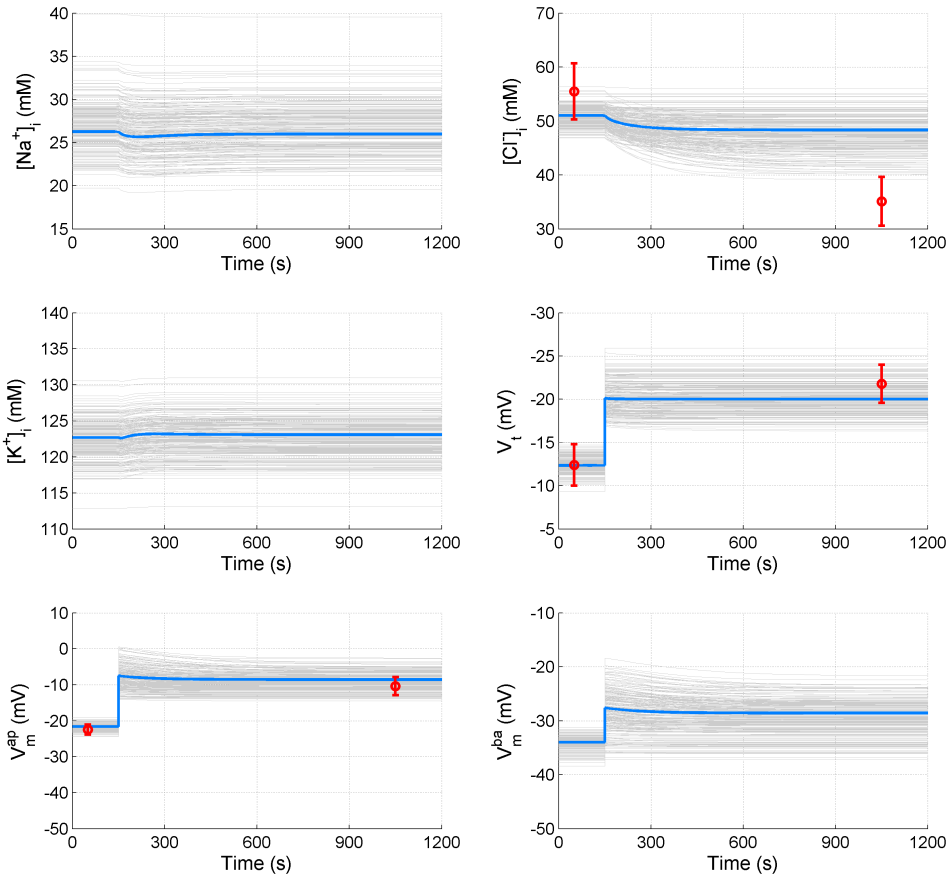

Figure 3.9: Simulations of removing Cl^- from the lumen perfusate in non-CF HNE cells, observed data are in red. Gray lines are traces given by the different parameter sets found by fitting to 200 different noisy data sets. The blue line is the trace predicted by the median of these parameter estimate distributions, displayed in Table 3.4.

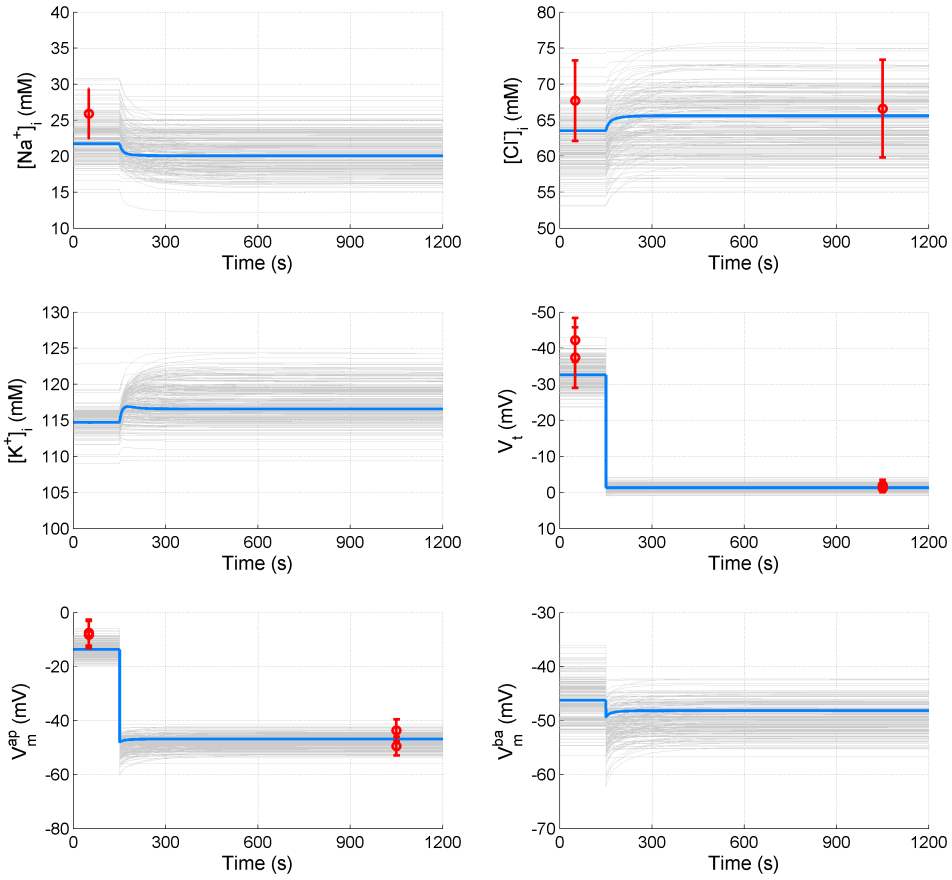

Figure 3.10: Simulation of amiloride addition in CF HNE cells. Best fit solution is shown in blue, with measured data in red. The distribution of different traces fitted to noisy data sets are shown as gray lines.

Figures 3.10 and 3.11 show the traces predicted by the optimal CF parameter values. The qualitative and quantitative agreement with the membrane potentials is again quite good. However, as discussed earlier, the model fails to predict an increase in internal Na^+ on addition of amiloride, which was observed in *in vitro* experiments in CF HNE cells, and this is the only major qualitative difference between prediction and observed data.

The model predictions with the optimal parameter estimates listed in Table 3.4 accurately reproduce the initial and final steady state values cellular variables take during these experiments. Hence one can be confident the parameter estimates I have made here give a realistic picture of the transport protein activity in the HNE cells in question. Interestingly our estimates here suggest that apical Cl^- and Na^+ permeability do vary significantly in CF, and of particular note it suggests ENaC activity must be increased markedly in CF relative to non-CF HNE cells.

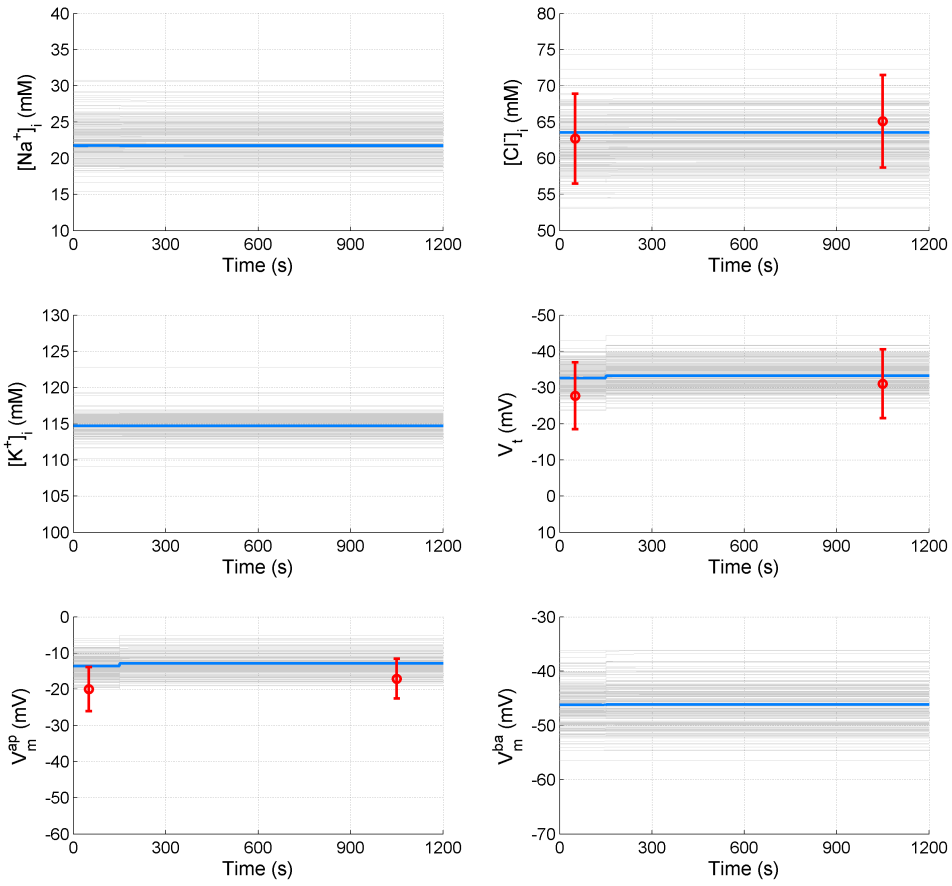

Figure 3.11: Simulation of reducing external Cl^- concentration in CF HNE cells. Best fit solution is shown in blue, with measured data in red. The distribution of different traces fitted to noisy data sets are shown as gray lines.

Case	$P^{pa}_{Na^+}$ non-CF	$P^{pa}_{Na^+}$ CF	$P^{pa}_{Na^+}/P^{pa}_{Cl^-}$	$P^{pa}_{Cl^-}/P^{pa}_{gluc^-}$
A	0.0350	0.0350	1.0	1.0
B	0.0350	0.0350	1.3	1.4
C	0.0329	0.0218	1.0	1.0
D	0.0367	0.0243	1.3	1.4

Table 3.5: List of different configurations parameter estimation was implemented under. The effect of paracellular selectivity, and differences in non-CF / CF paracellular permeability, were both investigated.

3.4.3 Influence of paracellular permeability and selectivity on estimates

In order to determine if the conclusion of increased $P^{ap}_{Na^+}$ in CF relative to non-CF epithelia was dependent on assumptions I had made regarding the permeability of the paracellular pathway, I performed a number of additional parameter estimation analyses. There is some limited evidence that the paracellular pathway may be less permeable in CF HNE cells than non-CF HNE cells (Willumsen and Boucher, 1989), and that the tight junctions may confer a cation selective conductance (Flynn et al., 2009; Levin et al., 2006). Hence I repeated the same parameter estimation analysis described in Section 3.2.5 in a number of different scenarios in order to investigate how strongly the apical Na^+ and Cl^- permeability estimates would be influenced by paracellular permeability and selectivity. The different paracellular permeability configurations considered are shown in Table 3.5, and I discuss in more details in the appendix (Section A.5) how I arrived at the specific values for $P^{pa}_{Na^+}$ and for the ratio $P^{pa}_{Na^+}/P^{pa}_{Cl^-}$.

The first analysis (Case A) is that which has already been outlined and discussed in preceding sections. It assumes paracellular permeability is the same in CF and non-CF cells, at the baseline value of $0.035\ \mu\mathrm{m/s}$ in both cases, and it assumes a non-selective paracellular permeability ($P^{pa}_{Na^+} \equiv P^{pa}_{Cl^-} \equiv P^{pa}_{K^+} \equiv P^{pa}_{gluc^-}$). In the next scenario considered (case B), paracellular characteristics of CF and non-CF cells are again the same, but I assume there is selectivity in the tight junctions, such that there is greater cation than anion permeability ($P^{pa}_{Na^+}/P^{pa}_{Cl^-} = 1.3$), and greater Cl^- than $\mathrm{gluconate}^-$ permeability ($P^{pa}_{Cl^-}/P^{pa}_{gluc^-} = 1.4$). The third case (case C) again assumes there is non-selective paracellular transport, but this time with a higher paracellular permeability in non-CF HNE cells ($P^{pa}_{Na^+} = 0.0329\ \mu\mathrm{m/s}$) than CF HNE cells ($P^{pa}_{Na^+} = 0.0218\ \mu\mathrm{m/s}$). The fourth and final situation (case D) assumes selectivity in the paracellular permeability (same values as case B), as well as higher paracellular permeability in non-CF cells $P^{pa}_{Na^+} = 0.0367\ \mu\mathrm{m/s}$ versus that in CF cells $P^{pa}_{Na^+} = 0.0243\ \mu\mathrm{m/s}$.

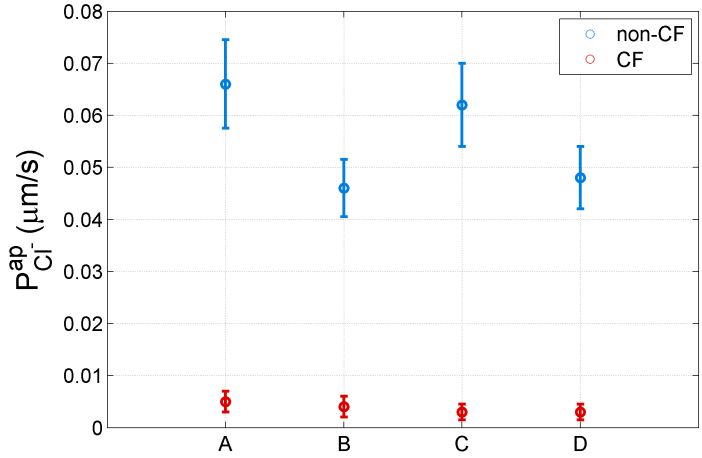

Figure 3.12: Estimates of apical Cl^- permeability inferred from CF (red) and non-CF (blue) HNE cell data. Each of the four CF / non-CF estimate pairs are under different assumptions regarding the paracellular permeability of the system. (A) baseline paracellular permeability and no selectivity, (B) baseline paracellular permeability and cation selectivity, (C) no selectivity and greater paracellular permeability in non-CF than CF case, and (D) cation-selectivity and greater paracellular permeability in non-CF cells than CF cells.

Figure 3.12 shows the resulting apical Cl^- permeability estimates in the four cases. In each case the median estimate of $P^{ap}_{Cl^-}$ is plotted along with a symmetrical error bar whose length is equal to the interquartile range of the distribution of estimated $P^{ap}_{Cl^-}$ values. One can clearly see that apical Cl^- permeability is significantly lower in the CF case regardless of our assumptions about selectivity and permeability of the paracellular pathway. Interestingly, the non-CF estimates of $P^{ap}_{Cl^-}$ in case B and D are both more than 25% smaller in magnitude than in the cases with a non-selective paracellular permeability.

Figure 3.13 highlights the estimates of apical Na^+ permeability in each of the different scenarios considered. The median $P^{ap}_{Na^+}$ value is plotted in each case along with an error bar whose length is given by the IQR of the distribution of estimated $P^{ap}_{Na^+}$ values. Again the conclusion that $P^{ap}_{Na^+}$ is increased in CF relative to non-CF HNE cells is robust to the different paracellular permeability configurations. However, it is also clear that the magnitude of paracellular Na^+ transport influences the value of ENaC permeability I estimate. When paracellular permeability is the same in both CF and non-CF epithelia, the CF estimate of $P^{ap}_{Na^+}$ is approximately 2.9 times greater than the non-CF estimate, but when I assume $P^{pa}_{Na^+}$ is 66% greater in non-CF cells, the difference in $P^{ap}_{Na^+}$ estimates is only 1.9 fold. The full list of transport parameter estimates can be seen in the appendix, Section A.7.

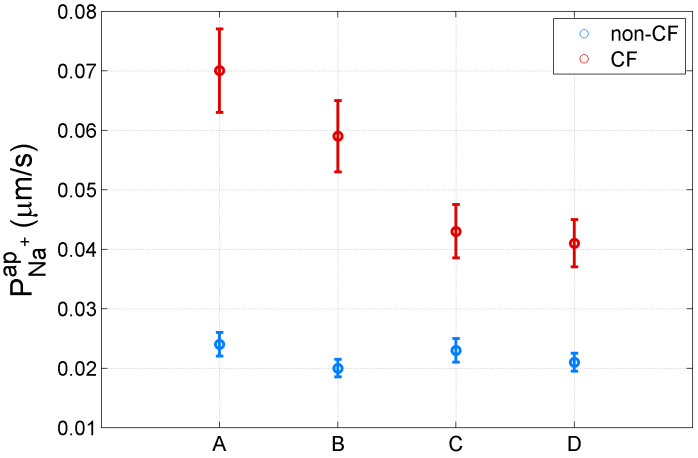

Figure 3.13: Estimates of apical Na^+ permeability inferred from CF (red) and non-CF (blue) HNE cell data. Each of the four CF / non-CF estimate pairs are under different assumptions regarding the paracellular permeability of the system. (A) baseline paracellular permeability and no selectivity, (B) baseline paracellular permeability and cation selectivity, (C) no selectivity and greater paracellular permeability in non-CF than CF case, and (D) cation-selectivity and greater paracellular permeability in non-CF cells than CF cells.

3.4.4 Summary

In this chapter I set out to determine, then to compare, the values of airway ion transport parameters, in both CF and non-CF human nasal epithelial cells. To constrain the model parameter values I used data available in the scientific literature, obtained from cultured HNE cells. This included time course data covering the addition of amiloride or reduction of $[Cl^-]_l$ at the apical membrane (Willumsen et al., 1989b; Willumsen and Boucher, 1989, 1991b,a). I thus formulated an optimisation problem to minimise the residual errors between the mathematical model's predictions for physiological properties, and those observed experimentally, by varying transport parameters of interest.

Using simulations made with parameter values optimised for non-CF epithelia, the model accurately fits the observed initial and final steady-state values for membrane and transepithelial potentials (V_m^{ap}, V_m^{ba}, and V_t) and ion concentrations ($[Na^+]_i$, $[Cl^-]_i$) both in amiloride addition and low Cl^- experiments. A similar analysis was carried out to identify parameter values best describing corresponding experimental data obtained on CF epithelia. The optimised parameter values for non-CF and CF epithelia are shown in Table 3.4.

The optimal parameter values obtained for ENaC and CFTR permeability are similar to those estimated experimentally (listed in Table 2.2). Examining the difference between opti-

mal CF and non-CF parameter values, I found not only that in CF $P^{ap}_{Cl^-}$ must be reduced (as expected) but also that the value of $P^{ap}_{Na^+}$ must be significantly increased.

Very little experimental data are available on the magnitude and characteristics of paracellular permeability. In order to determine if increased $P^{ap}_{Na^+}$ in CF epithelia was dependent on assumptions I had made regarding paracellular ion transport, I repeated the parameter estimation analysis assuming a lower P_{pa} in CF and/or a cation-selective paracellular transport (Levin et al., 2006; Flynn et al., 2009). I found that while these differences in paracellular transport do have an influence over the exact value of $P^{ap}_{Na^+}$ or $P^{ap}_{Cl^-}$ estimated, they do not alter how each of these parameters changes in CF relative to non-CF epithelia.

Chapter 4

Quantifying influence of transport parameters on epithelial electrophysiology

4.1 Introduction

In the preceding chapter, I estimated model parameters from time series data representing the mean behaviour of a number of HNE cell cultures, and found that there were some statistically significant differences between the transport parameter values estimated in CF and non-CF HNE cells. In this chapter, I will describe how I went on to determine whether or not these differences would be present, if I took into consideration the large culture to culture variation in properties such as membrane potentials and intracellular concentrations. I also address in a quantitative manner, the question of why these differences in parameter values should arise.

4.2 Methods

4.2.1 Monte Carlo filtering analysis

Although my initial parameter estimation results provide good evidence for a significant increase in $P_{Na^+}^{ap}$ in CF relative to non-CF HNE cells, I was conscious that the experimental data which I used for fitting my model output to, may not realistically capture the variability observed in cellular variable values. The data used recorded the mean behaviour of several different primary cultures of HNE cells. Variations in the experimental results obtained from these cells show that a large range of values of, for example, intracellular $[\mathrm{Na}^+]$, were observed in practice, rather than a single concentration being measured consistently. I wanted to make sure that by estimating parameter values from averaged data sets I did not exclude parameter sets that could account for both CF and non-CF data given the full range of possible variation (e.g. Willumsen and Boucher (1991b)). To achieve this, I carried out a Monte Carlo filtering analy-

sis, of the type outlined in Chapter 2, Section 2.3.3. I will describe the procedure briefly here again, in the context of the ion transport model (the filtering analysis is illustrated schematically in Figure 4.1).

First I used Monte Carlo sampling to randomly generate 10^6 parameter sets, sampling values for each transport parameter in θ_{sub} = ($P^{ap}_{Na^+}$, $P^{ap}_{Cl^-}$, P^{ba}_{K+}, $P^{ba}_{Cl^-}$, ρ_{NaK}, ρ_{NKCC}) from a uniform distribution on a bounded region (from zero to ten times) around the relevant baseline parameter value (Fig 4.1(a)). Then for each of these parameter sets, I determined the steady state values predicted for cellular variables, such as concentrations and membrane potentials, and also ran $+\mathrm{amiloride}$ and $+0[\mathrm{Cl}^-]_\mathrm{l}$ *in silico* experiments (Fig 4.1(b)). I then filtered the model outputs into different categories based on the observed constraints on certain electrophysiological properties of CF and non-CF HNE cells (see Table 4.2) (Fig 4.1(c)). This left me with a distribution of 415 parameter sets which reproduce observed non-CF HNE cell behaviour, and a separate distribution of 5373 parameter sets which reproduced the observed steady-state and kinetic behaviour of CF HNE cells (Fig 4.1(d)). Other parameter sets which produced physiologically unrealistic behaviour, or unstable kinetics, were discarded. Finally, the differences between non-CF and CF distributions could be assessed for each transport parameter in turn. Note the difference in the number of parameter sets remaining between normal and disease states arises due to the fact that certain constraints were less strict in the CF relative to the non-CF case, notably the bounds on values of $\Delta \mathrm{V_t} + 0\ [\mathrm{Cl}^-]_\mathrm{l}$.

4.2.2 *In vitro* data used to constrain allowed model outputs

The bounds on physiologically feasible CF and non-CF variable values can be seen in Table 4.2. I chose the lower and upper bounds on allowed cellular variables to be the 10th and 90th percentile respectively, of the distribution measured for each variable, wherever an appropriate distribution had been published. A distribution of steady state cellular variables has been published for $[\mathrm{Na}^+]$, $[\mathrm{Cl}^-]$, V^{ap}_m, V^{ba}_m and V_t in normal and CF HNE cells (Willumsen et al., 1989a,b; Willumsen and Boucher, 1991a,b). The upper and lower bounds on the allowed change in cellular variables due to a $+\mathrm{amiloride}$ or $+0[\mathrm{Cl}^-]_\mathrm{l}$ experiment were determined differently, as distributions of these quantities were not presented. Here data for initial and final variable values (say V_t before and after amiloride addition) was published as the mean value of the quantity in question, μ, plus or minus the standard error of the mean, SE. The mean change in the quantity in question is then given by $\mu_{diff} = \mu_{final} - \mu_{initial}$, and the standard error of the

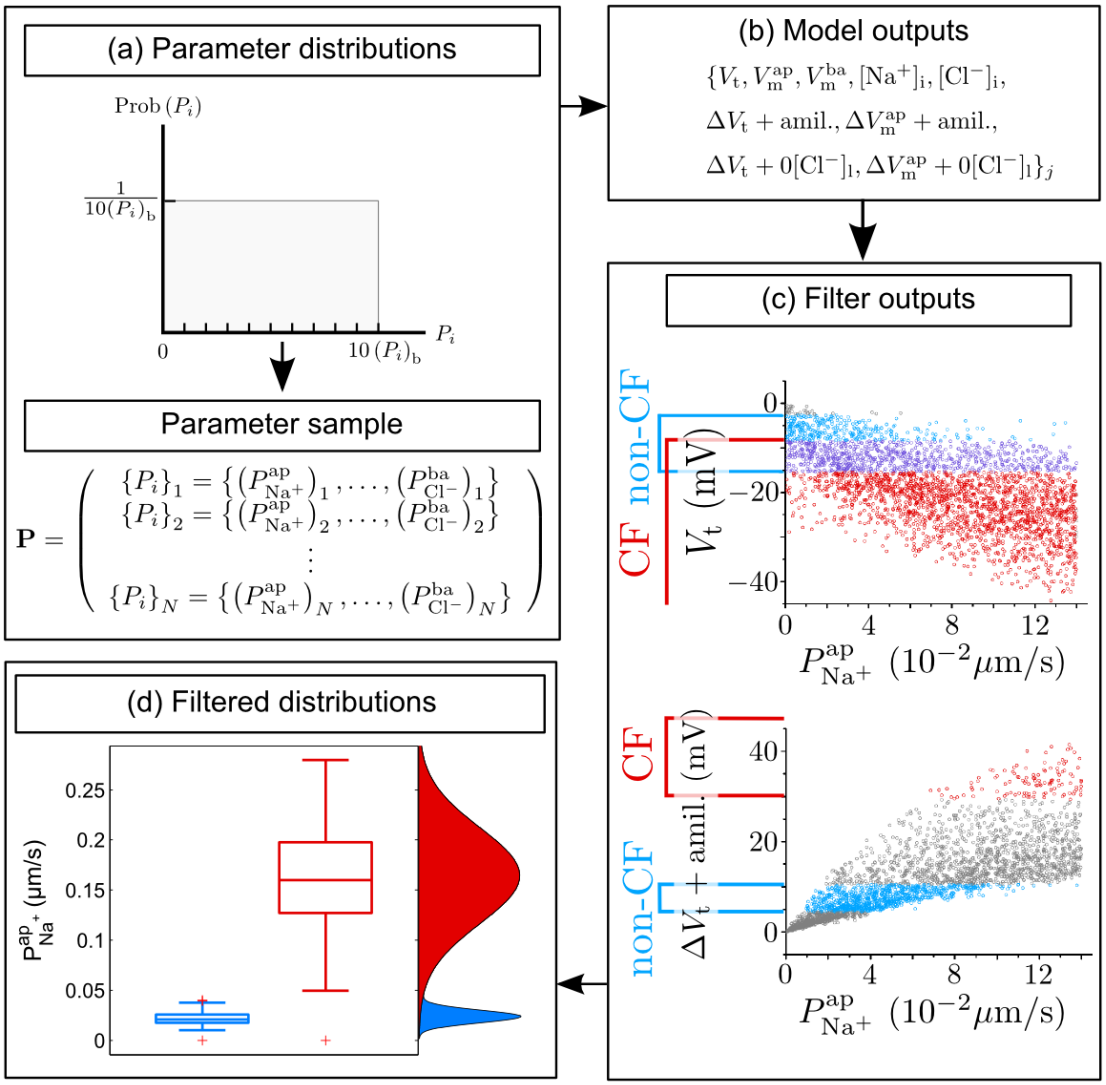

Figure 4.1: Schematic illustration of Monte Carlo filtering analysis. (a) A large number of parameter sets are randomly generated, and (b) the steady state and kinetic model properties predicted by these particular parameterisations are computed. (c) Parameter sets are filtered based on whether or not the properties they predicted lie within the range of values likely to be found in CF or non-CF HNE cells, and (d) the feasible parameter sets in each case, CF and non-CF, can then be assessed for differences.

Table 4.1: Region of parameter space used for Monte Carlo sampling. 10^6 parameter vectors were randomly chosen from the region between 0 and $10 \times P_b$, where P_b are the baseline literature estimates for each parameter value.

Parameter	Lower Bound	Upper Bound	Units
$P^{ap}_{Na^+}$	0.00	0.28	μm/s
$P^{ap}_{Cl^-}$	0.00	0.72	μm/s
$P^{ba}_{K^+}$	0.00	0.80	μm/s
$P^{ba}_{Cl^-}$	0.00	1.00	μm/s
ρ_{NaK}	0.00	4.00	10^{-10}mol/cm^2
ρ_{NKCC}	0.00	4.00	10^{-10}mol/cm^2

mean difference can be found via $SE^2_{diff} = SE^2_{initial} + SE^2_{final}$. Then finally the allowed upper and lower bounds on the quantity in question are determined with $\mu_{diff} \pm SE_{diff}$.

Table 4.2: Constraints on allowed variable values in CF and non-CF cells, based on data from primary cultures of HNE cells. Data used is from the HNE cell studies of Willumsen and Boucher (Willumsen et al. (1989a,b); Willumsen and Boucher (1991a,b))

		Non-CF		CF	
Property	Units	Lower	Upper	Lower	Upper
$[Na^+]_i$	mM	18.0	43.2	21.0	51.3
$[Cl^-]_i$	mM	32.5	84.4	32.5	84.4
V^{ap}_m	mV	-38.6	-14.6	-37.7	6.7
V^{ba}_m	mV	-45.1	-24.2	-59.3	-33.6
V_t	mV	-15.5	-2.7	-59.2	-8.2
ΔV^{ap}_m+amiloride	mV	-14.0	-5.0	-50.3	-29.0
ΔV_t+amiloride	mV	4.3	10.9	27.7	46.6
ΔV^{ap}_m+0$[Cl^-]_l$	mV	9.2	15.0	-5.3	11.1
ΔV_t+0$[Cl^-]_l$	mV	-13.0	-5.8	-16.5	9.9

4.2.3 Parameter sensitivity analysis

The data remaining from the Monte Carlo filtering analysis consists of a sample of physiologically feasible parameter sets along with the predicted steady state and kinetic model outputs ($(\{(\theta_{sub})_j, Y_j\} | j = 1, \ldots, 415)$ in the non-CF case). In order to quantitatively investigate the functional relationship between each individual transport parameter and the epithelial bioelectric properties in question, I carried out a variance-based sensitivity analysis using the 415 parameter sets in the non-CF distribution, along with their model outputs. I used a multiple linear regression model to implement the sensitivity analysis, outlined in Section 2.3.4.

Before performing the sensitivity analysis, parameter values are z-scored. That is, the mean and standard deviation of the remaining sample of values of an individual transport parameter, say $P^{ap}_{Cl^-}$, is calculated. Then each value in the remaining population of $P^{ap}_{Cl^-}$ is reduced by the mean value, and then normalised by the standard deviation. Doing this ensures that the range of values remaining for each parameter are on a similar scale. Once the population of parameter sets is z-scored, I fit a multiple regression model between input parameter sets $(\theta_{sub})_i$ and their set of predicted values for that a given output quantity Y_i, which is of the form of equation 2.47. Regression was performed using the function *regstats* in MATLAB Statistics Toolbox. The regression coefficients b_j determine the strength of the linear correlation between parameter θ_j and output Y_m. By comparing the magnitude of the linear regression coefficients I have a way of objectively determining the relative influence that transport parameters have on the physiological variable of interest.

This analysis is in the same spirit as the approaches outlined by Taylor et al. (2009), for determining how different conductances affect electrophysiological properties of a multi-compartmental cellular model of a neuron, and Sobie (2009), who performed parameter sensitivity analysis studies on computational models of cardiac myocytes.

4.3 Results

4.3.1 Feasible parameter distributions in CF and non-CF HNE cells

Table 4.1 lists the region of parameter space model behaviour was investigated in, and Figure 4.2 illustrates the distributions of transport parameter values which remain after applying the non-CF (blue) and CF (red) filters. The CF and non-CF distributions of remaining $P^{ap}_{Na^+}$ values are significantly different (the range $[q_1 - 1.5\,IQR, q_3 + 1.5\,IQR]$ in each case does not overlap), with apical Na^+ permeability being greater in the disease state (Figure 4.2(a)).

$P^{ap}_{Cl^-}$ is also constrained by the experimental data, see Figure 4.2(b). There is a trend for the apical Cl^- permeability to be lower in the CF case, the median CF value is lower than the median non-CF value, however there is significant overlap between the two distributions. As I have used relatively conservative constraints on the allowed values of $\Delta V_t + 0[\mathrm{Cl}^-]_\mathrm{l}$ in the CF case ($[-16.5, 9.9]\ \mathrm{mV}$), and since $P^{ap}_{Cl^-}$ is quite sensitive to the magnitude of $\Delta V_t + 0[\mathrm{Cl}^-]_\mathrm{l}$ (the results of the sensitivity analysis are displayed in Table 4.3), the range of allowed apical Cl^- permeability values has hence not been as tightly constrained as in the non-CF case.

The remaining distributions of the other parameters are not as well constrained by the

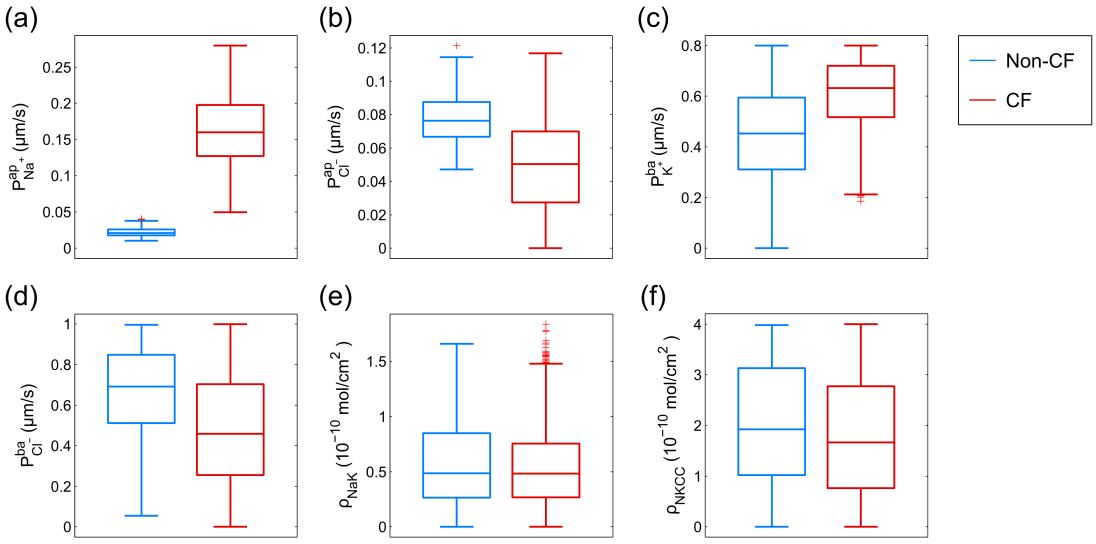

Figure 4.2: Boxplots showing distributions of each transport parameter found by constraining allowed model behaviour in non-CF (blue) and CF (red) states. Parameters varied were (a) P^{ap}_{Na+}, (b) P^{ap}_{Cl-}, (c) P^{ba}_{K+}, (d) P^{ba}_{Cl-}, (e) ρ_{NaK} and (f) ρ_{NKCC}. Each boxplot highlights the median (central line), lower quartile q_1 and upper quartile q_3 (lower / upper bounds of box). Whiskers on the boxplot highlight the range $[q_1 - 1.5\ IQR, q_3 + 1.5\ IQR]$ and red crosses indicate outliers which lie outside this range.

experimental data, and acceptable values tend to be limited only by the region of parameter space searched. Basolateral K^+ permeability is not constrained in the non-CF case, but does appear to have a strict lower bound in the CF case (Figure 4.2(c)). Basolateral Cl^- permeability does not differ significantly between the CF and non-CF cases, and is poorly constrained by the data in this region of parameter space, with only a lower bound evident in the non-CF distribution. Figure 4.2(e) highlights the remaining non-CF and CF distributions of ρ_{NaK}. There is a strict upper bound present in each distribution, but they do not differ significantly between the CF and non-CF states. Finally, Figure 4.2(f) shows the remaining CF and non-CF ρ_{NKCC} distributions. This parameter is not constrained by the data in either of the disease or normal states.

Thus, extending my analysis to take into account the full distribution of allowed cellular variable values, rather than focusing on mean behaviour, confirms that ENaC permeability must be increased in CF relative to non-CF cells, in order to explain the observed quantitative differences in electrophysiological properties. It also re-capitulates several of the other findings of Chapter 3, showing that apical Cl^- permeability is estimated to be lower in the CF case, and that the basolateral transport parameters P^{ba}_{K+}, P^{ba}_{Cl-}, ρ_{NaK} and ρ_{NKCC} are poorly constrained by the electrophysiological data available from $+\text{amiloride}$ and $+0[Cl^-]$ experiments on HNE

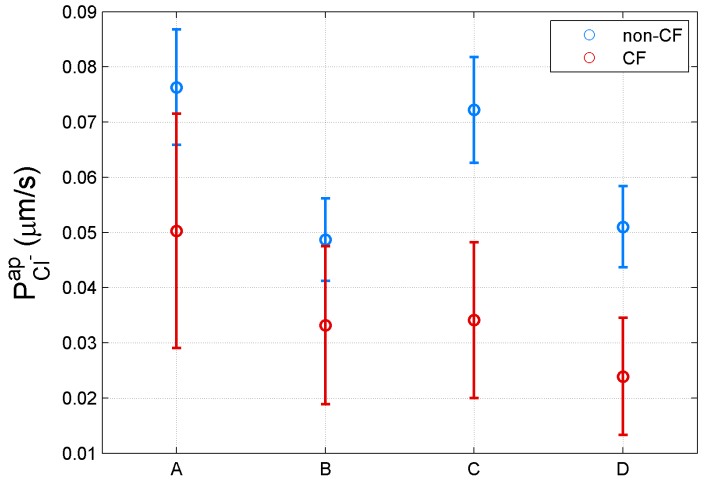

Figure 4.3: Feasible distributions of apical Cl^- permeability found via MC filtering analysis. Distributions shown were found using non-CF (blue) and CF (red) HNE cell data, and the data displayed are the median with error bars with length equal to the interquartile range of the distribution. Each of the four CF / non-CF distribution pairs are under different assumptions regarding the paracellular permeability of the system. (A) baseline paracellular permeability and no selectivity, (B) baseline paracellular permeability and cation selectivity, (C) no selectivity and greater paracellular permeability in non-CF than CF case, and (D) cation-selectivity and greater paracellular permeability in non-CF cells than CF cells.

cells.

4.3.2 Influence of paracellular permeability on feasible parameter distributions

As well as performing the MC filtering analysis with the baseline paracellular permeability (case A), I also repeated the analysis to assess whether increased shunt resistance in CF or selective paracellular permeability would significantly alter the outcomes. In line with my previous parameter estimation work, I separately investigated the effect of differential ionic selectivity along the paracellular pathway (case B), of reduced paracellular permeability in CF HNE cells (case C), and finally both reduced paracellular permeability in CF combined with selective paracellular transport (case D).

Again I found that neither a higher shunt resistance in CF, nor a cation-selective paracellular pathway, affected the conclusion that permeability distributions were shifted in CF epithelia. In particular median apical Cl^- permeability is decreased in each case relative to the median non-CF value found for $P^{ap}_{Cl^-}$ (Figure 4.3), and median apical Na^+ permeability is increased relative to median non-CF $P^{ap}_{Na^+}$ in each case (see Figure 4.4).

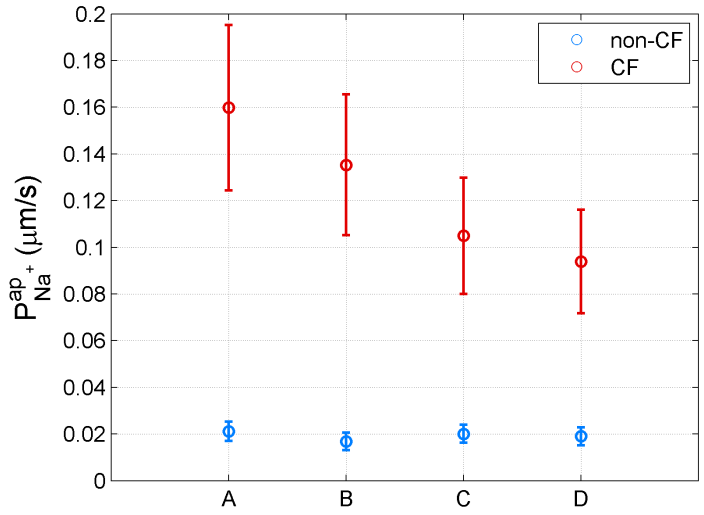

Figure 4.4: Feasible distributions of apical Na^+ permeability found via MC filtering analysis. Distributions shown were found using non-CF (blue) and CF (red) HNE cell data, and the data displayed are the median with error bars with length equal to the interquartile range of the distribution. Each of the four CF / non-CF distribution pairs are under different assumptions regarding the paracellular permeability of the system. (A) baseline paracellular permeability and no selectivity, (B) baseline paracellular permeability and cation selectivity, (C) no selectivity and greater paracellular permeability in non-CF than CF case, and (D) cation-selectivity and greater paracellular permeability in non-CF cells than CF cells.

4.3.3 Insights from parameter sensitivity analysis

The results of the sensitivity analysis are given in Table 4.3. For each of the three trans-epithelial PD measurements of interest, basal V_t, ΔV_t+amiloride and ΔV_t+0$[\mathrm{Cl}^-]_l$, the strength of influence of each transport parameter is quantified by the regression co-efficients b_j.

4.3.3.1 Hyperpolarised V_t in CF HNE cells is explained by increased $P^{ap}_{Na^+}$

Figure 4.5 (a) and (b) shows scatter plots of $P^{ap}_{Na^+}$ and $P^{ap}_{Cl^-}$, respectively (from the non-CF parameter value distributions), against basal (steady state) V_t predicted by each. Figure 4.5 (c) summarises the results of the sensitivity analysis. There is a negative correlation between $P^{ap}_{Na^+}$ and V_t apparent in panel (a), and confirmed by the large negative regression coefficient b_1 (-1.77 mV) in panel (c).

A significant correlation between $P^{ap}_{Cl^-}$ and V_t is not clear in panel (b). The sensitivity analysis confirms that while $P^{ap}_{Cl^-}$ does influence V_t to an extent, on average over this region of parameter space it has a much smaller effect than $P^{ap}_{Na^+}$, $P^{ba}_{K^+}$ or $P^{ba}_{Cl^-}$ (regression coefficient $b_2 = -0.03$ mV $< 2\%\ b_1$). Therefore an increase in $P^{ap}_{Na^+}$ is necessary to hyperpolarise basal V_t to the values seen in CF epithelia, while changes in $P^{ap}_{Cl^-}$ do not influence V_t to the same

Parameter	Coefficient	Basal V_t	ΔV_t+amiloride	ΔV_t+0[Cl$^-$]$_l$
P^{ap}_{Na+}	b_1	-1.77	1.76	-0.01
P^{ap}_{Cl-}	b_2	-0.03	-0.55	-1.60
P^{ba}_{K+}	b_3	-2.11	0.67	0.87
P^{ba}_{Cl-}	b_4	1.35	-0.04	-0.45
ρ_{NaK}	b_5	0.04	-0.37	-0.55
ρ_{NKCC}	b_6	0.35	-0.48	-0.44

Table 4.3: Linear regression coefficients b_j (units: mV) found by fitting multiple regression between z-scored transport parameters θ_j and model outputs $\mathbf{Y} = (V_t, \Delta V_t$+amiloride, ΔV_t+0[Cl$^-$]$_l$) for use in sensitivity analysis.

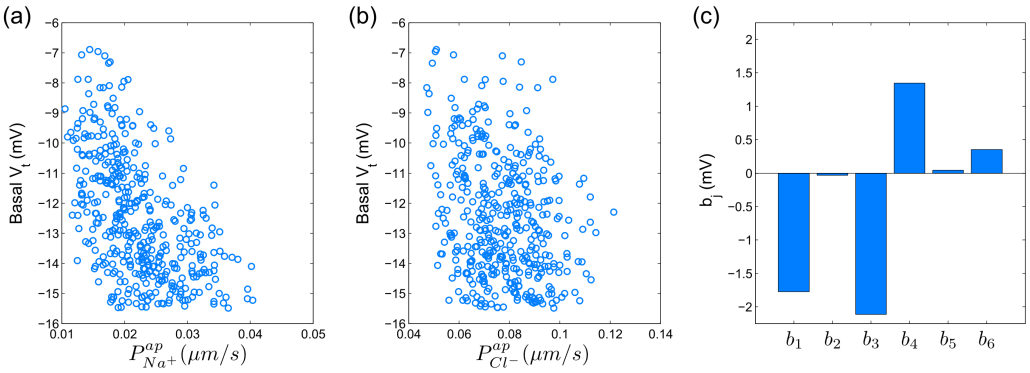

Figure 4.5: Basal V_t is plotted as a function of (a) P^{ap}_{Na+} and (b) P^{ap}_{Cl-}, for the 415 parameter sets belonging to the non-CF distribution. (c), strength of linear interaction (b_j) between transport parameters $(\theta_{sub})_{j=1\to6}$ = (P^{ap}_{Na+}, P^{ap}_{Cl-}, P^{ba}_{K+}, P^{ba}_{Cl-}, ρ_{NaK}, ρ_{NKCC}) found via sensitivity analysis. P^{ap}_{Na+} hyperpolarises V_t ($b_1 = -1.77$ mV), but changing P^{ap}_{Cl-} has little influence ($b_2 = -0.03$ mV).

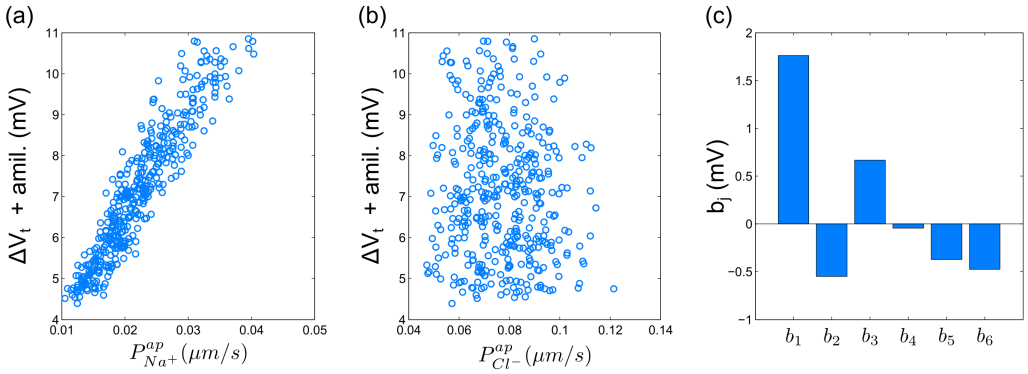

Figure 4.6: Amiloride-sensitive V_t is plotted as a function of (a) $P^{ap}_{Na^+}$ and (b) $P^{ap}_{Cl^-}$, for their non-CF distributions. (c) sensitivity analysis results plotting strength of interaction (b_j) between ΔV_t+amiloride and transport parameters $(\theta_{sub})_{j=1\rightarrow 6}$ = ($P^{ap}_{Na^+}$, $P^{ap}_{Cl^-}$, $P^{ba}_{K^+}$, $P^{ba}_{Cl^-}$, ρ_{NaK}, ρ_{NKCC}), found via sensitivity analysis. Apical Cl^- permeability tends to decrease amiloride sensitive V_t despite its limited influence on basal V_t.

degree.

4.3.3.2 Magnitude of amiloride-sensitive V_t can be increased by reducing $P^{ap}_{Cl^-}$

Figure 4.6 (a) and (b) illustrates the relationship between $P^{ap}_{Na^+}$ and $P^{ap}_{Cl^-}$ parameter values, respectively, from the non-CF distributions, and the corresponding predicted ΔV_t+amiloride. Not surprisingly, given ENaC channels are being blocked in these simulations, there is a positive correlation between $P^{ap}_{Na^+}$ and ΔV_t+amiloride. However, the relationship between ΔV_t+amiloride and $P^{ap}_{Cl^-}$ is less intuitively understood. The results of the sensitivity analysis in Figure 4.6(c) show that $P^{ap}_{Cl^-}$ has the third greatest influence on ΔV_t+amiloride (after $P^{ap}_{Na^+}$ and $P^{ba}_{K^+}$). While increasing $P^{ap}_{Na^+}$ and $P^{ba}_{K^+}$ tends to increase the magnitude of ΔV_t+amiloride, increasing $P^{ap}_{Cl^-}$ tends to decrease its magnitude.

4.3.3.3 Decreasing $P^{ap}_{Cl^-}$ cannot hyperpolarise basal V_t to the extent seen in CF

It is clear that $P^{ap}_{Cl^-}$ can influence basal V_t, even if it does not do so to the same extent as $P^{ap}_{Na^+}$. I wanted to determine, quantitatively, what magnitude of a change in basal V_t the model would predict upon loss of $P^{ap}_{Cl^-}$ alone, and compare this to the hyperpolarisation of V_t observed in CF. Therefore, for each parameter set producing plausible physiological values in the non-CF distribution, I set $P^{ap}_{Cl^-} = 0$ and found the new steady state of the system. I define $\Delta V_t(\text{CFTR block})$ as the difference between this new V_t, and the initial basal V_t when $P^{ap}_{Cl^-} \neq 0$.

I can analyse the magnitude of $\Delta V_t(\text{CFTR block})$ and its relationship to ΔV_t+0$[Cl^-]_l$

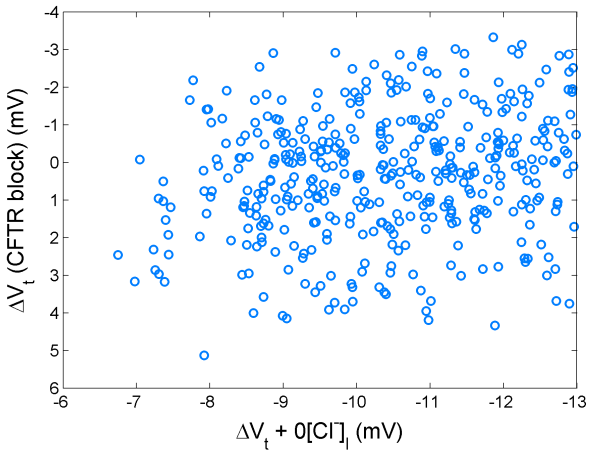

Figure 4.7: $\Delta V_t{+}0[\mathrm{Cl}^-]_\mathrm{l}$ is commonly used as a proxy measure for $P^{ap}_{Cl^-}$ in airway epithelial cells. Here it is plotted against V_t induced by blocking CFTR (i.e. $P^{ap}_{Cl^-} \rightarrow 0$), for the distribution of non-CF values found. For a given low Cl^- response, hyperpolarisation or depolarisation of basal V_t can occur, but there appears to be a limit on the hyperpolarisation possible (none greater than -4 mV), which is significantly less than the magnitude observed in CF.

(change in V_t induced by reducing $[\mathrm{Cl}^-]_\mathrm{l}$ which is commonly used as a surrogate measure of the underlying Cl^- conductance, see Figure 4.7). For a given $\Delta V_t{+}0[\mathrm{Cl}^-]_\mathrm{l}$, CFTR loss can depolarise or hyperpolarise V_t, depending on the magnitudes of the other transport parameter values. The average $\Delta V_t{+}0[\mathrm{Cl}^-]_\mathrm{l}$ observed experimentally in non-CF HNE cells was not greater than -15 mV (Willumsen et al., 1989b), a value close to that reported *in vivo*, in nasal PD measurements. However, the maximum hyperpolarisation achieved by blocking $P^{ap}_{Cl^-}$ was around -4 mV. This is much smaller in magnitude than the average hyperpolarisation seen in CF patients (and in primary cultures of CF HNE cells; (Willumsen and Boucher, 1991b)), which is around -20 mV (Knowles et al., 1995).

4.4 Discussion

4.4.1 CF / non-CF differences in $P^{ap}_{Na^+}$ and $P^{ap}_{Cl^-}$ are robust

In Chapter 3, after fitting my ion transport model to the mean behaviour of HNE cells, I found not only that $P^{ap}_{Cl^-}$ must be reduced, but also that $P^{ap}_{Na^+}$ had to increase to account for the bioelectric properties observed in the CF cells (Table 3.4). In this chapter I found that this prediction also holds, if I take into account cell to cell variation in cellular properties such as membrane potentials and intracellular concentrations. Specifically, parameter sets resulting in steady-state and kinetic characteristics typical of CF cells again included increased $P^{ap}_{Na^+}$ and reduced $P^{ap}_{Cl^-}$. The fact that this analysis did not make any initial judgements regarding

how parameters should vary in the disease state, and hence did not bias the analysis towards computing these results, gives me confidence in their validity and further demonstrates that the findings regarding ENaC and CFTR activities in CF HNE cells are robust.

4.4.2 Quantifying the influence of CFTR and ENaC currents on V_t

Previously published modelling work investigating the electrical coupling of CFTR and ENaC fluxes (Horisberger, 2003) showed that increasing apical Cl^- conductance could decrease amiloride-sensitive short-circuit current (I_{sc}) in a kidney epithelial cell model, and Falkenberg and Jakobsson note that I_{sc} is most sensitive to basal apical anion permeability, after the addition of amiloride (Falkenberg and Jakobsson, 2010). More recently, evidence from pig and human airway epithelial cell lines showed that experimentally decreasing apical Cl^- conductance can increase $\Delta V_t{+}\mathrm{amiloride}$ (Chen et al., 2010; Itani et al., 2011). The analysis in this chapter confirms that this relationship exists, qualitatively. However, this modelling approach enabled me to quantitatively determine the influence each transport parameter has on the electrical properties of the epithelium (see Table 4.3, and Figures 4.5 and 4.6). Thus, I can show that the magnitude of changes in going from non-CF to CF levels of anion permeability is not sufficient to explain the experimentally observed hyperpolarised basal V_t, the increased amiloride-sensitive V_t component, and the decreased $\Delta V_t{+}0[\mathrm{Cl}^-]_1$. In contrast, sensitivity analysis shows that $P^{ap}_{Na^+}$ significantly hyperpolarises basal V_t, and is the most important factor in determining the magnitude of $\Delta V_t{+}\mathrm{amiloride}$. Without altering $P^{ap}_{Na^+}$ from non-CF levels, the magnitude of the hyperpolarisation of basal V_t and of increased amiloride-sensitive V_t could not be explained.

4.4.3 How does apical Cl^- permeability influence amiloride sensitive V_t?

One can intuitively understand how the relative influences of ENaC and CFTR permeability on basal and amiloride-sensitive V_t arise, by examining the driving force for movement of Na^+ and Cl^- ions across the apical membrane. Basal V_t depends implicitly on apical Na^+ and Cl^- currents, and the changes in these currents with respect to permeability are proportional to driving force. Hence the relative driving force for movement of different ions explains the relative sensitivity of V_t to different permeabilities.

In the representative example of best-fit non-CF parameter values (Table 3.4), the driving force for Na^+ absorption across the apical membrane at steady state is $-66.3\ \mathrm{mV}$, as opposed to $+1.2\ \mathrm{mV}$ for Cl^- transport. At these physiological potentials, the Cl^- driving force is

thus $< 2\ \%$ of that for Na^+, consistent with the results of our sensitivity analysis: $P^{ap}_{Na^+}$ has a much greater influence on V_t than $P^{ap}_{Cl^-}$. How then, can we explain the influence of $P^{ap}_{Cl^-}$ on amiloride-sensitive V_t? After amiloride is added $I^{ap}_{Na^+}$ is dramatically reduced and V^{ap}_m changes, altering the apical Cl^- driving force and consequently $I^{ap}_{Cl^-}$. Again taking these best-fit parameters, this driving force goes from $+1.1\ \mathrm{mV}$ to $-10.1\ \mathrm{mV}$ for Cl^-, while $I^{ap}_{Na^+} = 0$. Therefore $P^{ap}_{Cl^-}$ now has a greater relative influence on V^{ap}_m and V_t, while $P^{ap}_{Na^+}$ can have no further effect.

4.4.4 Agreement with observed epithelial electrophysiological properties

The results of our sensitivity analysis are in agreement with a range of additional experimental data not used to constrain the model. For example, we observed basal V_t to be strongly dependent on $P^{ba}_{K^+}$ (hyperpolarising). This was found experimentally by Mall et al. (2000) who blocked basolateral K^+ channels in human bronchial epithelial (HBE) cells. Modelling studies have also shown that I_{sc} can be increased by stimulating basolateral K^+ currents (Falkenberg and Jakobsson, 2010), supporting the hypothesis that increased basolateral K^+ conductance is necessary to hyperpolarise the basolateral (and consequently, apical) membrane, providing an increased driving force for Cl^- secretion (Cotton, 2000). Further, V_t tends to be depolarised by $P^{ba}_{Cl^-}$ in our model, which agrees with the observations of Fischer and colleagues in human and bovine tracheal primary cultures (Fischer et al., 2007) who also found V_t to be dependent on $P^{ba}_{Cl^-}$.

Chapter 5

Quantitative analysis of nasal transepithelial potential recordings

5.1 Introduction

5.1.1 Nasal potential difference as a biomarker of CF disease

We saw in Section 1.2.4 that the measurement of nasal transepithelial potentials is widely used as an aid to CF diagnosis and as a biomarker in clinical trials. Hyperpolarised basal V_t and larger amiloride-sensitive V_t changes are hallmarks of CF disease that have become central to the debate on the role of sodium hyper-absorption in CF pathology. These same altered bioelectric properties are the foundation of therapeutic approaches aimed at reducing ENaC activity (Hofmann et al., 1998; Coote et al., 2009). Also, the response in V_t induced by a combination of a Cl^- free solution and $\mathrm{isoproterenol}$ addition was used as a biomarker during the clinical trials to assess the efficacy of the VX770 potentiator (Accurso et al., 2010).

The correct interpretation of transepithelial potentials therefore carries important implications for both understanding CF and assessing potential therapies. For example it is regularly assumed that there is a one to one correspondence between ENaC activity and the magnitude of $\Delta V_t + \mathrm{amiloride}$, and a linear relationship between CFTR activity and $\Delta V_t + 0[\mathrm{Cl}^-]_1$. However, to my knowledge, this assertion has not been assessed in a quantitative manner before. In this chapter I will address this question, as well as a number of other issues, using my mathematical modelling approach to analysing airway epithelial transport.

5.1.2 What issues with nasal PD measurements can modelling address?

In this chapter I will simulate standard nasal PD recordings using my mathematical model in order to address some of the questions surrounding the use of NPD tests as a biomarker of CF

disease. Initially I will address the question - how do the major transport pathways influence the nasal PD metrics commonly recorded? By simulating a nasal PD recording repeatedly, each time changing a single model parameter value, I can gain a better quantitative understanding of these relationships. While we know how ENaC and CFTR are expected to alter the recorded ΔV_t+amiloride and ΔV_t+0$[\mathrm{Cl}^-]_\mathrm{l}$ metrics, it is not clear that the influence on these metrics that other parameters can have, such as the basolateral K^+ and Cl^- permeabilities, has fully been appreciated. This exercise will highlight the other possible sources of variability in observed nasal PD traces.

5.2 Methods

5.2.1 Simulating nasal PD tests

It is possible to simulate the first three stages of a standard clinical nasal PD test using our mathematical model, in the same manner that I simulated *in vitro* Ussing chamber experiments. Appropriate changes to the model parameters are implemented to reflect the altered composition of the perfusing solution. As before, to model amiloride addition the parameter $P^{ap}_{Na^+}$ is set to zero, and to model the effect of a low Cl^- lumen solution, the external concentration $[\mathrm{Cl}^-]_l$ is reduced and the lumen $[\mathrm{gluconate}^-]_l$ is increased in its place. The main difference with the simulations in Chapter 3 and 4 is that in a nasal PD test these perturbations are carried out in sequence, whereas previously I had carried them out in separate simulations. During the nasal PD test once amiloride is applied it remains in the perfusing solution for the rest of the test, so that $P^{ap}_{Na^+}$ will remain zero when the Cl^- concentration in the external solution is reduced.

One other minor difference with the work outlined in Chapter 3 and 4, is in the ionic composition of the lumen solution in these simulations. Since I intended to compare my simulations to data from nasal PD recordings made in the clinic, I wanted to follow closely the solution exchange protocol that are actually used in these studies. In particular, for this work I used the perfusing solutions of Simmonds et al. (2011), as I would look to analyse their data using my model at a later stage (see Chapter 6). Simmonds et al. used a HEPES solution with a higher Cl^- concentration ($[\mathrm{Cl}^-]_\mathrm{l} = 151.7$ mM) than that used in the Ussing Chamber experiments of Willumsen and Boucher ($[\mathrm{Cl}^-]_\mathrm{l} = 120$ mM). In order to take this into account, I use the following fixed external concentrations to simulate the HEPES buffer, and HEPES buffer containing amiloride solutions perfusing the lumen; (in mM) $[\mathrm{Na}^+]_\mathrm{l} = 140$, $[\mathrm{Cl}^-]_\mathrm{l} = 145$, and $[\mathrm{K}^+]_\mathrm{l} = 5$. The low chloride HEPES solution contained a small change in

potassium concentration ($5.7 \rightarrow 11.7$ mM), as well as changes in chloride ($151.7 \rightarrow 11.7$ mM) and gluconate ($0 \rightarrow 145.4$ mM) concentrations. To take this into account the fixed concentration values I used to simulate the low chloride HEPES solution are (in mM): $[Na^+]_l = 140$, $[Cl^-]_l = 5$, $[gluc^-]_l = 140$, and $[K^+]_l = 5$. These values were chosen such that the total osmolarity remains at 290 mOsm/L in order to be iso-osmolar with the previous lumen solution, and with the solution in the serosal compartment. In order to achieve this condition of iso-osmolarity, and in order to introduce changes in Cl^- and $gluconate^-$ ($\Delta[Cl^-]_l = -140$ mM, $\Delta[gluc^-]_l = +140$ mM) that were similar in magnitude to those introduced in the Simmonds et al. work, I have not been able to incorporate the small change in potassium concentration present in their work. However as I do not consider apical K^+ channels, and potassium concentration is not considered to influence nasal PD significantly (Knowles et al., 1983), I assume this is a reasonable approximation to make.

In the analysis that follows I will focus on simulating the initial steady state configuration, followed by the system response to $+amiloride$ and $+0[Cl^-]_l$ solution exchange. The other common solution exchanges, adding isoproterenol and ATP to the lumen perfusate, are not modelled as they would require additional assumptions to implement, and hence would increase the complexity of the model further. For example, in order to implement the $+isoproterenol$ solution exchange, I would have to include parameters to quantify what percentage increase in existing CFTR activity would arise due to raising intracellular cAMP levels, and I would have to include a further parameter (possibly more) to characterise the kinetics of this process, as it tends to occur over a timescale of minutes.

5.2.1.1 Representative CF and non-CF nasal PD simulations

In order to validate this approach to modelling nasal PD tests, I will use the parameter estimates I found in Chapter 3 (Table 3.4) to simulate two representative traces. Figure 5.1 highlights these exemplary simulations, the blue trace results from the non-CF parameter set, and the red trace from the CF parameter values. Relative to patients with normally functioning CFTR channels, patients with a CF mutation generally exhibit a hyperpolarised basal V_t, increased amiloride-sensitive V_t and little or no change in V_t when the lumen Cl^- concentration is reduced. This is unsurprisingly what is observed in the example here, and the differences in each of the three nasal PD metrics is summarised in Figure 5.1(b). Using these simulations we can relate physiologically meaningful parameters, such as apical Cl^- and Na^+ permeability, to

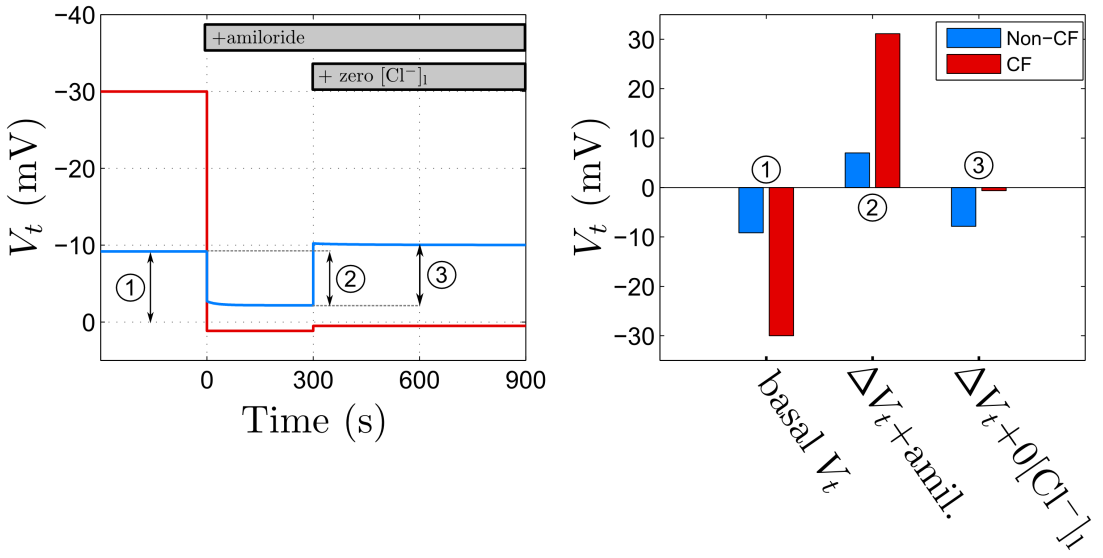

Figure 5.1: The left hand panel shows a simulation of the first two stages of a clinical nasal PD test. V_t is recorded at steady state, and after amiloride addition and removal of Cl^- from the lumen perfusate. The two simulations shown make use of the optimal non-CF (blue trace) and CF (red trace) parameter sets taken from Table 3.4. The values that are usually reported from a clinical nasal PD test are highlighted for the non-CF trace, and these are (1) basal V_t, (2) ΔV_t+amiloride and (3) ΔV_t+0$[\mathrm{Cl}^-]_\mathrm{l}$. The right hand panel compares the value of these metrics in the CF and non-CF cases. Basal V_t is more hyperpolarised in CF, ΔV_t+amiloride is increased in CF, and ΔV_t+0$[\mathrm{Cl}^-]_\mathrm{l}$ is reduced in CF.

relevant metrics like ΔV_t+amiloride or ΔV_t+0$[\mathrm{Cl}^-]_\mathrm{l}$ which are routinely made in the clinic.

5.2.2 Parameter sensitivity analysis

As mentioned previously, when interpreting nasal PD measurements, it is common to assume that ΔV_t+amiloride is determined *solely* by ENaC activity, and ΔV_t+0$[\mathrm{Cl}^-]_\mathrm{l}$ is similarly only determined by CFTR activity. To investigate to what extent this is a reasonable assumption, I wanted to determine quantitatively how these measurements were influenced by changes in the major ion transport pathways in HNE cells.

To this end, I performed a parameter sensitivity analysis, in the same spirit of that outlined in Section 4.2.3. For each model parameter of interest I initially simulated a standard nasal PD test using (a) the optimal non-CF transport parameters and (b) the optimal CF transport parameters, and repeated the simulations for different values of this parameter. In each case, the parameter was varied in steps of 10% between the limits of $\pm 50\%$ of its CF or non-CF estimated value.

Figure 5.2 shows the results of making these parameter changes on predicted nasal PD traces, for a selection of the parameters investigated. In each simulation, transport parameters

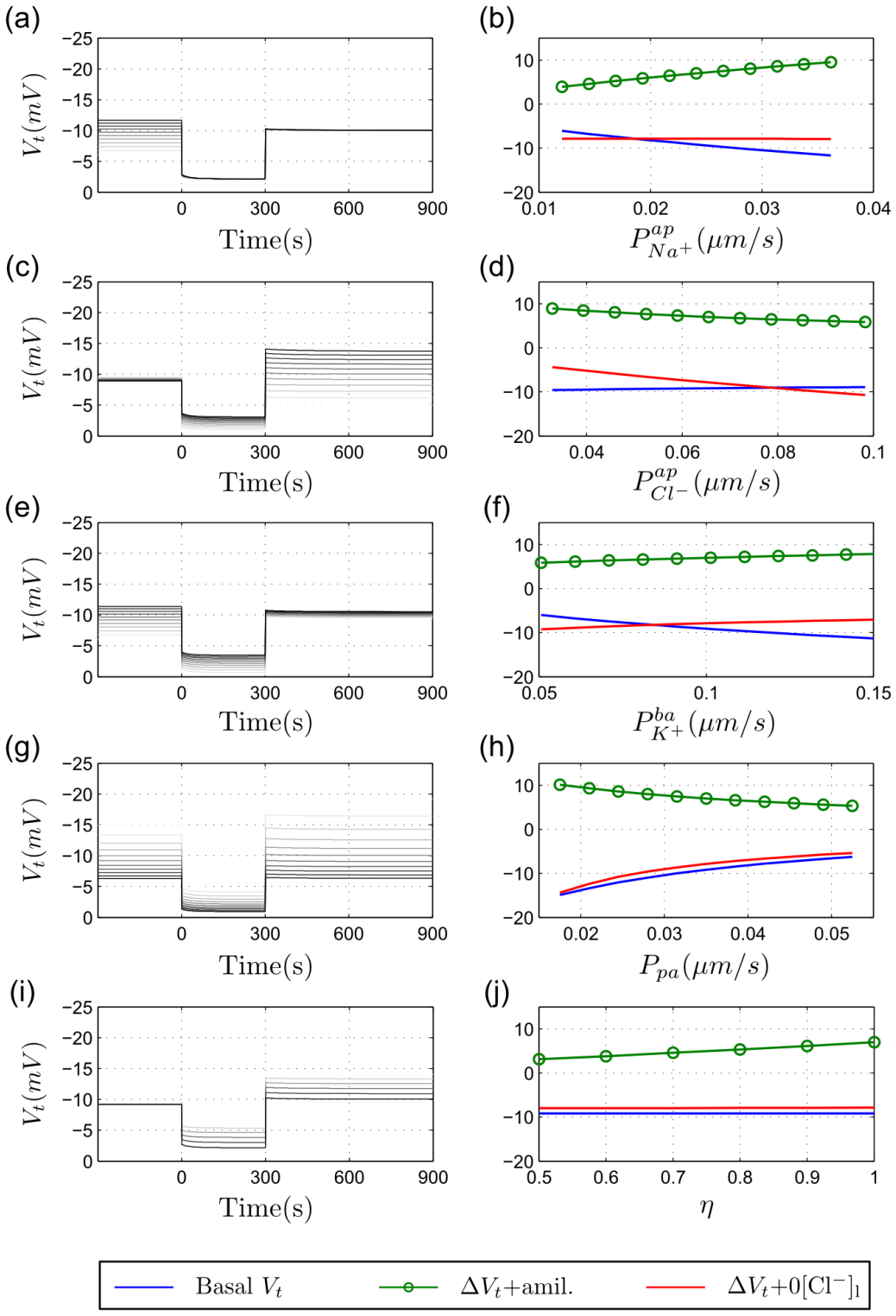

Figure 5.2: The panels on the left hand side show non-CF nasal PD simulations (amiloride and Cl^- free perfusion stages). A single parameter is varied in each, between $\pm 50\%$ of its optimal non CF value - (a) $P^{ap}_{Na^+}$, (c) $P^{ap}_{Cl^-}$, (e) $P^{ba}_{K^+}$, (g) P_{pa} and (i) η. Right hand panels show the corresponding variation in basal V_t (blue line), amiloride-sensitive V_t (green line with circles) and ΔV_t+0[Cl$^-$]$_l$ (red line) caused by varying these parameter values.

that are not being varied are set to their estimated non-CF values. In panels (a),(c),(e) and (g) it is assumed that $P^{ap}_{Na^+} \rightarrow 0$ when amiloride is added, whereas in simulations plotted in (i) I investigate the effect of only a fraction η of ENaC channels being blocked (i.e. $P^{ap}_{Na^+} \rightarrow (1-\eta)\, P^{ap}_{Na^+};\ 0 \leq \eta \leq 1$). The reason for considering this phenomenon (allowing a partial apical Na^+ permeability to remain after amiloride addition) will become clearer in Chapter 6, when I look at factors influencing amiloride insensitive V_t levels in the nasal PD traces of CF patients.

Beginning with apical Na^+ permeability, panel (a) shows the simulated nasal PD traces for various values of $P^{ap}_{Na^+}$, going from -50% of its optimum value (light gray line) to $+50\%$ of this value (black line). Panel (b) explicitly plots the nasal PD metrics basal V_t (blue line), amiloride sensitive V_t (green line with circles) and $\Delta V_t{+}0[\mathrm{Cl}^-]_\mathrm{l}$ (red line) as function of $P^{ap}_{Na^+}$. The subsequent panels show the result of varying $P^{ap}_{Cl^-}$ ((c) and (d)), $P^{ba}_{K^+}$ ((e) and (f)), P_{pa} ((g) and (h)) and finally η ((i) and (j)).

Table 5.1 summarises the results of this analysis for all model parameters investigated. The total change caused in a V_t metric by the $\pm 50\%$ parameter change is recorded in each entry. For example we can see from Figure 5.2(a), that changing $P^{ap}_{Na^+}$ from $0.0121 \rightarrow 0.0362\ \mu\mathrm{m/s}$ results in $\Delta V_t{+}\mathrm{amiloride}$ going from $3.9\ \mathrm{mV} \rightarrow 9.5\ \mathrm{mV}$, hence in Table 5.1 a value of $+5.60\ \mathrm{mV}$ is recorded for this particular entry. The table then allows us to compare quantitatively the influence each transport parameter has on the measured nasal PD values.

As the membrane potentials and permeabilities in a CF HNE cell are different to those present in non-CF cells, the driving forces for each ion are also different and one would expect that consequently the influence of each transport pathway on the measured V_t metrics may also diverge. Figure 5.3 shows the result of a parameter sensitivity analysis to investigate if this is the case. The analysis performed is analogous to that shown previously, except now the transport parameters are fixed to their estimated CF values. Visual inspection of these simulations alone can confirm that the sensitivity of the nasal PD metrics to membrane permeabilities is vastly different in this CF case, than in the non-CF case plotted in Figure 5.2. Table 5.2 gives the quantitative data for changes in V_t metrics found given $\pm 50\%$ changes in the model parameters of interest, and by comparing the values here with those in Table 5.1 we can confirm that the parameter - metric sensitivities are indeed quantitatively different as well.

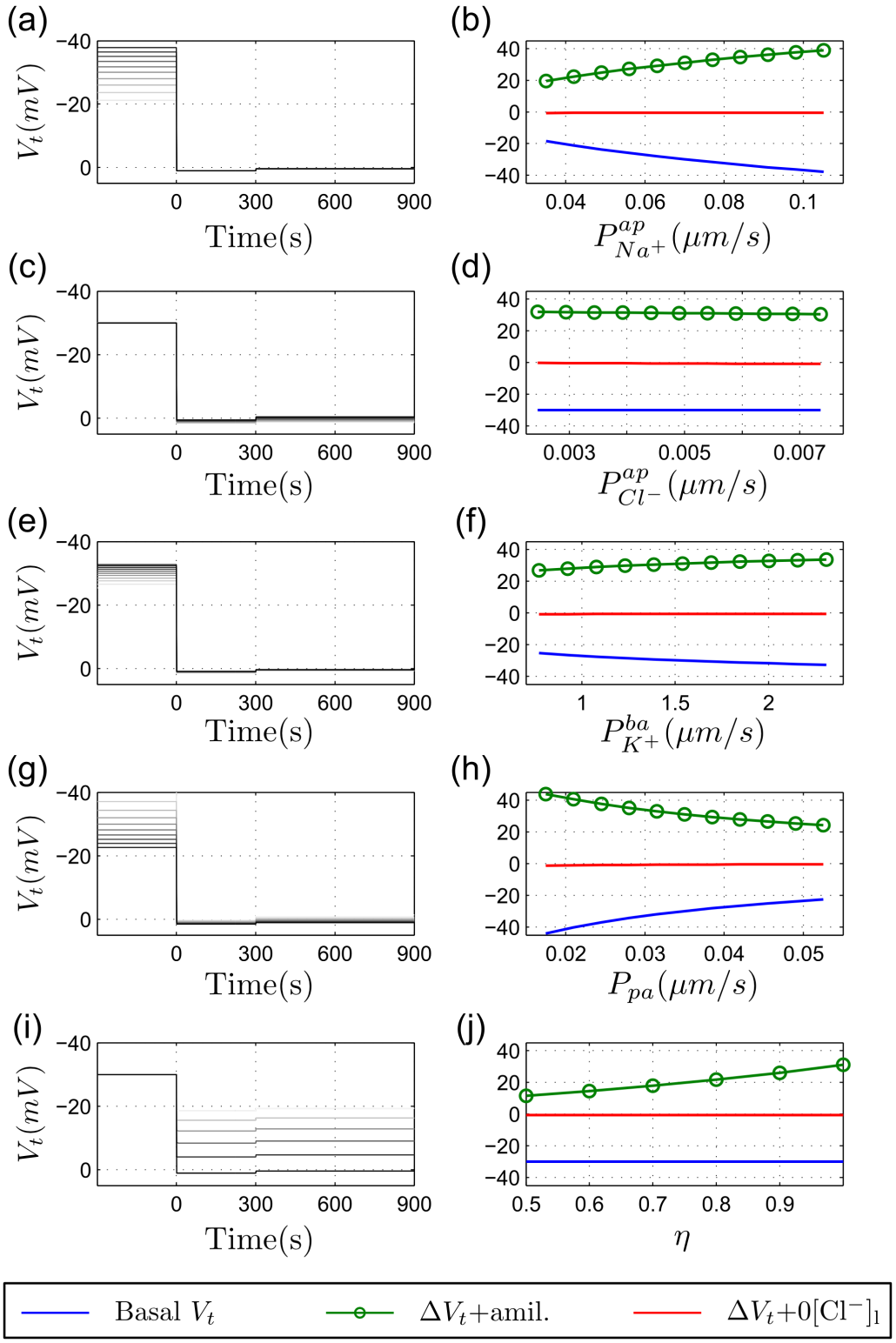

Figure 5.3: The panels on the left hand side show simulations of the first two stages of an nasal PD test (amiloride and Cl^- free perfusion) in a CF HNE cell. The following transport parameter is being varied in each panel - (a) P^{ap}_{Na+}, (c) P^{ap}_{Cl-}, (e) P^{ba}_{K+}, (g) P_{pa} and (i) η. Right hand panels show the corresponding variation in basal V_t (blue line), amiloride-sensitive V_t (green line with circles) and ΔV_t+0[Cl$^-$]$_l$ (red line) caused by varying these parameter values.

	Non-CF			
Parameter	baseline V_t mV	ΔV_t+amil. mV	ΔV_t+0$[\mathrm{Cl}^-]_\mathrm{l}$ mV	V_t after amil. mV
$P^{ap}_{Na^+}$	-5.58	5.60	-0.07	0.03
$P^{ap}_{Cl^-}$	0.68	-3.11	-6.32	-2.43
$P^{ba}_{K^+}$	-5.35	2.03	2.23	-3.32
$P^{ba}_{Cl^-}$	2.29	0.59	-1.74	2.89
ρ_{NaK}	-0.19	-0.21	-0.52	-0.41
ρ_{NKCC}	0.33	-0.68	-0.87	-0.35
P_{pa}	8.65	-4.75	8.99	3.90
η	0.00	3.89	0.15	3.89

Table 5.1: Table summarising the result of changing model transport parameters on measurements of nasal potential difference. Model transport parameters were set at their estimated non-CF values, then one at a time were varied from $-50\% \rightarrow +50\%$ of this value. The resulting changes in basal V_t, ΔV_t+amiloride and ΔV_t+0$[\mathrm{Cl}^-]_\mathrm{l}$ caused by this single parameter change are listed here, as well as the change in value of amiloride insensitive V_t.

5.3 Results

5.3.1 Non-CF sensitivity analysis

The analysis performed here to assess the influence of changing transport parameters on measured basal V_t, amiloride sensitive V_t and ΔV_t+0$[\mathrm{Cl}^-]_\mathrm{l}$ in non-CF HNE cells, recapitulates many of the insights from Chapter 4. I saw that $P^{ap}_{Na^+}$ is influential - the greater this permeability the more hyperpolarised V_t is and the greater ΔV_t+amiloride becomes. Similarly, basolateral K^+ permeability influences the baseline V_t value, tending to hyperpolarise it as the permeability increases, and $P^{ba}_{K^+}$ will also influence amiloride sensitive V_t, but not to the same extent to as $P^{ap}_{Na^+}$. It was also noted in Chapter 4 that increasing $P^{ap}_{Cl^-}$ tends to increase ΔV_t+0$[\mathrm{Cl}^-]_\mathrm{l}$ and decrease the measured amiloride sensitive V_t. The simulations displayed in Figure 5.2 and the quantitative data in Table 5.1 highlight these relationships again.

In the sensitivity analysis of Chapter 4 however, I did not vary paracellular permeability, whereas I do here and it has a significant effect on V_t (see panel (g) and (h) in Figure 5.2). In fact a $\pm 50\%$ change in P_{pa} results in a change in basal V_t ($+8.65$ mV) that is greater in magnitude than the equivalent change arising from a $\pm 50\%$ change in $P^{ap}_{Na^+}$ (-5.58 mV), and a greater change in ΔV_t+0$[\mathrm{Cl}^-]_\mathrm{l}$ ($+8.99$ mV) than the equivalent relative change induced by increasing $P^{ap}_{Cl^-}$ (-6.32 mV). The paracellular permeability does not have as great an influence on ΔV_t+amiloride (-4.75 mV) as $P^{ap}_{Na^+}$ ($+5.60$ mV) however. In general increasing P_{pa}

	CF			
Parameter	baseline V_t mV	ΔV_t+amil. mV	ΔV_t+0$[\mathrm{Cl}^-]_\mathrm{l}$ mV	V_t after amil mV
$P^{ap}_{Na^+}$	-19.37	19.37	0.01	0.00
$P^{ap}_{Cl^-}$	0.16	-1.37	-0.64	-1.21
$P^{ba}_{K^+}$	-7.37	6.78	0.30	-0.58
$P^{ba}_{Cl^-}$	5.29	-4.53	-0.20	0.76
ρ_{NaK}	1.22	-1.40	-0.08	-0.17
ρ_{NKCC}	0.00	-0.00	0.00	-0.00
P_{pa}	21.30	-19.72	0.86	1.58
η	0.00	19.70	0.10	19.70

Table 5.2: Table summarising the result of changing model transport parameters from their estimated CF values, on measurements of nasal potential difference. Parameters were varied from $-50\% \rightarrow +50\%$ of their estimated CF value, and the amiloride and Cl^- free solution stages of an nasal PD test were simulated. The resulting changes in basal V_t, ΔV_t+amiloride and ΔV_t+0$[\mathrm{Cl}^-]_\mathrm{l}$ caused by this single parameter change are listed here, as well as the change in value of amiloride insensitive V_t.

shorts the epithelium by reducing the resistance to direct lumen to serosal ion flow, and tends to dampen the changes in V_t that occur due to any changes to other permeabilities or external ion concentrations.

5.3.2 CF sensitivity analysis

When we assess the sensitivity of the baseline V_t in a CF HNE cell to changes in transport parameters, we see that the same factors are influential, paracellular permeability, apical Na^+ permeability and basolateral K^+ permeability. The effect of varying these parameters $\pm 50\%$ induces a greater magnitude of change in V_t than in the non-CF case (21.3, -19.4 and $-7.4\,\mathrm{mV}$ respectively), but the order of their relative influence is unchanged.

The interesting observation from Figure 5.3(a)-(h) is how little influence any of the membrane or paracellular permeabilities have on the magnitude of V_t the system relaxes to after amiloride is added. This only appears to be significantly influenced by η, which governs the fraction of apical Na^+ permeability blocked on amiloride addition. Looking at the data in Table 5.2 we can also see that changes to the value of ΔV_t+0$[\mathrm{Cl}^-]_\mathrm{l}$ are less than $1\,\mathrm{mV}$ in case of $\pm 50\%$ changes in all transport parameters. This is in contrast to the non-CF case where changes in $P^{ap}_{Cl^-}$ and P_{pa} cause changes of $-6.32\,\mathrm{mV}$ and $8.99\,\mathrm{mV}$ respectively.

	CF cells with incomplete amiloride block			
	baseline V_t	ΔV_t+amil.	ΔV_t+0$[\mathrm{Cl}^-]_\mathrm{l}$	V_t after amil
Parameter	mV	mV	mV	mV
$P^{ap}_{Na^+}$	-19.37	14.62	-0.02	-4.76
$P^{ap}_{Cl^-}$	0.16	-1.06	-0.66	-0.90
$P^{ba}_{K^+}$	-7.37	5.51	0.28	-1.86
$P^{ba}_{Cl^-}$	5.29	-3.61	-0.19	1.68
ρ_{NaK}	1.22	-1.03	-0.08	0.19
ρ_{NKCC}	0.00	-0.00	0.00	0.00
P_{pa}	21.30	-14.27	0.95	7.03
η	-	-	-	-

Table 5.3: Table summarising the result of changing model transport parameters on measurements of nasal potential difference, assuming only 90% of apical Na^+ permeability is blocked by amiloride. As in Table 5.1 and 5.2, the change in the values of basal V_t, ΔV_t+amiloride and ΔV_t+0$[\mathrm{Cl}^-]_\mathrm{l}$ caused by varying a single model parameter, are listed in mV.

5.3.3 Investigating partial block of ENaC channels

To investigate the effect of only partially blocking ENaC channels, I introduced the parameter η, such that the permeability changes from $P^{ap}_{Na^+} \rightarrow (1-\eta)\, P^{ap}_{Na^+}$ when amiloride is added, where in all previous simulations it would have changed to zero, i.e. $\eta = 1$ and hence $P^{ap}_{Na^+} \rightarrow 0$. I then varied the fraction of ENaC channels blocked from between 50% and 100%, and looked at the resulting nasal PD traces. Figure 5.2(i) and (j) show the results when all transport parameters are set to their estimated non-CF values, and Figure 5.3(i) and (j) the equivalent simulations with transport parameters at CF estimated values.

In the non-CF simulations, varying η by 50% leads to changes in amiloride insensitive V_t of $3.89\ \mathrm{mV}$, which is the same order of magnitude as the change induced by other transport parameters (see Table 5.1). However, in the case of CF simulations, a 50% variation in η induces a $19.7\ \mathrm{mV}$ increase in the amiloride insensitive V_t value, an order of magnitude greater than the next greatest change of $1.58\ \mathrm{mV}$ caused by changing P_{pa}.

Given this knowledge, I performed a third sensitivity analysis, now assuming that each patient had $P^{ap}_{Na^+}$ reduced by 90% on addition of amiloride, instead of a complete reduction (The value of $\eta = 0.9$ was chosen arbitrarily). I kept all model parameters apart from η at their estimated CF value, and then performed nasal PD simulations while changing one parameter at a time $\pm 50\%$ of the aformentioned CF estimated value. The results of this analysis are presented in Table 5.3. If a fraction of $P^{ap}_{Na^+}$ remains after the amiloride solution perfusion,

then the value of V_t that the system relaxes to can be influenced by both P_{pa} ($+7.03$ mV) and $P^{ap}_{Na^+}$ (-4.76 mV), to a greater extent than if amiloride completely blocked all apical Na^+ transport.

5.4 Discussion

5.4.1 How do the major transport proteins alter nasal PD metrics?

I showed that it was possible to simulate the first two solutions exchanges of a standard nasal PD measurement, in the same manner as I had previously simulated Ussing Chamber experiments in Chapter 3 and 4. I then went on to investigate the sensitivity of standard nasal PD measurements to changes in individual transport parameters. As well as varying the membrane permeability and pump / co-transporter density parameters as before (in Chapter 4), in this set of analyses I also varied paracellular permeability. On this occasion I performed three separate analyses, assuming transport parameters were fixed at previously estimated (1) non-CF and (2) CF values, as well as (3) investigating the effect of incomplete amiloride block of $P^{ap}_{Na^+}$, on the results of the sensitivity analysis in the CF case.

The sensitivity analysis provided the following insights:

- Non-CF: The influence of transport parameters is generally the same as observed previously (see Table 4.3), however I also took into account variation in P_{pa} on this occasion. Basal V_t is sensitive to (in order of influence) P_{pa}, $P^{ap}_{Na^+}$, $P^{ba}_{K^+}$ and $P^{ba}_{Cl^-}$. $\Delta V_t{+}\mathrm{amiloride}$ is sensitive to $P^{ap}_{Na^+}$, P_{pa}, $P^{ap}_{Cl^-}$ and $P^{ba}_{K^+}$, while $\Delta V_t{+}0[\mathrm{Cl}^-]_\mathrm{l}$ is sensitive to P_{pa}, $P^{ap}_{Cl^-}$, $P^{ba}_{K^+}$ and $P^{ba}_{Cl^-}$.

- Non-CF: Increasing P_{pa} tends to decrease the magnitude of all three nasal PD metrics, that is, decreasing the paracellular resistance tends to dampen the magnitude of ΔV_t caused by the solution exchanges.

- CF: Baseline V_t and $\Delta V_t{+}\mathrm{amiloride}$ are strongly influenced by P_{pa}, $P^{ap}_{Na^+}$, $P^{ba}_{K^+}$ and $P^{ba}_{Cl^-}$. The other transport parameters have very little influence on these aspects of simulated CF nasal PD traces.

- CF: If it is assumed that amiloride completely blocks all apical Na^+ transport (i.e. $P^{ap}_{Na^+} \rightarrow 0$), $\pm 50\%$ changes in transport parameter values only induce subsequent changes in V_t of the order of $\pm 1 - 2$ mV. Large variations in amiloride *insensitive*

V_t (of the order of $10\ \mathrm{mV}$) therefore cannot be explained by variations in membrane or paracellular permeabilities in this situation.

- CF: Allowing for partial block of ENaC channels on amiloride addition ($P^{ap}_{Na^+} \rightarrow (1-\eta)\, P^{ap}_{Na^+}; 0 \leq \eta \leq 1$) increases the sensitivity of V_t to transport parameters after amiloride addition. For example, when I assume only 90% of apical Na^+ permeability is blocked on amiloride addition, changes in amiloride insensitive V_t of the order of $10\ \mathrm{mV}$ can be explained by $\pm 50\%$ changes in P_{pa} and $P^{ap}_{Na^+}$.

5.4.2 Summary

At the beginning of this chapter I stated that it was commonly assumed that $\Delta V_t{+}\mathrm{amiloride}$ could be used as a biomarker of ENaC activity, and similarly $\Delta V_t{+}0[\mathrm{Cl}^-]_\mathrm{l}$ could be used as a biomarker of CFTR activity. I have shown via the sensitivity analysis in this chapter that $P^{ap}_{Na^+}$ and $P^{ap}_{Cl^-}$ are indeed capable of increasing the magnitude of these two nasal PD metrics, and the relationship in both cases is approximately linear over the region of parameter space searched. Given this fact, one could be forgiven to think about equating a fixed percentage change in say, $\Delta V_t{+}\mathrm{amiloride}$, with a certain percentage change in $P^{ap}_{Na^+}$. However, I also saw that amiloride sensitive V_t can be significantly influenced by changes in other parameters, particularly P_{pa} and $P^{ba}_{K^+}$. Attributing a change in $\Delta V_t{+}\mathrm{amiloride}$ to one of these parameters, without justifying why it could not have been caused by a change in the other two, could hence be misleading. This highlights one of the problems with attempting to reverse engineer transport parameter estimates from nasal PD measurements. In the next chapter I will address this issue in more detail, investigating the problem of estimating transport parameter values directly from a patient's nasal PD trace.

Chapter 6

Estimating parameters from individual transepithelial potential recordings

6.1 Introduction

In the previous chapter I investigated quantitatively how measurements of airway ion transport commonly made in the clinic, were influenced by membrane transport parameters, using estimates of parameter values in non-CF and CF HNE cells (Table 3.4) as reference points. I now want to investigate the feasibility of inferring these parameter values directly from nasal PD measurements, in a manner analogous to that outlined previously which utilised *in vitro* measurements (see Section 3.2.5). I was fortunate to be given access to a substantial set of nasal PD recordings made by physicians at the Royal Brompton Hospital, and I will make use of this data throughout. I will now outline a number of the specific questions I hope to address in this chapter.

6.1.1 Can variations in CFTR and ENaC activity explain variable nasal PD data?

Given a cohort of nasal PD traces, I will use my modelling framework to estimate the values of $P^{ap}_{Na^+}$ and $P^{ap}_{Cl^-}$ from each individual set of V_t measurements (basal V_t, ΔV_t+amiloride, and ΔV_t+0$[\mathrm{Cl}^-]_\mathrm{l}$). I will then investigate if allowing these two parameters to vary (i.e. $P^{ap}_{Na^+}$, $P^{ap}_{Cl^-}$ free to vary) is sufficient to reasonably explain the variability that exists in the group of patient nasal PD traces. If this is not sufficient to accurately reproduce all traces, I will endeavour to understand what aspects of the nasal PD recordings they fail to explain. I can combine this knowledge along with the insights from the sensitivity analysis in Chapter 5, to assess what factors are likely to account for any additional variability. Consequently I will investigate if

estimating three, and finally four, transport parameters from each nasal PD trace improves the ability to reproduce all nasal PD traces in the data set.

6.1.2 Can all parameters be identified from nasal PD traces?

Given that nasal PD traces are recorded non-invasively *in vivo*, we do not typically have any information on intracellular concentrations or on individual membrane potential values. This lack of information limits the ability of a single V_t trace to constrain the values of all transport parameters. Here I will address the question of when degenerate parameter estimates might arise, and what implications this would have for our ability to uniquely identify physiological parameters.

6.1.3 Are permeability estimates more informative than nasal PD metrics?

Finally, given the results of previous analyses, I will investigate whether or not there are any significant correlations between the estimated values of model parameters and the measures of disease severity, such as FEV_1, in this particular data set. This will go some way in determining the value of using transport parameter estimates, over raw nasal PD measurements, in assessing a person's underlying physiology.

6.2 Methods

6.2.1 Patient data from clinical study of CF severity

As mentioned in the introduction to this chapter, I have kindly been given access to a data set of nasal PD recordings made by clinicians at the Royal Brompton Hospital. In their study, the researchers were investigating potential links between measures of airway ion transport and disease severity, as well as correlations between CFTR function and extended disease survival. The data set consists of 92 different nasal PD traces recorded from 74 different patients (18 patients with 2 recordings, 54 with a single recording). Patients recruited to the study had a confirmed diagnosis of CF (with pancreatic insufficiency) and class I-III disease causing mutations on both alleles. Each patient's age and sex, as well as information on their lung function is contained in the data set. Patients' lung function is assessed by common spirometry measures, the *forced expiratory volume in 1 second* (FEV_1) and the *forced vital capacity* (FVC). Patients were recruited for the study based on their age, being in one of two groups: young (age 18-23 years) or Old (age $\geq$ 40 years). Patients in the younger group were also further classified by disease severity as either "Young/Mild" or "Young/Severe", based on how their lung

capacity compared to the expected value for their age, height and BMI (% of predicted FEV_1 value). In their analysis of this data set Simmonds et al. found that there was a statistically significant correlation between $\Delta V_t{+}\mathrm{amiloride}$ and FEV_1, suggesting an association between ENaC activity and disease severity. However there was no significant link between length of survival and $\Delta V_t{+}0[\mathrm{Cl}^-]_\mathrm{l}$, which was assumed to be an indicator of residual CFTR function (Simmonds et al., 2011).

Each trace was recorded using the following protocol and a representative example can be seen in Figure 6.1 (Note description of solutions used was previously given in Section 5.2.1). Initially a HEPES buffer solution (high Na^+, Cl^-, low K^+) is perfused across the lumen surface and the maximum (most negative) stable potential achieved is recorded as the *baseline* V_t. The red dashed line (marked 1 in Figure 6.1) highlights the baseline V_t value in this case. After recording basal V_t, a HEPES buffer solution containing amiloride (100 μM) is passed across the epithelial surface for five minutes. The amiloride sensitive V_t (labelled 2) can then be determined by the difference between the initial baseline V_t, and the new value of V_t the trace stabilises at . The HEPES + amiloride solution is followed by a low chloride HEPES + amiloride solution, where the Cl^- solution is reduced by two orders of magnitude. This is perfused for five minutes, after which again the new stable V_t level is noted and the change in V_t due to the low Cl^- solution can be determined (labelled 3 in example). Finally a low chloride HEPES + amiloride + isoprenaline solution is perfused for a final five minutes, from which $\Delta V_t{+}\mathrm{iso.}$ and $\Delta V_t{+}(0[\mathrm{Cl}^-]_\mathrm{l} + \mathrm{iso.})$ can be determined. These last two metrics are not highlighted here as I do not model the $+\mathrm{isoprenaline}$ stage, but this information is present in the Royal Brompton data set.

From the cohort of CF nasal PD traces, I only retained for further analysis those traces where the three nasal PD metrics of interest to me (basal V_t, $\Delta V_t{+}\mathrm{amiloride}$ and $\Delta V_t{+}0[\mathrm{Cl}^-]$) could be unambiguously measured, as in the example just discussed. The criteria I used for selection was to retain traces where V_t relaxed to a new equilibrium level before the second solution exchange occurred. Those traces where V_t had not relaxed to a new steady state level five minutes after amiloride addition were not retained for further analysis. An example of such an ambiguous trace is shown in Figure 6.2. Here it is not clear that V_t has stabilised before the low Cl^- solution is introduced, as the PD appears to be still depolarising. In cases like this, the assumptions I make to model the nasal PD test may not be accurate. For example, I assume that

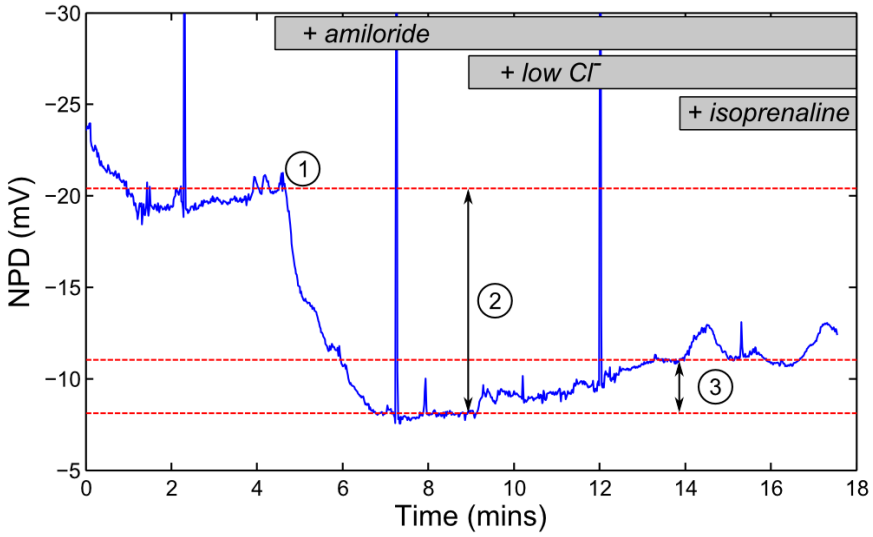

Figure 6.1: Nasal transepithelial potential recording from a CF patient (blue trace). The red dashed lines highlight the values of V_t that are used to measure baseline PD (1), amiloride sensitive PD (2) and (3) $\Delta V_t{+}0[\mathrm{Cl}^-]_\mathrm{l}$. The PD is relatively stable before each of the three solution exchanges.

when amiloride is added $P^{ap}_{Na^+}$ will then be zero, however in this trace it may be more realistic that $P^{ap}_{Na^+}$ transitions to zero over a period of 10-15 minutes.

6.2.1.1 Summary statistics for nasal PD data

After selecting from the clinical data set only those traces with unambiguous PD metrics, I was left with a group of 42 separate traces (32 patients with one trace, 5 with two traces - a full list of the nasal PD measurements is in the appendix, see Section A.10). The distributions of baseline V_t, amiloride-sensitive V_t, and $\Delta V_t{+}0[\mathrm{Cl}^-]_\mathrm{l}$ in this remaining population of traces are plotted in Figure 6.3.

There are a number of interesting features of this data set that are worth pointing out here.

- There is a statistically significant correlation between baseline V_t and amiloride sensitive V_t, the Spearman correlation coefficient $\rho = -0.8352$, with $p << 0.001$. The more hyperpolarised basal V_t is the greater the corresponding $\Delta V_t{+}\mathrm{amiloride}$.

- Some traces display a large amiloride *insensitive* V_t. For example, traces that have a basal V_t of approximately -45 mV showed values of $\Delta V_t{+}\mathrm{amiloride}$ ranging from around $17 - 37$ mV. Patients with the same baseline V_t can exhibit amiloride insensitive V_t values that that differ by tens of millivolts.

- There are four traces that exhibit values of $\Delta V_t{+}0[\mathrm{Cl}^-]_\mathrm{l}$ which are much greater than

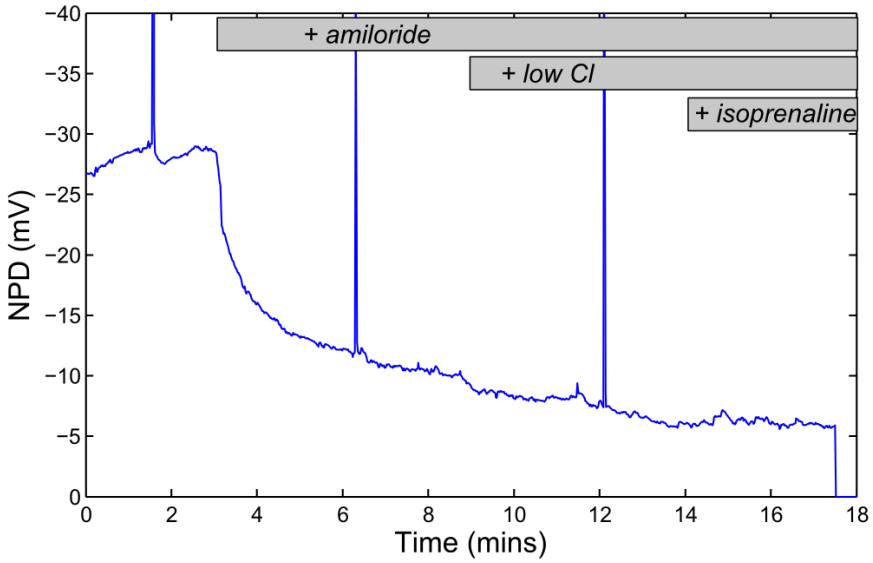

Figure 6.2: An example of a nasal PD trace where it is difficult to separate the amiloride sensitive V_t component, from the change induced due to the low Cl^- solution exchange. At the time of this solution exchange V_t is still depolarising, and it appears that the amiloride continues to have a depolarising effect beyond this point, when its effect is usually assumed to be complete. Hence, due to this ambiguity, I did not include any of the nasal PD traces which did not have a clear, stable V_t value before the start of each solution exchange.

expected in CF patients (i.e. $\Delta V_t{+}0[\mathrm{Cl}^-]_\mathrm{l} < -10$ mV). This was noted by Simmonds et al. and suggests that the three patients from which these recordings were made have levels of apical Cl^- conductance similar to non-CF patients.

- There are no traces where $\Delta V_t{+}0[\mathrm{Cl}^-]_\mathrm{l} > 0$. That is, in the traces I have analysed, introducing a Cl^- free solution in the lumen induces a hyperpolarisation of V_t and never a depolarisation.

Table 6.1 gives a breakdown by patient group of the median and interquartile range (IQR) for each of these three nasal PD metrics. The table also lists the p-values found when the Kruskal Wallis statistical test was used to assess whether or not there is a statistically significant difference between the NPD metrics observed in each patient group. This information is displayed graphically in Figure 6.4(a)-(c). The boxplots display the group median (red line), first (q_1) and third (q_3) quartiles (upper/lower bounds of blue box), and any points larger than q_3 + $1.5(IQR)$ or smaller than q_1 $-1.5(IQR)$ are marked as outliers (note the interquartile range IQR is given by $q_3 - q_1$).

In panel (a), baseline V_t across the Old, Young/Severe and Young/Mild groups are compared. The subset of traces I have analysed retain the qualitative features found by Simmonds et

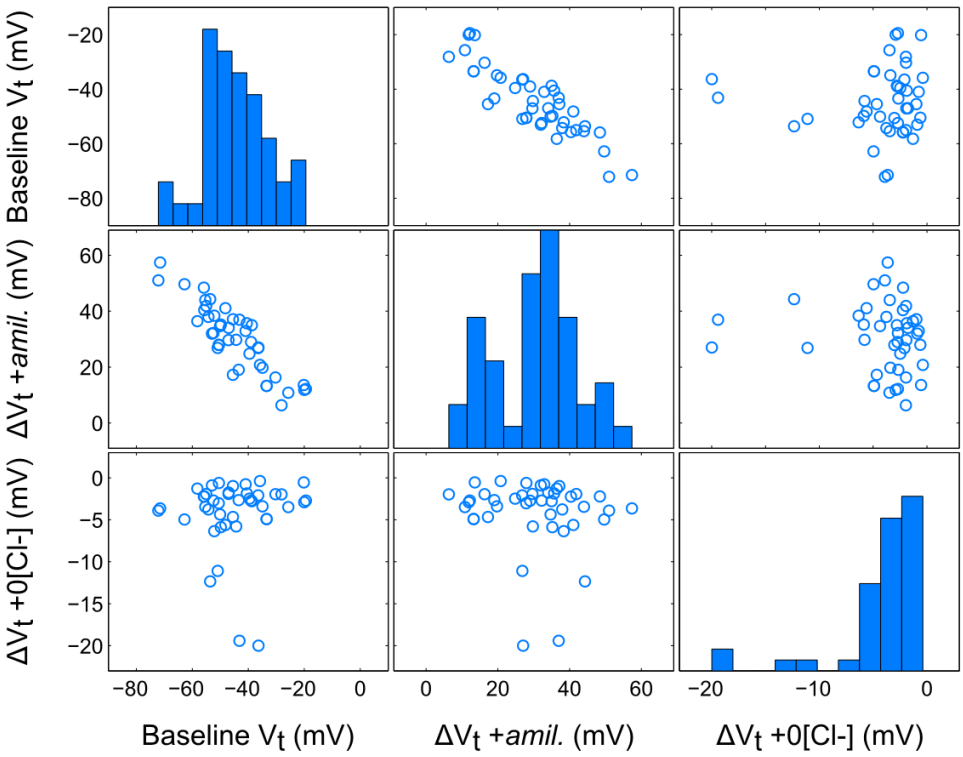

Figure 6.3: Overview of the V_t measurements in the subset of 42 nasal PD traces I retained for further analysis. Median values for each of the nasal PD metrics are: basal V_t, -46.3 mV; ΔV_t+amiloride, 32.1 mV; ΔV_t+0$[Cl^-]_l$, -2.8 mV. Note the strong correlation between baseline PD and amiloride sensitive PD, and a number of anomalous ΔV_t+0$[Cl^-]_l$ values which are more typical of non-CF traces.

		Patient group				
		All	Old	Young/Severe	Young/Mild	p-value
NPD metric		n=42	n=16	n=15	n=11	
Baseline V_t	median	-46.3	-46.8	-50.6	-40.5	0.13
	IQR	16.5	17.5	14.1	17.3	
ΔV_t+amil.	median	32.1	35.6	32.2	29.0	0.25
	IQR	17.2	16.4	12.4	18.0	
ΔV_t+0$[Cl^-]_l$	median	-2.8	-4.1	-2.7	-2.7	0.10
	IQR	2.7	4.0	2.3	1.4	

Table 6.1: Summary of the nasal potential differences measurements made from a cohort of patients with CF. The median and interquartile ranges (IQR) are listed for the entire group, as well as for the subsets of Old, Young/Severe and Young/Mild groups. All PD values displayed are in units of mV. The differences in each nasal PD metric observed in the Old, Young/Mild and Young/Severe groups were tested for significance using the Kruskal-Wallis test, however none of the differences were signficant at the $p < 0.05$ level.

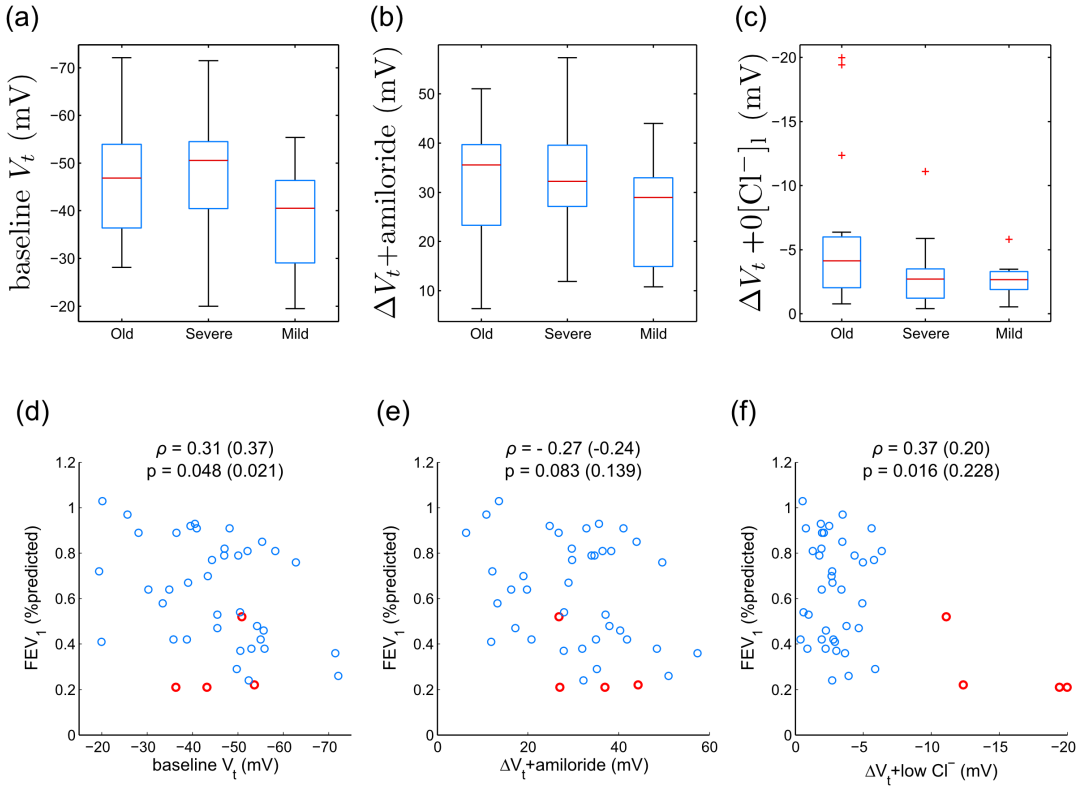

Figure 6.4: Panel (a),(b) and (c) plot the measurements of baseline V_t, amiloride sensitive V_t and ΔV_t+0$[\mathrm{Cl}^-]_1$ respectively, made from CF patients that have been categorised into groups as either Old, Young/Severe or Young/Mild. Each boxplot highlights the median (central line), lower quartile q_1 and upper quartile q_3 (lower / upper bounds of box). Whiskers on the boxplot highlight the range $[q_1 - 1.5\ IQR, q_3 + 1.5\ IQR]$ and red crosses indicate outliers which lie outside this range. The difference between the nasal PD metrics between any two of these groups is not statistically significant. Panels (d), (e) and (f) plots FEV_1 from all 42 traces, against the same three nasal PD measures. Data from patients exhibiting unusually large values for ΔV_t+0$[\mathrm{Cl}^-]_1$ have been marked as outliers and highlighted in red. The correlation coefficients between the respective quantities are given in each plot, first including outliers, and also excluding outliers (value given in brackets). I find there is a statistically significant correlation ($p < 0.05$) between baseline V_t and FEV_1 values, regardless of whether the outlier traces are included.

al., in order of the most hyperpolarised median baseline V_t, the groups are ranked Young/Severe, Old and Young/Mild. The difference in median values between Young/Mild and Young/Severe groups is around $10\ \mathrm{mV}$ but it is not statistically significant given the large variation in basal V_t within groups. Panel (b) shows how $\Delta V_t{+}\mathrm{amiloride}$ varies between the three groups, the median is greatest in the Old group followed by Young/Severe then Young/Mild groups, although again as there is significant overlap in the observed values and because of the low sample size in this subset of traces, the difference between any two of the group medians is not statistically significant. Finally, panel (c) plots $\Delta V_t{+}0[\mathrm{Cl}^-]_\mathrm{l}$ in the three severity categories. Here we can clearly see the outliers in the Old and Young/Severe categories with $\Delta V_t{+}0[\mathrm{Cl}^-]_\mathrm{l} < -10\ \mathrm{mV}$ which were highlighted in the preceding section. Apart from the outliers the distributions of the three groups are similar, and again I find no statistically significant difference in median $\Delta V_t{+}0[\mathrm{Cl}^-]_\mathrm{l}$ between any two of the three groups.

Panels (d)-(f) in Figure 6.4 plot the relationships between FEV_1 and each V_t metric. The correlation between each pair is quantified by the Spearman correlation coefficient ρ, and the statistical significance of this correlation is specified by a corresponding p-value. Note I have also computed the correlation coefficients that are found if I do not include the 4 traces that have $\Delta V_t{+}0[\mathrm{Cl}^-]_\mathrm{l} < -10\ \mathrm{mV}$ - the new correlation coefficients are given in brackets, and these data points are highlighted in red in the scatter plots. Panel (d) shows that baseline PD is correlated with FEV_1, the more hyperpolarised your baseline V_t the lower your predicted lung function, and this relationship is statistically significant regardless of whether or not the patients with residual Cl^- channel function are included. Panel (e) shows a scatter plot of $\Delta V_t{+}\mathrm{amiloride}$ against FEV_1. There is a trend for an increased amiloride sensitive V_t to lower the FEV_1, but it is not statistically significant. Panel (f) shows that there is only a significant correlation between FEV_1 and $\Delta V_t{+}0[\mathrm{Cl}^-]_\mathrm{l}$ if I include the traces with abnormally large levels of Cl^- conductance.

Table 6.1 summarises the median values for each quantity of interest, in each patient group. How does the data set compare with that of Simmonds et al. once I have chosen the subset of nasal PD traces for further analysis? Simmonds et al. found (a) that the Young/Severe group had a greater amiloride sensitive V_t than the Young/Mild group, and (b) that FEV_1 was correlated to baseline V_t as well as $\Delta V_t{+}\mathrm{amiloride}$. The trend seen in (a) remains in this subset but it is not statistically significant, possibly due to the reduced sample size. The same can be said for the

relationship between amiloride sensitive V_t and FEV_1. However, baseline V_t and FEV_1, are significantly correlated in the remaining sample. The subset of traces I analysed hence retain several of the characteristics of the general data set.

6.2.2 Estimating transport parameters from nasal PD data

6.2.2.1 Estimating $P^{ap}_{Cl^-}$ and $P^{ap}_{Na^+}$ from a single nasal PD trace

Following on from my initial analysis of the raw data in the Royal Brompton data set, I wanted to see if I could reproduce the nasal PD metrics present in the patient group (Figure 6.3) by only varying the values of $P^{ap}_{Na^+}$ and $P^{ap}_{Cl^-}$. To address this question, I performed parameter estimation on the 42 different nasal PD traces, in order to estimate individual values of $P^{ap}_{Cl^-}$ and $P^{ap}_{Na^+}$ from each trace. The parameter estimation as before was implemented by minimising an appropriate objective function, which in this case was

$$\underset{P^{ap}_{Na^+}, P^{ap}_{Cl^-}}{\text{minimize}} \sum_{k=1}^{3} \left(\hat{V}_t(t_k) - V_t(t_k) \right)^2 \tag{6.1}$$

Here t_k are the time points at which V_t was measured just before a solution exchange. A pair of parameter values $\{P^{ap}_{Na^+}, P^{ap}_{Cl^-}\}$ was estimated from the set of V_t values obtained from an individual nasal PD trace, and it was assumed that all other transport parameters were at the CF values estimated previously (see Table 3.4). It was also assumed that amiloride completely blocked all ENaC channels in each patient (i.e. $\eta = 1$) and hence did not contribute to patient to patient variability. Each parameter estimation was implemented as an optimisation problem, using the *lsqnonlin* function.

6.2.2.2 Estimating three transport parameters

The next stage of the analysis I carried out was to determine whether allowing the model have three free parameters would improve its ability to reproduce the full range of nasal potential difference measurements in the clinical data set. From the sensitivity analyses performed I had observed that P_{pa}, $P^{ba}_{K^+}$ and η could significantly influence the simulated CF nasal PD traces. Therefore I separately investigated estimating one of P_{pa}, $P^{ba}_{K^+}$, or η, at the same time as both $P^{ap}_{Na^+}$ and $P^{ap}_{Cl^-}$.

Paracellular permeability or basolateral K^+ permeability were estimated by minimising the objective function 6.1 as a function of either $\left(P^{ap}_{Na^+}, P^{ap}_{Cl^-}, P_{pa}\right)$ or $\left(P^{ap}_{Na^+}, P^{ap}_{Cl^-}, P^{ba}_{K^+}\right)$ respectively. Both could be carried out with the *lsqnonlin* function. The only difference here is

that now one of P_{pa} or $P_{K^+}^{ba}$ is a free parameter to be estimated, rather than fixed at its CF value (estimated in Chapter 3) as it had been while the previous objective function 6.1 was being optimised.

When estimating η as well as $P_{Na^+}^{ap}$ and $P_{Cl^-}^{ap}$, the objective function was again the same as that in 6.1 apart from the third degree of freedom. However, as η represents the proportion of ENaC channels that are blocked by amiloride, it can only take a value between 0 and 1. Hence, if the unconstrained minimisation using *lsqnonlin* estimated a value of η greater than 1, I did not keep that set of parameter estimates. Instead I carried out a constrained minimisation with the function *fmincon* in MATLAB Optimisation Toolbox, with the constraint $0 \leq \eta \leq 1$.

6.2.2.3 Estimating four transport parameters

If I naively assume I can estimate 4 model parameters from three V_t data points, this leads to problems with the ability to identify unique values for model parameters. To highlight this point, I attempted to estimate 4 model parameters, $P_{Na^+}^{ap}$, $P_{Cl^-}^{ap}$, P_{pa} and η, from a single CF patient nasal PD trace. $P_{Na^+}^{ap}$ and $P_{Cl^-}^{ap}$ were chosen again since the aim of the exercise has always been to infer CFTR and ENaC activity from these CF patients recordings, while P_{pa} and η were chosen as they had the most significant influence on basal V_t and V_t after amiloride addition in CF nasal PD simulations (see Chapter 5, Section 5.3.3). The parameter estimation was implemented in the same manner as described in the previous section, except four parameters were now estimated instead of three. On finding the parameter values that were found to minimise the objective function value, I then went on to assess the uniqueness of these estimates, by computing the profile likelihood for each of the four parameters I was attempting to estimate.

6.3 Results

6.3.1 Estimates of $P_{Cl^-}^{ap}$ and $P_{Na^+}^{ap}$ in cohort of CF nasal PD data

I estimated individual values for $P_{Cl^-}^{ap}$ and $P_{Na^+}^{ap}$ from each of the 42 separate nasal PD traces I had selected for analysis from the Royal Brompton data set (the full set of nasal potential difference measurements used in this analysis can be inspected in the appendix, Section A.10). Figure 6.5(a) shows the resulting squared residual values found by the minimisation algorithm, plotted against the sum of squared residuals. It is clear in each case that the residual error due to fitting the value of V_t after amiloride addition is the largest contributor to the total error, much greater than the errors due to fitting basal V_t or V_t after Cl^- free solution perfusion. Figure

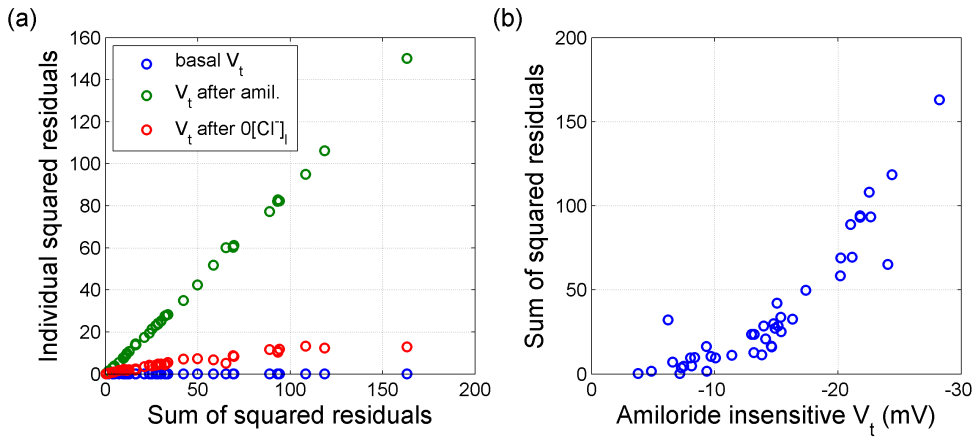

Figure 6.5: (a) Individual residual errors plotted against the minimum value of the objective function 6.1 found for each of the 42 individual nasal PD traces, allowing only $P^{ap}_{Na^+}$ and $P^{ap}_{Cl^-}$ to vary. In all cases, the error due to not fitting the value of V_t after amiloride addition correctly (green), is greater than the error between predicted and observed baseline V_t (blue) and between predicted observed value of V_t after external Cl^- is reduced (red). (b) The total error found is proportional to the level of this amiloride insensitive V_t.

6.5(b) then plots the minimum value found for the sum of squared residuals in each case, as a function of the value of V_t after amiloride itself. This highlights that the total error is correlated with the magnitude of amiloride *insensitive* V_t.

To highlight this two examples are shown in Figures 6.6 and 6.7. In the first example, Figure 6.6, the blue dotted line is the nasal PD trace recorded from a CF patient, and the three values of V_t from this recording that are used to determine basal V_t, ΔV_t+amiloride and ΔV_t+0$[\mathrm{Cl}^-]_\mathrm{l}$ are highlighted in red. The grey dashed line shows the nasal PD trace predicted by the model, found as a result of varying $P^{ap}_{Na^+}$ and $P^{ap}_{Cl^-}$ in order to minimise error between the three measured V_t data points and the predicted V_t points. In this case, the simulated nasal PD trace does a good job of reproducing the necessary V_t values, even if it is obviously a very idealised trace in comparison to the noisy recording.

In the second example however, Figure 6.7, the fit to the observed data is quite poor. While the model can accurately fit the baseline transepithelial potential, the value it predicts once $P^{ap}_{Na^+} \rightarrow 0$ is approximately $10\ \mathrm{mV}$ out from the actual observed value. Similarly, the model then does not accurately reproduce the value of V_t after the low Cl^- solution is introduced. Given how sensitive we have seen our estimates of $P^{ap}_{Na^+}$ and $P^{ap}_{Cl^-}$ are to ΔV_t+amiloride and ΔV_t+0$[\mathrm{Cl}^-]$ respectively, in this case it is probable that I am overestimating the ENaC and CFTR activity.

The insight I gained here is that it is not possible to explain the range of values of nasal po-

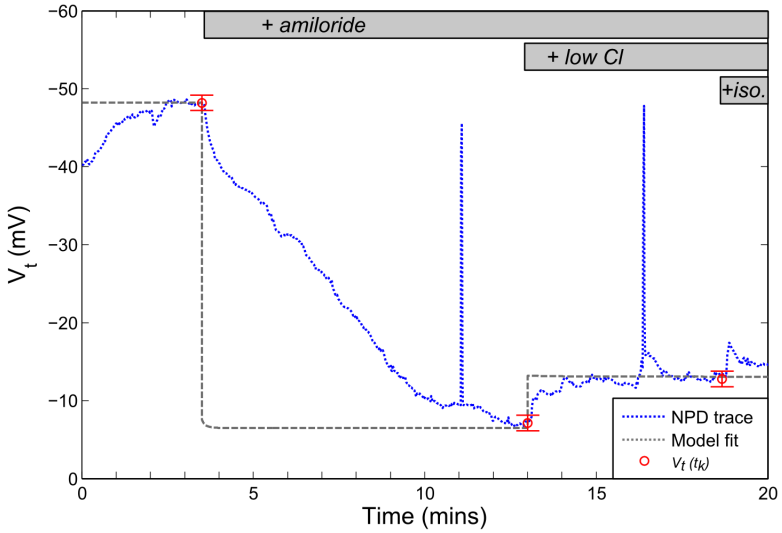

Figure 6.6: Nasal PD recording taken from a CF patient (blue dotted line). The three values of V_t used to determine basal V_t, ΔV_t+amiloride and ΔV_t+0[Cl^-] are highlighted in red. The grey dashed line shows the nasal PD simulation predicted by the model, which minimises difference with the observed V_t data by varying $P^{ap}_{Na^+}$ and $P^{ap}_{Cl^-}$.

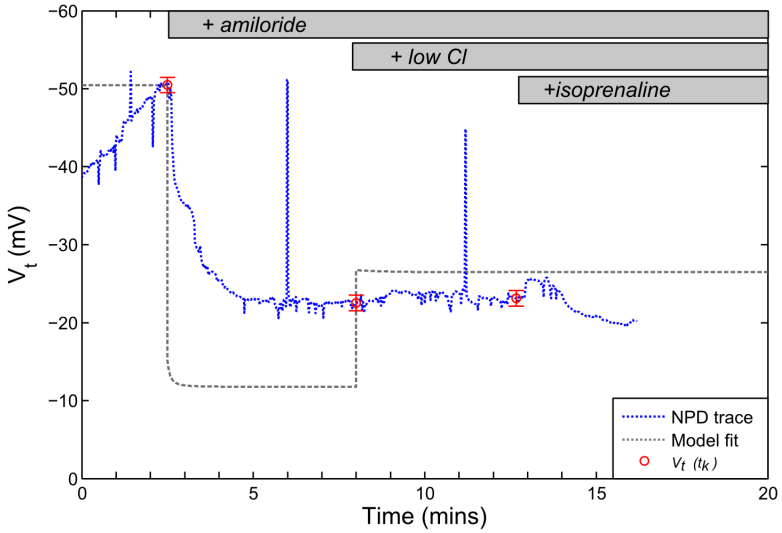

Figure 6.7: Nasal PD recording from a CF patient that displays an apparently large amiloride insensitive V_t. It is not possible to reproduce these V_t levels using the model system, by only varying apical Na^+ and Cl^- permeability. The solution which minimises the objective function in this case (gray dashed line) overestimates the amiloride sensitive V_t, and also overestimates ΔV_t+0[Cl^-]$_l$.

tential difference measurements in the Royal Brompton data set (Table 6.1) by simply assuming patient to patient variability in apical Na^+ and Cl^- permeability. This is primarily as varying these parameters cannot alter the value of V_t after amiloride addition significantly, relative to the level of variation seen in the patient cohort, if we assume $P^{ap}_{Na^+} \rightarrow 0$ on amiloride addition. However, this should not be entirely surprising given what I observed in the sensitivity analyses of the previous chapter. There I found (see Table 5.2 and 5.3) that membrane permeabilities and paracellular permeabilities could only cause changes in the level of amiloride insensitive V_t on the order of $5 - 10\ \mathrm{mV}$, if I allowed *incomplete* block of ENaC channels.

There is a clear conclusion to be made from this, and that is that variability in raw nasal PD traces collected from CF patients in this data set, cannot be explained simply by different CFTR and ENaC activities - if we assume our model system and nasal PD protocol is a realistic picture of the physiological processes generating these traces. It is particularly clear that if I assume all apical Na^+ current is blocked by amiloride, I cannot explain the traces where there is a significant amiloride *insensitive* V_t remaining. Another factor must be responsible for this observed variation, and I will now assess a number of possible explanations. In particular I will look at allowing a third transport parameter to be adjustable, and determine if this will significantly improve the ability of the ion transport model to reproduce these large amiloride insensitive V_t values in the CF patient group.

6.3.2 Estimates of three model parameters in cohort of CF nasal PD data

6.3.2.1 Estimates of $P^{ap}_{Na^+}$, $P^{ap}_{Cl^-}$ and P_{pa}

Figure 6.8(a) shows the individual squared residuals plotted against the minimum objective function value found in each of the 42 separate optimisation exercises, when $P^{ap}_{Na^+}$, $P^{ap}_{Cl^-}$ and P_{pa} are allowed to vary. As in Figure 6.5(a), the largest error arises from the inability to reproduce the value of V_t after amiloride addition. Similarly, in Figure 6.8(b) I see that the larger the amiloride insensitive V_t, the greater the error in the best fit solution that I found via optimisation - this is the same trend I saw when only estimating $P^{ap}_{Na^+}$ and $P^{ap}_{Cl^-}$ (see Figure 6.5(b)).

Estimating a third parameter value, that of P_{pa}, does allow me to increase the range of nasal potential difference measurements reproduced - that is there is a quantitative improvement in the ability to fit the traces. Over the 42 traces analysed, the median reduction in the minimum objective values found is 0.98%. However, the systematic inability to account for large amiloride insensitive V_t values remains, and hence allowing for patient to patient vari-

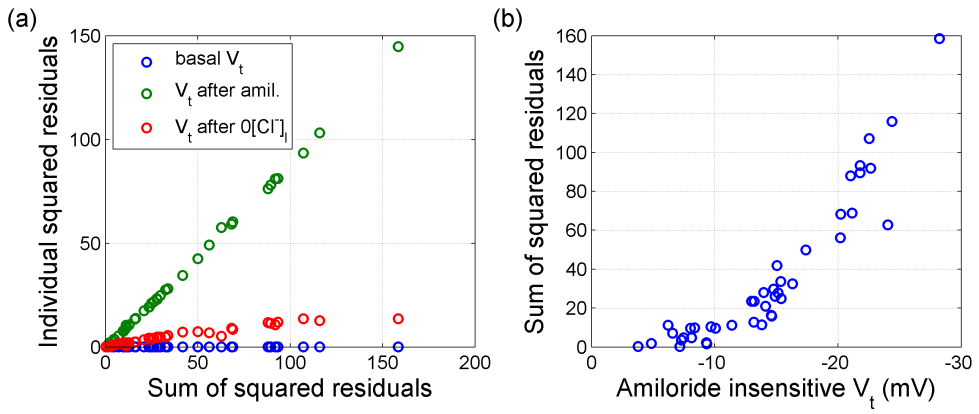

Figure 6.8: (a) Minimum objective function values found when varying $P^{ap}_{Na^+}$, $P^{ap}_{Cl^-}$ and P_{pa} in order to fit the model prediction to observed V_t values. The largest component of the total error is coming from the second residual (fit to V_t value after amiloride addition). (b) The minimum objective value found is correlated to the amiloride sensitive V_t value, suggesting that variability in paracellular permeability cannot explain the large amiloride insensitive V_t seen in some patients.

ability in paracellular permeability cannot fully explain this feature of the CF patient nasal PD traces. This is consistent with the sensitivity analysis where I note that amiloride insensitive V_t was significantly more sensitive to P_{pa}, if amiloride block of $P^{ap}_{Na^+}$ was incomplete.

6.3.2.2 Estimates of $P^{ap}_{Na^+}$, $P^{ap}_{Cl^-}$ and $P^{ba}_{K^+}$

Looking at the magnitude of the objective function values arrived at when $P^{ap}_{Na^+}$, $P^{ap}_{Cl^-}$ and $P^{ba}_{K^+}$ are allowed to vary (Figure 6.9), there is a noticeable improvement in the ability to fit these traces, relative to the minimum errors achieved when only apical Na^+ and Cl^- permeabilities were estimated, or when estimating $P^{ap}_{Na^+}$, $P^{ap}_{Cl^-}$ and P_{pa}. However, there is a still a trend for those traces that are not adequately fit to have a large error if the amiloride insensitive V_t value is significantly hyperpolarised (see Figure 6.9(b)).

Another important observation from this exercise, is that the estimated parameter values may not be physiologically realistic, given only these three degrees of freedom. Figure 6.10 plots, (a), estimated $P^{ap}_{Na^+}$ against measured basal V_t values, (b), estimated $P^{ap}_{Cl^-}$ versus measured ΔV_t+0$[\mathrm{Cl}^-]_l$ and (c), estimated $P^{ba}_{K^+}$ versus amiloride insensitive V_t values. While the estimates of apical Na^+ and Cl^- permeability are not unreasonable (median values of 0.082 μm/s and 0.054 μm/s respectively), several of the $P^{ba}_{K^+}$ estimates made here are 3-4 orders of magnitude greater than the estimates made from *in vitro* data in Chapter 3 and 4. The median estimated basolateral K^+ permeability in this group of nasal PD recordings is 73.0 μm/s, where as in Chapter 3 the median CF estimate was 1.540 μm/s, and the median es-

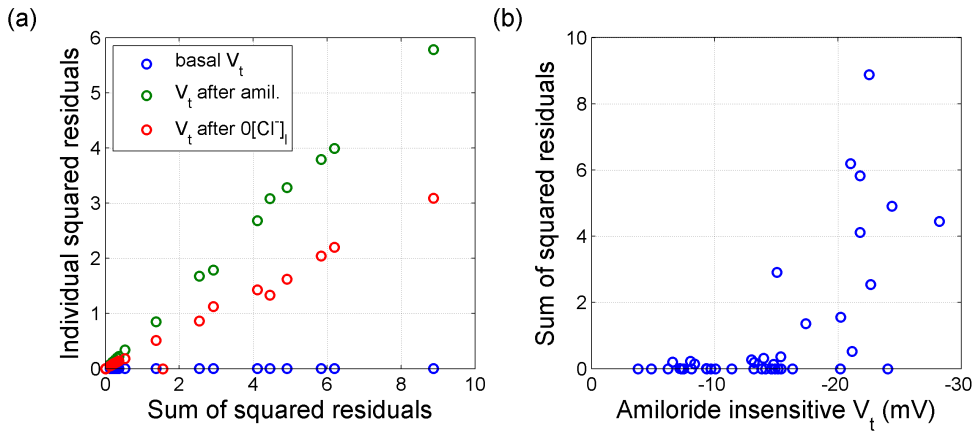

Figure 6.9: (a) Minimum objective function values found when varying $P^{ap}_{Na^+}$, $P^{ap}_{Cl^-}$ and $P^{ba}_{K^+}$ in order to fit model predictions to observed V_t values. Although many traces can be fit with little error, the largest component of the total error is still due to an inability to fit the level of V_t remaining after amiloride addition. (b) There is a trend for the minimum objective value found to correlate with to the amiloride sensitive V_t value.

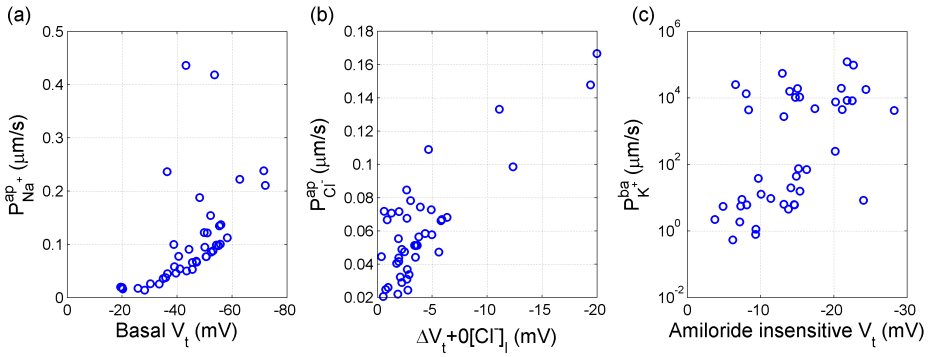

Figure 6.10: Summary of estimated values of (a) $P^{ap}_{Na^+}$, (b) $P^{ap}_{Cl^-}$ and (c) $P^{ba}_{K^+}$ made from nasal PD recordings made in CF patients. Estimated parameter values are plotted with V_t metrics baseline V_t, ΔV_t+0[Cl$^-$] and V_t after amiloride addition respectively. Note large values of estimated $P^{ba}_{K^+}$ are made from traces with large amiloride insensitive V_t values.

timate in Chapter 4 was $0.632\ \mu\mathrm{m/s}$. Hence, although the model fits the V_t trace with this level of basolateral potassium permeability, and the corresponding concentration and membrane potential kinetics are physiologically realistic in these nasal PD simulations, it remains to be seen if it would still be realistic in other scenarios where potassium transport is perturbed directly.

6.3.2.3 Estimates of $P^{ap}_{Na^+}$, $P^{ap}_{Cl^-}$ and fraction of $P^{ap}_{Na^+}$ blocked by amiloride

On minimising 6.1 as a function of $\left(P^{ap}_{Na^+}, P^{ap}_{Cl^-}, \eta\right)$ for each of the patient traces, I found contrary to the previous parameter estimation exercises, I could now fit the majority of the 42 traces very well - the median objective value in this case is $7\ \times 10^{-19}$. Figure 6.11 shows this, plotting the minimum objective function found in each case. This suggests that allowing for partial block rather than complete block of ENaC channels on amiloride addition, can account

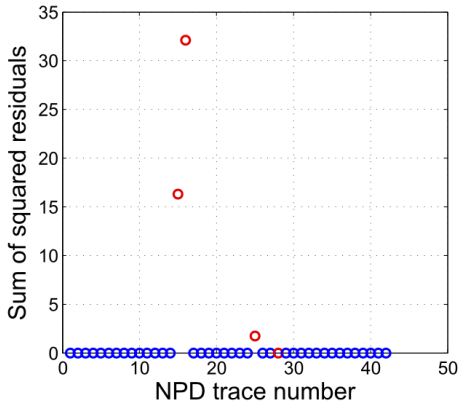

Figure 6.11: Minimum objective value function found when reproducing 42 individual nasal PD traces by varying $P^{ap}_{Na^+}$, $P^{ap}_{Cl^-}$ and η. Traces with $\Delta V_t{+}0[\mathrm{Cl}^-]_l < -10$ mV are highlighted in red.

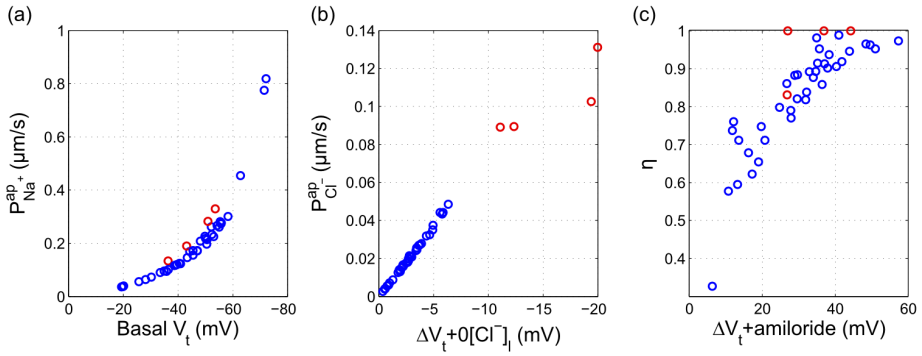

Figure 6.12: Parameter estimates found when fitting cohort of CF NPD traces by varying $P^{ap}_{Na^+}$, $P^{ap}_{Cl^-}$ and η only. (a) Estimated $P^{ap}_{Na^+}$ plotted as a function of measured basal V_t. (b) Estimated $P^{ap}_{Cl^-}$ plotted as a function of measured $\Delta V_t{+}0[\mathrm{Cl}^-]_l$ values. (c) Estimated partial block parameter η plotted against measured amiloride sensitive V_t values observed. Note data from the four traces exhibiting $\Delta V_t{+}0[\mathrm{Cl}^-]_l < -10$ mV have been highlighted in red.

for the wide range of nasal PD values measured in the clinical data set. The only traces that were not satisfactorily reproduced were those that exhibited unusual $\Delta V_t{+}0[\mathrm{Cl}^-]_\mathrm{l}$ values (< -10 mV), and they have been highlighted in red in Figure 6.11.

Figure 6.12 shows the relationships between the estimated values of the three transport parameters in question, $P^{ap}_{Na^+}$, $P^{ap}_{Cl^-}$ and η, and the measured nasal PD values, basal V_t, $\Delta V_t{+}0[\mathrm{Cl}^-]_\mathrm{l}$ and $\Delta V_t{+}\mathrm{amiloride}$. In panel (a) $P^{ap}_{Na^+}$ estimates are plotted against basal V_t values. Traces with a very hyperpolarised basal V_t (less than -70 mV), give rise to large estimates for apical Na^+ permeability here, on the order of 0.8 μm/s, which is an order of magnitude greater than the estimate made using the *in vitro* data set in Chapter 3 (0.07 μm/s).

Estimates of $P^{ap}_{Cl^-}$ are plotted against measurements of $\Delta V_t{+}0[\mathrm{Cl}^-]_\mathrm{l}$ in panel (b). There is a clear linear correlation between the two. This suggests that the change in V_t observed is primarily a result of the underlying CFTR activity, even if there is a significant non-zero ENaC current after amiloride addition. It also suggests if ENaC and CFTR are indeed the only two channels whose expression level varies significantly in the nasal epithelium of CF patients, then this low Cl^- solution exchange is a good indicator of that patient's underlying CFTR activity and could be used as a reliable indicator of changes in its residual function. It is worth noting as well, that the "outlier" traces (those with $\Delta V_t{+}0[\mathrm{Cl}^-]_\mathrm{l} < -10$ mV) are estimated to have much greater apical Cl^- permeability than the rest of the cohort, as one might intuitively have expected. Panel (c) of Figure 6.12 plots estimated values of η against amiloride sensitive V_t measurements, and there is a strong correlation between the two.

Although I have satisfactorily reproduced the range of measured nasal PD values in the majority of cases, by varying the apical permeability and fractional block parameters, it is not clear that the resulting parameter estimates I have found are physiologically realistic. In particular as just discussed, several values of ENaC permeability are estimated to be an order of magnitude greater than the values estimated to be present in CF HNE cells from *in vitro* Ussing Chamber experiments. It may be that as basal V_t is strongly influenced by $P^{ap}_{Na^+}$, that the extremely hyperpolarised traces can only be fit in this scenario with excessively large Na^+ permeabilities. If the model had further degrees of freedom, perhaps other parameters (say P_{pa}) could also account for some of the range of V_t values measured, and more reasonable levels of $P^{ap}_{Na^+}$ would be estimated. In the next section, I will go on to investigate this scenario, by estimating 4 transport parameters from individual patient nasal PD traces.

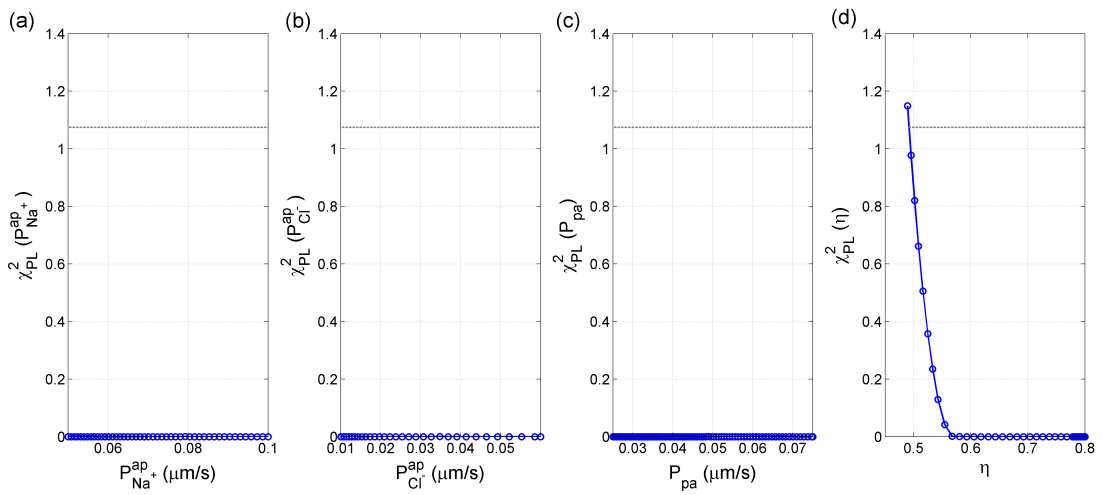

Figure 6.13: Estimates of 4 model parameters were made, given only the set of nasal PD metrics baseline V_t (-25.7 mV), ΔV_t+amiloride ($+10.8$ mV) and ΔV_t+0$[Cl^-]_l$ (-3.5 mV). The profile likelihoods for the following parameters were computed: (a) $P^{ap}_{Na^+}$, (b) $P^{ap}_{Cl^-}$, (c) P_{pa} and (d) η. Regions of parameter space where χ^2_{PL} (line with circles) is flat with no well defined minimum signify issues with parameter identifiability. The dashed line on each plot defines the threshold $\Delta\alpha$ in the profile likelihood required to give a 70% confidence limit for a given parameter.

6.3.3 Issues with parameter identifiability

The next question that arises is whether allowing the model system four degrees of freedom (i.e. estimating four parameters) - would allow me to reproduce the range of nasal PD measurements observed in the clinical data set, while also resulting in physiologically reasonable parameter estimates.

The trace I used for this illustrative example, consists of basal $V_t = -25.71$ mV, V_t after amiloride addition $= -14.88$ mV and V_t after perfusion of a Cl^- free solution, $= -18.36$ mV. The global minimum objective function I find is $\chi^2 = 1.6 \times 10^{-20}$, given by the parameter vector, $\hat{\theta} = \{P^{ap}_{Na^+}, P^{ap}_{Cl^-}, P_{pa}, \eta\} = 0.0793\ \mu$m/s$, 0.0348\ \mu$m/s$, 0.0489\ \mu$m/s$, 0.5803$.

Figure 6.13(a) plots the resulting profile likelihood I found for $P^{ap}_{Na^+}$, calculated around its initial estimated value. The threshold Δ_α that the profile likelihood needs to breach in order to determine confidence intervals for a 70% probability of finding the true value of $P^{ap}_{Na^+}$ is given by $\Delta_\alpha = \left(\chi^2(0.7, 1) - \chi^2(\hat{\theta})\right) = 1.0742$ (since minimum of χ^2_{PL} is 0 in this case). However, the profile likelihood for $P^{ap}_{Na^+}$ is flat over the range of values searched here, $0.05\ \mu$m/s$ < P^{ap}_{Na^+} < 0.1\ \mu$m/s, suggesting the value of this parameter is not identifiable within this region of parameter space. Figure (b) and (c) similarly show the χ^2_{PL} trajectorys determined for $P^{ap}_{Cl^-}$ and P_{pa} respectively, and in both cases the parameters are unidentifiable in

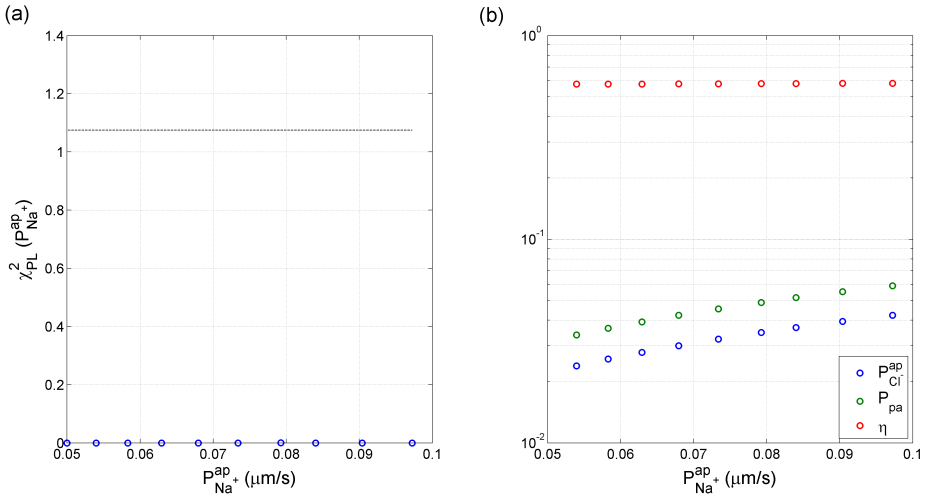

Figure 6.14: Panel (a) plots several particular values of $P^{ap}_{Na^+}$ (taken from 6.13(a)) that lie in the region of parameter space where the computed profile likelihood for this parameter is flat. Panel (b) then plots the parameters $P^{ap}_{Cl^-}$, P_{pa}, η as a function of $P^{ap}_{Na^+}$, along the manifold that keeps $\chi^2_{PL} = 0$. This is a picture of a discrete family of distinct parameter sets, that will give degenerate nasal PD traces.

the regions of parameter space searched. Figure (d) shows the profile likelihood determined for η in this case. χ^2_{PL} is flat for $\eta \geq 0.58$ again highlighting an issue with identifiability in this region of parameter space, however it increases for $\eta < 0.58$ and breaches the threshold for a 70% confidence interval at $\eta = 0.49$.

The next step I followed, was to take the parameter sets which gave rise to the flat profile likelihood for $P^{ap}_{Na^+}$, and then plotted the model solutions predicted by these sets of parameter values. Figure 6.14(a) shows the values of $P^{ap}_{Na^+}$ for which $\chi^2_{PL} = 0$, and panel (b) shows the corresponding values that $P^{ap}_{Cl^-}$, P_{pa} and η must take in order for χ^2_{PL} to remain 0 while the value of $P^{ap}_{Na^+}$ increases.

Figure 6.15 then shows the traces of cellular variable values produced along this particular manifold of parameter space. Here the solutions are colour coded from white to black, as $P^{ap}_{Na^+}$ increases in value in the range $0.05 \rightarrow 0.1$ μm/s. The first thing to notice is in panel (d), which displays the predicted V_t traces, as well as the measured values of V_t used in the parameter estimation and profile likelihood calculations (highlighted in red). Here we see visually the effect of the degeneracy, despite the different parameter sets used for each simulation, they all predict the same V_t values, at the time points measurements are made at. Hence if we only use these V_t measurements these solutions become indistinguishable and we cannot uniquely identify values for the parameters of interest.

In the other panels (a), (b), (c), (e) and (f), the predicted membrane potential traces and internal concentrations do differ significantly. It hence may be possible to uniquely identify values for $P^{ap}_{Na^+}$, $P^{ap}_{Cl^-}$, P_{pa} and η if measurements of the other cellular variables were available. However, in the absence of additional measurements, we can make the assumption that the internal ion concentrations *in vivo* are similar to those measured *in vitro*, and investigate what parameter estimates this leads to.

6.3.3.1 Knowledge of internal $[\mathrm{Na}^+]$ and $[\mathrm{Cl}^-]$ alters identifiability of parameters

In order to investigate how knowing the internal concentrations would change the ability to estimate parameter values, I repeated the preceding parameter estimation exercise. However, I now included the intracellular Na^+ and Cl^- concentrations in the objective function as follows

$$\underset{P^{ap}_{Na^+},P^{ap}_{Cl^-},P_{pa},\eta}{\text{minimize}} \quad \sum_{k=1}^{3}\left(\hat{V}_t(t_k)-V_t(t_k)\right)^2+\left(\frac{[\hat{\mathrm{Na}^+}]_\mathrm{i}(t_0)-[\mathrm{Na}^+]_\mathrm{i}(t_0)}{\hat{\sigma}_{[\mathrm{Na}^+]_\mathrm{i}}(t_0)}\right)^2+\ldots \left(\frac{[\hat{\mathrm{Cl}^-}]_\mathrm{i}(t_0)-[\mathrm{Cl}^-]_\mathrm{i}(t_0)}{\hat{\sigma}_{[\mathrm{Cl}^-]_\mathrm{i}}(t_0)}\right)^2 \tag{6.2}$$

$$\text{subject to } \; 0\leq\eta\leq 1$$

Only the initial, steady state values of $[\mathrm{Na}^+]_\mathrm{i}$ and $[\mathrm{Cl}^-]_\mathrm{i}$ were included in the objective function. The values used were those measured in CF HNE cells *in vitro*; $[\hat{\mathrm{Na}^+}]_\mathrm{i}(t_0)=25.9\pm3.5\ \mathrm{mM}$ and $[\hat{\mathrm{Cl}^-}]_\mathrm{i}(t_0)=67.7\pm5.6\ \mathrm{mM}$, which had previously been introduced in Chapter 3 (see Table 3.3).

The global minimum objective function value found (again using the *lsqnonlin* function) is now $\chi^2(\hat{\theta})=1.852$, given by the parameter vector $\hat{\theta}=\{P^{ap}_{Na^+},P^{ap}_{Cl^-},P_{pa},\eta\}=\{0.0910\ \mu\mathrm{m/s},0.0398\ \mu\mathrm{m/s},0.0556\ \mu\mathrm{m/s},0.582\}$. The combination of the three V_t measurements and initial Na^+ and Cl^- concentrations can no longer be reproduced perfectly by the model system. To assess if the issue with identifiability was also resolved, I again computed the profile likelihood for each of the four parameters being estimated, starting at the point in parameter space which minimised the objective function in 6.2.

The new profile likelihood trajectories are shown in Figure 6.16 for (a) $P^{ap}_{Na^+}$, (b) $P^{ap}_{Cl^-}$, (c) P_{pa} and (d) η, and these can be compared with those which were calculated previously in Figure 6.13. In each case χ^2_{PL} is now convex, and we can determine unique estimates for these four parameters. The threshold for a 70% probability of finding the true value of one of these

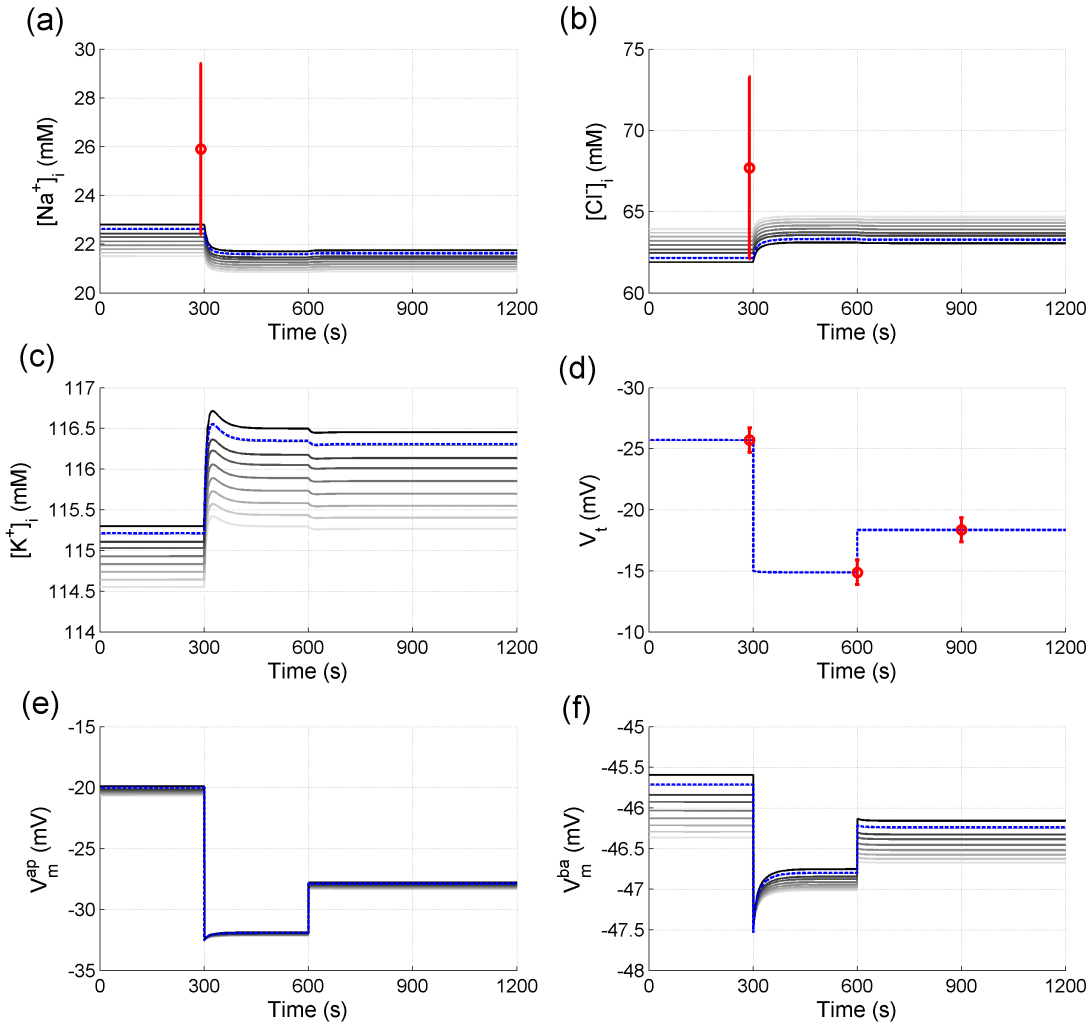

Figure 6.15: The parameter sets shown in Figure 6.14(b) were used to simulate several CF nasal PD traces (+amiloride and $+0[Cl^-]_l$ stages). Panels (a)-(c) show internal ion concentrations $[Na^+]_i$, $[Cl^-]_i$ and $[K^+]_i$ respectively, and (d)-(f) plot the electrical state of the cell, V_t, V_m^{ap} and V_m^{ba}. V_t data used for parameter estimation is shown in red in panel (d), and the traces coloured from white to black (in order of increasing $P_{Na^+}^{ap}$) highlight the degenerate solutions which all produce the same V_t metrics. The dashed blue traces show the unique "best-fit" solution found, if initial Na^+ and Cl^- concentrations are used in the objective function (values used are plotted in red in panels (a) and (b) respectively).

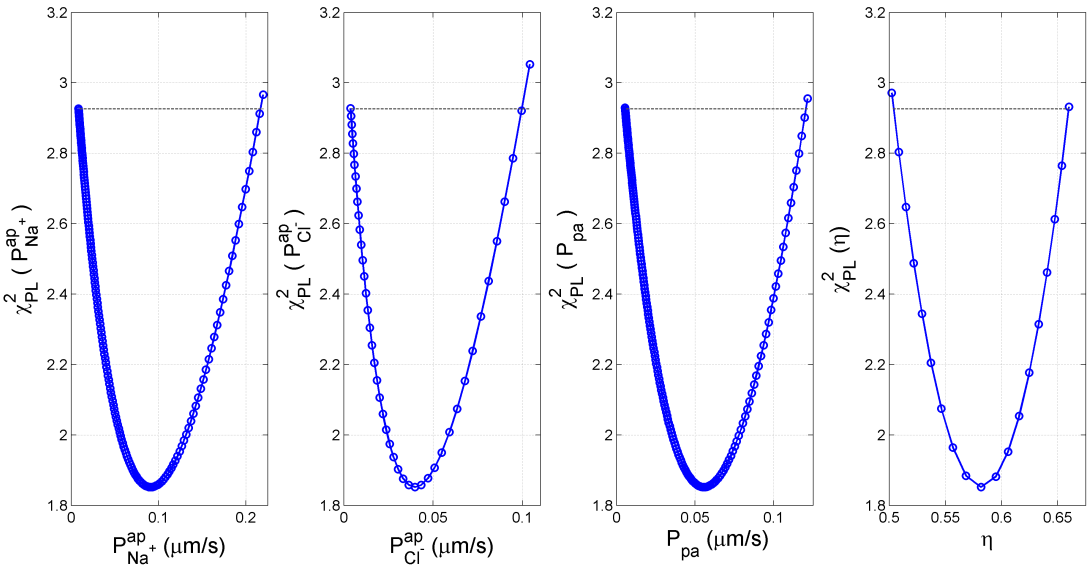

Figure 6.16: Estimates of $P^{ap}_{Na^+}$, $P^{ap}_{Cl^-}$, P_{pa}, and η were made given nasal PD metrics baseline V_t (-25.7 mV), ΔV_t+amiloride ($+10.8$ mV) and ΔV_t+0[Cl$^-$]$_l$ (-3.5 mV), and assuming known initial conditions $[\mathrm{Na}^+]_\mathrm{i} = 25.9 \pm 3.5$ mM and $[\mathrm{Cl}^-]_\mathrm{i} = 67.7 \pm 5.6$ mM. The profile likelihood was then computed for each of the four parameters around the respective values that minimised $\chi^2(\theta)$. Compared with those seen in Figure 6.13, the χ^2_{PL} trajectories are now convex and I can make a unique estimate for each parameter of interest.

parameters is now $\chi^2_{PL} = 1.85 + 1.07 = 2.92$ (since $\chi^2(0.7, 1) = 1.0742$), for example we would conclude that there is a 70% chance of finding the true value of $P^{ap}_{Na^+}$ within the range of values $[0.009, 0.216]$ μm/s (a range of $-90\% \rightarrow +137\%$ of the estimated true value). This highlights the fact that having additional information on the intracellular concentrations during nasal PD recordings, even just the initial steady state conditions, can greatly improve our ability to constrain membrane transport parameters.

6.3.4 Estimates of $P^{ap}_{Na^+}$, $P^{ap}_{Cl^-}$, P_{pa} and η in CF nasal PD traces

For the final stage of my analysis of the nasal PD records from the Royal Brompton data set, I estimated values for $P^{ap}_{Na^+}$, $P^{ap}_{Cl^-}$, P_{pa}, and η from each patient's nasal PD trace, using the method outlined in the previous section. Each patient has a set of three V_t metrics, and I assume the initial intracellular $[\mathrm{Na}^+]$ and $[\mathrm{Cl}^-]$ are also known, and are the same for each patient. This then allows me to determine a cohort of estimated parameter values, representing each patient's airway epithelial transport physiology. I also had the FEV_1 values for each patient, which is a measure of their disease severity. By investigating the relationship between estimated permeability parameters and FEV_1 values I intended to see if there would be any suggestion of an association between the disease severity and the apparent underlying ion channel activity.

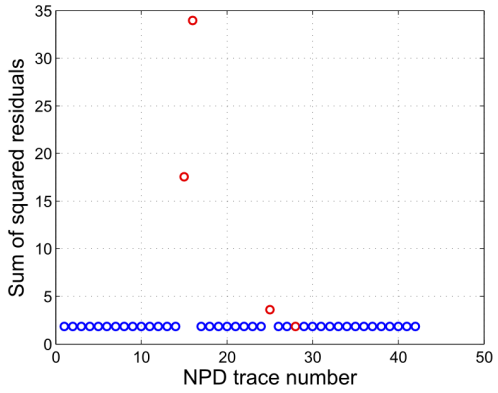

Figure 6.17: Estimates of $P^{ap}_{Na^+}$, $P^{ap}_{Cl^-}$, P_{pa} and η were made from 42 individual nasal PD traces (assuming initial $[\mathrm{Na}^+]_i$ and $[\mathrm{Cl}^-]_i$ are the same in each patient). The minimum value of $\chi^2(\theta)$ found in each case is plotted here. The median value is 1.85, but several traces have values of $\chi^2(\theta)$ significantly greater than this, indicating they have not been fit satisfactorily. These outliers correspond to those traces with $\Delta V_t{+}0[\mathrm{Cl}^-]_\mathrm{l} < -10\mathrm{mV}$ (highlighted in red)

.

Figure 6.17 shows the minimum objective function values found across the cohort of nasal PD traces. Again, the majority of traces are fit reasonably well, apart from a number of traces with $\Delta V_t{+}0[\mathrm{Cl}^-]_\mathrm{l} < -10$ mV which are highlighted in red.

Figure 6.18 shows the estimated parameter values found from the group of 42 nasal PD traces. Panel (a) plots the relationship between basal V_t measurements and estimated $P^{ap}_{Na^+}$ values. As before there is a strong non-linear correlation between the two quantities, however now the range of values estimated is more reasonable. Very hyperpolarised traces of around -70 mV give rise to $P^{ap}_{Na^+} \approx 0.4$ μm/s. Noticeably, the two traces with $\Delta V_t{+}0[\mathrm{Cl}^-]_\mathrm{l} \approx -20$ mV are poorly reproduced, and the corresponding estimates of $P^{ap}_{Na^+}$ do not follow the general trend.

Panel (b) highlights the relationship between estimated $P^{ap}_{Cl^-}$ and measured $\Delta V_t{+}0[\mathrm{Cl}^-]_\mathrm{l}$, and, as seen in previous exercises there is an approximately linear relationship between the two. Panel (c) plots estimated P_{pa} against basal V_t and there is a non-linear relationship between these two quantities. Traces which have been poorly fit give rise to estimates of P_{pa} that do not follow the trend observed with the rest of the population, as was the case with estimates of $P^{ap}_{Na^+}$ from these particular traces. Finally, panel (d) shows estimated fraction of ENaC channels blocked on addition of amiloride, η, plotted against measured $\Delta V_t{+}\mathrm{amil.}$. There is a positive correlation seen in this plot - those traces with a large amiloride sensitive V_t tend to be best fit with values of η near to 1 (close to complete block of $P^{ap}_{Na^+}$).

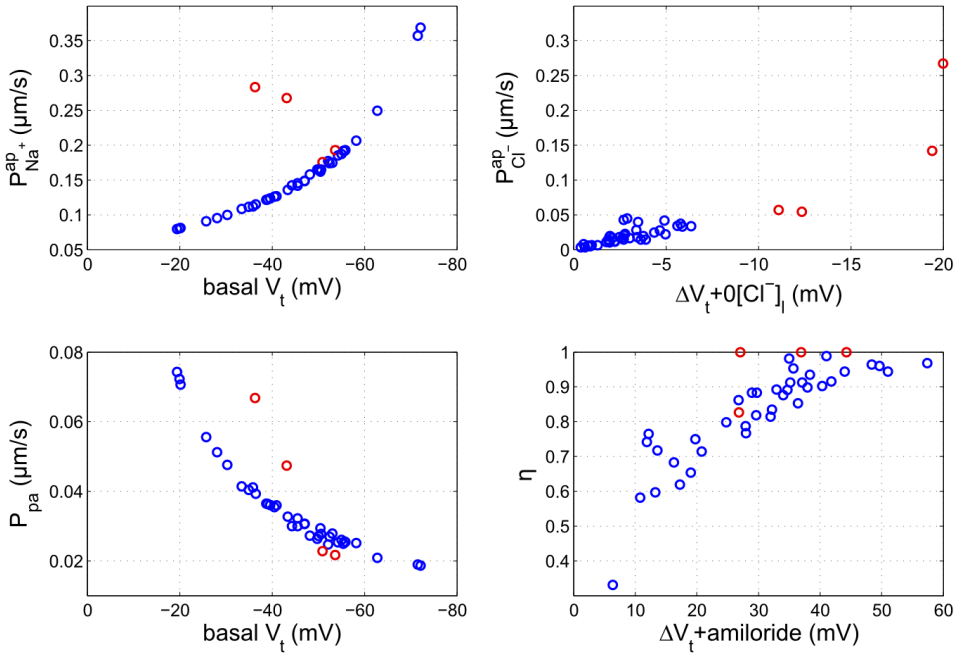

Figure 6.18: Estimates of $P^{ap}_{Na^+}$, $P^{ap}_{Cl^-}$, P_{pa} and η were made from each nasal PD trace in the CF patient cohort (assuming initial $[\mathrm{Na}^+]_i$ and $[\mathrm{Cl}^-]_i$ are the same in each patient). The resulting distributions of parameter values are shown. (a) $P^{ap}_{Na^+}$ and (c)P_{pa} have non-linear relationships with baseline V_t. (c)$P^{ap}_{Cl^-}$ is linearly correlated with $\Delta V_t{+}0[\mathrm{Cl}^-]_\mathrm{l}$. (d) The estimated value of η is largely determined by its relationship with $\Delta V_t{+}\mathrm{amiloride}$. Note data from the four traces exhibiting $\Delta V_t{+}0[\mathrm{Cl}^-]_\mathrm{l} < -10$ mV have been highlighted in red.

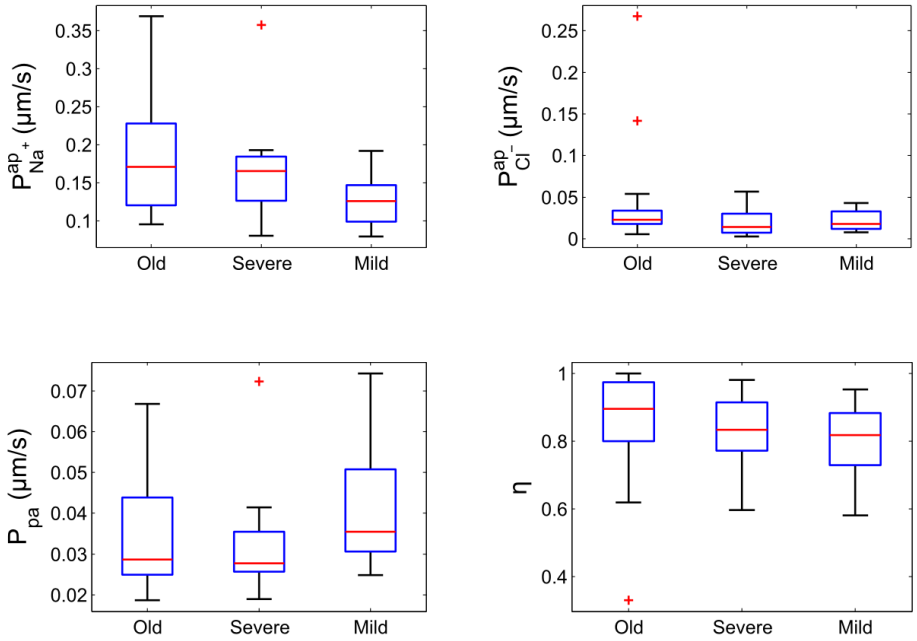

Figure 6.19: Parameters (a) $P^{ap}_{Na^+}$, (b) $P^{ap}_{Cl^-}$, (c) P_{pa}, and (d) η were estimated using nasal PD measurements taken from a cohort of CF patients. Patients were categorised as Old, Young/Severe or Young/Mild based on their age and lung function, and parameter estimates in each category are compared here. Each boxplot highlights the median (central line), lower quartile q_1 and upper quartile q_3 (lower / upper bounds of box). Whiskers on the boxplot highlight the range $[q_1 - 1.5\ IQR, q_3 + 1.5\ IQR]$ and red crosses indicate outliers which lie outside this range.

However, despite the difficulty in reproducing a couple of outliers, the majority of the 42 traces can be explained relatively well by variations in these 4 model parameters, and the corresponding estimated values of these parameters are physiologically realistic.

6.3.5 Correlations between FEV_1 data and nasal PD metrics

Given that I felt that these parameter estimates were physiologically realistic, I wanted to see if there were any clear relationships between them and the measured FEV_1 values associated with each trace. As when comparing measured V_t values to FEV_1 values earlier in this chapter, I performed the analysis in two separate parts. First, I divided parameter estimates into groups based on patient severity (itself determined by FEV_1 value), and compared the median estimated value in the Old, Young/Severe, and Young/Mild groups. Secondly, treating FEV_1 as a continuous variable this time, I determined if there were any statistically significant correlations between the FEV_1 values and estimated parameter values, across the cohort of 42 nasal PD traces.

Metric		Patient group All n=42	Old n=16	Young/Severe n=15	Young/Mild n=11	p-value
$P^{ap}_{Na^+}$	median	0.153	0.171	0.165	0.126	0.060
	IQR	0.066	0.107	0.058	0.048	
$P^{ap}_{Cl^-}$	median	0.018	0.023	0.014	0.018	0.147
	IQR	0.022	0.016	0.023	0.021	
P_{pa}	median	0.030	0.029	0.028	0.036	0.186
	IQR	0.015	0.019	0.010	0.020	
η	median	0.879	0.895	0.835	0.819	0.294
	IQR	0.179	0.173	0.143	0.154	

Table 6.2: Transport parameter values in a cohort of CF patients, estimated from individual nasal PD traces. Note permeablity values are given in units of $\mu\mathrm{m/s}$. The median and interquartile range (IQR) are given for the distribution of parameter values in each patient group. A breakdown of statistics by patient category is also given. The differences in transport parameter values estimated in the Old, Young/Mild and Young/Severe groups were tested for significance using the Kruskal-Wallis test, however none of the differences were signficant at the $p < 0.05$ level.

Figure 6.19 shows boxplots of the distributions of estimated parameter values, classified by patient type as Old, Young/Severe or Young/Mild. Panel (a) shows estimated $P^{ap}_{Na^+}$ distributions, panel (b) shows the equivalent $P^{ap}_{Cl^-}$ boxplots, (c) gives the same for P_{pa} and finally (d) shows the estimated η distributions. Table 6.2 summarises the median and interquartile ranges of each distribution, for each category as well as the for the entire group. The Kruskal-Wallis test was used to assess the significance of differences in median NPD metric values between the three patient groups, and the p-values found are also listed in this table. There were no significant ($p < 0.05$) differences in estimated transport parameter values across patient groups.

Finally, Figure 6.20 plots the FEV_1 values versus the estimated parameter values. Each panel also gives the Spearman correlation coefficient between the two quantities along with the statistical significance of that correlation. From panel (a) we can see that there is strong correlation between apical Na^+ permeability and FEV_1 values, which has a significance level $p = 0.001$. Here the higher the value of $P^{ap}_{Na^+}$ the poorer the level of lung function. None of the other transport parameter - FEV_1 correlations are statistically significant at the $p = 0.05$ level.

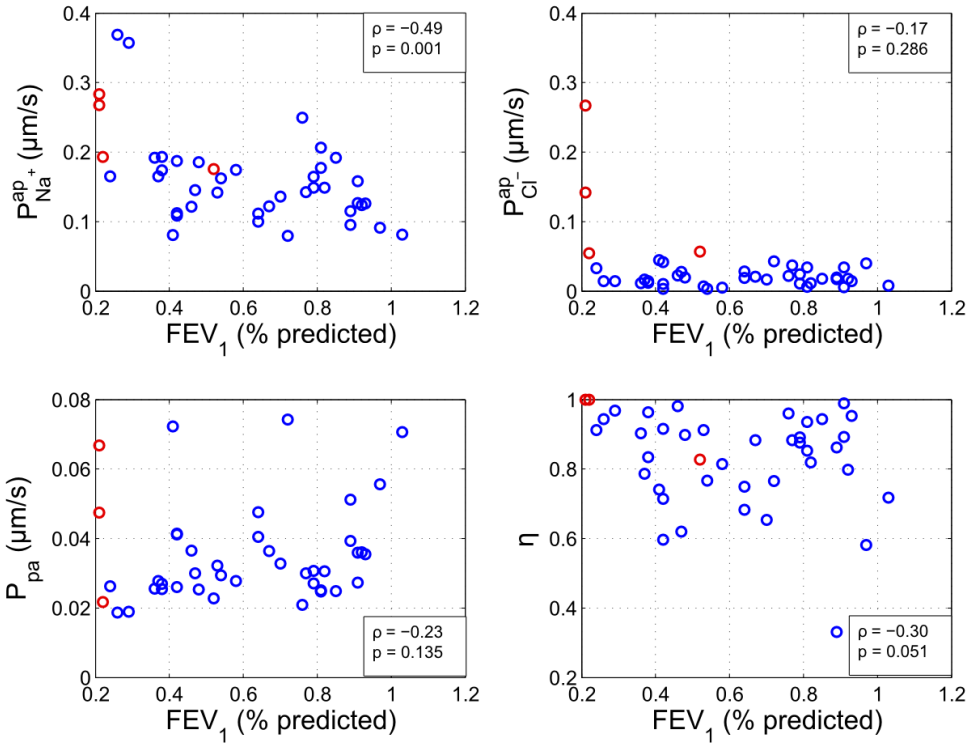

Figure 6.20: Parameters (a) P^{ap}_{Na+}, (b) P^{ap}_{Cl-}, (c) P_{pa}, and (d) η were estimated using nasal PD measurements taken from a cohort of CF patients. These estimates are plotted relative to their expected lung function here, given by the $FEV_1(\%\text{predicted})$ scores. Correlations between parameter estimates and FEV_1 scores are plotted on each panel (ρ) along with the associated statistical significance (p). The correlation between P^{ap}_{Na+} estimates and FEV_1 values is deemed to be statistically significant, suggesting an association between increased apical Na^+ permeability and reduced lung function. Note estimates made from outlier traces with $\Delta V_t{+}0[\mathrm{Cl}^-]_\mathrm{l} < -10$ mV are highlighted in red.

6.4 Discussion

6.4.1 Insights from analysis of raw nasal PD data

Before beginning modelling and parameter estimation work, I analysed a set of nasal PD traces from CF patients. The cohort displays the expected characteristics of CF nasal PD metrics; hyperpolarised baseline V_t, large amiloride sensitive V_t, and little evidence of Cl^- secretion (i.e. low $\Delta V_t{+}0[\mathrm{Cl}^-]_\mathrm{l}$ values). Simmonds et al. also commented on a number of patients with unusually large values of $\Delta V_t{+}0[\mathrm{Cl}^-]_\mathrm{l} < -10\ \mathrm{mV}$, values more in line with those expected in non-CF patients.

As well as these general insights, I made a number of specific observations regarding the subset of 42 nasal PD traces that I selected for further analysis;

- Baseline V_t and amiloride sensitive V_t exhibit a strong linear relationship, with a Spearman correlation coefficient $\rho = -0.8352$.

- Several traces exhibit large amiloride *insensitive* V_t, 28% having V_t after amiloride addition $\leq -20\ \mathrm{mV}$.

- No trace exhibited depolarisation on removal of lumen Cl^-, i.e. $\Delta V_t{+}0[\mathrm{Cl}^-]_\mathrm{l} < 0\ \mathrm{mV}$ in all instances.

The forced expiratory volume in one second (FEV_1) was measured for each CF patient whose nasal PD was recorded. This metric could then be used as a measure of lung function for the patient, and was compared with the measured V_t metrics. Patients were also categorised into three different groups, Old, Young/Mild and Young/Severe, based on their age, and their relative FEV_1 score. The observations I made at this point were as follows:

- The differences in median basal V_t, $\Delta V_t{+}\mathrm{amiloride}$ and $\Delta V_t{+}0[\mathrm{Cl}^-]_\mathrm{l}$, between any two of the three patient groups, were not statistically significant as determined by the Kruskal-Wallis test.

- Basal V_t and FEV_1 are correlated (Spearman correlation coefficient of $\rho = 0.37$), but there is no significant correlation between FEV_1 and $\Delta V_t{+}\mathrm{amiloride}$ or $\Delta V_t{+}0[\mathrm{Cl}^-]_\mathrm{l}$ (assuming outlier traces are excluded).

6.4.2 CFTR and ENaC activity cannot explain all variability in nasal PD data

After performing the various sensitivity analysis exercises in Chapter 5, I went on to estimate values of $P^{ap}_{Na^+}$ and $P^{ap}_{Cl^-}$, from each of the 42 patient nasal PD traces. Here I assumed all other parameters were fixed at previously estimated CF values. Following on from this initial parameter estimation exercise, I made several further analyses estimating the value of three transport parameters at a time. I made the following observations:

- Nasal PD traces with large amiloride *insensitive* V_t are poorly fit when only $P^{ap}_{Na^+}$ and $P^{ap}_{Cl^-}$ vary from patient to patient. Hence changes in ENaC and CFTR activity alone could not adequately explain the full variation of nasal PD measurements observed in this cohort of CF patients.

- The "goodness-of-fit" is inversely related to the magnitude of this amiloride insensitive V_t. This follows intuitively from one of my earlier observations, where I saw that assuming 100% block of ENaC current would prevent large variation in the new resting V_t value after amiloride addition, with only slightly hyperpolarized ($> -10\ \mathrm{mV}$) amiloride-insensitive V_t values possible.

- Allowing for variation in one of $P^{ba}_{K^+}$ or P_{pa}, can account for part, but not all of large variation in amiloride insensitive V_t. However, there are questions over how physiologically realistic the resulting estimates of these extra transport parameters are.

- Allowing variation in the fraction of $P^{ap}_{Na^+}$ that is blocked on amiloride addition, η, as well as apical Na^+ and Cl^- permeability, I found that I could explain the observed range of values of amiloride insensitive V_t. However, the resulting estimates of $P^{ap}_{Na^+}$ are quite large (an order of magnitude greater than *in vivo* estimates in some cases) and it is not certain that they are physiologically realistic.

- A small number of nasal PD traces with $\Delta V_t + 0[\mathrm{Cl}^-]_\mathrm{l} < -10\ \mathrm{mV}$ remain poorly fit even when allowing $P^{ap}_{Na^+}$, $P^{ap}_{Cl^-}$ and η to vary. The estimates for apical Cl^- permeability found from these traces are significantly larger than those of the rest of the patient group, reinforcing the suggestion that these patients have normal levels of Cl^- channel activity. The poor fit found by my model in this case, may suggest these patients are closer to a non-CF phenotype and would be better fit by assuming fixed parameters were set at the non-CF levels rather than CF levels as they had been in this study.

6.4.3 Number of transport parameters identifiable from nasal PD is limited

I had found evidence to suggest that variation in three transport parameters did not satisfactorily explain the range of observed V_t values in the CF patient data set. I went on to investigate whether allowing variation in 4 transport parameters could improve this situation, and in doing so addressed the question of whether transport parameter values could be uniquely determined, given the limited number of V_t observations I was using in each estimation. I came to the following conclusions:

- Assuming only baseline V_t, ΔV_t+amiloride and ΔV_t+0$[\mathrm{Cl}^-]_\mathrm{l}$ are used for estimation, it is in general not possible to uniquely identify four transport parameter values. In the case of estimating $P^{ap}_{Na^+}$, $P^{ap}_{Cl^-}$, P_{pa}, and η, I saw that there was a family of solutions which would all produce the same values for these three nasal PD measures.

- Sets of parameter values that produced degenerate nasal PD traces made different predictions for internal ion concentrations, and also different predictions for apical and basolateral membrane potentials, during these simulations.

- It is possible to distinguish between degenerate solutions, if we assume knowledge about the internal state of the cell to begin with. I found that by assuming internal $[\mathrm{Na}^+]$ and $[\mathrm{Cl}^-]$ were known at steady state, and these values are included in the objective function used for parameter estimation, then I could uniquely identify values for $P^{ap}_{Na^+}$, $P^{ap}_{Cl^-}$, P_{pa} and η from an individual nasal PD trace.

6.4.4 Are estimated permeabilities more informative than V_t metrics?

The final analysis I performed, was to estimate $P^{ap}_{Na^+}$, $P^{ap}_{Cl^-}$, P_{pa} and η for each of the 42 CF patient nasal PD traces (assuming initial $[\mathrm{Na}^+]_\mathrm{i}$ and $[\mathrm{Cl}^-]_\mathrm{i}$ were known). I then looked at the relationships between the resulting distribution of parameter estimates, the measured V_t metrics, and the measures of lung function (individual FEV_1 values). I made the following observations:

- $P^{ap}_{Na^+}$ and P_{pa} are largely determined by the baseline V_t value, $P^{ap}_{Cl^-}$ is correlated to ΔV_t+0$[\mathrm{Cl}^-]_\mathrm{l}$, despite variations in three other transport parameters, and estimated η is correlated with the measured ΔV_t+amiloride.

- There is no statistically significant difference between the estimated median value of either $P^{ap}_{Na^+}$, $P^{ap}_{Cl^-}$, P_{pa} or η across the Old, Young/Severe and Young/Mild groups.

- There is a statistically significant correlation between FEV_1 values and estimated $P^{ap}_{Na^+}$ values (Spearman correlation coefficient $\rho = -0.49$). Increased apical Na^+ permeability is correlated with reduced lung function.

The observations here regarding relationships between FEV_1 values and apical Na^+ permeability are perhaps not too surprising. Simmonds et al. noted (as we did, see 6.4(d)) that baseline V_t was correlated to FEV_1 values, and I have seen that the estimated values of $P^{ap}_{Na^+}$ are determined largely by the baseline V_t value. Hence one would intuitively expect there would be a similar correlation between the FEV_1 values and these $P^{ap}_{Na^+}$ estimates.

This should not detract from the potential utility of this combined biophysical modelling and parameter estimation approach. I have shown that it is possible to make quantitative estimates of apical Na^+ and Cl^- permeabilities for an individual patient, as well as other important transport parameters, given only their nasal PD trace. In clinical trials assessing the effect of drug or gene therapy on epithelial ion transport in cystic fibrosis *in vivo*, this could be used as an analysis technique to complement existing methods, potentially giving a deeper insight into the biophysicsal mechanisms underlying any apparent improvements in disease severity.

Chapter 7

Conclusion

At the beginning of this thesis I set out a list of objectives that I hoped to achieve through my research activity. In this chapter I will summarise my work towards meeting these objectives, with particular emphasis on the material outlined in Chapters 3 - 6 which constitutes original research contributions. I will end by discussing some potential avenues for future research work of this nature.

7.1 Contributions

7.1.1 Physiologically realistic model of ion transport in human nasal epithelia

My initial research goal was to develop a mathematical model of electrolyte transport in human airway epithelial cells. This model would need to be capable of relating the biophysical state of the cell, in terms of membrane potentials and intracellular ion concentrations, to the transport physiology underlying these properties, characterised by the expression levels and activity of different membrane proteins.

In Chapter 2 I outlined the development of the mathematical model, and validated its basic behaviours. Given a set of initial estimates for the major ion transport parameters (Table 2.2), my model reproduced several of the electrophysiological features of a human airway epithelial cell under open circuit conditions. This included amongst others: low intracellular $[\mathrm{Na}^+]$ and high intracellular $[\mathrm{K}^+]$, a lumen negative transepithelial potential difference, and a large driving force for Na^+ absorption across the apical membrane (see Table 2.3).

This aspect of my work was not in itself novel. My mathematical model is motivated by the general framework of Latta et al. (1984), and shares similarities with several previous models of epithelial transport published by Hartmann and Verkman (1990), Duszyk and French (1991), Horisberger (2003), and Garcia et al. (2013).

7.1.2 Ability to simulate common Ussing chamber experiments

In Section 3.2.1, I described how one could use this mathematical modelling framework to simulate Ussing chamber experiments. I outlined how one could model the effect of introducing a transport inhibitor to the bath solution, or how an ion replacement experiment could be performed, by making appropriate changes to the model parameter values.

In particular, I simulated the effect of amiloride being added to the lumen solution, by setting the apical Na^+ permeability parameter, $P^{ap}_{Na^+}$, to zero (Section 3.2.2). I saw that given the initial reference parameters, my model produced the expected depolarisation of V_t on blocking ENaC channels, as well as a decrease in the internal Na^+ concentration. I also simulated replacing Cl^- ions in the lumen compartment with $\mathrm{gluconate}^-$ ions (Section 3.2.3). On performing this ion replacement simulation, with the same reference parameter values, my model produced a hyperpolarisation of V_t as would be expected for a human airway epithelial cell with a significant apical Cl^- permeability.

These simulations demonstrated that, one, the modelling framework could be used to successfully implement simulations of Ussing chamber experiments common in the study of epithelial transport, such as amiloride addition or removal of lumen Cl^-, and two, that my mathematical model made physiologically realistic predictions for the transient behaviour of transepithelial potential difference in these scenarios.

7.1.3 Ability to estimate transport parameters from electrophysiological data

In Chapter 3 I showed that it was possible to estimate transport parameter values from *in vitro* electrophysiological measurements made on HNE cells. I simulated $+\mathrm{amiloride}$ and $+0[\mathrm{Cl}^-]_\mathrm{l}$ interventions with my mathematical model, and by varying the parameters $P^{ap}_{Na^+}$, $P^{ap}_{Cl^-}$, $P^{ba}_{K^+}$, $P^{ba}_{Cl^-}$, ρ_{NaK} and ρ_{NKCC}, I could accurately reproduce the time evolution of cellular variables $[\mathrm{Na}^+]_\mathrm{i}$, $[\mathrm{Cl}^-]_\mathrm{i}$, V^{ap}_m and V_t during these experiments. Employing an algorithm in order to systematically minimise the discrepancy between model predictions and observed cellular properties, I was able to estimate values for each of the 6 parameters listed, as well as determining confidence intervals for these estimates.

A similar approach was recently taken by Garcia et al. (2013), and although there are differences in the details of how they implement the parameter estimation, the general premise is the same. They showed that by simulating a number of different Ussing Chamber experiments it was possible to constrain significant numbers of major ion transport parameters. The values they

estimate for $P^{ap}_{Na^+}$ and $P^{ap}_{Cl^-}$ in non-CF HNE cells ($0.017\ \mu\mathrm{m/s}$ and $0.043\ \mu\mathrm{m/s}$ respectively), are remarkably similar to the values I arrived at, $P^{ap}_{Na^+} = 0.024 \pm 0.004\ \mu\mathrm{m/s}$ and $P^{ap}_{Cl^-} = 0.066\ \pm 0.017\ \mu\mathrm{m/s}$. The fact that this approach to parameter estimation has been carried out independently in a similar study, gives us further confidence in its validity.

7.1.4 Quantified activity of transport proteins in CF and non-CF HNE cells

The most significant original contribution I made in the course of my PhD research, was to determine quantitatively the value of key transport parameters, apical Na^+ and Cl^- permeability, not only in non-CF but also in CF HNE cells. This allowed me to ascertain if in cystic fibrosis disease there were significant differences in the activity of CFTR and ENaC channels, relative to the their basal activity in non-CF epithelia.

In Chapter 3 I showed that the estimates of $P^{ap}_{Na^+}$ in CF HNE cells were higher than in non-CF HNE cells, that the estimates of $P^{ap}_{Cl^-}$ were lower in CF cells, and that these differences were statistically significant. In Chapter 4 I found that my estimate of the relative non-CF / CF differences in these parameter values remained unchanged, even when allowing for large cell to cell variation in biophysical properties used to estimate their values. In other words the results of my analysis did not depend on the assumption of mean behaviour of HNE cells.

To my knowledge no other study has performed this analysis and given this insight. In determining that apical Na^+ permeability must be increased in the CF HNE cells, in order to explain the hyperpolarised basal V_t and increased amiloride sensitive V_t, I had ruled out the possibility these phenomena, of the observed magnitude, could arise as a result of electrical coupling of CFTR and ENaC currents. That is, there is no evidence that loss of apical Cl^- conductance alone could explain these bioelectric properties, suggesting this line of reasoning should not be pursued any further.

7.1.5 Quantified influence of transport parameters on epithelial properties

In Chapter 4, I investigated the relationships between parameters of ion transport, such as membrane permeabilities, and electrophysiological properties, basal V_t, $\Delta V_t{+}\mathrm{amiloride}$ and $\Delta V_t{+}0[\mathrm{Cl}^-]_\mathrm{l}$. In order to quantify these relationships, I performed a variance based parameter sensitivity analysis, relating model parameters to model outputs via a multiple regression model. The major insights I found from this analysis, with regard to non-CF HNE cells, are summarised as follows:

- Basal V_t in HNE cells is most sensitive to changes in apical Na^+ permeability and ba-

solateral K^+ permeability. Increasing both $P^{ap}_{Na^+}$ and $P^{ba}_{K^+}$ tends to hyperpolarise the value V_t takes at a steady state. Apical Cl^- permeability has little or no influence on the resting transepithelial PD, explaining why loss of CFTR permeability cannot account for the significant hyperpolarisation observed in CF epithelia. The different sensitivities can be understood in terms of the different magnitude of driving forces for movement of the ions along these respective pathways.

- Amiloride sensitive V_t is most sensitive to $P^{ap}_{Na^+}$. $\Delta V_t + \mathrm{amiloride}$ can also be influenced to a lesser extent by $P^{ap}_{Cl^-}$, with increasing apical Cl^- permeability decreasing its magnitude. The change in driving force for movement of Cl^- across the apical membrane after amiloride addition, can explain why $P^{ap}_{Cl^-}$ influences V_t in these simulations, but cannot change V_t under normal resting conditions.

- $\Delta V_t + 0[Cl^-]_l$ is most sensitive to changes in $P^{ap}_{Cl^-}$, as one would expect. Interestingly, the other apical permeability parameter, $P^{ap}_{Na^+}$, has very little influence on this metric, suggesting it is a reasonable means of inferring the underlying levels of Cl^- transport in HNE cells.

To my knowledge, this is the first rigorous elucidation of quantitative membrane permeability - transepithelial PD relationships in human airway epithelia. While in Chapter 3, I showed it was possible to quantify individual membrane permeabilities, this was not the only aim of my research, as it is in recent similar studies (see Garcia et al. (2013)). Here, I have not only asked *what* values ion permeabilities take in CF relative to non-CF epithelia (quantification), which is in itself informative, but I also addressed the question of *why* the permeabilities differ. Via this sensitivity analysis I have gained the insights provided above, and these gave answers relevant to several controversial questions regarding the relationship between CFTR and ENaC activities in cystic fibrosis disease.

7.1.6 Ability to simulate clinical nasal PD recordings

In Chapter 5 I showed how one could simulate several stages of a clinical nasal PD test, using the same approach as I had outlined for simulating Ussing chamber experiments in Chapter 3. This highlighted how one could relate the parameters of airway ion transport that are commonly recorded in the clinic, for example baseline V_t, $\Delta V_t + \mathrm{amiloride}$ and $\Delta V_t + 0[Cl^-]_l$, to parameters that characterise the actual physiological state of the patient in question, such as apical

Na^+ and Cl^- permeability.

Using the estimated values of transport parameters in non-CF and CF HNE cells (that I had found in Chapter 3) as a starting point, I investigated how the commonly measured V_t metrics responded to changes in these underlying parameters. As in Chapter 4, this took the form of a parameter sensitivity analysis, however here I also took into account variations in paracellular permeability, P_{pa}, and assessed how the results of the sensitivity analysis differed, depending on whether the reference state was a CF or non-CF HNE cell.

The outcome of the non-CF sensitivity analysis largely reproduced the insights gained in the earlier, similar analysis of Chapter 4. One new point of note was that changes in P_{pa} had a large influence on all three V_t metrics, and the greater the paracellular permeability, the lower the magnitudes of these measurements. Repeating the analysis with CF reference parameter values, showed that P_{pa}, $P^{ba}_{K^+}$ and $P^{ap}_{Na^+}$ again had large influences on basal V_t and $\Delta V_t{+}\mathrm{amiloride}$. Interestingly however, after amiloride addition (assuming all ENaC channels are blocked), no parameter could significantly influence the transepithelial PD (either amiloride insensitive V_t or $\Delta V_t{+}0[Cl^-]_l$), save for a $\approx 1-2$ mV change for a $\pm 50\%$ movement in parameter value.

Following up from this insight, I investigated how these nasal PD measurements would vary if only a certain fraction of ENaC channels were blocked on amiloride addition, rather than assuming a 100% block. In both the CF and non-CF simulations, incomplete block of $P^{ap}_{Na^+}$ significantly affected the predicted $\Delta V_t{+}\mathrm{amiloride}$ and had little or no effect on predicted $\Delta V_t{+}0[Cl^-]_l$ (the effect was most pronounced in the CF case). Finally, I repeated the CF sensitivity analysis, assuming now that $P^{ap}_{Na^+}$ would be reduced to 10% of its initial value on amiloride addition, rather than reduced completely such that $P^{ap}_{Na^+} = 0$. This changed the sensitivity of V_t post amiloride addition to certain transport parameters, most notably apical Na^+ permeability and paracellular permeability.

These analyses constitute an original contribution, as previously the theoretical underpinnings of the standard nasal PD test carried out in clinical studies of cystic fibrosis have not, to my knowledge, been investigated in a computational modelling study of this nature. Another novel contribution is the insight that in theory the transepithelial PD is insensitive to large changes in transport parameters, post amiloride addition, if all ENaC channels are blocked and no further apical Na^+ transport is possible. As there is often significant patient to patient variability in

the value of V_t measured after amiloride addition, this provides further evidence that perhaps not all Na^+ transport is being abolished during these tests, either due to technical difficulties with the application of amiloride, or due to the presence of a pool of amiloride insensitive Na^+ channels in the apical membrane of HNE cells.

7.1.7 Investigate viability of parameter estimation from clinical nasal PD traces

The final contribution of my thesis was a feasibility or "proof-of-principle" study, where I investigated the viability of quantifying transport parameters directly from clinical nasal PD measurements. Previously I had seen that it was possible to quantify membrane permeabilities given *in vitro* Ussing chamber recordings, and now I wanted to ascertain if using the same approach with *in vivo* nasal transepithelial PD recordings would prove to be informative. Ideally, given a set of nasal PD recordings from a cohort of patients, I would like to determine the distribution of transport parameters in that group, and use this information to gain some insight into what aspect of transport physiology is liable to be causing patient to patient variations in nasal V_t metrics.

I determined in this chapter, that differences in $P^{ap}_{Na^+}$ and $P^{ap}_{Cl^-}$ alone cannot account for the distribution of nasal PD metrics in a cohort of CF patients (for which I had data). This related specifically to the level of V_t remaining post amiloride addition, which varied significantly in this clinical group. I found that the data could only be fitted satisfactorily if I assumed not all ENaC channels were being blocked, and estimated the actual block fraction η individually from each trace.

I also highlighted in this chapter, the limitations placed on estimating transport parameter values, given only nasal PD metrics. I showed that given basal V_t, V_t after amiloride addition and V_t after luminal Cl^- removal, three parameters could be uniquely estimated, but not four. I found that estimating four parameters from V_t data alone would lead to degeneracies, and therefore we could not assign specific physiological parameter values to a given nasal PD trace. It was necessary to assume some information regarding intracellular ion concentrations was known, in order to resolve the issue of degenerate parameter estimates.

Finally, given the assumption that initial intracellular Na^+ and Cl^- concentration were the same in each patient, I estimated the values of $P^{ap}_{Na^+}$, $P^{ap}_{Cl^-}$, P_{pa} and η from a group of CF patients. I then compared how the distributions of parameter estimates differed by patient group, Old, Young/Severe or Young/Mild, and looked for correlations between these parameter values,

and metrics of lung function, such as the forced expiratory volume in one second (FEV_1). Although there was no statistically significant difference between estimated parameter values across the three patient groups, one interesting finding that was that estimated $P^{ap}_{Na^+}$ values were strongly correlated to FEV_1 values, suggesting a link between increased ENaC activity and reduced lung function in CF.

This chapter highlighted some of the problems related to using V_t metrics alone to infer the membrane ion permeability of an individual. Although these issues may be well known, it is the first time to my knowledge, that an actual demonstration of the possible degenerate nasal PD traces has been given. I showed that the exact same values for basal V_t, ΔV_t+amiloride, and ΔV_t+0$[\mathrm{Cl}^-]_\mathrm{l}$, can be produced by any number of different values of $P^{ap}_{Na^+}$, $P^{ap}_{Cl^-}$, P_{pa} and η, provided we are not worried about what the intracellular conditions or individual membrane potential values are. This has important implications for how nasal PD recordings are interpreted, and particularly how one would interpret changes in a given metric over time. It has been assumed for example, that changes in ΔV_t+0$[\mathrm{Cl}^-]_\mathrm{l}$ in a given patient over time, correspond directly to changes in CFTR permeability in that patient. However I have shown that it would be possible to reproduce such V_t metrics with any value of $P^{ap}_{Cl^-}$, provided the other transport parameters take appropriate values, hence placing the reasoning behind using ΔV_t+0$[\mathrm{Cl}^-]_\mathrm{l}$ metrics in clinical trials into doubt.

7.2 Further model development and future applications

7.2.1 Incorporating bicarbonate transport and cell pH

As discussed briefly in Chapter 1, there is evidence that disruption to bicarbonate transport in the human airways plays a pivotal role in the progression of CF lung disease. One hypothesis proposes that loss of bicarbonate transport onto the airway surfaces, reduces the pH of the surface fluids, thereby reducing the ability of bacteria to kill inhaled pathogens (Pezzulo et al., 2012). A second hypothesis gives evidence that reduced bicarbonate concentrations on the airway surface (caused by reduced secretion) leads to increased mucus viscosity, and that resulting thick mucus is the cause of lung disease in CF (Quinton, 2008, 2010). At the root of both hypotheses is abnormal bicarbonate transport in airway epithelial cells, due to mutated CFTR ion channels through which HCO_3^- ions can permeate.

In order to incorporate bicarbonate transport and a description of the cell's pH, into the current model framework, several adjustments would need to be made to the current frame-

work. This would include the inclusion of two new ionic species, H^+ and HCO_3^-, and also the inclusion of further transport proteins, responsible for moving bicarbonate and protons in and out of epithelial cells in the airways. From a modelling perspective, this means having two new variables (thus two new ODEs), plus several new parameters to describe the relative expression level of different proton and bicarbonate exchangers and transporters.

Another difference to keep in mind when modelling H^+ and HCO_3^- transport, is that unlike Na^+,Cl^- and K^+ ions, we cannot reasonably assume that they do not take part in chemical reactions in the intracellular compartment. For example, one would have to model H^+ ions binding to impermeant buffer ions in the cell, B^-, and the effect of H^+ ions combining with HCO_3^- to form H_2CO_3. The number of free protons or bicarbonate ions in the cell would then be less than the total numbers of these ions entering the cell

$$\frac{d[H^+]_f}{dt} = \frac{1}{f_{H^+}([H^+]_f, [HCO_3^-]_f)} \left(J^{in}_{H^+} - J^{out}_{H^+}\right) \tag{7.1}$$

$$\frac{d[HCO_3^-]_f}{dt} = \frac{1}{f_{HCO_3^-}([H^+]_f)} \left(J^{in}_{HCO_3^-} - J^{out}_{HCO_3^-}\right) \tag{7.2}$$

The buffering functions f_{H^+} and $f_{HCO_3^-}$ in equations 7.1 and 7.2 respectively, account for the proton and bicarbonate ions that participate in binding reactions. They are given by the following expressions, and their derivation can be found in the appendix, Section A.8

$$f_{H^+}\left([H^+]_f, [HCO_3^-]_f\right) = 1 + \frac{K_{HB}[B^-]_t}{(K_{HB} + [H^+]_f)^2} + \frac{[HCO_3^-]_f}{K_{H_2CO_3}} \tag{7.3}$$

$$f_{HCO_3^-}\left([H^+]_f\right) = 1 + \frac{[H^+]_f}{K_{H_2CO_3}} \tag{7.4}$$

In order to be able to integrate the new set of model ODEs numerically, one would require values for K_{HB}, $K_{H_2CO_3}$, and an estimate of the total impermeant buffer in HNE cells, $[B^-]_t$.

It would be necessary as well to decide which proton and anion exchanger and transporter proteins should be included in the expanded model system. As a useful starting point, one could incorporate those described by Falkenberg and Jacobsson in their model epithelial system (Falkenberg and Jakobsson, 2010). These authors developed a physiologically realistic model of ion transport in human bronchial epithelial cells, which included an accurate description of how cell pH changed during Ussing chamber experiments. In their model they included a sodium bicarbonate cotransporter, an anion exchanger and a sodium hydrogen exchanger in the

basolateral membrane (see Section 1.1.3.4).

While a generic Michaelis-Menten type function can be used to model the cycle rate of each of these additional transport proteins, this introduces further model parameters. For each exchanger or transporter, there would be at least an additional two half-saturation constants to consider, plus another parameter to represent the expression level of that protein in the membrane. Therefore including only those proteins considered by Falkenberg and Jacobsson would add on the order of 10-15 new model parameters, when one considers the saturation constants, expression levels, the details of H^+ and HCO_3^- buffering, and values of the external proton and bicarbonate concentrations. Considering there is already a large number of parameters in the model I have outlined in Chapter 2, this would make the prospect of carrying out parameter estimation in this expanded model quite daunting, given the general paucity of intracellular recordings during Ussing chamber experiments that one could use for constraining model output. On the other hand, it does seem probable that one could gain useful qualitative insights into the bicarbonate and pH kinetics in HNE cells during Ussing chamber experiments, by implementing some of the ideas outlined here. For example one could ask, how does the apical bicarbonate flux change as a function of CFTR and ENaC activity?

7.2.2 Model with variable Airway Surface Liquid compartment

The current mathematical model could be extended in order to investigate the delicate balance of ion and water transport between epithelial cells in the airways and the airway surface liquid (ASL). This would entail modifying the description of the lumen compartment, which in the research outlined in this thesis, has a constant ionic composition (and no variation in volume). The unchanging luminal compartment would be replaced by a compartment with variable volume, and variable ionic composition, like the intracellular compartment in the current model framework.

One implication of making this change, would be to increase the number of state variables from from six to ten, incorporating the four new variables that describe the ASL compartment: ASL volume (W_{ASL}), moles of Na^+ (Na^+_{ASL}), moles of Cl^- (Cl^-_{ASL}) and moles of K^+ (K^+_{ASL}). Consequently, the number of ODEs required to describe the kinetics of the cell plus

ASL system would also increase to ten, the new ODEs being as follows:

$$\frac{dW_{ASL}}{dt} = J_w^{ap} \tag{7.5}$$

$$\frac{dNa^+_{ASL}}{dt} = \left(I^{ap}_{Na^+} + I^{pa}_{Na^+}\right)/Fz_{Na^+} \tag{7.6}$$

$$\frac{dCl^-_{ASL}}{dt} = \left(I^{ap}_{Cl^-} + I^{pa}_{Cl^-}\right)/Fz_{Cl^-} \tag{7.7}$$

$$\frac{dK^+_{ASL}}{dt} = I^{pa}_{K^+}/Fz_{K^+} \tag{7.8}$$

Given the increased dimensionality of the ODE system, it may be more difficult to solve $f(x, \theta) = 0$ in order to find satisfactory steady state solutions. However, the number of model parameters will not increase significantly in this new framework, if one considers a model with the same transport pathways as described in this thesis. In that case the current CF and non-CF parameter estimates could be used as an initial starting point, from which to investigate the properties of this expanded system.

7.2.2.1 Investigation of relationship between V_t and ASL depth

Changes in transepithelial PD are used to quantify the CF disease state (see 1.2.4), and ASL dehydration has been causally related to this disease state (Boucher, 2007a,b). However it is not known if there is a well defined relationship between basal V_t and ASL depth. Using a similar approach to that outlined in this report, I can hope to begin to answer questions such as, is there a linear monotonic relationship between V_t and ASL depth? Or can homeostatic conditions be maintained without any correlation between these two properties?

7.2.2.2 Investigate potential strategies for airway re-hydration

This extended ASL plus cell model could also be used to determine strategies for increasing the volume of the ASL layer by pharmacologically modulating different transport proteins. With a quantitative description of electrolyte transport between HNE cell and ASL, it may be possible to determine how much water can be drawn onto the mucosal surface for a certain increase in membrane permeability to a given ion for example. Therefore it may be useful in comparing the relative efficacy of different strategies for hydrating the airway surfaces.

7.2.3 Use of model and identifiability analysis in experimental design

In Chapter 6 I investigated the potential utility of this mathematical modelling framework to estimate physiological parameters from nasal PD traces. There are difficulties with the current

approach, as only using data for V_t, ΔV_t+amiloride and ΔV_t+0$[\mathrm{Cl}^-]_l$ limits the number of parameter values that we can estimate, without resorting to making assumptions regarding the cell's intracellular state, or with regard to the values other transport parameters remain fixed at, if they are not being estimated.

There are two potential ways forward that I see, that may help overcome this problem. One potential solution is to model the next stage of the nasal PD test. In the standard nasal PD test, after the removal of Cl^- from the lumen perfusate, the solution to be added contains a β-agonist which will raise intracellular cAMP concentration and increase CFTR activity, leading to a consequent change in V_t. The benefit of including this stage is that we could include the next commonly used nasal PD measurement, ΔV_t+isoproterenol, in our objective function for parameter estimation, giving us more power to constrain parameter values. The downside is that we would need to include further parameters to determine how much CFTR activity increases once isoproterenol is added, and over what time period the increase takes place. The simplest assumption to make is that apical Cl^- permeability increases by a fixed amount ξ immediately as isoproterenol is added, in the same manner as apical Na^+ permeability goes to zero instantaneously on addition of amiloride in my Ussing chamber simulations. That is

$$P^{ap}_{Cl^-} \rightarrow \xi \left(P^{ap}_{Cl^-}\right); \;\; \{\xi > 1\} \tag{7.9}$$

One could assume that all patients experience the same relative increase in CFTR activity, or one could try and estimate ξ individually from each nasal PD trace, as I had done with the block fraction η in Chapter 6. In the case of estimating the increase ξ each time, it is likely that the ability to constrain further transport parameters would be limited.

A different approach to take, would be to try and determine in advance, a set of solution exchanges which would be most informative in determining parameter values, particularly in satisfactorily estimating values of $P^{ap}_{Na^+}$, $P^{ap}_{Cl^-}$, $P^{ba}_{K^+}$ and P_{pa} from a V_t trace alone. To begin with, one could experiment on an ad hoc basis with different solution exchanges that could reasonably be carried out in a clinical situation. For example, instead of reducing lumen Cl^- from $140\ \mathrm{mM}$ to $5\ \mathrm{mM}$ in one go, it could be performed in stages, say $40\ \mathrm{mM}$ at a time. The lumen Cl^- could be removed *before* amiloride is added, or a solution exchange introducing a large K^+ concentration could be incorporated. The general idea in each case would be to make an initial assumption regarding transport parameter values, run one of these devised sets of

solution exchanges, then try and reverse engineer the original parameter values given only the values of V_t that the system relaxes to after each perturbation. In each case one could determine whether parameter values of interest were practically identifiable given the resulting set of V_t values, and determine how tightly constrained parameter values were in cases where they were identifiable.

Appendices

Appendix A

Supplementary material

A.1 Constants and fixed model parameter values

Table A.1: Fixed parameter values used in mathematical model. Subscripts i, l & s refer to intracellular, luminal and serosal quantities respectively

Property	Parameter	Value	Units	Reference
Paracellular permeability	P_{pa}	0.035	$\mu\mathrm{m/s}$	(Willumsen and Boucher, 1989)
Activity coefficient	γ	0.77	–	(Hille, 2001)
Membrane H_2O conductance	L_w	220	$\mu\mathrm{m/s}$	(Falkenberg and Jakobsson, 2010)
Partial molar volume H_2O	v_w	1.805×10^{-5}	$\mathrm{m^3/mol}$	(Warren et al., 2009)
Moles impermeable anions	ψ_i	2.375×10^{-15}	mol	–
External osmolarity	$[S]_{l,s}$	290	mOsm	–
External $\mathrm{Na^+}$	$[\mathrm{Na^+}]_{\mathrm{l,s}}$	140	mM	(Willumsen et al., 1989b)
External $\mathrm{Cl^-}$	$[\mathrm{Cl^-}]_{\mathrm{l,s}}$	120	mM	(Willumsen et al., 1989b)
External $\mathrm{K^+}$	$[\mathrm{K^+}]_{\mathrm{l,s}}$	5	mM	(Willumsen et al., 1989b)
External impermeable anions	$\psi_{l,s}$	25	mM	–
Membrane capacitance	C_m	1	$\mu\mathrm{F/cm^2}$	(Hille, 2001)
Faraday constant	F	96485	$\mathrm{C/mol}$	(Hille, 2001)
Universal gas constant	R	8.314	$\mathrm{J/molK}$	(Hille, 2001)
Temperature	T	310	K	(Hille, 2001)

A.2 Derivation of Goldman-Hodgkin-Katz flux equation

Fick's law relates the diffusive flux $J_{diff}(x,t)$ of a particle to it's concentration profile $c(x,t)$ via the diffusion co-efficient D.

$$J_{diff}\left(x,t\right) = -D\,\frac{\partial}{\partial x}c\left(x,t\right) \tag{A.1}$$

The flux of ions J_{drift} due to the presence of an electric potential $\psi\left(x,t\right)$ is given by

$$J_{drift}(x,t) = -c(x,t)uzF\frac{\partial}{\partial x}\psi\left(x,t\right) \tag{A.2}$$

where u is the *molar mechanical mobility* of the ion, z is the valence, and F is the Faraday constant.

The molar mechanical mobility u_n of a specific ion n is related to it's diffusion co-efficient D_n by the Einstein relation, $D_n = u_n RT$ where R is the universal gas constant, and T is the absolute temperature. Therefore the net flux of an ion n due to both diffusion and drift is given by

$$J_n\left(x,t\right) = -D_n\frac{\partial c_n\left(x,t\right)}{\partial x} - u_n z_n F c_n\left(x,t\right)\frac{\partial \psi\left(x,t\right)}{\partial x} \tag{A.3}$$

Current density is related to flux via $I_n(x,t) = z_n F J_n(x,t)$, and from this we arrive at the following expression, known as the Nernst-Planck equation (Weiss, 1996)

$$I_n\left(x,t\right) = -u_n z_n F c_n\left(x,t\right)\left(\frac{RT}{c_n\left(x,t\right)}\frac{\partial c_n\left(x,t\right)}{\partial x} + z_n F\frac{\partial \psi\left(x,t\right)}{\partial x}\right) \tag{A.4}$$

An analytical solution to the Nernst-Planck equation can be found for the *steady state flux* J_n across a membrane separating two well mixed solutions under certain assumptions. A schematic of this particular scenario is shown in Figure A.1.

Under the constant field assumption, electric field $\epsilon = -\partial\psi/\partial x$ is constant, therefore

$$\frac{\partial \psi}{\partial x} = \frac{\Delta\psi}{\Delta x} = -\frac{V_m}{L} \tag{A.5}$$

where the membrane potential V_m is defined as $V_m^i - V_m^o$, and L is the width of the membrane.

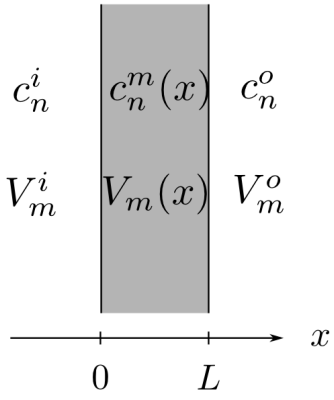

Figure A.1: Steady state electro-diffusion in one dimension across a membrane (grey area). The concentration inside, c_n^i, and outside, c_n^i, are constant, and vary with position x within the membrane. In the constant field approximation there is a constant electric potential gradient within the membrane, $\partial\psi(x)/\partial x = (V_m^o - V_m^i)/L$, where $V_m^i - V_m^o$ is the transmembrane potential difference.

Replacing A.5 in A.3 one finds

$$J_n = -D_n \frac{dc_n(x)}{dx} + u_n z_n F c_n(x) \frac{V_m}{L} \tag{A.6}$$

remembering that since we are now considering a steady state, concentration is a function of x only and flux becomes a constant J_n. Re-arranging in terms of concentration, and replacing u_n with D_n/RT one finds

$$\frac{dc_n(x)}{dx} = \frac{z_n F V_m}{RTL} c_n(x) - J_n/D_n \tag{A.7}$$

By separation of variables one can arrive at the following differential equation

$$\frac{dc_n}{-\frac{J_n}{D_n} + \frac{z_n F V_m}{RTL} c_n} = dx \tag{A.8}$$

The ion concentration inside the cell is assumed to be known and constant, with value c_n^i, and similarly the concentration outside the cell is assumed to be a constant c_n^o. To determine the ionic concentrations *within the membrane*, we utilise the fact that at the membrane boundaries, the concentrations are a constant times the concentration on the opposite side of the interface. This constant is called the *partition coefficient* k_n, and the concentrations within the membrane at the internal and external boundaries, are hence given by $c_n^m(0) = k_n c_n^i$ and $c_n^m(L) = k_n c_n^o$

respectively (Note I have used superscript m to denote concentration within the membrane).

Given this information we can now integrate A.8 within the membrane, using the limits $x = 0$ to $x = L$ and $c_n = c_n^i k_n$ to $c_n = c_n^o k_n$, to arrive at the expression

$$\frac{RTL}{z_n F V_m} \ln \left(\frac{-\frac{J_n}{D_n} + \frac{z_n F V_m}{RTL} k_n c_n^o}{-\frac{J_n}{D_n} + \frac{z_n F V_m}{RTL} k_n c_n^i} \right) = L \tag{A.9}$$

which, after taking the exponential of each side, becomes

$$-\frac{J_n}{D_n} + \frac{z_n F V_m}{RTL} k_n c_n^o = \left(-\frac{J_n}{D_n} + \frac{z_n F V_m}{RTL} k_n c_n^i \right) e^{\frac{z_n F V_m}{RT}} \tag{A.10}$$

Re-arranging in terms of the steady state flux J_n one arrives at the following expression

$$J_n = \frac{z_n F V_m}{RT} \left(\frac{k_n D_n}{L} \right) \left(\frac{c_n^i - c_n^o e^{-\frac{z_n F V_m}{RT}}}{1 - e^{-\frac{z_n F V_m}{RT}}} \right) \tag{A.11}$$

Defining the membrane permeability as $P_n = (k_n D_n)/L$, and now computing the current density per unit area (multiplying by $z_n F$), we arrive at the constant field flux equation or the Goldman-Hodgkin-Katz equation

$$I_n = P_n \frac{z_n^2 F^2 V_m}{RT} \frac{c_n^i - c_n^o e^{-\frac{z_n F V_m}{RT}}}{1 - e^{-\frac{z_n F V_m}{RT}}} \tag{A.12}$$

Note that in practice I will use ion activities in place of ion concentrations in equation A.12. The two are related via $a_n = \gamma_n c_n$ where γ_n is the *activity co-efficient* of ion n.

A.3 Smith-Crampin $\mathrm{Na}^+ - \mathrm{K}^+ - \mathrm{ATPase}$ active transport model

A full description of the sodium potassium pump model is available in Smith and Crampin (2004), I use their model description and parameter values in my work. A brief description of the pump model is outlined here. Flux from the sodium potassium pump, $J_{NaK}(t)$, is given by

$$J_{NaK}(t) = \rho_{NaK}\nu_{NaK}(t) \tag{A.13}$$

where $\nu_{NaK}(t)$ is the turnover rate of an individual pump protein, and ρ_{NaK} is the number of pump proteins per unit area of the basolateral membrane (a free parameter in my model). The turnover rate is given by

$$\nu_{NaK}(t) = \frac{\alpha_1^+\alpha_2^+\alpha_3^+\alpha_4^+ - \alpha_1^-\alpha_2^-\alpha_3^-\alpha_4^-}{\Sigma} \tag{A.14}$$

where $\alpha_{1,2,3,4}^{+/-}$ are the forward and backward rate constants of the reduced 4 stage pump cycle:

$$\alpha_1^+ = \frac{k_1^+\widetilde{Na_i^+}^3}{\left(1+\widetilde{Na_i^+}\right)^3 + \left(1+\widetilde{K_i^+}\right)^2 - 1} \tag{A.15}$$

$$\alpha_2^+ = k_2^+ \tag{A.16}$$

$$\alpha_3^+ = \frac{k_3^+\widetilde{K_s^+}^2}{\left(1+\widetilde{Na_s^+}\right)^3 + \left(1+\widetilde{K_s^+}\right)^2 - 1} \tag{A.17}$$

$$\alpha_4^+ = \frac{k_4^+\widetilde{MgATP}}{1+\widetilde{MgATP}} \tag{A.18}$$

$$\alpha_1^- = k_1^-\,[\mathrm{MgADP}] \tag{A.19}$$

$$\alpha_2^- = \frac{k_2^-\widetilde{Na_s^+}^3}{\left(1+\widetilde{Na_s^+}\right)^3 + \left(1+\widetilde{K_s^+}\right)^2 - 1} \tag{A.20}$$

$$\alpha_3^- = \frac{k_3^-[\mathrm{Pi}][\mathrm{H}^+]}{1+\widetilde{MgATP}} \tag{A.21}$$

$$\alpha_4^- = \frac{k_4^-\widetilde{K_i^+}^2}{\left(1+\widetilde{Na_i^+}\right)^3 + \left(1+\widetilde{K_i^+}\right)^2 - 1} \tag{A.22}$$

Normalised concentrations:

$$\widetilde{Na_i^+} = [\mathrm{Na}^+]_i / k_{d,Na_i^+} \quad \text{(A.23)}$$

$$\widetilde{K_i^+} = [\mathrm{K}^+]_i / k_{d,K_i^+} \quad \text{(A.24)}$$

$$\widetilde{Na_s^+} = [\mathrm{Na}^+]_s / k_{d,Na_s^+} \quad \text{(A.25)}$$

$$\widetilde{K_s^+} = [\mathrm{K}^+]_s / k_{d,K_s^+} \quad \text{(A.26)}$$

$$\widetilde{MgATP} = [\mathrm{MgATP}] / k_{d,MgATP} \quad \text{(A.27)}$$

Voltage dependent dissociation constants:

$$k_{d,Na_s^+} = k^0_{d,Na_s^+} exp\left\{\frac{(1+\Delta)FV_m^{ba}}{3RT}\right\} \quad \text{(A.28)}$$

$$k_{d,Na_i^+} = k^0_{d,Na_i^+} exp\left\{\frac{\Delta FV_m^{ba}}{3RT}\right\} \quad \text{(A.29)}$$

Free inorganic phosphate is given by

$$[\mathrm{Pi}] = \frac{[\Sigma\mathrm{Pi}]_i}{1 + [\mathrm{K}^+]_i / k_{d,H^+Pi} + [\mathrm{H}^+] / k_{d,H^+Pi} + [\mathrm{Na}^+]_i / k_{k,Na^+Pi}} \quad \text{(A.30)}$$

The term Σ in the denominator of A.14 is given by a sum of permutations of the rate constants

$$\begin{aligned}\Sigma = {} & \alpha_1^-\alpha_2^-\alpha_3^- + \alpha_1^-\alpha_2^-\alpha_4^+ + \alpha_1^-\alpha_3^+\alpha_4^+ + \alpha_2^+\alpha_3^+\alpha_4^+ + \\ & \alpha_2^-\alpha_3^-\alpha_4^- + \alpha_1^+\alpha_2^-\alpha_3^- + \alpha_1^+\alpha_2^-\alpha_4^+ + \alpha_1^+\alpha_3^+\alpha_4^+ + \\ & \alpha_1^-\alpha_3^-\alpha_4^- + \alpha_2^+\alpha_3^-\alpha_4^- + \alpha_1^+\alpha_2^+\alpha_3^- + \alpha_1^+\alpha_2^+\alpha_4^+ + \\ & \alpha_1^-\alpha_2^-\alpha_4^- + \alpha_1^-\alpha_3^+\alpha_4^- + \alpha_2^+\alpha_3^+\alpha_4^- + \alpha_1^+\alpha_2^+\alpha_3^+ \end{aligned} \quad \text{(A.31)}$$

Rate constants used in the pump model are $k_1^+ = 1050\ \mathrm{s}^{-1}$, $k_1^- = 172.1\ \mathrm{s}^{-1}\mathrm{mM}^{-1}$, $k_2^+ = 481\ \mathrm{s}^{-1}$, $k_2^- = 40.1\ \mathrm{s}^{-1}$, $k_3^+ = 2000\ \mathrm{s}^{-1}$, $k_3^- = 79,287.1\ \mathrm{s}^{-1}\mathrm{mM}^{-2}$, $k_4^+ = 320\ \mathrm{s}^{-1}$, $k_4^{-1} = 40.1\ \mathrm{s}^{-1}$. Dissociation constants used are $k^0_{d,Na_s^+} = 15.5$ mM, $k^0_{d,Na_i^+} = 2.49$ mM, $k_{d,K_s^+} = 0.213$ mM, $k^0_{d,K_i^+} = 0.5$ mM, $k_{d,MgATP} = 2.51$ mM, $k_{d,K^+Pi} = 292$ mM, $k_{d,H^+Pi} = 1.69 \times 10^{-4}$ mM, and $k_{d,Na^+Pi} = 224$ mM. Other parameters fixed in this model are $[\Sigma\mathrm{Pi}]_i = 4.2$ mM, $[\mathrm{H}^+]_i = 8 \times 10^{-5}$ mM, $[\mathrm{MgATP}] = 9.8$ mM, $[\mathrm{MgADP}] = 0.01$ mM, and $\Delta = -0.031$.

Note that in practice, I convert ion concentrations to ion activities ($a_n = \gamma c_n$) before

computing equations A.23 - A.26, since under physiological conditions the intra- and extracellular solutions considered will not behave as ideal electrolytes.

A.4 Benjamin-Johnson NKCC cotransporter model

A full description of kinetic model and parameter values used in this model of the NKCC cotransporter is given in Benjamin and Johnson (1997). I describe it briefly here. The basolateral flux due to cotransport is given by $J_{NKCC}(t) = \rho_{NKCC}\nu_{NKCC}(t)$ where ν_{NKCC} (a free parameter in my model) is the number of cotransporters per unit area of the basolateral membrane, and $\nu_{NKCC}(t)$ is the turnover rate of a single cotransport protein, given by

$$\nu_{NKCC}\,(t) = \frac{k_f^{full}k_f^{empty}[Na^+]_s[K^+]_s[Cl^-]_s^2 - k_b^{full}k_b^{empty}[Na^+]_i[K^+]_i[Cl^-]_i^2}{\sum_{n=1}^{16} Z_{nkcc}^n} \tag{A.32}$$

The terms Z_{nkcc}^n are determined as follows

$$Z_{nkcc}^1 = Z_1\left[Cl^-\right]_i \tag{A.33}$$

$$Z_{nkcc}^2 = Z_2\left[Na^+\right]_s \tag{A.34}$$

$$Z_{nkcc}^3 = Z_3\left[Cl^-\right]_i\left[K^+\right]_i \tag{A.35}$$

$$Z_{nkcc}^4 = Z_4\left[Cl^-\right]_s\left[K^+\right]_s \tag{A.36}$$

$$Z_{nkcc}^5 = Z_5\left[Cl^-\right]_i^2\left[K^+\right]_i \tag{A.37}$$

$$Z_{nkcc}^6 = Z_6\left[Cl^-\right]_s\left[K^+\right]_s\left[Na^+\right]_s \tag{A.38}$$

$$Z_{nkcc}^7 = Z_7\left[Cl^-\right]_i^2\left[K^+\right]_i\left[Na^+\right]_i \tag{A.39}$$

$$Z_{nkcc}^8 = Z_8\left[Cl^-\right]_s^2\left[K^+\right]_s\left[Na^+\right]_s \tag{A.40}$$

$$Z_{nkcc}^9 = Z_9\left[Cl^-\right]_i^2\left[K^+\right]_i\left[Na^+\right]_i\left[Na^+\right]_s \tag{A.41}$$

$$Z_{nkcc}^{10} = Z_{10}\left[Cl^-\right]_i\left[Cl^-\right]_s^2\left[K^+\right]_s\left[Na^+\right]_s \tag{A.42}$$

$$Z_{nkcc}^{11} = Z_{11}\left[Cl^-\right]_i^2\left[K^+\right]_i\left[Na^+\right]_i\left[Cl^-\right]_s\left[Na^+\right]_s \tag{A.43}$$

$$Z_{nkcc}^{12} = Z_{12}\left[Cl^-\right]_i\left[K^+\right]_i\left[Cl^-\right]_s^2\left[K^+\right]_s\left[Na^+\right]_s \tag{A.44}$$

$$Z_{nkcc}^{13} = Z_{13}\left[Cl^-\right]_i^2\left[K^+\right]_i\left[Cl^-\right]_i^2\left[K^+\right]_s\left[Na^+\right]_s \tag{A.45}$$

$$Z_{nkcc}^{14} = Z_{14}\left[Cl^-\right]_i^2\left[K^+\right]_i\left[Na^+\right]_i\left[Cl^-\right]_s\left[K^+\right]_s\left[Na^+\right]_s \tag{A.46}$$

$$Z_{nkcc}^{15} = Z_{15}\left[Cl^-\right]_i^2\left[K^+\right]_i\left[Na^+\right]_i\left[Cl^-\right]_s^2\left[K^+\right]_s\left[Na^+\right]_s \tag{A.47}$$

$$Z_{nkcc}^{16} = K_{Cl}^2K_KK_{Na}(k_b^{empty} + k_f^{empty}) \tag{A.48}$$

where the coefficients Z_n are given by

$$Z_1 = K_{Cl}K_K K_{Na} k_b^{empty} \quad \text{(A.49)}$$

$$Z_2 = K_{Cl}^2 K_k k_f^{empty} \quad \text{(A.50)}$$

$$Z_3 = K_{Cl}K_{Na} k_b^{empty} \quad \text{(A.51)}$$

$$Z_4 = K_{Cl}K_K k_f^{empty} \quad \text{(A.52)}$$

$$Z_5 = K_{Na} k_b^{empty} \quad \text{(A.53)}$$

$$Z_6 = K_{Cl} k_f^{empty} \quad \text{(A.54)}$$

$$Z_7 = k_b^{empty} + k_b^{full} \quad \text{(A.55)}$$

$$Z_8 = k_f^{full} + k_f^{empty} \quad \text{(A.56)}$$

$$Z_9 = K_{Na}^{-1} k_b^{full} \quad \text{(A.57)}$$

$$Z_{10} = K_{Cl}^{-1} k_f^{full} \quad \text{(A.58)}$$

$$Z_{11} = K_{Cl}^{-1} K_{Na}^{-1} k_b^{full} \quad \text{(A.59)}$$

$$Z_{12} = K_{Cl}^{-1} K_K^{-1} k_f^{full} \quad \text{(A.60)}$$

$$Z_{13} = K_{Cl}^{-2}\ K_K^{-1}\ k_b^{full} \quad \text{(A.61)}$$

$$Z_{14} = K_{Cl}^{-1} K_K^{-1} K_{Na}^{-1} k_b^{full} \quad \text{(A.62)}$$

$$Z_{15} = K_{Cl}^{-2} K_K^{-1} K_{Na}^{-1} \left(k_b^{full} + k_f^{full} \right) \quad \text{(A.63)}$$

$$k_b^{empty} = \frac{K_{Cl}^2\ K_K\ K_{Na}\ k_f^{full} k_f^{empty}}{K_{Cl}^2 K_K K_{Na} k_b^{full}} \quad \text{(A.64)}$$

Rate constants and dissociation constants used in this model are $K_{Cl} = 2.42$ mM, $K_{Na} = 22.38$ mM, $K_K = 234.74$ mM, $k_f^{empty} = 37,767\ \text{s}^{-1}$, $k_f^{full} = 1406\ \text{s}^{-1}$, $k_b^{empty} = 13,196\ \text{s}^{-1}$, $k_b^{full} = 4025\ \text{s}^{-1}$ and they are also taken from Benjamin and Johnson (1997).

Note that in practice, I convert ion concentrations to ion activities ($a_n = \gamma c_n$) before computing equations A.32 - A.48, since under physiological conditions the intra- and extracellular solutions considered will not behave as ideal electrolytes.

A.5 Determining paracellular permeability from shunt resistance

In my model I assume that under resting conditions the paracellular pathway is only permeable to $\mathrm{Na}^+, \mathrm{K}^+$ and Cl^- ions, therefore the total paracellular or *shunt* current will be given by

$$I_s = I^{pa}_{Na^+} + I^{pa}_{Cl^-} + I^{pa}_{K^+} \tag{A.65}$$

Assuming the paracellular currents are accurately described by the GHK formalism A.2, and that the cation/anion permeability ratio is $1/\lambda$, then in the limit of identical bathing solutions this expression reduces to

$$I_s = P_{pa}\left(V_t\gamma F^2\right)/RT\left([\mathrm{Na}^+] + [\mathrm{K}^+] + \lambda[\mathrm{Cl}^-]\right) \tag{A.66}$$

where $P_{pa} \equiv P^{pa}_{Na^+} \equiv P^{pa}_{K^+}$ is the permeability of the pathway to cations. Shunt resistance R_s is related to shunt current via $I_s = V_t/R_s$ therefore

$$P_{pa} = \frac{1/R_s}{\left(F^2\gamma/RT\right)\left([\mathrm{Na}^+] + [\mathrm{K}^+] + \lambda[\mathrm{Cl}^-]\right)} \tag{A.67}$$

Mean shunt resistance was measured to be $412\ \Omega\,\mathrm{cm}^2$ and $623\ \Omega\,\mathrm{cm}^2$ for non-CF and CF HNE cells respectively (Willumsen and Boucher, 1989), with solution composition $[\mathrm{Na}^+] = 140\ \mathrm{mM}$, $[\mathrm{Cl}^-] = 120\ \mathrm{mM}$, and $[\mathrm{K}^+] = 5.2\ \mathrm{mM}$. For a non-selective pathway $\lambda = 1$, we find that

$$P^{non-CF}_{pa} = 3.29074 \times 10^{-8}\ \mathrm{m/s} = 0.0329\ \mu\mathrm{m/s} \tag{A.68}$$

$$P^{CF}_{pa} = 2.17616 \times 10^{-8}\ \mathrm{m/s} = 0.0218\ \mu\mathrm{m/s} \tag{A.69}$$

If we assume a cation selective paracellular pathway with $\lambda = 1/1.3$ (Levin et al., 2006; Flynn et al., 2009) the values we find are

$$P^{non-CF}_{pa} = 3.67442 \times 10^{-8}\ \mathrm{m/s} = 0.0367\ \mu\mathrm{m/s} \tag{A.70}$$

$$P^{CF}_{pa} = 2.42989 \times 10^{-8}\ \mathrm{m/s} = 0.0243\ \mu\mathrm{m/s} \tag{A.71}$$

All parameter estimation and Monte Carlo filtering analyses were carried out with the following paracellular transport configurations: (A) P_{pa} unchanged in CF and non-selective, (B) P_{pa}

unchanged in CF and cation-selective , (C) P_{pa} reduced in CF relative to non-CF and non-selective, (D) P_{pa} reduced in CF relative to non-CF and cation selective.

For simulations where I assumed a cation selective P_{pa}, I also assumed that $P^{pa}_{Cl^-} = 1.4\ P^{pa}_{gluc^-}$. I estimated the ratio of 1.4 based on recreating the experiments of Coakley et al. (2003) who found a permeability ratio $P^{pa}_{Cl^-} > P^{pa}_{gluc^-}$.

A.6 Effect of including $[\mathrm{Na^+}]_\mathrm{i}$ kinetics on CF parameter estimates

Parameter	(A) Including $[\mathrm{Na^+}]_\mathrm{i}$		(B) Excluding $[\mathrm{Na^+}]_\mathrm{i}$	
	Median	IQR	Median	IQR
$P^{ap}_{Na^-}$	0.070	0.011	0.070	0.014
$P^{ap}_{Cl^-}$	0.004	0.005	0.005	0.004
$P^{ba}_{K^+}$	0.886	4.716	1.540	6.835
$P^{ba}_{Cl^-}$	0.370	1.837	0.568	2.414
ρ_{NaK}	0.942	3.405	1.250	4.239
ρ_{NKCC}	3632	14243	1990	16267

Table A.2: Transport parameter values estimated using experimental data from CF HNE cells. The experimental data used for constraining model behaviour was the same in both cases, apart from the value of $[\mathrm{Na^+}]_\mathrm{i}$ after amiloride addition, which was included in the objective function in case A, but was not included in case B. Estimates of $P^{ap}_{Cl^-}$ and $P^{ap}_{Na^+}$ are not altered significantly by the inclusion or exclusion of this extra observation. The median values of the basolateral transport parameters are different in both cases, but the differences are small relative to the uncertainty in each estimate.

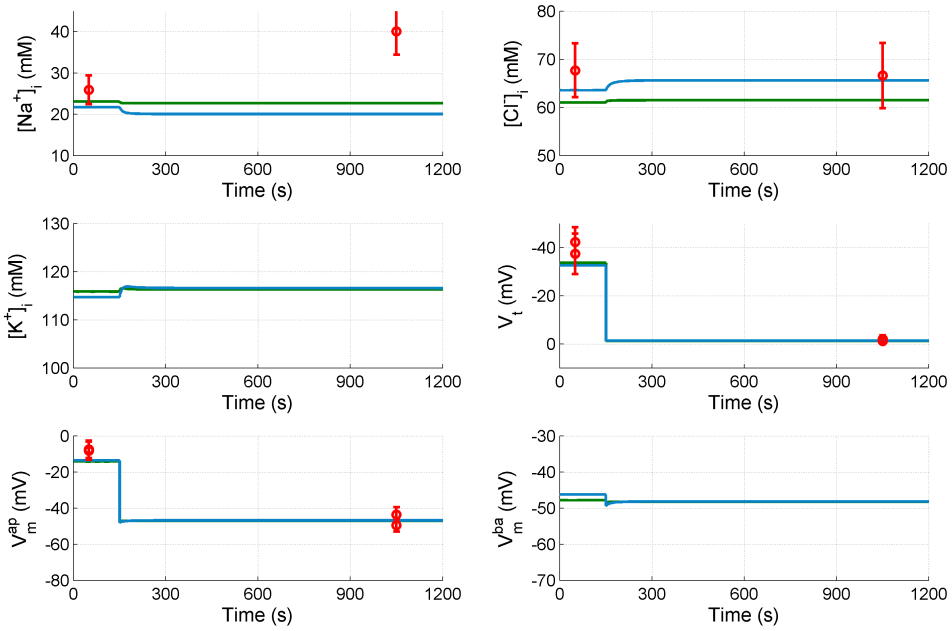

Figure A.2: Including post amiloride addition $[Na^+]_i$ in the objective function when estimating transport parameter values in CF HNE cells leads to different "optimum" solutions. Here the best fit solution when the additional Na^+ observation is included, is in green, and the blue trace is the best fit solution when the additional observation is not included in the fitting process. Experimental observations and associated uncertainties are plotted in red in each panel. In these simulations the model system cannot qualitatively reproduce an increase in $[Na^+]_i$ after amiloride is added (at $t = 150$ s), hence if this observation is included in the fitting process, parameter values move such that $\Delta[Na^+]_i + \text{amiloride}$ tends towards zero. This is not necessarily a physiologically realistic situation, as I am forcing the system to fit a behaviour it cannot predict.

A.7 Influence of paracellular permeability and selectivity on parameter estimates

Parameter estimation described in Section 3.4.3 was carried out in four different scenarios, to assess the influence that the magnitude of paracellular permeability and selectivity ratios had on estimated transport parameter values, particularly those of $P^{ap}_{Na^+}$ and $P^{ap}_{Cl^-}$. The results of this work are shown in Tables A.3 and A.4.

Parameter	(A) Baseline $P^{pa}_{Na^+}$, no selectivity				(B) Baseline $P^{pa}_{Na^+}$, cation selective			
	Non-CF		CF		Non-CF		CF	
	Median	IQR	Median	IQR	Median	IQR	Median	IQR
$P^{ap}_{Na^-}$	0.0241	0.0039	0.0701	0.0140	0.0202	0.0031	0.0589	0.0121
$P^{ap}_{Cl^-}$	0.0655	0.0166	0.0049	0.0043	0.0462	0.0113	0.0041	0.0041
$P^{ba}_{K^+}$	0.1014	0.0733	1.5398	6.8347	0.0781	0.0395	1.1377	5.9989
$P^{ba}_{Cl^-}$	0.0955	0.1146	0.5679	2.4145	0.0586	0.0560	0.3902	2.1851
ρ_{NaK}	0.1325	0.0906	1.2501	4.2394	0.1008	0.0544	0.9035	3.7991
ρ_{NKCC}	0.1991	0.4076	1990	16266	0.1543	0.2811	3159	11639
$P^{pa}_{Na^+}$	0.035	-	0.035	-	0.035	-	0.035	-
$P^{pa}_{Na^+}/P^{pa}_{Cl^-}$	1.0	-	1.0	-	1.3	-	1.3	-
$P^{pa}_{Cl^-}/P^{pa}_{gluc^-}$	1.0	-	1.0	-	1.4	-	1.4	-

Table A.3: Results of parameter estimation via minimisation of residual error between model predictions and CF and non-CF HNE cell data. (A) Estimates of transport parameters found when paracellular permeability is assumed to be fixed at the baseline estimate in both CF and non-CF simulations, and is assumed to be the same for all ions. (B) Estimates of transport parameter values found when assuming baseline $P^{pa}_{Na^+}$ with a cation selective paracellular pathway, and a $\mathrm{Cl}^-/\mathrm{gluconate}^-$ paracellular selectivity ratio greater than 1.

Parameter	(C) $P^{pa}_{Na^+}$ reduced in CF, no selectivity				(D) $P^{pa}_{Na^+}$ reduced in CF, cation selective			
	Non-CF		CF		Non-CF		CF	
	Median	IQR	Median	IQR	Median	IQR	Median	IQR
$P^{ap}_{Na^-}$	0.0227	0.0036	0.0429	0.0087	0.0212	0.0033	0.0409	0.0083
$P^{ap}_{Cl^-}$	0.0616	0.0155	0.0030	0.0028	0.0484	0.0118	0.0028	0.0029
$P^{ba}_{K^+}$	0.0947	0.0688	0.9047	4.2966	0.0819	0.0402	0.7824	4.8400
$P^{ba}_{Cl^-}$	0.0898	0.1077	0.2974	1.5111	0.0614	0.0592	0.2715	1.7954
ρ_{NaK}	0.1246	0.0836	0.6753	3.2724	0.1056	0.0584	0.6263	3.2322
ρ_{NKCC}	0.1871	0.3827	1538	14355	0.1612	0.2938	1441	13628
$P^{pa}_{Na^+}$	0.0329	-	0.0218	-	0.0367	-	0.0243	-
$P^{pa}_{Na^+}/P^{pa}_{Cl^-}$	1.0	-	1.0	-	1.3	-	1.3	-
$P^{pa}_{Cl^-}/P^{pa}_{gluc^-}$	1.0	-	1.0	-	1.4	-	1.4	-

Table A.4: Results of parameter estimation via minimisation of residual error between model predictions and CF and non-CF HNE cell data. (C) Estimates of transport parameters found when the magnitude of paracellular permeability is reduced in CF relative to non-CF simulations, and paracellular selectivity is assumed to be the same for all ions. (D) Estimates of transport parameter values found when assuming $P^{pa}_{Na^+}$ is reduced in CF simulations, and both the $\mathrm{Na}^+/\mathrm{Cl}^-$ and $\mathrm{Cl}^-/\mathrm{gluconate}^-$ paracellular selectivity ratios are greater than 1.

A.8 Modelling H^+ and HCO_3^- transport

In this section I will give a brief outline of how transport of bicarbonate and protons could be incorporated into the existing model of ion transport in HNE cells.

To begin with, I assume that H^+ is present in three forms in the intracellular compartment; free protons, $[H^+]_f$, protons bound to impermeant buffer, $[HB]$, and protons bound to bicarbonate ions in the form $[H_2CO_3]$. This gives for the total proton concentration in the cell

$$[H^+]_t = [H^+]_f + [HB] + [H_2CO_3] \tag{A.72}$$

Free H^+ and impermeant buffer ions B^- combine according to the following reaction

$$[H^+]_f + [B^-]_f \rightleftharpoons [HB] \tag{A.73}$$

If we assume this reaction is at rapid equilibrium such that

$$\frac{[H^+]_f[B^-]_f}{[HB]} = K_{HB} \tag{A.74}$$

and the total impermeant buffer $[B^-]_t = [B^-]_f + [HB]$ is constant, then we can determine the

free buffer in terms of the total buffer and the free protons, via

$$[B^-]_f = [B_t^-]\left(1 + \frac{[H^+]_f}{K_{HB}}\right)^{-1} \tag{A.75}$$

The amount of protons bound to buffer at any time is given, via equation A.74, by

$$[HB] = \frac{[H^+]_f[B^-]_f}{K_{HB}} \tag{A.76}$$

If we now replace $[B^-]_f$ in this expression with the right hand side of A.75, we find

$$[HB] = [H^+]_f \frac{[B^-]_t}{K_{HB} + [H^+]_f} \tag{A.77}$$

When we replace A.77 in the equation for total protons in the cell we find

$$[H^+]_t = [H^+]_f\left(1 + \frac{[B^-]_t}{K_{HB} + [H^+]_f}\right) + [H_2CO_3] \tag{A.78}$$

Next we consider the total amount of HCO_3^- in the cell, which is either free or bound to protons, such that

$$[HCO_3^-]_t = [HCO_3^-]_f + [H_2CO_3] \tag{A.79}$$

Again, assuming rapid equilibrium free protons, $[H^+]_f$, and free bicarbonate, $[HCO_3^-]_f$, we can write for the total amount of free bicarbonate (analogous to equation A.75)

$$[HCO_3^-]_f = [HCO_3^-]_t\left(1 + \frac{[H^+]_f}{K_{H_2CO_3}}\right)^{-1} \tag{A.80}$$

And in the same manner as equation A.77, we can determine the number of bicarbonate ions bound to protons, in terms of free protons, and total bicarbonate

$$[H_2CO_3] = [H^+]_f\left(\frac{[HCO_3^-]_t}{K_{H_2CO_3} + [H^+]_f}\right) \tag{A.81}$$

Finally, adding this into the expression for the total H^+ in the cell, we get

$$[H^+]_t = [H^+]_f\left(1 + \frac{[B^-]_t}{K_{HB} + [H^+]_f} + \frac{[HCO_3^-]_t}{K_{H_2CO_3} + [H^+]_f}\right) \tag{A.82}$$

The total amount of H^+ in the cell can only change if H^+ ions flow into or out of the cell

$$\frac{d[H^+]_t}{dt} = J_{H^+}^{in} - J_{H^+}^{out} \tag{A.83}$$

Using the chain rule we can relate changes in free H^+ to the total H^+ in the cell

$$\frac{d[H^+]_t}{dt} = \frac{d[H^+]_t}{d[H^+]_f}\frac{d[H^+]_f}{dt} \tag{A.84}$$

We can determine $d[H^+]_t/d[H^+]_f$ from the expression we have previously determined for total $[H^+]_t$, equation A.82

$$\begin{aligned}\frac{d[H^+]_t}{d[H^+]_f} &= \frac{d}{d[H^+]_f}\left([H^+]_f\left(1 + \frac{[B^-]_t}{K_{HB} + [H^+]_f} + \frac{[HCO_3^-]_t}{K_{H_2CO_3} + [H^+]_f}\right)\right) &\text{(A.85)}\\ &= 1 + \frac{K_{HB}[B^-]_t}{(K_{HB} + [H^+]_f)^2} + \frac{[HCO_3^-]_f}{K_{H_2CO_3}} &\text{(A.86)}\end{aligned}$$

Replacing A.86 in A.84 we have

$$\frac{d[H^+]_t}{dt} = \left(1 + \frac{K_{HB}[B^-]_t}{(K_{HB} + [H^+]_f)^2} + \frac{[HCO_3^-]_f}{K_{H_2CO_3}}\right)\frac{d[H^+]_f}{dt} \tag{A.87}$$

If I now define a buffering function

$$f_{H^+}\left([H^+]_f, [HCO_3^-]_f\right) = 1 + \frac{K_{HB}[B^-]_t}{(K_{HB} + [H^+]_f)^2} + \frac{[HCO_3^-]_f}{K_{H_2CO_3}} \tag{A.88}$$

Then I can define the rate of change of free H^+ in the cell as

$$\begin{aligned}\frac{d[H^+]_f}{dt} &= \frac{1}{f_{H^+}}\frac{d[H^+]_t}{dt} &\text{(A.89)}\\ &= \frac{1}{f_{H^+}}\left(J_{H^+}^{in} - J_{H^+}^{out}\right) &\text{(A.90)}\end{aligned}$$

The expression we arrive at states that free H^+ in the cell changes due to net influx / efflux of protons into the cell, but there is a buffering effect present (taken into account by the function f_{H^+}) which dampens the rate at which changes in $[H^+]_f$ take place, as some protons which enter the cell will bind to impermeant buffer B^- or to free bicarbonate to form $[H_2CO_3]$.

Similarly, for free bicarbonate concentration in the cell, we can define a buffering function

(from A.80)

$$f_{HCO_3^-}\left([H^+]_f\right) = \frac{d[HCO_3^-]_t}{d[HCO_3^-]_f} \quad (A.91)$$

$$= 1 + \frac{[H^+]_f}{K_{H_2CO_3}} \quad (A.92)$$

Then the rate of change of free bicarbonate, as a function of influx and efflux of this ion, is given by

$$\frac{d[HCO_3^-]_f}{dt} = \frac{1}{f_{HCO_3^-}\left([H^+]_f\right)}\left(J^{in}_{HCO_3^-} - J^{out}_{HCO_3^-}\right) \quad (A.93)$$

A.9 MATLAB source code

All simulations and data analysis were performed using MATLAB Release R2010b, along with MATLAB Optimisation Toolbox and Statistics Toolbox from the same release.

The MATLAB source code used to perform the simulations and data analysis described in this thesis is available as an electronic supplement. In the case of physical copies of this thesis they are stored on a CD/DVD attached inside the back cover. These files will also be made available online to accompany the final electronic version of this thesis, which will be available at the UCL Discovery website (discovery.ucl.ac.uk) once approved.

A.10 Clinical Nasal Potential Difference data set

Trace	Category	Nasal PD measurements (mV)					FEV_1
		Basal	After amil.	ΔV_t+amil.	After $0[Cl^-]_l$	ΔV_t+$0[Cl^-]_l$	
CF5a	Young/Mild	-25.7	-14.9	10.8	-18.4	-3.5	0.97
CF29a	Young/Mild	-20.2	-6.6	13.6	-7.1	-0.5	1.03
CF45	Young/Mild	-39.6	-14.8	24.8	-17.3	-2.5	0.92
CF51	Young/Mild	-47.1	-17.4	29.7	-19.3	-1.9	0.82
CF52	Young/Mild	-40.5	-4.9	35.7	-6.7	-1.9	0.93
CF59	Young/Mild	-44.3	-14.6	29.7	-20.4	-5.8	0.77
CF60	Young/Mild	-43.4	-24.4	19.0	-27.1	-2.7	0.70
CF70	Young/Mild	-19.4	-7.3	12.2	-10.0	-2.7	0.72
CF72	Young/Mild	-39.0	-10.1	29.0	-12.8	-2.7	0.67
CF73	Young/Mild	-55.4	-11.4	44.0	-14.9	-3.5	0.85
CF77	Young/Mild	-47.0	-13.0	34.0	-14.8	-1.8	0.79
CF7b	Old	-54.2	-16.3	37.9	-20.1	-3.8	0.48
CF9a	Old	-52.2	-13.8	38.4	-20.2	-6.4	0.81
CF10a	Old	-58.2	-21.8	36.4	-23.1	-1.3	0.81
CF11a	Old	-36.3	-9.3	27.0	-29.3	-20.0	0.21
CF11b	Old	-43.2	-6.2	36.9	-25.6	-19.4	0.21
CF12a	Old	-41.0	-8.0	32.9	-8.8	-0.8	0.91
CF12b	Old	-48.2	-7.2	41.0	-12.8	-5.6	0.91
CF13a	Old	-28.1	-21.8	6.3	-23.8	-2.0	0.89
CF13b	Old	-36.5	-9.7	26.8	-11.8	-2.1	0.89
CF14a	Old	-50.1	-15.4	34.7	-19.7	-4.4	0.79
CF15a	Old	-62.8	-13.2	49.6	-18.1	-5.0	0.76
CF17a	Old	-34.9	-15.2	19.8	-18.6	-3.4	0.64
CF17b	Old	-30.3	-14.0	16.3	-15.9	-2.0	0.64
CF19a	Old	-53.6	-9.3	44.3	-21.7	-12.4	0.22
CF20b	Old	-45.5	-28.2	17.3	-32.9	-4.7	0.47
CF25a	Old	-72.1	-21.1	51.0	-25.0	-3.9	0.26
CF1	Young/Severe	-50.9	-24.1	26.8	-35.2	-11.1	0.52
CF2b	Young/Severe	-50.6	-22.7	27.9	-25.7	-3.0	0.37
CF3a	Young/Severe	-55.9	-7.5	48.4	-9.7	-2.2	0.38
CF26a	Young/Severe	-20.0	-8.1	11.9	-11.0	-2.9	0.41
CF30a	Young/Severe	-55.0	-13.2	41.8	-15.1	-1.9	0.42
CF30b	Young/Severe	-35.8	-15.1	20.8	-15.4	-0.4	0.42
CF67	Young/Severe	-33.5	-20.2	13.3	-25.1	-4.9	0.58
CF39	Young/Severe	-38.8	-3.8	35.0	-6.6	-2.8	0.42
CF47	Young/Severe	-55.7	-15.3	40.4	-17.6	-2.2	0.46
CF48	Young/Severe	-71.5	-14.1	57.4	-17.8	-3.7	0.36
CF49	Young/Severe	-49.8	-14.6	35.2	-20.5	-5.9	0.29
CF61	Young/Severe	-52.4	-20.2	32.2	-22.9	-2.7	0.24
CF65	Young/Severe	-53.0	-21.0	32.0	-21.9	-0.9	0.38
CF69	Young/Severe	-50.5	-22.5	28.0	-23.1	-0.6	0.54
CF76	Young/Severe	-45.5	-8.4	37.1	-9.4	-1.0	0.53

Bibliography

F J Accurso, S M Rowe, J P Clancy, M P Boyle, J M Dunitz, P R Durie, S D Sagel, D B Hornick, M W Konstan, S H Donaldson, R B Moss, J M Pilewski, R C Rubenstein, A Z Uluer, M L Aitken, S D Freedman, L M Rose, N Mayer-Hamblett, Q Dong, J Zha, A J Stone, E R Olson, C L Ordoñez, P W Campbell, M A Ashlock, and B W Ramsey. Effect of VX-770 in persons with cystic fibrosis and the G551D-CFTR mutation. *The New England Journal of Medicine*, 363(21):1991–2003, November 2010.

R W Albers. Biochemical aspects of active transport. *Annual Review of Biochemistry*, 36: 727–56, January 1967.

O Bardou, N T N Trinh, and E Brochiero. Molecular diversity and function of K+ channels in airway and alveolar epithelial cells. *American Journal of Physiology. Lung Cellular and Molecular Physiology*, 296(2):L145–55, February 2009.

B A Benjamin and E A Johnson. A quantitative description of the Na-K-2Cl cotransporter and its conformity to experimental data. *American Journal of Physiology. Renal Physiology*, 273 (3):F473–482, 1997.

B K Berdiev, Y J Qadri, and D J Benos. Assessment of the CFTR and ENaC association. *Molecular BioSystems*, 5(2):123–7, March 2009.

R C Boucher. Regulation of airway surface liquid volume by human airway epithelia. *Pflügers Archiv European Journal of Physiology*, 445(4):495–8, January 2003.

R C Boucher. Cystic fibrosis: a disease of vulnerability to airway surface dehydration. *Trends in Molecular Medicine*, 13(6):231–40, June 2007a.

R C Boucher. Airway surface dehydration in cystic fibrosis: pathogenesis and therapy. *Annual Review of Medicine*, 58:157–70, January 2007b.

R C Boucher, M J Stutts, M R Knowles, L Cantley, and J T Gatzy. Na+ transport in cystic fibrosis respiratory epithelia. Abnormal basal rate and response to adenylate cyclase activation. *Journal of Clinical Investigation*, 78(5):1245–52, November 1986.

R C Boucher, C U Cotton, J T Gatzy, M R Knowles, and J R Yankaskas. Evidence for reduced Cl-and increased Na+ permeability in cystic fibrosis human primary cell cultures. *Journal of Physiology*, 405(1):77, 1988.

J K Bubien. Epithelial Na+ channel (ENaC), hormones, and hypertension. *The Journal of Biological Chemistry*, 285(31):23527–31, July 2010.

J-H Chen, D A Stoltz, P H Karp, S E Ernst, A A Pezzulo, T O Moninger, M V Rector, L R Reznikov, J L Launspach, K Chaloner, J Zabner, and M J Welsh. Loss of Anion Transport without Increased Sodium Absorption Characterizes Newborn Porcine Cystic Fibrosis Airway Epithelia. *Cell*, 143(6):911–923, December 2010.

R D Coakley, B R Grubb, A M Paradiso, J T Gatzy, L G Johnson, S M Kreda, W K O'Neal, and R C Boucher. Abnormal surface liquid pH regulation by cultured cystic fibrosis bronchial epithelium. *Proceedings of the National Academy of Sciences of the United States of America*, 100(26):16083–8, December 2003.

J F Collawn, A Lazrak, Z Bebok, and S Matalon. The CFTR and ENaC Debate - How Important is ENaC in CF Lung Disease? *American Journal of Physiology. Lung Cellular and Molecular Physiology*, 0005:1141–1146, April 2012.

K Coote, H C Atherton-Watson, R Sugar, A Young, A MacKenzie-Beevor, M Gosling, G Bhalay, G Bloomfield, A Dunstan, R J Bridges, J R Sabater, W M Abraham, D Tully, R Pacoma, A Schumacher, J Harris, and H Danahay. Camostat attenuates airway epithelial sodium channel function in vivo through the inhibition of a channel-activating protease. *The Journal of Pharmacology and Experimental Therapeutics*, 329(2):764–74, May 2009.

C U Cotton. Basolateral potassium channels and epithelial ion transport. *American Journal of Respiratory Cell and Molecular Biology*, 23(3):270–2, September 2000.

E A Cowley and P Linsdell. Characterization of basolateral K+ channels underlying anion secretion in the human airway cell line Calu-3. *Journal of Physiology*, 538(Pt 3):747–57, February 2002.

C B Coyne, T M Gambling, R C Boucher, J L Carson, and L G Johnson. Role of claudin interactions in airway tight junctional permeability. *American Journal of Physiology. Lung Cellular and Molecular Physiology*, 285(5):L1166–78, November 2003.

R G Crystal, S H Randell, J F Engelhardt, J Voynow, and M E Sunday. Airway epithelial cells: current concepts and challenges. *Proceedings of the American Thoracic Society*, 5(7):772–7, September 2008.

A W Cuthbert. New horizons in the treatment of cystic fibrosis. *British Journal of Pharmacology*, 163(1):173–83, May 2011.

J C Davies, E W F W Alton, and A Bush. Cystic fibrosis. *BMJ (Clinical research ed.)*, 335 (7632):1255–9, December 2007.

J A Dodge, P A Lewis, M Stanton, and J Wilsher. Cystic fibrosis mortality and survival in the UK: 1947-2003. *European Respiratory Journal*, 29(3):522–6, March 2007.

S H Donaldson and R C Boucher. Sodium channels and cystic fibrosis. *Chest*, 132(5):1631–6, December 2007.

P K Dudeja, N Hafez, S Tyagi, C A Gailey, M Toofanfard, W A Alrefai, T M Nazir, K Ramaswamy, and F J Al-Bazzaz. Expression of the Na+/H+ and Cl-/HCO-3 exchanger isoforms in proximal and distal human airways. *The American Journal of Physiology*, 276(6 Pt 1):L971–8, June 1999.

M Duszyk and A S French. An analytical model of ionic movements in airway epithelial cells. *Journal of Theoretical Biology*, 151(2):231–247, July 1991.

C V Falkenberg and E Jakobsson. A biophysical model for integration of electrical, osmotic, and pH regulation in the human bronchial epithelium. *Biophysical Journal*, 98(8):1476–85, April 2010.

H Fischer, B Illek, W E Finkbeiner, and J H Widdicombe. Basolateral Cl channels in primary airway epithelial cultures. *American Journal of Physiology. Lung Cellular and Molecular Physiology*, 292(6):L1432–43, June 2007.

A N Flynn, O A Itani, T O Moninger, and M J Welsh. Acute regulation of tight junction ion

selectivity in human airway epithelia. *Proceedings of the National Academy of Sciences of the United States of America*, 106(9):3591–6, March 2009.

D C Gadsby, P Vergani, and L Csanády. The ABC protein turned chloride channel whose failure causes cystic fibrosis. *Nature*, 440(7083):477–83, March 2006.

E A Gaillard, P Kota, M Gentzsch, N V Dokholyan, M J Stutts, and R Tarran. Regulation of the epithelial Na+ channel and airway surface liquid volume by serine proteases. *Pflügers Archiv European Journal of Physiology*, 460(1):1–17, June 2010.

GJ M Garcia, R C Boucher, and TC Elston. Biophysical Model of Ion Transport across Human Respiratory Epithelia Allows Quantification of Ion Permeabilities. *Biophysical Journal*, 104 (3):716–726, February 2013.

H Garty and L G Palmer. Epithelial sodium channels: function, structure, and regulation. *Physiological Reviews*, 77(2):359–96, April 1997.

C Goubau, M Wilschanski, V Skalická, P Lebecque, K W Southern, I Sermet, A Munck, N Derichs, P G Middleton, L Hjelte, R Padoan, M Vasar, and K De Boeck. Phenotypic characterisation of patients with intermediate sweat chloride values: towards validation of the European diagnostic algorithm for cystic fibrosis. *Thorax*, 64(8):683–91, August 2009.

M Haas and B Forbush. The Na-K-Cl cotransporter of secretory epithelia. *Annual Review of Physiology*, 62:515–34, January 2000.

T Hartmann and A S Verkman. Model of ion transport regulation in chloride-secreting airway epithelial cells. Integrated description of electrical, chemical, and fluorescence measurements. *Biophysical Journal*, 58(2):391–401, August 1990.

Q He, S T Halm, J Zhang, and D R Halm. Activation of the basolateral membrane Cl- conductance essential for electrogenic K+ secretion suppresses electrogenic Cl- secretion. *Experimental Physiology*, 96(3):305–16, March 2011.

B Hille. *Ion channels of excitable membranes*. Sinauer, 2001.

T Hofmann, M J Stutts, A Ziersch, C Rückes, W M Weber, M R Knowles, H Lindemann, and R C Boucher. Effects of topically delivered benzamil and amiloride on nasal potential

difference in cystic fibrosis. *American Journal of Respiratory and Critical Care Medicine*, 157(6 Pt 1):1844–9, June 1998.

J-D Horisberger. ENaC-CFTR interactions: the role of electrical coupling of ion fluxes explored in an epithelial cell model. *Pflügers Archiv European Journal of Physiology*, 445(4):522–8, January 2003.

S K Inglis, M R Corboz, and S T Ballard. Effect of anion secretion inhibitors on mucin content of airway submucosal gland ducts. *The American Journal of Physiology*, 274(5 Pt 1):L762–6, May 1998.

O A Itani, F S Lamb, J E Melvin, and M J Welsh. Basolateral chloride current in human airway epithelia. *American Journal of Physiology. Lung Cellular and Molecular Physiology*, 293 (4):L991–9, October 2007.

O A Itani, J-H Chen, P H Karp, S E Ernst, S Keshavjee, K Parekh, J Klesney-Tait, J Zabner, and M J Welsh. Human cystic fibrosis airway epithelia have reduced Cl- conductance but not increased Na+ conductance. *Proceedings of the National Academy of Sciences of the United States of America*, 108(25):10260–5, June 2011.

E Kerem, J Reisman, M Corey, G J Canny, and H Levison. Prediction of mortality in patients with cystic fibrosis. *The New England Journal of Medicine*, 326(18):1187–91, April 1992.

M R Knowles, J T Gatzy, and R C Boucher. Increased bioelectric potential difference across respiratory epithelia in cystic fibrosis. *The New England Journal of Medicine*, 305(25):1489–95, December 1981.

M R Knowles, J T Gatzy, and R C Boucher. Relative ion permeability of normal and cystic fibrosis nasal epithelium. *Journal of Clinical Investigation*, 71(May), 1983.

M R Knowles, A M Paradiso, and R C Boucher. In vivo nasal potential difference: techniques and protocols for assessing efficacy of gene transfer in cystic fibrosis. *Human Gene Therapy*, 6(4):445–55, April 1995.

V Koefoed-Johnson and H H Ussing. The nature of the frog skin potential. *Acta Physiologica Scandinavica*, 42(3-4):298–308, June 1958.

M W Konstan, P B Davis, J S Wagener, K A Hilliard, R C Stern, L J H Milgram, T H Kowalczyk, S L Hyatt, T L Fink, C R Gedeon, S M Oette, J M Payne, O Muhammad, A G Ziady, R C Moen, and M J Cooper. Compacted DNA nanoparticles administered to the nasal mucosa of cystic fibrosis subjects are safe and demonstrate partial to complete cystic fibrosis transmembrane regulator reconstitution. *Human Gene Therapy*, 15(12):1255–69, December 2004.

J L Kreindler, K W Peters, R A Frizzell, and R J Bridges. Identification and membrane localization of electrogenic sodium bicarbonate cotransporters in Calu-3 cells. *Biochimica et Biophysica Acta*, 1762(7):704–10, July 2006.

R Latta, C Clausen, and L C Moore. General method for the derivation and numerical solution of epithelial transport models. *The Journal of Membrane Biology*, 82(1):67–82, January 1984.

M H Levin, J K Kim, J Hu, and A S Verkman. Potential difference measurements of ocular surface Na+ absorption analyzed using an electrokinetic model. *Investigative Ophthalmology & Visual Science*, 47(1):306–16, January 2006.

V L Lew, H G Ferreira, and T Moura. The behaviour of transporting epithelial cells. I. Computer analysis of a basic model. *Proceedings of the Royal Society of London. Series B, Containing papers of a Biological character. Royal Society (Great Britain)*, 206(1162):53–83, November 1979.

G L Lukacs and A S Verkman. CFTR: folding, misfolding and correcting the ΔF508 conformational defect. *Trends in Molecular Medicine*, 18(2):81–91, March 2012.

M Mall, A Wissner, R Schreiber, J Kuehr, H H Seydewitz, M Brandis, R Greger, and K Kunzelmann. Role of K(V)LQT1 in cyclic adenosine monophosphate-mediated Cl(-) secretion in human airway epithelia. *American Journal of Respiratory Cell and Molecular Biology*, 23 (3):283–9, September 2000.

MATLAB. *Version 7.11.0 (R2010b)*. The MathWorks Inc., Natick, Massachusetts, 2010.

P G Middleton, D M Geddes, and E W Alton. Protocols for in vivo measurement of the ion transport defects in cystic fibrosis nasal epithelium. *European Respiratory Journal*, 7(11): 2050–2056, November 1994.

S L Moser, S A Harron, J Crack, J P Fawcett, and E A Cowley. Multiple KCNQ potassium channel subtypes mediate basal anion secretion from the human airway epithelial cell line Calu-3. *The Journal of Membrane Biology*, 221(3):153–63, February 2008.

J A Novotny and E Jakobsson. Computational studies of ion-water flux coupling in the airway epithelium. II. Role of specific transport mechanisms. *American Journal of Physiology*, 270 (6 Pt 1):C1764–72, June 1996a.

J A Novotny and E Jakobsson. Computational studies of ion-water flux coupling in the airway epithelium. I. Construction of model. *American Journal of Physiology*, 270(6 Pt 1):C1751–63, June 1996b.

D Parker and A Prince. Innate immunity in the respiratory epithelium. *American Journal of Respiratory Cell and Molecular Biology*, 45(2):189–201, August 2011.

A A Pezzulo, X X Tang, M J Hoegger, M H A Alaiwa, S Ramachandran, T O Moninger, P H Karp, C L Wohlford-Lenane, H P Haagsman, M van Eijk, B Bánfi, A R Horswill, D A Stoltz, P B McCray, M J Welsh, and J Zabner. Reduced airway surface pH impairs bacterial killing in the porcine cystic fibrosis lung. *Nature*, 487(7405):109–13, July 2012.

R L Post, C Hegyvary, and S Kume. Activation by Adenosine Triphosphate in the Phosphorylation Kinetics of Sodium and Potassium Ion Transport Adenosine Triphosphatase. *The Journal of Biological Chemistry*, 247(20):6530–6540, October 1972.

J H Poulsen. Bicarbonate Conductance and pH Regulatory Capability of Cystic Fibrosis Transmembrane Conductance Regulator. *Proceedings of the National Academy of Sciences*, 91 (12):5340–5344, June 1994.

P M Quinton. Cystic fibrosis: impaired bicarbonate secretion and mucoviscidosis. *The Lancet*, 372(9636):415–417, 2008.

P M Quinton. Role of epithelial HCO3- transport in mucin secretion: lessons from cystic fibrosis. *American Journal of Physiology. Cell Physiology*, 299(6):C1222–33, December 2010.

I H Quraishi and R M Raphael. Computational model of vectorial potassium transport by cochlear marginal cells and vestibular dark cells. *American Journal of Physiology. Cell Physiology*, 292(1):C591–602, January 2007.

F Ratjen and G Döring. Cystic fibrosis. *The Lancet*, 361(9358):681–689, 2003.

A Raue, C Kreutz, T Maiwald, J Bachmann, M Schilling, U Klingmüller, and J Timmer. Structural and practical identifiability analysis of partially observed dynamical models by exploiting the profile likelihood. *Bioinformatics*, 25(15):1923–9, August 2009.

A Raue, C Kreutz, T Maiwald, U Klingmuller, and J Timmer. Addressing parameter identifiability by model-based experimentation. *IET Systems Biology*, 5(2):120–30, March 2011.

L Reuss. Ussing's two-membrane hypothesis: the model and half a century of progress. *The Journal of Membrane Biology*, 184(3):211–7, December 2001.

J Rommens, B Kerem, N Alon, R Rozmahel, Z Grzelczak, J Zielenski, S Lok, N Plavsic, J Chou, and al. Et. Identification of the cystic fibrosis gene: cloning and characterization of complementary DNA. *Science*, 245(4922):1066–1073, September 1989.

S M Rowe, S Miller, and E J Sorscher. Cystic fibrosis. *The New England Journal of Medicine*, 352(19):1992–2001, May 2005.

S M Rowe, J P Clancy, and M Wilschanski. Nasal potential difference measurements to assess CFTR ion channel activity. *Methods in Molecular Biology (Clifton, N.J.)*, 741:69–86, January 2011.

A Saltelli. *Sensitivity Analysis in Practice: A Guide to Assessing Scientific Models*. John Wiley & Sons, 2004.

S G Schultz, R A Frizzell, and H N Nellans. An equivalent electrical circuit model for "sodium-transporting" epithelia in the steady-state. *Journal of Theoretical Biology*, 65(2):215–29, March 1977.

N J Simmonds, L D'Souza, M Roughton, E W F W Alton, J C Davies, and M E Hodson. Cystic fibrosis and survival to 40 years: a study of cystic fibrosis transmembrane conductance regulator function. *European Respiratory Journal*, 37(5):1076–82, May 2011.

J J Smith, S M Travis, E P Greenberg, and M J Welsh. Cystic fibrosis airway epithelia fail to kill bacteria because of abnormal airway surface fluid. *Cell*, 85:229–236, 1996.

N P Smith and E J Crampin. Development of models of active ion transport for whole-cell modelling: cardiac sodium-potassium pump as a case study. *Progress in Biophysics and Molecular Biology*, 85(2-3):387–405, 2004.

E A Sobie. Parameter sensitivity analysis in electrophysiological models using multivariable regression. *Biophysical Journal*, 96(4):1264–74, February 2009.

M J Stutts. Cystic Fibrosis Transmembrane Conductance Regulator Inverts Protein Kinase A-mediated Regulation of Epithelial Sodium Channel Single Channel Kinetics. *Journal of Biological Chemistry*, 272(22):14037–14040, May 1997.

M J Stutts, C U Cotton, J R Yankaskas, E Cheng, M R Knowles, J T Gatzy, and R C Boucher. Chloride uptake into cultured airway epithelial cells from cystic fibrosis patients and normal individuals. *Proceedings of the National Academy of Sciences of the United States of America*, 82(19):6677–81, October 1985.

M J Stutts, C Canessa, J Olsen, M Hamrick, J Cohn, B Rossier, and R C Boucher. CFTR as a cAMP-dependent regulator of sodium channels. *Science*, 269(5225):847–850, August 1995.

R Tarran, L Trout, S H Donaldson, and R C Boucher. Soluble mediators, not cilia, determine airway surface liquid volume in normal and cystic fibrosis superficial airway epithelia. *The Journal of General Physiology*, 127(5):591–604, May 2006.

A L Taylor, J-M Goaillard, and E Marder. How multiple conductances determine electrophysiological properties in a multicompartment model. *Journal of Neuroscience*, 29(17):5573–86, April 2009.

J Vanlier, C A Tiemann, P A J Hilbers, and N A W van Riel. An integrated strategy for prediction uncertainty analysis. *Bioinformatics*, 28(8):1130–5, April 2012.

M R Villareal. Respiratory_system_complete_en.svg. *Wikimedia Commons*, 2007a. [Online; accessed 30-October-2013].

M R Villareal. Scheme_facilitated_diffusion_in_cell_membrane-en.svg. *Wikimedia Commons*, 2007b. [Online; accessed 30-October-2013].

M R Villareal. Scheme_sodium-potassium_pump-en.svg. *Wikimedia Commons*, 2007c. [Online; accessed 30-October-2013].

N J Warren, M H Tawhai, and E J Crampin. A mathematical model of calcium-induced fluid secretion in airway epithelium. *Journal of Theoretical Biology*, 259(4):837–49, August 2009.

A M Weinstein. Chloride transport in a mathematical model of the rat proximal tubule. *American Journal of Physiology. Renal Physiology*, 263(5):F784–798, November 1992.

A M Weinstein. Modeling epithelial cell homeostasis: assessing recovery and control mechanisms. *Bulletin of Mathematical Biology*, 66(5):1201–40, September 2004.

T F Weiss. *Cellular Biophysics, Volume 1: Transport*. The MIT Press, 1996.

DC Whitcomb and GB Ermentrout. A mathematical model of the pancreatic duct cell generating high bicarbonate concentrations in pancreatic juice. *Pancreas*, 29(2):30–40, 2004.

N K Wills, L Reuss, and S A Lewis. *Epithelial transport: a guide to methods and experimental analysis*. Springer, 1996.

N J Willumsen and R C Boucher. Shunt resistance and ion permeabilities in normal and cystic fibrosis airway epithelia. *American Journal of Physiology*, 256(5 Pt 1):C1054–63, May 1989.

N J Willumsen and R C Boucher. Sodium transport and intracellular sodium activity in cultured human nasal epithelium. *American Journal of Physiology*, 261(2 Pt 1):C319–31, August 1991a.

N J Willumsen and R C Boucher. Transcellular sodium transport in cultured cystic fibrosis human nasal epithelium. *American Journal of Physiology. Cell Physiology*, 261(2):C332–341, 1991b.

N J Willumsen, C W Davis, and R C Boucher. Cellular Cl- transport in cultured cystic fibrosis airway epithelium. *American Journal of Physiology*, 256(5 Pt 1):C1045–53, May 1989a.

N J Willumsen, C W Davis, and R C Boucher. Intracellular Cl- activity and cellular Cl- pathways in cultured human airway epithelium. *American Journal of Physiology*, 256(5 Pt 1): C1033–44, May 1989b.

M Wilschanski and Y Yahav. Gentamicin-induced correction of CFTR function in patients with cystic fibrosis and CFTR stop mutations. *The New England Journal of Medicine*, 349(15): 1433–1441, 2003.

J J Wine and N S Joo. Submucosal glands and airway defense. *Proceedings of the American Thoracic Society*, 1(1):47–53, January 2004.